Computational Analysis of Dynamic Bone Structure and Processes
–Osteocyte Networks & Healing–

Dissertation
zur Erlangung des akademischen Grades
doctor rerum naturalium
(Dr. rer. nat.)
im Fach Physik
eingereicht an der

Mathematisch-Naturwissenschaftlichen Fakultät
der Humboldt-Universität zu Berlin

von
Diplom Physiker Felix Repp

Präsident der Humboldt-Universität zu Berlin
Prof. Dr. Jan-Hendrik Olbertz

Dekan der Mathematisch-Naturwissenschaftlichen Fakultät
Prof. Dr. Elmar Kulke

Gutachter: 1. Prof. Dr. Dr. h.c. Peter Fratzl
2. Prof. Dr. Igor M. Sokolov
3. Prof. Dr. Philipp J. Thurner

Tag der mündlichen Prüfung: 30. März 2015

KURZFASSUNG

Das menschliche Skelett besteht aus einem dynamischen Material welches in der Lage ist zu heilen, sowie sich durch strukturellen Umbau an mechanische Beanspruchung anzupassen. In dieser Arbeit ist die mechanische Regulierung dieser Prozesse untersucht worden, die durch spezialisierte Knochenzellen ermöglicht werden. Hierfür ist ein Computermodell, sowie die dreidimensionale Abbildung des Knochens und die Auswertung dieser Bilder benutzt worden.

An dem Heilungsprozesses von Knochen sind verschiedene Gewebetypen beteiligt. Dabei hängt die räumliche und zeitliche Anordnung dieser Gewebe von der mechanischen Belastung ab. Ein Computermodell, welches den vollständigen Verlauf der Heilung beschreibt, wurde mit der dokumentierten Gewebeentwicklung eines Tierexperimentes an Schafen zu verglichen. Verschiedene Hypothesen, wie die mechanische Stimulation die Bildung verschiedene Gewebe beeinflusst, wurden getestet. Wir beobachteten, dass die mittlere Phase des Heilungsverlaufes, in welcher Knorpel im Frakturspalt gebildet wird, am meisten durch die mechanischen Regulation beeinflusst wird. Zwar ließen sich durch den Vergleich mit dem Tierexperiment keine der Hypothesen verwerfen, jedoch konnten wir Vorschläge machen, worauf bei zukünftigen Experimenten verstärkt geachtet werden soll.

Es wird angenommen dass der Umbauprozesses des Knochens vom dichten Netzwerk der Osteozyten mechanisch reguliert wird. Diese Zellen sind in den Knochen eingebettet und über ein dichtes Netzwerk aus engen Kanälen, den sogenannten Canaliculi, miteinander verbunden. Gefärbt mit Rhodamin, wurde dieses Netzwerk mittels konfokaler Mikrokopie dreidimensional abgebildet. Spezielle Routinen zur Auswertung der Netzwerkorientierung sowie dessen Dichte wurden entwickelt. Dabei haben wir uns auf strukturelle Bausteine des Knochens, sogenannte Osteone, im Oberschenkelknochen von gesunden Frauen mittleren Alters, konzentriert. Innerhalb dieser Osteone haben wir hohe Schwankungen der Netzwerkdichte, mit ausgedehnten Bereichen ohne Netzwerk gefunden. Der größte Teil des Netzwerkes ist radial zum Zentrum des Osteones ausgerichtet. Dies entspricht der Richtung in der Knochengewebe aufgebaut wird. Die Orientierung des zu dieser Richtung senkrechten Anteils des Netzwerkes rotiert abhänging von der Position entlang der Aufbaurichtung. Dies verdeutlicht den Zusammenhang zwischen der Netzwerkorientierung und der Vorzugsrichtung des Kollagens, dem faserigen Bestandteils des Knochens. Dieses drehende Verhalten der Canaliculi entspricht dem “twisted plywood” Modell der Orientierung des Kollagens. Allerdings zeigt die Auswertung der Daten zusätzliche strukturelle Unterschiede im Netzwerk. Zukünftig sollten diese neuen quantitativen Beschreibungen des Osteozytennetzwerkes genutzt werden, um den Einfluss von mechanischer Belastung, des Alters und Knochenkrankheiten auf die Architektur des Netzwerkes zu untersuchen.

ABSTRACT

Our skeleton is composed of a dynamic material that is capable of healing and of adapting to changing mechanical loads through structural remodeling by specialized bone cells. In this thesis the mechano-regulation of these dynamic processes are addressed using computer modeling and 3-dimensional imaging and image analysis.

During bone healing an intricate pattern of different newly formed tissues around the fracture site can be observed that evolves in time and is influenced by the mechanical loading. Using a computer model which is describing this temporal-spatial evolution of tissue types for the full time-course of healing, this evolution is compared to the documented evolution of an animal experiment on sheep. Different hypotheses were tested how the mechanical stimulation results in the formation of different tissues. We found that the intermediate phase of healing, where cartilage forms in the fracture gap, is strongest influenced by changes in the mechano-regulation. However, the comparison with the outcome of the animal experiments does not allow to falsify any of the hypotheses, but suggests a different design of future animal experiments.

Bone remodeling is thought to be mechano-regulated by the dense network of osteocytes. These osteocytes are embedded in bone and are connected to each other via a network of narrow canaliculi. The 3-dimensional structure of the network was imaged using rhodamine staining and laser scanning confocal microscopy. Image analysis tools were developed to determine the network topology and to analyze its density and orientation. The analysis focused on osteons, the building blocks of cortical bone, in samples taken from the femur of middle-age, healthy women. Within an osteon we found a large variability of the network density with extensive regions without network. Most of the network is oriented radially towards the center of the osteon, i.e. parallel to the direction in which the bone material is deposited. The network perpendicular to this direction twists when moving along the direction of bone deposition. A correlation with the main orientation of collagen – the fibrous constituent of bone – was detected, showing that the orientation of the canaliculi agrees with the twisted plywood model for the collagen orientation. However, our data indicates additional structural changes in the network alignment. In the future the new quantitative description of the osteocyte cell network as explored in this thesis should be applied to study how mechanical loading, age and bone diseases change the architecture of the network.

CONTENTS

CHAPTER 1

INTRODUCTION

1.1 Motivation

Bone is the biggest and heaviest of all human organs with remarkable mechanical properties, e.g. its hardness. These properties have been recognized more than 40000 years ago, when bones were used as a material to build tools and musical instruments [Zhang et al., 1999]. The fact that such man-made objects as well as fossils endure until today might provide the impression that bone is a very static material.

While being tough and durable, in a living system, bone shows remarkable dynamic properties. Bone is not a homogeneous material and therefore requires an elaborate growing mechanism. Its mechanical robustness arises from an intricate hierarchical structure that adapts to the mechanical demands on the bone [Roux, 1885; Wolff, 1893; Frost, 1988; Weinkamer and Fratzl, 2011].

Much knowledge about the structure of the bone and its relationship to its mechanical function is already known, but not only is it interesting how such a complex tissue can be formed, it should also be understood that a strong and healthy bone is not to be taken for granted. Many bone diseases exist that result in reduced bone quality [Seeman and Delmas, 2006] that is not suited for everyday loads. The best known examples are osteogenesis imperfecta, also termed brittle bone disease and osteoporosis. To understand bone diseases and to find possible treatments, an improved understanding of the dynamic processes such as bone formation as well as bone remodeling is needed.

Adaptation of bone to mechanical loads results in structures that provide great stability while at the same time allow the weight of the bones to be minimal. Bone formation and remodeling is therefore carefully regulated. In a regulated system, the classical terminology is that of actuators, sensors, and controllers. In the case of bone, the actuators are specialized cells that can build new bone (osteoblasts) and resorb bone (osteoclasts). The sensing and control of bone remodeling is thought to occur with embedded bone cells called osteocytes. Osteocytes are cells that live in small voids within mineralized bone called lacunae which are connected to each other by an intricate network of small canals called canaliculi. The network consisting of the lacunae and the connections between them is referred to as osteocyte lacuno-canalicular network (OLCN). The complexity of these networks suggests that a collective functioning of connected osteocytes might be able to have certain processing capabilities and even memory [Turner et al., 2002]. This network is important for communication of the osteocytes with each other as well as signaling to other cells [Dallas et al., 2013]. Additionally the OLCN has most likely a major role in sensing deformation of the bone induced by loading [Burger et al., 1999; Klein-Nulend et al., 2013]. In this work, the architecture of the OLCN was studied, with special interest in how it relates to the specific bone structure and organization built at the same time as the osteocyte network was formed.

Mechanical conditions do not only regulate bone growth and adaptation in response to everyday loads, they also regulate bone healing after a fracture [Pauwels, 1960; Carter et al., 1988]. It is well known that a fracture needs to be stabilized to be able to heal, but if no load at all is allowed during healing, the healing process will be less successful. A part on the thesis focuses on the question to what extend a local mechanical control can regulate bone tissue development as observed during the healing process.

1.2 Studying Bones, Experimental Approaches vs. Modeling

Material scientists do not rely only on measuring macroscopic mechanical properties such as stiffness to analyze structures. Bone tissue material properties can be measured on the nano to micron scale using specialized methods such as nano-indentation or scanning acoustic microscopy (micron-scaled). In order to understand how macroscopic properties relate to nano- and microscopic properties, an understanding of the bone structure across these length scales is necessary. Much knowledge about bone arises from structural studies using microscopes. While light microscopy was the major tool in the 17–19th century, in the second half of the 20th century, electron microscopy began to be heavily used to study bone samples [Marotti, 1990]. Despite the fact that 3D imaging methods (i.e. with computed tomography [Feldkamp et al., 1989]) have already being used to study bone micro structure for 35 years, most descriptions of bone are based on qualitative 2-dimensional (2D) observation, from which 3-dimensional (3D) interpretations can sometimes be concluded.

A typical limitation in studying bone is that living bone cannot be directly examined, because the bone sample must be cut. To learn about the effect of time on bone development, or the effect of different conditions on bone within *in vivo* experiments, observations have to be performed on different samples of bone, typically originating from different donors. This does not only raise the problem of inter-individual bone differences, but also requires meaningful quantities for statistical comparison. Some conclusions about the transient development of the bone formation process can be drawn when specific markers are used in living bone. These markers are administered to the patient or the animal and accumulate in the newly formed bone, thus providing insight into the time development if several distinct labels are used at different time points [Frost, 1969]. This analysis still requires the extraction of the bone from the donor so that it may be cut and prepared for observation.

To study active processes in living tissue, especially the living cells, cell biologists perform *in vitro* experiments [Kalajzic et al., 2013]. This is a useful tool to study the response of cells to controlled stimuli. However, how much of the cell behavior in the artificial *in vitro* conditions resembles their normal functions in bone is not always clear [Marotti, 1996].

While cell biologists, biologists, biochemists, and physiologists study bone, physicists can contribute to bone research in several specific ways:

- designing and interpreting experimental and analytical devices, e.g. for mechanical testing or imaging and using this methodology for characterizing the bone material
- providing new ideas for a systematic visualization and quantification especially of large 3D data sets
- modeling the time development of biological processes to learn about the regulating processes that give rise to the observed resulting structures.

1.3 Aim of the Work

To learn about bone and its response to its mechanical environment, two different approaches were used in this thesis: on one hand a computer model of bone healing was used to study mechano-regulation on the tissue level, on the other hand, *ex vivo* images of osteocyte cell networks were examined, quantified, and analyzed.

During bone healing, new bone is formed during a relatively short time, with many similarities with the process of ossification that occurs during skeletal growth and development [Gerstenfeld et al., 2003; Shapiro, 2007]. The shorter time scales for bone healing make it feasible to study the bone healing process under controlled clinical conditions. The computer model used to investigate mechano-regulation of bone healing was designed to be comparable to results from a clinical fracture healing study in sheep, which has been performed at the Charité [Epari et al., 2006]. Based on the histological data from this study, Vetter et al. [2010] concluded a "mean healing path" which consists of 6 images showing the arrangement of tissues at six different stages of the healing process. Using this histological data as well as material testing data (nanoindentation) the spatial arrangement and the material properties of different skeletal tissues the experimental observations can be compared with the outcome of a computer model. Vetter et al. [2011b] further developed a lean model for bone healing that describes tissue development as a function of mechanical stimulation. As many biological processes are complex and finding the parameters that regulate them is very dificult, this work aimed to use a lean model with only a few parameters and a quantitative comparison of the spatial distribution of the time development of different skeletal tissues between *in vivo* experiments and model predictions. Using suitable parameters, this model mimicked basic features of the early healing process.

As part of this work, the bone healing model was extended to include the process of bone resorption, which allows to model the changes in healing bone until the bone is fully restored. Furthermore by changing the mechano-regulation of the model, hypotheses on how local cellular control can influence the overall tissue development were tested. The results of the modified models were compared and the implications of the findings are discussed with respect to how future investigations can address remaining questions. While in this part bone cells during bone healing were treated and modeled implicitly, in the second study, 3D images of osteocyte networks were obtained using confocal microscopy and were analyzed with tools that were developed for this data.

Even though the importance of the OLCN is generally accepted [Aarden et al., 1994; Bonewald, 2006], very little quantitative data describing these networks are available [Sugawara et al., 2005; Kerschnitzki et al., 2013]. Very often, network analysis depends on the interpretation of 2D images [Marotti et al., 1995a; Ferretti et al., 1999]. This thesis presents a 3D study of the OLCN in human osteons within cortical bone. Osteons represent a localized structural and functional bone unit which can be easily recognized by light microscopy. Osteons also have a reasonably well described formation process [Parfitt, 1994], and they provide structural elements that have been the subject of many structural analyses [Knese et al., 1954; Skedros et al., 2011; Shahar et al., 2011].

While the 3D analysis of osteocyte networks is not novel to our institute [Kerschnitzki et al., 2013], this work extends previous methods by correlating OLCN properties quantified for the first time to the local osteonal lamellar structure that was imaged simultaneously. Not only could we address the question of how the orientation of the OLCN is related to the osteonal bone tissue material that hosts these structures, but we can quantify the OLCN and how its orientation is related to the osteonal formation process that happens simultaneously with the construction of the OLCN [Palumbo et al., 2004]. Recognizing architectural features that arise due to limitations of the osteonal formation process leads to hypotheses describing how the OLCN is adapted to certain functions within osteons. Besides the use of algorithms that were developed in our department to skeletonize 3D image data of the connection between osteocytes which allows a comprehensive analysis of the network, in this work, a computational framework was developed to process 3D confocal images of the OLCN and the lamellar structures. Many novel descriptors of the osteocyte network were then computed and visualized.

1.4 Structure of this Work

Chapter 2 aims to introduce the reader to the terminology as well as the current understanding of the topics related to this work and highlights open questions about bone healing, OLCNs and osteons in order to associate the results of the two studies with the current research. A brief overview on the structural features of bone will provide a contextual perspective of osteons and how they are formed. To be able to discuss the orientation of the osteocyte network with respect to the surrounding extracellular matrix, several published descriptions regarding the collagen arrangement are presented. While the collagen orientation within the lamellae has been the subject of many studies, no simple model describes all of the observed features. Not only are the details of the lamellar bone structure unsolved, it also remains unclear how much these lamellar patterns are arranged by the cells that formed the lamellar bone. Since both, lamellae as well as osteocytes, are easily observed with optical microscopes many fundamental observations date back more than 100 years ago. Therefore this chapter reviews several publications from the last two centuries. As recent reviews summarize proposed functions of the osteocyte network [Bonewald, 2011; Schaffler et al., 2014], only the basic ideas are described. The description of bone healing is limited to the minimum background material necessary to understand the context of the model used, as our perspective on this subject has been explained previously [Vetter, 2010].

Both topics of the work: healing (Chapter 3) and on osteocyte networks (Chapter 4) each include seperated sections on methods, results and discussion. Chapter 3 is based on a manuscript submitted to "Medical & Biological Engineering & Computing". Besides the study of the healing process to a point where conditions before the fracture are restored, three different hypotheses on the mechano-regulation are tested and the effects on the healing process are compared after free parameters in the model are adjusted. Chapter 4 describes all the steps performed to obtain quantitative descriptions from images of the OLCN, as well as on the images containing the information of lamellar organization. The analysis can be separated into three different topics. The first topic is the study of inhomogeneities of OLCN density, especially with respect to the direction in which the network was constructed. Second, the orientation of the OLCN is analyzed and compared to the structure of the osteon. In the last topic, relationships between the lamellar arrangement and the arrangement of the cell network are examined.

Chapter 2

Background

Bones, like any other organ, cannot be understood completely when studied isolated from the living body, as there is a complex interaction of the bone with the organism, and the organism's environment. The function of bone is not purely limited to mechanical roles, such as protecting soft organs, or transmitting forces and sound, but bone is also essential for the synthesis of blood* and has an important role in metabolism e.g. as storage for calcium and phosphorus, as summarized in the top level of Figure 2.1 which visualizes the **topics of this chapter and their relation**. While these metabolic and synthetic functions are important, many of the structural features of bone can be explained by the structural adaptation to mechanical needs and the loading conditions present in bone. How the dynamic changes in these structural features are regulated by the mechanical conditions is the focus of this work. Bone is composed of cells, and inorganic and organic materials. The material itself is composed of collagen fibers, non-collagenous proteins, and a mineral of calcium phosphate (apatite) (left-hand side of Figure 2.1). This mineralized extracellular matrix (ECM) is most important for the material properties of bone. The cells within bone on the other hand are not only important for the metabolic functions but also make bone a dynamic material (right-hand side of Figure 2.1). The most important cells in bone are osteoblasts that build new bone material, osteoclasts which resorb bone and, embedded in the bone matrix, are osteocytes which control the activity of the two other cell types.

An important aim of our research group is to learn more about the role of cells in controlling the dynamic processes in bone, in particular the mechano-regulation of these processes. Unfortunately the effects of such dynamic processes on bone cannot be easily studied in real time. Another complication of studying dynamic processes in bone is that the details of the static, *ex vivo* bone structure are only partly understood. This chapter provides background information about bone structure and function at different length scales in order to provide the context for our novel observations, and describe which research frontiers could benefit from our results. Figure 2.1 shows the relationships between the different topics of this thesis, with the key subjects of this chapter highlighted in red, and the aspects which are a minor focus of this thesis highlighted in blue.

The most abundant type of cells within bone are osteocytes. Osteocytes originate from

---

*This happens in the bone marrow.

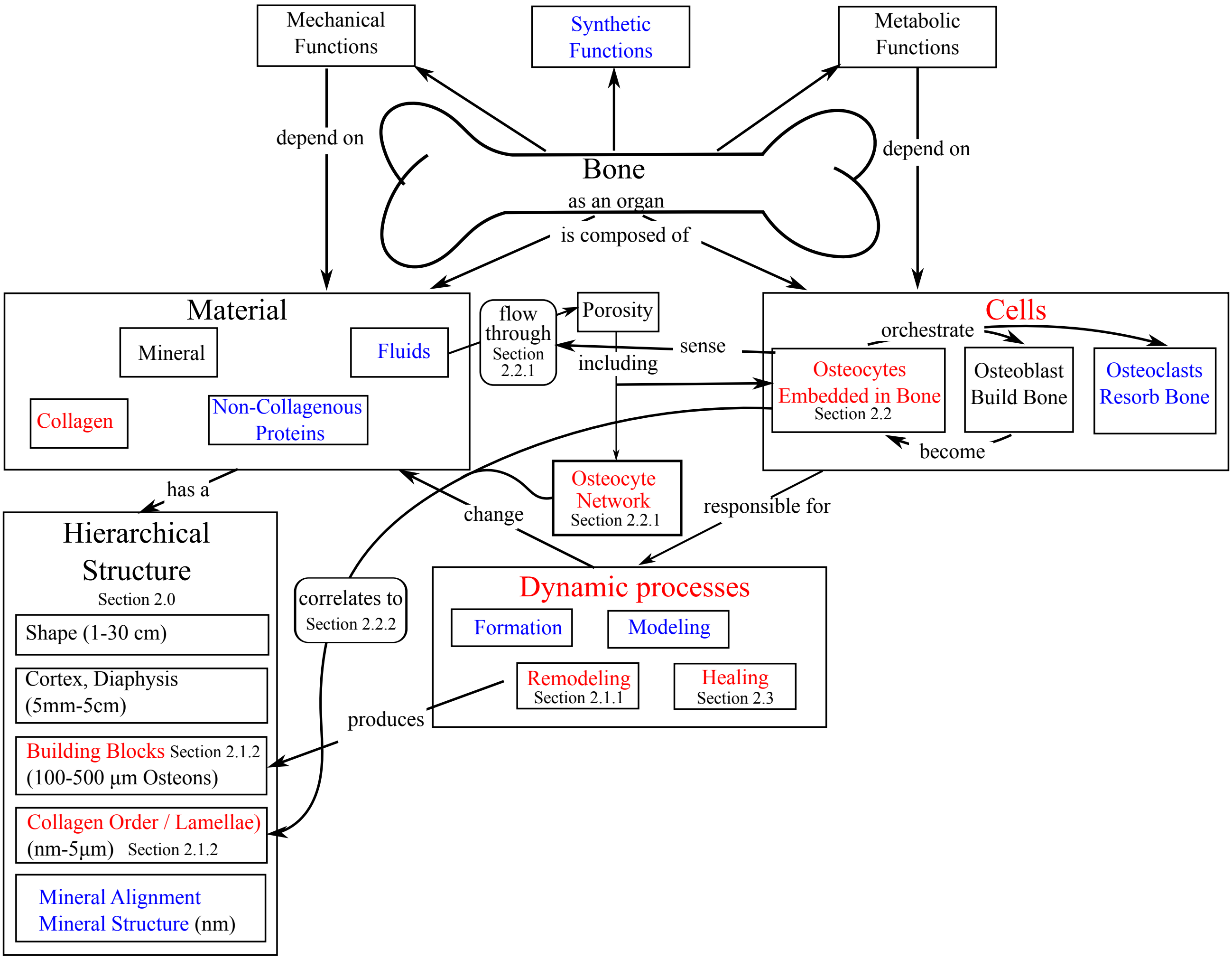

Figure 2.1: Relationship of the content of of this chapter. Red colored topics are discussed in more detail, blue topics are of minor interest for this work. While the cells and the dynamic processes that change the material are most important, structural aspects of the material will also be discussed as they are the result of dynamic processes. Osteocytes, which are supposed to orchestrate osteoblasts during remodeling, are embedded in the bone matrix and form an extensive network. This structure of the network determines fluid transport essential for nutrition and communication. Osteocytes are further proposed to sense fluid flow as induced by loading, which assigns them a key role in mechano-regulation in bone.

osteoblasts, which are bone cells synthesizing collagen for new ECM formation. During the ECM production process, some of the osteoblast cells become embedded within the newly-forming ECM. Once embedded, these cells are called osteocytes (Section 2.2). Within the ECM, osteocytes are connected to each other through canaliculi, forming an extensive cellular network. Many functions (Section 2.2.1) of osteocytes and their network have been proposed, assigning them a major role in bone. In particular, they are thought to play a key role in coordinating dynamic bone processes.

In a continious process called remodeling, bone cells called osteoclasts locally resorb old bone, and osteoblasts rebuild new bone (Section 2.1.1). A typical organized bone substructure arising from this remodeling process is an osteon. One part of this thesis deals with the analysis of the osteocyte network architecture within such osteons. Osteons are composed of structural subfeatures which are circular layers of ECM arranged like the annual rings of wood; these rings are called lamellae (Section 2.1.2). Osteocyte network properties are related to the lamellar structure, as well to the osteonal formation process (Section 2.2.2). Lamellae, which are an ordered motif of osteonal collagen, are on the same length scale as osteocytes, and can be visualized with optical techniques.

2.0.1 Hierarchical Structure of Bone

The organization of collagen on the micrometer scale is only one of several levels of a hierarchical structure that have an effect on the mechanical properties of the bone [Rho et al., 1998; Weiner and Wagner, 1998; Fratzl and Weinkamer, 2007; Reznikov et al., 2014a]. At larger length scales, the shapes of bones differ significantly. These differences can be related to the different mechanical functions of the bones. For example, the skull is composed of flat bones that protect the sensitive brain, and the vertebrae allow complex movements while protecting the spinal cord. The bones that were studied in this work are long bones in particular femur and tibia. These bones carry most of the body's weight, and must withstand the large forces experienced during movement.

Bones are composed of regions that can be classified as either spongy/trabecular bone, which has many voids on the mm scale, or compact/cortical bone, which is much denser and only has pores on the μm scale. The bone type studied in this work is compact bone, and the investigation of this work focuses on its pores. Long bones (Figure 2.2) are composed mostly of compact bone, which is also referred to as cortex. The ends of long bones contain trabecular bone, but these regions are not part of this study. The cortex of adult human long bone consists almost completely of lamellar bone. Depending on the cortex formation process, different micro-structural patterns arise. In this thesis we study cylindrical structures called secondary osteons which are formed by bone remodeling, i.e. the replacement of older bone tissue by new bone (Section 2.1.1)*.

---

*Opposed to secondary osteons, primary osteons are not the result of a remodeling process but are present in primary bone. Following the definition of Marotti [1996], primary bone consist of mineralized cartilage, minor amounts of disorganized (also called "woven") bone, as well as primary osteons which were build into cavities within these other structures. Another structure within primary bone are circumferential lamellae, which are parallel to the outer surface of the cortex and are formed during radial growth of the bone. Secondary osteons can be identified by the patterns of the lamellae and the degree of mineralization, which arise from the replacement of bone during the remodeling (e.g. secondary

The ends of long bones, called the epiphyses, are filled with trabecular bone, while the shaft in the middle of the bone, called the diaphysis, contains almost no trabeculae. Both, diaphysis and epiphysis are filled with bone marrow responsible for blood cell production. The outer surface of bone is covered with a cellular connective tissue called periosteum. The periosteum is not only important for bone growth, but also essential for bone healing [Gerstenfeld et al., 2003] (Section 2.3), as it is a source for progenitor and stem cells that can differentiate into different cell types promoting healing. All of the bone, even the dense cortex is highly vascularized.

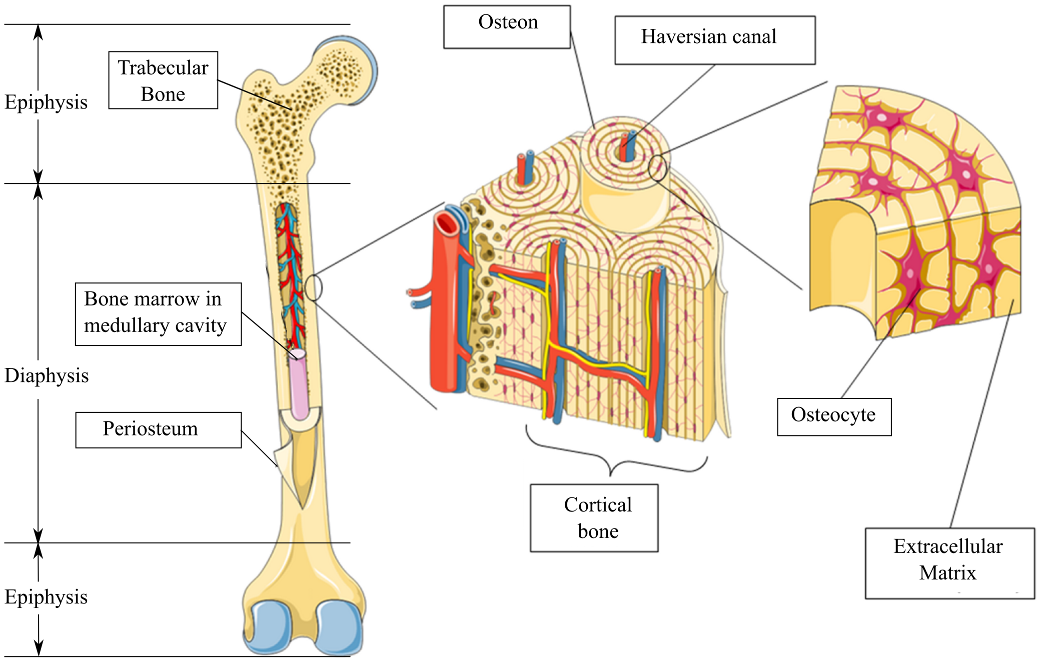

Figure 2.2: Structure of a long bone. While the epiphysis consists mostly of trabecular bone, the diaphysis is composed of cortical bone. Cortical bone is relatively dense, with some voids for blood vessels (Haversian canal) to supply the cells embedded within the bone (osteocytes). In the diaphysis, the medullary cavity is filled with bone marrow. Adapted from Bao et al. [2013], Figure 1, licensed under Creative Commons Attribution 3.0 [2007]

Bone ECM is produced by osteoblasts, which first produce the collagenous matrix (osteoid) that mineralizes by incorporating apatite crystals at a later time point. The organic component of the ECM matrix consists mainly of type I collagen, which is a chainlike protein that forms a triple helix. Many collagen molecules align parallel with respect to each other, forming collagen fibrils. Opposed to the classification of bone according to its porosity, bone can also be classified in terms of its organization of collagen on a (sub-)micron-scale. Woven bone is composed of a disorganized extracellular collagen matrix, while lamellar bone contains collagen that is arranged in layers. Within these layers, the fibrils form bundles that are called collagen fibers. While woven bone is mechanically weaker than lamellar bone, it is formed more rapidly than lamellar bone.

---

osteons overlap with older osteons) as well as the presence of a cement line (Section 2.1.1). In the rest of the work primary and secondary osteons will not be explicitly distinguished but we typically refer to secondary osteons as they are more frequent in adult bone.

Woven bone is often produced first, in order to create a scaffold for the production of the more robust lamellar bone [Ferretti et al., 2002; Liu et al., 2010]. How the collagen gets aligned during the bone formation process, and in particular how this process is influenced by the mechanics, remains an open question.

Although the collagen orientation in woven and lamellar bone differ, both bone types are stiff because the collagen, which is a relatively ductile material, is mineralized [Jäger and Fratzl, 2000]. The mineral in bone is carbonated apatite [de Jong, 1926]. Bone mineral is reported to be located in gap regions within collagen fibrils, as well as along the surface of collagen fibrils [Weiner and Traub, 1986; Landis et al., 1996b; McNally et al., 2012]. Bone mineral composition and shape is not the focus of this work, but it should be stated that these properties change with time. The potential role of osteocytes in affecting bone mineral will be discussed in Section 2.2.1.

Besides the dynamic changes in bone mineral composition and structure, there are several processes through which the structure of bone changes on larger length scales.

2.1 Bone as Dynamic Material

Bone is a dynamic material with a constantly changing structure on many length scales. Bone is known to adapt to meet its mechanical property requirements [Wolff, 1893; Frost, 1988; Weinkamer and Fratzl, 2011]. These adaptation processes even continue after the growth of the bone has terminated. Historically, two processes have been distinguished: bone modeling and bone remodeling. During **modeling**, bone is resorbed at some locations, and build up at others. Through this sculpting process, trabecular bone densities and orientations adjust to current bone loading conditions [Saparin et al., 2011] and cortical thickness can be increased as consequence of intensive loading [Haapasalo et al., 1996; Heinonen et al., 2001]. Modeling is the process through which structural adaptation of bone is made. During **remodeling**, bone is locally resorbed, and the void is replaced with new bone. While the “external” structure is virtually unchanged, the collagen in the new bone may have a different fibrillar orientation. This different collagen fibril orientation changes the local bone material properties in order to adapt to the present mechanical conditions. It has also been proposed that remodeling targets bone which has suffered micro-damage due to repetitive loading [Burr, 1993]. Remodeling micro-damaged bone could minimize the risk of fatigue fracture (see Section 2.2.1). Both modeling and remodeling processes are used during healing of a bone fracture. The process of bone **healing** is described in Section 2.3.

2.1.1 Cortical Bone Remodeling

In most mammals, and some other vertebrates with long life spans, cortical bone remodeling can be observed by the patterns produced by the successive replacement of bone. Bone remodeling proceeds in a way that is similar to the digging of a long tunnel and successive re-filling of the produced cavity. The digging is performed by specialized cells called osteoclasts which are followed by osteoblasts that fill the tunnel with new bone.

This process results in the formation of a new osteon (Figure 2.2). The term "basic multicellular units" (BMU) [Frost, 1963] has been used to denote the interplay between the osteoclasts that resorb bone by advancing a "cutting cone" and the osteoblasts that fill the cavity by means of a "closing cone" (see Figure 2.3).

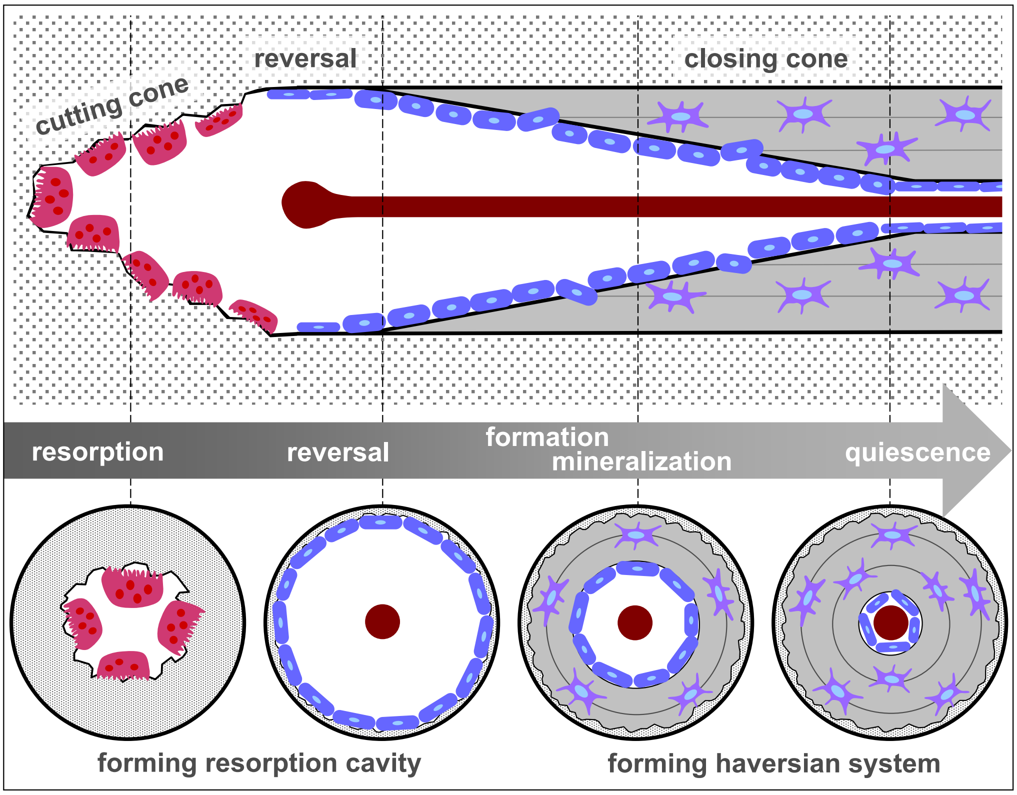

Figure 2.3: Formation of an osteon. The upper part of the image shows a section parallel to the long axis of an osteon, the lower sequence shows transverse sections at the indicated positions. New cortical bone formation starts with the resorption phase. Osteoclasts resorb bone, excavating a tunnel through the ECM. Osteoblasts migrate behind the osteoclasts, along the new tunnel surface. After a reversal phase, which results in the appearance of a cement line, osteoblasts begin to fill the cavity with osteoid. Some of the osteoblasts become embedded within the new osteoid, and later become osteocytes, within the new osteon. Figure from Kerschnitzki [2013] with kind permission from the autor.

The formation of a new osteon by the process of bone remodeling can be divided into more detailed, partly overlapping phases [Frost, 1963; Van et al., 1982]: activation, resorption, reversal, formation, mineralization, and quiescence, as shown in Figure 2.3. After selection of a target area for remodeling, osteoclast precursor cells are recruited [Vaes, 1988]. During *activation*, the precursor cells arrive via the vascular system, and differentiate into osteoclasts [Boyle et al., 2003]. *Resorption* takes place as mineral is dissolved in an acidic micro-environment generated by the osteoclasts where they are attached to the bone. After mineral dissolution, the collagenous matrix is degraded by enzymes [Teitelbaum, 2000]. During the *reversal* phase, the newly formed bone surface is smoothed, and a non-fibrous substance is deposited on the surface [Parfitt, 1984] resulting in a highly mineralized feature referred to as cement line [Skedros et al., 2005].

Osteoblasts (for a review see [Neve et al., 2011]) fill the resorption cavity during the *formation* phase. During this process, some of the osteoblasts cease producing collagen, and become embedded within the newly-formed osteoid, where they later differentiate into osteocytes (see Section 2.2). *Mineralization* of the extracellular matrix begins 2–3 days after osteoid formation, and occurs in two phases: crystal nucleation and crystal growth [Ascenzi et al., 1965]. The detailed nucleation and growth processes are not yet understood, but nucleation is reported to be initiated by vesicles that originate from the osteoblasts [Mahamid et al., 2011]. Mineral crystal growth is thought to proceed because bone fluid is supersaturated with calcium and phosphate [Anderson, 1981; Omelon et al., 2013].

As the internal bone surface area decreases with reducing cavity radius, approximately 60% of the osteoblastic population are thought to undergo apoptosis [Jilka et al., 1998]. The *quiescence* phase completes the remodeling cycle. In this phase, the remaining osteoblasts within the cavity become bone lining cells [Miller and Jee, 1987]. These bone lining cells cover the inner surface area of the tubular cavity. As bone remodeling progresses, a new blood vessel grows within the tubular cavity called Haversian canal. The final result of cortical remodeling is a new osteon.

The control mechanisms of the activation and the successive stages of bone remodeling are only partly understood [Jaworski, 1984]. Osteocytes are thought to play an important rule in controlling the key steps of the remodeling process (see Section 2.2.1), but direct *in vivo* experimental evidence is difficult to obtain. One experimental method for studying the dynamics of bone formation within the osteon uses fluorescent double labels. With this technique, fluorescent labels are injected into a living animal at two different time points. The labels attach to the mineral of newly formed bone [Frost, 1969]. Using this method, the matrix apposition rate, defined as the thickness of newly mineralized bone within a certain time interval can be measured. The matrix apposition rate was found to decrease exponentially on a timescale of 10–28 days [Martin, 2000]. The BMU tunnels through approximately 2–6 mm of cortical bone [Parfitt, 1983] with a characteristic speed of 20–40 μm/day [Parfitt, 1994]. The BMU terminates after typically 6–12 months by fusing with another osteon.

2.1.2 Structure of the Osteon and Lamellar Arrangement of Collagen

As a result of their formation process, osteons have a cylindrical shape, with a typical diameter of 150–300 μm [Britz et al., 2009]. However, deviations from the cylindrical shape are also observed [Knese et al., 1954]. Osteons are well-aligned (inclination angle $< 15°$) with the main axis of the principal stress component in the cortical bone [Heřt et al., 1994]. Their spatial arrangement appears to enable an efficient supply of nutrients from the blood vessel in the center of the osteon to the cells in the surrounding bone tissue [Shahar et al., 2011].

Havers [1691] observed not only the canal-like bone structures that house the blood vessels within bone (now called Haversian canal), but he also observed concentric bone rings around each blood vessel. These rings, called lamellae, have an average thickness of

4–6 μm [Pazzaglia et al., 2011]*. Lamellae can be observed with many different methods: reflection microscopy with a polished sample, polarized light microscopy (Figure 2.4(b)), scanning and transmission electron microscopy (SEM, TEM) (Figure 2.4(a)), acoustic microscopy, and others.

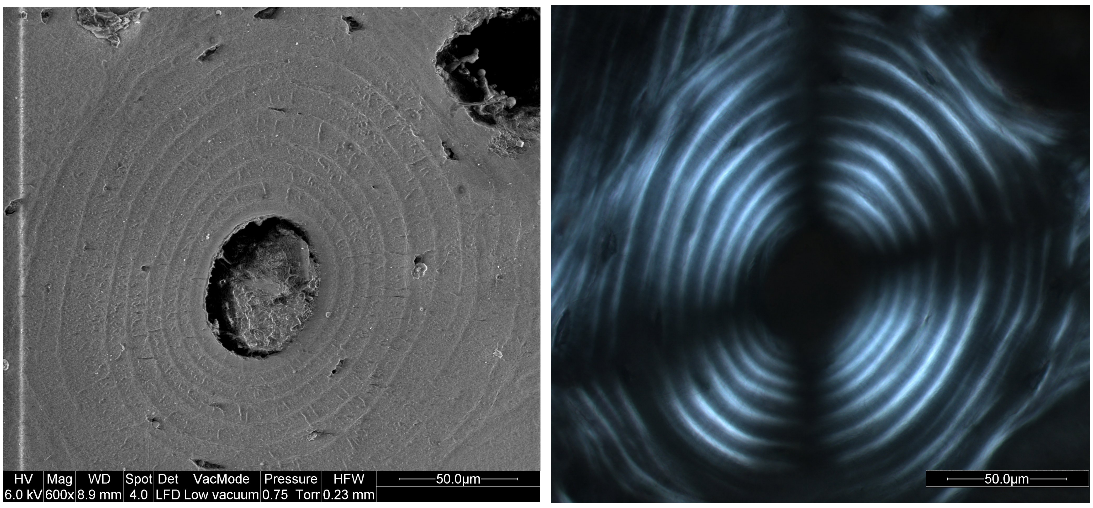

(a) Scanning electron microscopy (b) Polarized light microscopy

Figure 2.4: Lamellar substructure of an osteon: (a) electron backscattered image of a polished bone sample measured by scanning electron microscopy (SEM). (b) on the right an image of the same sample taken with polarized light and linear polarizing filters crossed orthogonally. Due to the birefringence of collagen, the polarization of the light is rotated if collagen is aligned in the plane of the image and, therefore, such a region appears bright in the image. The dark cross in the image arises when one of the polarizers is parallel with the preferred collagen orientation.

The general interpretation of these observed lamellar rings is that **collagen arrangement** varies between different **lamellae**. However, it is surprising that, while quite detailed descriptions of fibrillar arrangements were reported more than 100 years ago [Kölliker, 1859; Ebner, 1887; Gebhardt, 1905], there is still no general agreement on how to interpret the observed image contrasts. Therefore there is also no current agreement on how to define a lamella, and how the collagen is arranged [Marotti et al., 2013].

It is agreed that collagen molecules form fibrils with a diameter of roughly 100 nm [Landis et al., 1996a] in a highly ordered organization. These fibrils aggregate to form fibers or fiber bundles with diameter ranging from less than 1 μm to a few μm [Reznikov et al., 2014a]. In many cases a predominant orientation of collagen fibrils within a lamella can be observed, as presented in Figure 2.5. The simplified picture of parallel collagenous fibers, described in 1859 by Kölliker [1859], remains a frequently used description, even though it was already corrected in 1875 [Ebner, 1875]. Modern imaging techniques verify early observations by light microscopy [Ebner, 1875; Weidenreich, 1923] that instead of an arrangement of parallel collagen fibers, the collagen arrangement appears as fibrils assembled into interwoven mats, with rhombus-like holes (Figure 2.6).

---

[*] In this case the thickness refers to the distance of similar appearing rings. Often in literature the thickness of different appearing rings are listed separately.

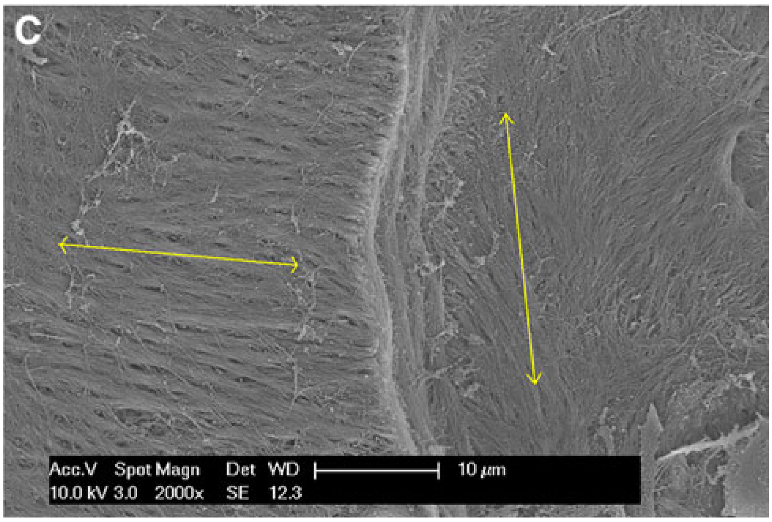

Figure 2.5: Two bone lamellae within a cutting cone of a forming osteon, imaged with SEM. Local resorption of osteoclasts exposes a lamella (right of the bright vertical feature) which is partly covered by a lamella which is not resorbed (left). Different predominant orientations of the fibrillar collagen matrix can be recognized (indicated by yellow arrows). From [Pazzaglia et al., 2011], Figure 4(c), with kind permission from Springer Science and Business Media.

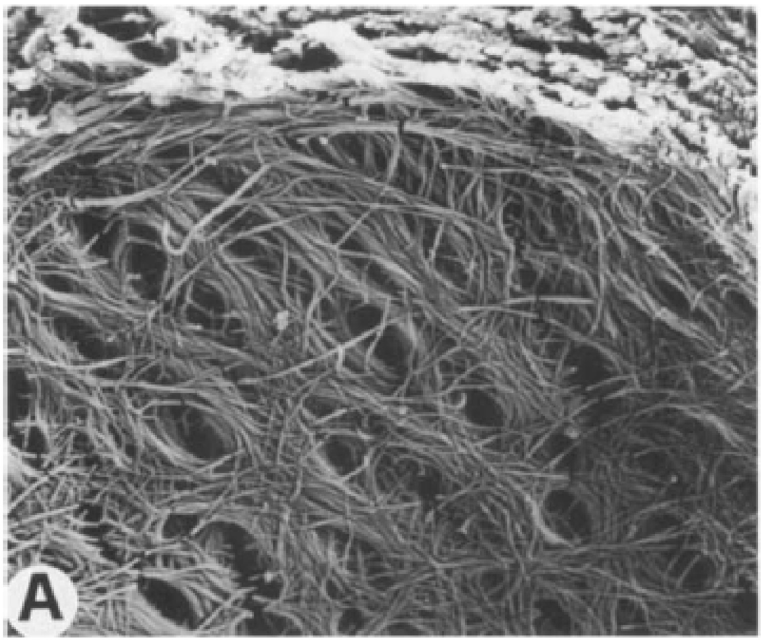

Figure 2.6: Collagen fibrils within the surface of a lamella lining the outside of a Haversian canal. Collagen fibrils form an interwoven mat, where the holes on this surface (diameter 0.1–0.5 μm) are the ends of canaliculi that are filled by cell processes of osteocytes in living bone. In this image it is difficult to identify a preferred orientation of the collagen arrangement on a larger length scale. From Marotti [1993], Figure 5(a) with kind permission from Springer Science and Business Media

There are different explanations of the strong contrast observed with polarized light microscopy, which give rise to the alternating pattern of dark and bright lamellae (Figure 2.4(b)). The standard textbook explanation is that this pattern is due to different orientations of collagen in dark and bright lamellae. Due to the birefringence of collagen, bright lamellae are interpreted as regions where collagen fibers are oriented in the plane of the image, while dark regions have a collagen fiber orientation that is perpendicular to the image plane. Comparison of observations by polarized light and SEM agree with this description [Reid, 1986]. An alternative model argues that the observed contrast between lamellae is due to different collagen densities, or the degree of order between lamellae. In the following, evidence for both explanations is presented, first for the collagen orientation model and then for the density/order model.

The interpretation of distinct **lamellae as distinct layers as in plywood** is considered to be an over-simplification. While some models describe lamellae as structural elements with a common collagen orientation, there is evidence that in some cases, instead of a stepwise change between lamellae, as observed i.e. in commercial plywood, collagen orientation changes in a continuous fashion [Ascenzi and Benvenuti, 1986; Giraud-Guille, 1988; Weiner et al., 1997]. In this model, which is referred to as the **twisted plywood model**, collagen is arranged in sheets called sublamellae that change orientation in a cholesteric manner. This model was based on features observed in 2D SEM and TEM images. Using the fact that the long axis of bone minerals are aligned parallel to the long axis of collagen fibers [Robinson and Watson, 1952; Landis et al., 1996a; Jaschouz et al., 2003]), Wagermaier et al. [2006] measured collagen orientation, interpreting x-ray diffraction patterns that were obtained under several angles. The X-ray scattering measurements indicated a continuous change in orientation within lamellae, but with sudden jumps of the orientation angle between different lamellae.

While these descriptions of collagen orientation being constant within the sheet which defines a sublamella provide the most accepted current model of collagen orientation, some observations [Pannarale et al., 1994; Boyde and Hobdell, 1968; Ascenzi and Lomovtsev, 2006] report that the main collagen orientation is only defined locally, and varies within one sublamella. Additionally a small fraction of fibrils were observed to run perpendicular to this sheet [Marotti et al., 2013; Reznikov et al., 2014a]. These reports suggest that the subject of collagen orientation within lamellae is complex and raise the question what defines a lamella.

As an alternative explanation for the contrast observed in polarized light images of different lamellae, several researchers proposed **structural differences between lamellae** in terms of density and order. Ranvier [1889]; Ziegler [1906]; Ruth [1947]; Rouiller et al. [1952] claimed that the ratio of collagen to mineral content is different in dark and bright lamellae. Recent measurements using spatially resolved Raman spectroscopy could not verify such differences in densities [Schrof et al., 2014]. Marotti [1993] became the most active supporter of this explanation after his collagen orientation observations on edges of prismatic samples. These samples were thick sections with a 90° edge that he studied at a 45° angle using SEM. He noted that the lamellar structure did not change dependent orientation to the sample surface. Based on the observations that cells (i.e. more precisely the lacunae, which are occupied by osteocytes) were observed only in collagen-poor dark lamellae. Marotti introduced the following distinction: "loose cellular" lamellae corresponding to the dark lamellae, and “dense acellular” lamellae corresponding to the bright ones. He published further support of this model that included functional considerations [Marotti, 1996; Marotti et al., 2013].

The observation of lamellae not changing appearance on the edge of a prismatic sample and osteocytes being present only in loose lamellae was criticized by Yamamoto et al. [2000] who provided examples that this is not always the case. However, recent observations using 3D imaging methods indicate that the dissent between the apparently contradictory models arises because more than one property is not constant in osteonal bone: SEM imaging of cortical bone samples sectioned with Focused Ion Beam (FIB) milling, which removes a 10 nm layer of bone before imaging the next layer [Reznikov et al., 2013] observed three types of patterns in rat bone lamellae: regions that agree with the rotated plywood model (fanning sublamellae), regions with constant orientation (unidirectional sublamellae) as well as regions with hardly any discernible order (disordered sublamellae). The same type of structural motives were also found in a human osteon using the same FIB/SEM combination method [Reznikov et al., 2014b] as well as synchrotron X-ray phase nano-tomography [Varga et al., 2013]. Therefore the the interpretations of lamellae obviously depends strongly on which individual osteon is imaged, and also what sample preparation method is used [Yamamoto et al., 2000]. The description of Reznikov et al. [2014b] that human lamellar bone is made of two distinct matrix materials, with differing arrangement of the mineral particles with respect to the collagen fibrils* echoes the description of different ECM materials in “loose” and “dense” lamellae Marotti [1996].

The difficulty in formulating a general description of how the collagen matrix is arranged within osteons might be related to the observation of **different types of osteons**. Gebhardt [1905] described tissue orientations within osteons (Figure 2.7), and classified them in three different groups (well aware that there are many more patterns): dark, bright, and alternating osteons corresponding to their appearance using polarized light microscopy. As the name indicates, bright osteons appear almost homogeneously bright in the polarized light microscope and, analogous, for dark osteons. It is not always clear which type of osteon is used when descriptions of the lamellae are reported in the literature. Applying the collagen orientation model, the interpretation of this different appearance is that the predominant collagen orientation is either longitudinal, transverse or alternating with respect to the long axis of the osteon [Ascenzi and Bonucci, 1968]. Not only the alternating osteons, which will be analyzed in this thesis, have lamellar features: e.g. in dark osteons the main collagen orientation was observed to oscillate in a steep angle with respect to the long axis [Gebhardt, 1905]. Martin et al. [1996a] added “hooped” osteon to the list, i.e. osteons with a dark center, but a bright ring around the dark center. Skedros et al. [2011] extended this osteonal classification scheme by introducing a scoring system consisting of 12 morphotypes that illustrate the “individuality” of osteons, and therefore highlighting the difficulty in producing a general description of their substructure.

When Gebhardt [1905] proposed the plywood structure of the osteon, he also **inter-**

---

*The discussion if minerals are located within the collagen fibrils or around them is as old as the discussion about the differences between lamellae ([Kölliker and Ebner, 1889; Ebner, 1887]).

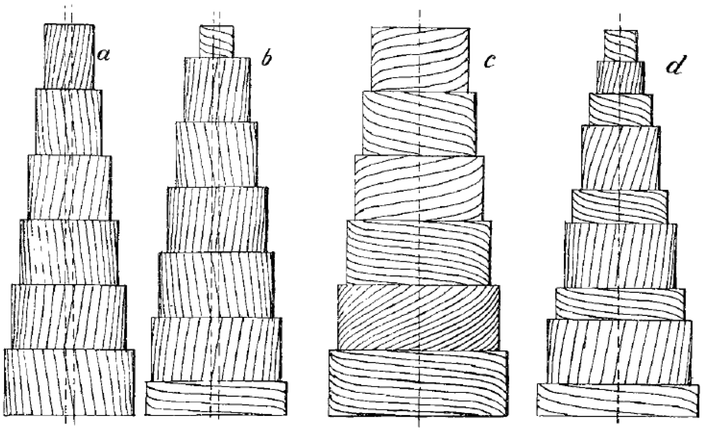

Figure 2.7: Description of the osteons with different angles of collagen fiber orientation with respect to the long axis of the osteon [Gebhardt, 1905].

preted the three different classes of osteons in terms of **mechanical properties**. Mechanical testing has demonstrated that different lamellar patterns can be related to different material properties [Ascenzi and Bonucci, 1976]. For example, bright and alternate osteons exhibited a higher ultimate tensile strength than dark osteons.

Several studies demonstrated that in regions where high compressive loads are dominant, the collagen matrix tends to be oriented perpendicular to the direction of the force. In contrast, bone regions that experience typically tensile strains demonstrate a collagen orientation that is preferably parallel to the stress axis [Boyde and Riggs, 1990; Riggs et al., 1993; Skedros et al., 1996, 2009; Martin et al., 1996a]. A higher elastic modulus and fracture toughness under 4-point bending was also correlated to bone samples with a higher concentration of dark osteons [Martin et al., 1996b]. In addition, in cortical bone samples that typically contain only a few osteons, such as goat leg bone, more osteons were found in regions that experience predominantly compressive loads [Mayya et al., 2013]. These observations suggest an influence of mechanical stimuli on the formation of new osteons.

The question remains: how does the **lamellar pattern** in osteons arise during the **formation process**? The two main hypotheses are that either the osteoblasts are actively involved in collagen orientation, or that collagen self-assembly is sufficient to arrange the collagen orientation [Giraud-Guille et al., 2003; Giraud Guille et al., 2005]. Gegenbaur [1864] and Waldeyer [1865] (cited in Knese and Harnack [1962]) suggested that lamellae are formed due do a rhythmic activity of the osteoblasts, where each cycle produces one lamella. This hypothesis has been recently revisited by Pazzaglia et al. [2010]. Marotti [1996] remarked similarities between the formation of collagen dense lamellae with cell rich lamellae with the process of lamellar bone being formed on top of woven bone, which has also a high osteocyte density (Section 2.0.1, 2.2.2). He further discussed how a coordination of the bone deposition within the dense lamellae could be dependent on the control of the osteocytes located in the loose lamellae.

Jones et al. [1975] showed that the orientation of elongated osteoblasts is correlated with the fiber organization of the underlying collagen, but it is not known if the osteoblasts create the underlying collagen fiber organization, or if the osteoblast align along an orientation which is already present. Yamamoto et al. [2012] and Pazzaglia et al. [2011] discuss how osteoblasts arrange collagen fibers by a collective movement; when they change migration directions, they create the twisted plywood pattern. What makes the arrangement of collagen fiber by the cells very interesting is that the direct influence of the cells on the orientation of the collagen could explain the correlation with the directions of applied stress. This type of mechano-regulation during osteon formation requires a sensing of mechanical stimuli. The most prominent candidates for this task are the osteocytes.

2.2 Osteocytes

As described in Section 2.1.1, when osteoblasts are embedded within the extracellular matrix produced during bone formation, they differentiate and become osteocytes (details of the differentiation process will be described in Section 2.2.2.1). Osteocytes outnumber all other cells in bone, with approximately 20000–70000 osteocytes per mm^3 of cortical bone [Dong et al., 2014; Hannah et al., 2010]. Their life expectancy, estimated to be up to 25 years, is very long among cell types [Frost, 1963]. Osteocytes can easily be identified in thin sections of bone by using light microscopy (Figure 2.8(a)). Strictly speaking, most imaging techniques do not show the cells themselves, but the voids in which the cells are located. These voids in which the osteocytes reside are called lacunae (Figure 2.8(b)). The shapes of the osteocyte lacunae depend on the type of bone (lamellar or woven), and the bone formation process (Section 2.2.2). We focused our work on lamellar bone in which lacunae appear almond-shaped; the principal axis of the osteocyte lacunae are 18 μm, 9 μm and 5 μm on average [Dong et al., 2014].

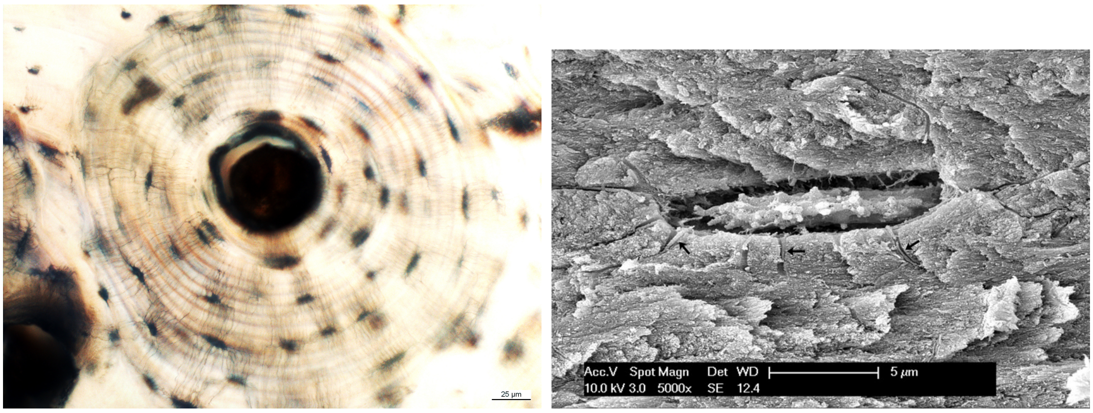

(a) Light microscopy of an osteon with osteocytes

(b) SEM of an osteocyte within its lacuna

Figure 2.8: (a) Osteocyte lacunae within an osteon can be easily identified as small dark spots by using light microscopy. (b) An osteocyte within its lacuna, imaged in a fractured bone sample using SEM. Arrows indicate the cell processes within the canaliculi which ruptured due to a shrinkage of the cell during sample preparation. Subfigure (b) is reprinted from Pazzaglia et al. [2010], Figure 6, with kind permission from Springer Science and Business Media.

The most remarkable feature of **osteocytes** is the extensive **network** that they form, extending long cell processes called dendrites through the mineralized ECM to connect with other osteocytes. These dendrites also connect to cells residing at the bone surface, which are the active osteoblasts as well as the quiescent bone lining cells. The network between the osteocytes is composed of narrow canals (canaliculi) in which the osteocyte dendrites are housed. Similar to the osteocytes, the network can be observed more easily by imaging the canaliculi instead of the dendrites within them. The diameter of the canaliculi is about 150–550 nm [Marotti, 1990; You et al., 2004] and the diameter of the dendrites is roughly 100 nm [You et al., 2004]. This network comprising both lacunae and canaliculi is termed **osteocyte lacuno-canalicular network (OLCN)**. Its architecture is a major subject of this work.

It has been shown that gap junctions exist between dendrites of neighboring osteocytes, as well as between osteocytes and osteoblasts on the bone surface [Doty, 1981; Palumbo et al., 1990a]. The extensive osteocyte network thus has certain similarities with those of neuronal networks, and the functional syncytium of astrocytes [Bonewald, 2005]. This connectivity also suggests an important role in several dynamic bone processes.

From a historical perspective, when the lacunae where first observed [Deutsch, 1834; Miescher and Müller, 1836] they were thought to contain most of the the bone mineral, and give rise to the white color of bone*. It did not take long until Bruns [1841] suggested that these the OLCN forms a porous network and can therefore be used to distribute fluids through the network.

2.2.1 Function of Osteocytes and the Osteocyte Network

As osteocytes are embedded into the mineralized bone matrix, it is difficult to observe them directly, in order to study their function. While the detailed function of the osteocytes and the role of the network is not completely understood, as mentioned in the previous section, the dense network and the long osteocyte life expectancy suggests an important role in dynamic bone processes including mineral homeostasis, repair of fatigue damage, as well as bone adaptation to external forces [Schaffler et al., 2014]. Additional support for these functions comes from several *in vitro* studies in which osteocyte-like cells respond to mechanical stimulation [Taylor et al., 2007; Adachi et al., 2009]. In similar studies, several signaling pathways have been identified which enable the control of osteoblasts and osteoclasts during the process of bone remodeling (see reviews of Bonewald [2007] and Atkins and Findlay [2012]). As osteocytes are located within mineralized bone tissue, the osteocyte network is the only connection from the osteocyte to the blood vessel in the middle of the osteon, and therefore determines endocrine† signaling and nutrition supply of the osteocyte [Arnold et al., 1971; Knothe Tate, 2003]. In addition to biochemical signaling through the OLCN, it was suggested that communication between osteocytes via gap junctions allows certain processing capabilities, as well as memory [Turner et al., 2002]. The challenges in directly observing the function of the *in vivo* osteocyte makes it difficult to determine how much the osteocyte network plays a role in the osteocyte function, and/or if osteocytes act on their own. In the following,

---

*This was due to the contrast observed by light microscopy with respect to the clear appearance of thin polished bone (Figure 2.8(a), [Müller, 1836]).

†Endocrine signals are hormones transmitted via the circulatory system typically secreted by specialized glands. In contrast the local signaling between osteocytes, osteoblasts, and osteoclasts is referred to as paracrine signaling.

the most actively discussed functions of the osteocyte network are summarized.

The locations where bone remodeling occurs through active BMU's may depend on the degree of **fatigue damage** in that volume of bone [Martin and Burr, 1982; Burr, 1993; Verborgt et al., 2000]. Fatigue damage of bone results from repetitive loading during daily activities. This repeated loading leads to micro-cracks that could result in the disruption of osteocyte processes and in osteocyte death. Consequently, after osteocyte death, the lacuna and surrounding canaliculi close due to mineralization: a process named micropetrosis [Frost, 1960]. Osteocyte death is hypothesized to affect the balance of hormones that control osteoblast, and therefore could explain the initialization of bone remodeling [Kennedy et al., 2012]. While this proposed regulation of BMU activity assigns the ability of osteocytes to influence bone remodeling, the adaptation of bone to mechanical stimuli calls for a more elaborate control mechanism than osteocyte death.

Many types of cells, not only osteocytes, have been shown to be mechanosensitive. However, the experimentally observed strain levels that results in a cellular response to mechanical stimulation were often magnitudes higher than the strains expected in bone under loading from daily activities [Thompson et al., 2012]. Both the osteocyte location within the bone and the structure of the osteocyte network make them candidates for a major role in **mechanotransduction** (i.e. the translation of a mechanical force experienced by a tissue to a chemical signal produced by cells within that tissue [Burger et al., 1999]). A possible mechanism for sensing of tissue deformation is cellular sensing of fluid flows induced by the deformation. Since the Harversian canals have a much larger diameter than the canaliculi, pressures in the Haversian canals are much more rapidly equalized than within the canaliculi, resulting in a pressure gradient between the Haversian canal and the OLCN [Knothe Tate, 2003; Cowin et al., 2009]. Simulations have shown that the expected flow rates within canaliculi are comparable to flows that resulted in cellular responses in *in vitro* experiments [You et al., 2000]. Several sensors within the osteocyte cytoskeleton and membrane have been proposed to detect bone tissue strains. However, neither the precise mechanism for sensing strain, nor how this signal is communicated to osteoblast and osteoclasts is well understood [Wang et al., 2007]. Besides the magnitude of tissue deformation, the frequency and duration of applied loads influences the osteocyte response [Rubin and McLeod, 1994; Qin et al., 1998; Case et al., 2011].

Osteocytes have also been proposed to **control osteoblasts during bone formation** as they close the tunnel of forming osteons (Figure 2.3) [Marotti, 2000; Martin, 2000]. It has been suggested that the observed decreases in rate of bone formation (Section 2.1.1) is a result of osteocytes secreting sclerostin which is a negative regulator of bone formation [Bezooijen et al., 2005; Bonewald and Johnson, 2008]. The fate of osteoblasts within the active BMU - undergoing apoptosis, or becoming embedded in the new collagenous matrix where they differentiate to osteocytes - is thought to be regulated by osteocytes communicating through the OLCN.

The significance of the OLCN in distributing fluids/substances from the Haversian canals to the extracellular matrix has been proposed more than 150 years ago [Bruns, 1841]. How far osteocytes **control** this fluid flux, as well as and the **mineralization of osteoid** is still under investigation. Observation of the presence of intracellular mineral vesicles in osteoblasts as well as in osteocytes [Mahamid et al., 2011] hint that those cells may influence ECM mineralization. The fact that neither lacunae nor canaliculi mineralize as long as the osteocyte is alive, even though the surroundings are saturated with respect to mineral [Thompson et al., 2011], demonstrates that to some extent, osteocytes influence the mineralization of their surrounding ECM.

There is growing evidence that osteocytes directly contribute to calcium homeostasis by a mechanism of local demineralization of bone called **osteocytic osteolysis**. The dissolution of bone mineral releases bioavailable calcium ions into solution [Qing and Bonewald, 2009]. Due to a canalicular density of approximately $0.55 - 0.86$ canaliculi per μm^2 [Cardoso et al., 2013] the surface area accessible to osteocytes is up to 100 times larger than the surface area accessible to osteoclasts including periosteal and endosteal surfaces, trabecular as well as Haversian surfaces [Aarden et al., 1994]. 3D Analysis of OLCN in bovine bone showed that 80 % of the bone matrix is closer than 1.4 μm to the nearest canaliculi [Kerschnitzki et al., 2013]. The high surface area of the OLCN makes the story of osteocytic osteolysis very appealing. The theory that osteocytes could demineralize bone through the OLCN was promoted already 40 years ago, based on the observations of enlarged lacunae in cases of calcium deficiency [Bélanger, 1969], increased PTH levels [Baud, 1962], micro-gravity [Rodionova et al., 2002], immobilization [Krempien et al., 1976], hibernation, as well as lactation [Kwiecinski et al., 1987]. A controversial debate started, as several studies could not validate those findings. The strong opposition [Parfitt, 1977; Marotti, 1990] argued that the previously observed, enlarged lacunae were due to different types of bone formation, age of the osteocyte, different locations in the bone, or observational orientation effects. Therefore the enlarged lacunae did not reflect a genuine lytic process in the sense of a decomposition of bone. However, recently the theory of osteocytic osteolysis has again gained more attention*.

All these possible OLCN functions depend on the structure of the network, as both communication and transport of material is only possible via the interconnected canaliculi. **Fluid transport** either by diffusion, driven by a pressure gradient due to loading, or even actively controlled by osteocytes [Arnold et al., 1971] is likely a key component for a functional, healthy bone tissue. There are several factors other than the OLCN architecture that would affect fluid transport through the network. Fluid fluxes are strongly dependent on the diameter of the canaliculi, and the diameter of the dendrites within the canaliculi. Protrusions of the canaliculus wall, as well as proteoclycans connecting the dendrites to the extracellular matrix [You et al., 2004] termed tethers also disturb the canalicular fluid flow. These tethers might be associated with osteocyte mechanosensitivity as forces on the tethers deform the dendrites [Wang et al., 2007]. Another factor that could affect fluid flow through the canaliculi is roughness of the canalicular wall. This has been recently studied with a volumetric resolution of a few nm, and has been used to model fluid flow within the network [Kamioka et al., 2012]. Fluid permeability through the OLCN is a function that is strongly dependent on the molecular weight of the fluid components. Paracrine signaling molecules such as sclerostin and RANKL (a hormone important in the regulation of bone resorption) have molecular masses of 20–30 kDa, not much smaller than the limit of 70 kDa which was reported as the maximum

---

*Especially due to the work of Linda Bonewald, Anna Teti and their groups [Teti and Zallone, 2009; Qing and Bonewald, 2009; Wysolmerski, 2012].

weight for molecular transport through the canaliculi. Therefore, these important signaling molecules could require a non-passive load-induced fluid flow, or an active osteocytic process for efficient molecular transport through the OLCN [Tami et al., 2003].

2.2.2 The Relationship of Osteocytes to Bone Formation and Collagen Structure

Studying the structure of the OCLN may provide insights into it functions. However, the OCLN architecture and osteocyte morphology could also be strongly influenced as the network is formed together with the whole osteon. Osteocyte morphology has been related to the specific bone environment by Ferretti et al. [2002]; this study concluded that two distinct types of bone formation involved different osteocyte differentiation modi. In a bone formation process termed “static bone formation”, osteoblasts produce unmineralized osteoid in an uncoordinated way, resulting in unordered collagen structure in the ECM. In this work, we focus on lamellar bone which is produced by a different process termed “dynamic bone formation”. In dynamic bone formation, osteoblasts orient along already existing bone surfaces, polarize* and produce ordered, lamellar bone [Palumbo et al., 2004] in an coordinated collective fashion [Kollmannsberger et al., 2011]. Osteocytes originating from dynamic bone formation appear flatter, with more, longer and more parallel organized dendrites than osteocytes embedded in bone produced by static bone formation [Ferretti et al., 2002]. Furthermore, the number of osteocytes per bone volume is lower in dynamically formed bone [Kerschnitzki et al., 2013].

The correlation between the osteocyte shape/OLCN structure and the organized/disorganized bone types was verified by [Kerschnitzki et al., 2011a], and has been used to gain understanding of bone formation processes [Ferretti et al., 2006]. The osteocyte shape and OLCN structure also allowed insight into the bone formation processes during bone healing [Kusuzaki et al., 2000]. Due to the close relationship between the formation of new bone and the differentiation of osteocytes, which includes the formation of the OLCN, Rensberger and Watabe [2000] used 2D images to measure the degree of canaliculi orientation to discuss the evolutionary relationships between the bones of birds, mammals and dinosaurs.

2.2.2.1 Differentiation of Osteoblasts to Osteocytes

As osteoblasts are embedded in newly forming bone, they undergo several changes in the course of what is called differentiation as they transform into an osteocyte (review by Knothe Tate et al. [2004]). With the differentiation the functions of the cell also the cell morphology change. E.g. embedded osteoblasts lose a high fraction of their organelles, as they no longer need them to syntheses collagen [Mikuni-Takagaki et al., 1995; Franz-Odendaal et al., 2006] resulting in a reduced cell volume. The most obvious differentiation change between osteoblasts and osteocytes is the growth of the characteristic cell processes (dendrites) that are housed in the canaliculi.

---

[*] Polarization means the breaking of symmetry, e.g. the secretion of collagen happens only on the one side of the cell that faces the bone.

In dynamic bone formation, the **differentiation from osteoblasts to osteocytes** is described by several steps [Palumbo, 1986; Palumbo et al., 1990a; Nefussi et al., 1991], as shown in Figure 2.9. Osteoblasts that are committed to differentiation (*Preosteocytes type 1*) first increase their contact surface with the surface of unmineralized bone (osteoid). This cell-spreading results in the cells lagging behind the other osteoblasts that continue form new osteoid. *Preosteocytes of type 2*, also known as osteoblastic osteocytes, are no longer associated with the layer of active osteoblasts, but are not yet fully embedded within the new bone matrix. These type 2 preosteocytes begin to grow thick and short dendrites from their cell surface that is facing the previously deposited bone. When completely embedded in the unmineralized osteoid, *preosteocytes of type 3* grow slender cell processes on the opposite side of their cell body (e.g. the side facing the layer of osteoblasts from which they came). These cell processes make contact with the osteoblasts building the new bone on the surface of the osteoid. When the mineralization front arrives at the location of the type 3 preosteocyte, the *osteocyte* has reached its mature state. Estimations of the timescale for this process range from approximately two [Young, 1962] up to 20 days, depending on the animal species and position in the bone tissue [McCulloch and Heersche, 1988].

2.2.2.2 Orientation of Osteocyte Lacunae and the Canalicular Network

As stated in the beginning of Section 2.2 osteocyte lacunae in lamellar bone appear almond-shaped, and therefore have three principal axes with differing lengths. Kölliker [1859] described that the shortest axis is parallel to the lamella normal, a result of the flattening of the osteoblast in a direction parallel to the bone surface. The long axis was described as parallel to the collagen orientation [Gebhardt, 1905; Marotti, 1979; Ascenzi et al., 2008], which is, according to Jones et al. [1975] also the case for osteoblasts. Marotti and Muglia [1988] reported that osteocyte density within loose lamellae is higher, or even strictly limited to loose lamellae [Marotti et al., 1995b, 2013]. As stated previously, this result is doubted by other scientists in the field [Yamamoto et al., 2000]. Ardizzoni [2001] further reported a lamellar thickness is proportional to the dimensions of the lacunae.

Not only the orientation of osteocytes/lacunae reflects the formation process of the bone, but the majority of the canaliculi also run perpendicular to the lamellae, towards the blood vessel in the Haversian canal [Bruns, 1841] fit the description of how preosteocytes of type 3 grow their cell processes. However, a fraction of the OLCN was also observed to lie parallel to the lamellae [Kölliker, 1859]. Smith [1960] observed a higher number of canaliculi within lamellae with collagen that is aligned orthogonal to the plane of the section, indicating an alignment of canaliculi parallel to the collagen orientation. Reznikov et al. [2014b] described an accumulation of canaliculi within the disordered bone ECM. Another way to describe the canalicular orientation is to relate their orientation to their closest lacuna. Depending on their origin either on the flat surfaces of the oblate osteocytes or on the rim of the cells, these dendrites have been described as primary dendrites and secondary dendrites, respectively [Ferretti et al., 1999]. Making a similar distinction Pazzaglia et al. [2012a] introduced the terms “radial” and “equatorial” dendrites.

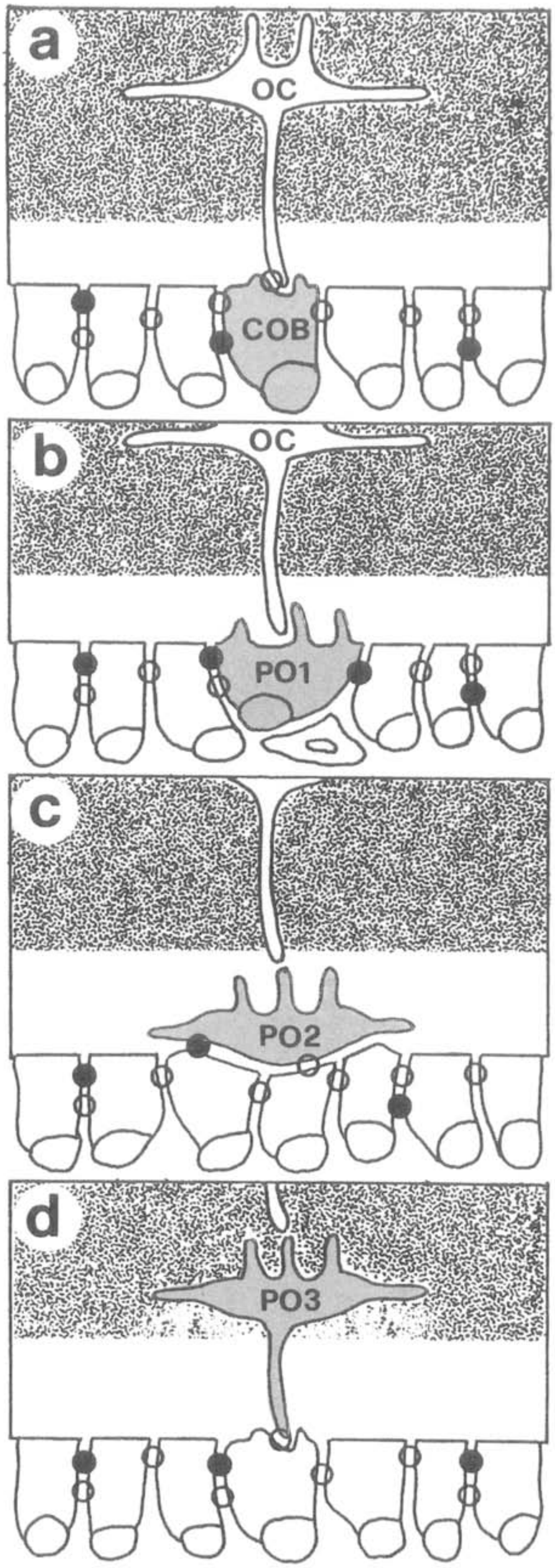

Figure 2.9: Differentiation of an osteoblast to an osteocyte. (a)During the bone formation process (bone is formed downwards in this schematic), osteoblasts are connect with each other, and with osteocytes embedded in the matrix via gap junctions. (b) Osteoblasts committed to differentiation spread on the bone surface, slowing down their migration relative to the other osteoblasts, becoming preosteocytes type 1. (c) When embedded within the still unmineralized bone (osteoid), they first grow thick, short dendrites on the side of the cell that faces the bone. (d) As bone formation continues, they form long slender cell processes to stay in contact with the osteoblasts on the bone surface. Image reprinted from [Palumbo et al., 1990b] with permission from Elsevier.

In an electron microscopy study Pazzaglia et al. [2010] observed a network of cell processes parallel to the bone surface underneath the osteoblasts, extending parallel to the osteoid surface which were in contact with the dendrites of embedded osteocytes (Figure 2.10). They also argued that these processes could be used to align the collagen. Possibly these cell processes are the ones that form the equatorial canaliculi (see also [Menton et al., 1984; Yamamoto et al., 2012]).

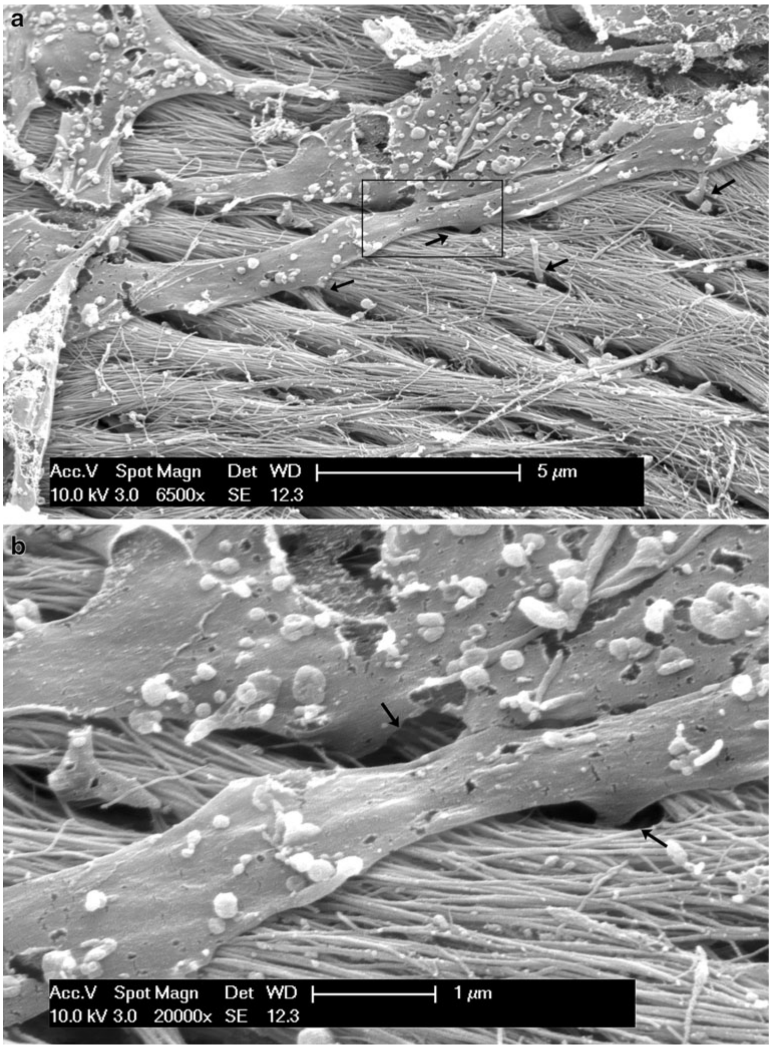

Figure 2.10: SEM image of cell processes underneath a (removed) osteoblast at the forming surface of an osteon. Thick flat cell processes extending parallel to the surface are thought to belong to the osteoblasts, while slender cell processes from osteocytes can be seen protruding from the canaliculus (black arrows). In the magnified lower image, it appears that the thick processes are branching and also enter into the canaliculi. Image reprinted from Pazzaglia et al. [2010], Figure 5, with kind permission from Springer Science and Business Media.

2.2.3 Studying Osteocyte Networks

Most of the morphological observations of the osteocytes and their network are based on 2D images of bone sections, generated by either light microscopy, TEM or SEM. The first advances in studying the 3D OLCN structures were achieved by casting the OLCN with resin, followed by dissolution of the extracellular matrix [Abe et al., 1992]. The 3D resin structures were then observed using SEM. 2D images of these cast structures provided a fair impression of the complexity of the 3D network arrangement [Pazzaglia and Congiu, 2013].

Several true 3D imaging methods have since been applied to the study of osteocyte/lacuna arrangement in bone [Schneider et al., 2010]. The serial application of focused ion beam milling that removes thin (approximatly 10 nm) layers of bone, followed by the use of electron microscopy to image the newly sectioned surfaces **FIB/SEM** were applied to study collagen arrangement, but they are also used to study the OLCN [Schneider et al., 2011; Reznikov et al., 2013].

Synchrotron-radiation-based micro **computed tomography** (SR-CT) is typically used to visualize osteocyte lacunae, and evaluate their size, shape, and arrangement [Hannah et al., 2010; Mader et al., 2013]. Recently it was demonstrated that a resolution high enough to visualize canaliculi can be obtained [Pacureanu et al., 2012] and was used to demonstrate that the mineral content is increased close to the canaliculi [Hesse et al., 2014b]. Unfortunately, to obtain such high resolution information, only a few beamlines can be used, and precise sample preparation is needed due to limitations in sample size. Kamioka et al. [2009] achieved an even higher resolution by using computed tomography based on images obtained by ultra high voltage electron microscopy of 3 μm thick sections. With the same technique Kamioka et al. [2012] imaged dendrites in canaliculi with a 2.4 nm resolution within sample sections that were 80 nm thick.

Confocal microscopy allows visualizing the canalicular network, even though the diameter of the canaliculi is below the wavelength of light, and therefore at the length scale of the resolution of the microscope. Fluorescent dyes such as rhodamine diffused through the canalicular network have be used to visualize the network in 3D [Anderson et al., 2008; Ciani et al., 2009; Kerschnitzki et al., 2011b; Sharma et al., 2012]. The resolution of the microscope determines the width of the observed fluorescence signal, which is smaller than the typical distance between the canaliculi, allowing to image the topology of the network. With this technique the OLCN data was obtained which was then analyzed as described in Chapter 4 in this thesis. Cell-specific markers have also been used to study the osteocyte network [Kamioka et al., 2001; van Hove et al., 2009], as they label the dendrites that located within the canaliculi.

The difficulties in directly observing the function of the osteocytes makes **computational models** a useful tool to test possible hypothesis about the formation of the network and transport through it. Models exist that predict refilling dynamics, and thus 3D structure of the forming osteons, based on inhibitory biochemical signals such as sclerostin that are secreted by the osteocytes, as well as geometrical factors such as the radius of the osteon [Polig and Jee, 1990; Buenzli et al., 2013]. Ascenzi et al. [2004] made a mathematical model to arrange the position and orientation of osteocytes in osteons including collagen orientation. In this model, which was used for mechanical assessment of bone, canaliculi are limited to being modeled as straight connections. First advances in incorporating the OLCN architecture as obtained by confocal microscopy to fluid flow models have been achieved for small samples [Anderson et al., 2008].

2.3 Healing

A bone fracture implicates a dramatic loss of function and a severe damage not only to the bone tissue. The dislocation of the bone fracture ends brings along damage of the vascular system, connective tissue and might lead to bone necrosis, i.e. death of the bony tissue. Under adequate mechanical and biological conditions bone has the ability to heal, returning to the prefractured state. The healing bone does not form scar tissue and its functionality is completely restored. There are two basic modes of how bone healing occurs. In rare cases, when there is no gap between the bone ends and the bone is mechanically stable, bone can heal directly without the formation of additional callus tissue (primary bone healing), e.g. via the formation of new osteons bridging the two bone ends. Usually secondary bone healing is observed and, therefore, only this mode of healing will be described in the following. Secondary (indirect) healing includes the formation of a callus, initially composed of soft tissues like fibrous tissue and cartilage.

2.3.1 Bone Healing in Animal Models

Progress of our understanding of bone healing largely depends on large **animal bone defect models** [Reichert et al., 2009] and rodent animal models [Garcia et al., 2013]. To obtain reproducible initial conditions often osteotomies are induced: in a surgical procedure the bone is cut in two with a saw instead of being fractured. This results in relatively smooth “fracture” surfaces. Most of the times defect models are used where a gap of well-defined size between the osteotomy ends is assured. Fixation devices, either external or internal within the marrow cavity, are used to provide a defined mechanical stability.

Secondary bone healing involves several phases overlapping in time [Gerstenfeld et al., 2003]. As schematically shown in Figure 2.11, after the formation of a haematoma and an inflammatory reaction, first new soft tissue is formed in the region around the fracture site. This soft callus is then transformed into other tissues with bone formation periosteally, followed by a bridging of the fracture ends with cartilage. The cartilage successively ossifies and mechanically weak woven bone is remodeled to lamellar bone [Shapiro, 2007; Liu et al., 2010]. Eventually resorption removes the superfluous bone, resulting in a full restoration of the bone.

Our computational work is based on an animal experiment of 32 sheeps, where an osteotomy in the middle of the tibia (i.e. shinbone) was performed [Epari et al., 2006]. The separated bone ends were stabilized with a distance of 3 mm between them by an external, rather rigid fixator. Animals were sacrificed at 2, 3, 6 or 9 weeks after the osteotomy. Longitudinal histological sections were obtained and stained to identify different tissues within the callus including cartilage and bone.

To account for the inter-individual variability between the animals, Vetter et al. [2010] used advanced averaging techniques to extract a sequence of six images from the histological sections of the 32 sheep. These **averaged images** are interpreted as the progression of healing in a typical sheep advancing through different **stages** (Figure 2.12), very much along the description in the literature (e.g. Figure 2.11). The stages were defined based on specific morphological features of the tissues within the callus. The first image (Stage II) from the early preparative phase shows that after last remnants of haematoma (Stage I, not shown) disappeared, the callus consists predominantly of granulation and fibrous tissue with the first signs of bone formation periosteally. These periosteal bony protru-

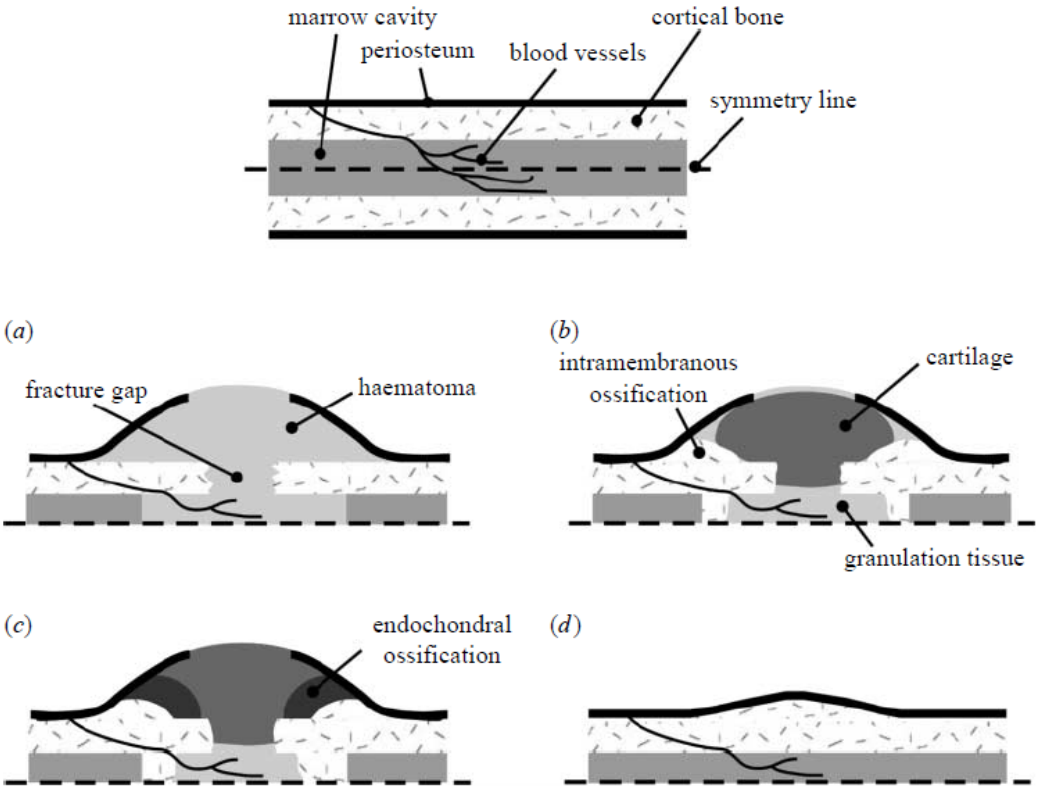

Figure 2.11: Schematic phases of secondary healing in a longitudinal cross section. Compared to the full cross section (top), subfigures (a-d) show only half of the fracture callus, assuming symmetry. (a) The damage of the bone and consequently the vascularization yields to the formation of a callus initially filled with a haematoma. (b) Periostally, away from the fracture gap, bone is formed in a process called intramembranous ossification, while close to the fracture cartilage forms. (c) This cartilage starts to be replaced by bone (endochondral ossification). (d) After a successful healing, when the fracture gap is closed and all the cartilage has been replaced by bone, a small bony callus remains, which will be remodeled, given enough time. Image reprinted from Geris et al. [2009] by permission of the Royal Society.

sions are bridged by cartilage in the outer osteotomy zone at Stage III. In Stage IV this bridge is replaced by bone. In Stage V a connection between the medial and lateral side of the cortex can be seen. During the early remodeling phase (Stage VI), bone resorption leads to a reduction in size of the bony callus (Figure 2.12). A final image shows a fully restored cortex which would occur after successful healing a long time after the experiment finished. These six images of bone healing in a “typical sheep” are used for comparison with the computationally obtained images of tissue patterns.

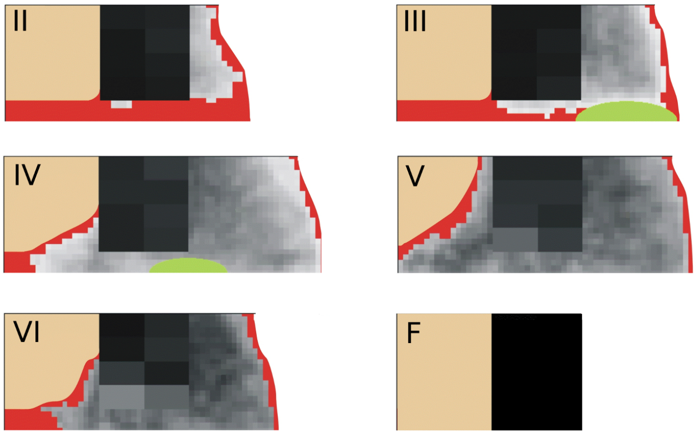

Figure 2.12: Different stages of a complete course of healing: Bone is marked gray where darker colors represent higher bone density and consequently higher stiffness; fibrous tissue is colored red, cartilage green and bone marrow beige. The images represent a quarter of a longitudinal section, with symmetry planes at the left and lower side of the images (see Figure 2.11 for the complete geometry of an osteotomy). Each of the 6 images shows averaged experimental data of Stages II–VI [Vetter et al., 2010] plus the final stage of the restored cortex.

2.3.2 Bone Healing as a Mechanobiological Process

The formation of a callus during healing consisting of diverse tissues with different mechanical properties that fit the mechanical needs in the specific location suggests a **mechanically controlled** healing process [Pauwels, 1960]. Perren and Cordey [1980] proposed the “interfragmentary strain theory”, a simple but instructive mechanobiological concept, which states that in the callus only the type of tissue can be formed, which sustains the local mechanical strain. Therefore, soft tissues are formed in regions of the callus with large local strains, while bone is formed in regions of low strains. Similiar to osteoblast forming bone tissue, fibrous tissue and cartilage are formed by fibroblasts and chondroblasts receptively. All of them are from the same cell line, e.g. origin from mesenchymal stem cells.

While the osteocytes might also play some role in mechano-regulation during the remodeling stages of healing, during the early phases of bone healing, it is thought that mechanosensitive stem cells, e.g. mesenchymal or more likely pluripotent cells [Kasper et al., 2007] play a key role. Those cells which migrate into the haematoma of the callus, differentiate according to their mechanical stimulation [Kelly and Jacobs, 2010] and other influences [Bruder et al., 1994; Discher et al., 2009]. These other factor include geometry [Kilian et al., 2010], oxygen tension [Malladi et al., 2006; Meyer et al., 2010] and growth factors [Worster et al., 2001]. Figure 2.13 shows schematically how these influences result in different tissues, and compares this to our model.

The main motivation for **computer simulations** of bone healing is to clarify whether the observed evolution of the tissue patterns can be understood as the result of a feedback between the mechanical stimulation and the cell differentiation process. Stimulation results in tissue differentiation and an overall stiffening of the callus, which as a consequence reduces the mechanical stimulus and triggers new cell differentiation. Computer simulations of bone healing are typically based on an iterative algorithm, where first the callus is subdivided into smaller volume elements and then at each time step a mechanical assessment in the different volume elements in the callus are performed. Based on this assessment mechanical stimuli are calculated for each volume element. These calculated stimuli are then fed into the crucial mechanobiological rules, which describe changes in cell concentrations or tissue properties as a function of mechanical stimulation and result in an increase of elastic modulus of each volume element. In case cell concentrations are modeled, their effect on the tissue properties require an additional step. After the incrementation of the elastic modulus, a new mechanical assessment has to be performed and the iteration cycle closes. The proposed algorithms differ in the used mechanical stimuli and the mechanobiological rules [Geris et al., 2009; Isaksson, 2012]). Questions that have been addressed concern the influence of the osteotomy gap size [Lacroix and Prendergast, 2002; Gómez-Benito et al., 2005], the mechanical loading (compressive, torsional, ...)[Isaksson et al., 2006a], the fixator stiffness [Reina-Romo et al., 2011], frequency of loading [Gómez-Benito et al., 2011], the nature of the mechanical stimulus (shear strain, second invariant, fluid flow,...)[Isaksson et al., 2006b], the sources of the pluripotent cells [Lacroix et al., 2002; Vetter et al., 2011b] as well as the influence of vascularization [Geris et al., 2008; Checa and Prendergast, 2009]. These computational studies were reviewed in the thesis of Vetter [2010]. In more recent computational work Burke and Kelly [2012] published a healing model studying the effect of oxygen tension using the averaged healing images of Vetter et al. [2010] to validate the model. Steiner et al. [2013] investigated validity of their model using different loading conditions, showing that healing does not depend on the assumption of purely axial loading when uncertain parameters are calibrated. Most models assume axial symmetry, allowing to reduce the computational effort. With advances of computational power, 3D models using more realistic geometries have been shown to be feasible [Byrne et al., 2011], allowing to minimize uncertainties in the loading conditions.

For the simulation presented in this thesis, a model is used which was developed in our research group [Vetter et al., 2011b]. In this approach an aim was to reduce the number of model parameters. Consequently, a detailed biological description is avoided and biological factors influencing healing are summarized by a scalar biological potential, which diffuses from given sources into the callus (Figure 2.13(b)). Changes in tissue type depend on an adequate mechanical stimulus but can only happen if all biological needs as described by the biological potential are present. The model allows ossifica-

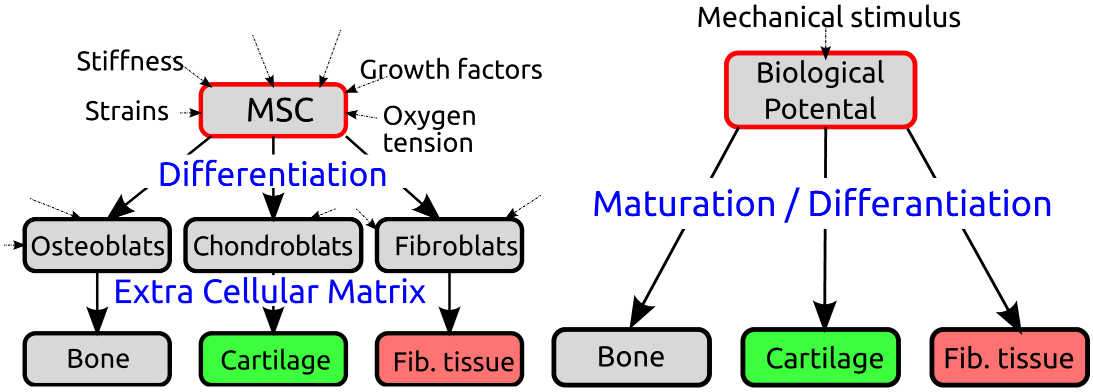

(a) Schematic understanding of bone healing (b) Simplified schematics as modeled

Figure 2.13: Schematic representation of bone healing and how it is modeled [Vetter et al., 2011b]. (a) Mesenchymal stem cells (MSC)/pluripotent cells differentiate into tissue forming cells depending on many factors of which strains are only one. Many influencing factors are poorly understood or not even known (arrows without caption). (b) Focusing on the influence of mechanical stimulation cells and their biological stimulation are summarized as a “biological potential”. Only if all necessary conditions are fit (high value of the biological potential), tissue can maturate and differentiate to different types of tissue according to the mechanical stimulation.

tion via the two observed mechanisms, intermembranous ossification, i.e. direct bone formation, or endochondral ossification, i.e. ossification via a transient formation of cartilage. Mechano-regulation of tissue differentiation is implemented by threshold values of the mechanical stimulus. Parameter studies have been performed on these mechano-regulatory threshold parameters. Using this model approach Vetter et al. [2011b] found good agreement for the early healing stages between model and the experiment when sources of biological potential were assumed mostly at the periost, and minor contribution by the endosteal marrow space. After testing different mechanical stimuli, the absolute value of the volumetric strain was selected as to be most appropriate to be used in the simulations. As an extension of this model to describe the full course of healing was part of the research work presented in this thesis, a more detailed mathematical description of the model and its extensions will be given in Section 3.2.

Chapter 3

Bone Healing

The computational work on bone healing presented in this thesis is based on the model developed by Vetter et al. [2011b]. Several modifications in the model have been implemented to allow addressing new questions as presented in the following section.

3.1 Aim

The computer model was extended to describe the complete healing process until conditions of the pre-fractured bone are virtually restored. For this objective the process of **bone resorption** had to be considered, which causes a removal of the superfluous bony callus in late phases of healing. It is studied to what extent the inclusion of an additional simple mechanobiological rule describing resorption affects the overall course of healing and results in a development of tissue patterns comparable to the animal experiment (Section 2.3.1).

The focus of the work is to investigate three specific scenarios regarding the connection between the **local mechano-regulation on the cellular level** and the resulting evolution of tissue patterns during healing. Although cells and their behavior are not explicitly modeled, the phenomenological mechanobiological rules allow addressing certain aspects of the control on the tissue level. We introduce three biologically motivated changes in the mechano-regulation and test how these changes affects the progression of healing.

(i) It is clear that some time is necessary between the sensation of the mechanical stimulus by pluripotent cells and their differentiation and eventually formation of new tissue. Consequently, in the computer experiments not the actual mechanical stimulus, but a stimulus some days in the past is used to control tissue formation. In the simulations the time interval of the delay is varied and whether the mechanical stimulus at the beginning of the time interval or a stimulus integrated over the whole interval is used. In the following these studies are referred to as “delayed stimulus”.

(ii) Healing is thought to be controlled via mechanical thresholds, i.e. certain processes are activated once the cells feel a mechanical stimulus, which exceeds a certain value. Knowing about biological variability, it is a clear idealization that all the pluripotent cells possess exactly the same mechanical thresholds [Khayyeri et al., 2011]. Under studies referred to as "variable mechanosensitivity", we investigate how fuzzy mechanical thresholds influence the tissue patterns observed during healing.

(iii) It is unclear whether an appropriate mechanical stimulus is needed only once for triggering tissue formation and maturation and then the process continues, or if an appropriate mechanical stimulus has to be maintained over the whole time to promote the process. We studied two different scenarios. First, that late soft tissue maturation is independent from the mechanical stimulus. Second, that the very early phase of cartilage formation is decoupled from mechanics. These investigations are presented as "committed maturation".

In the model parameters for the mechano-regulation, i.e. the threshold values for the mechanical stimulus deciding on tissue differentiation, are not known. They are chosen based on a parameter study to ensure the best possible agreement with the experiment at an early stage of healing when cartilage is present in the callus (Stage III, see Section 2.3.1). One faces now the problem that by implementing changes in the mechano-regulation as suggested in the points (i)–(iii) above, the best agreement between simulation and experiment get lost using unchanged parameters for the mechano-regulation. The only way to guarantee a "fair" comparison between different scenarios of the mechano-regulation is first to perform a parameters study to determine the best choice of the mechano-regulation parameters with respect to agreement with the experiment, and then to run the simulation to study the course of bone healing till the full restoration of the fractured bone.

3.2 Materials and Methods

3.2.1 Mechanobiological Regulation

The following presentation of the model starts with its core, i.e. how a mechanical stimulus regulates the formation and maturation of new tissue. The specific implementation of the model to describe the osteotomy experiment on sheep and the used parameters are presented in Section 3.2.2.

For the description in the computer model the callus is subdivided into **small 3-dimensional volume elements**. Each volume element is assigned a tissue type (tt), which can be granulation/fibrous tissue, cartilage or bone. The second parameter assigned to each volume element is its elastic modulus (E_{tt}) which changes during healing. Starting the simulation with the callus region filled with granulation/fibrous tissue, i.e. the tissue of lowest modulus E_{fib}^{min}, the healing process implies both a maturation of the tissue (i.e. an increase of the elastic modulus E by ΔE), as well as a change of the tissue type. Changes in the elastic modulus (ΔE) are controlled locally by a scalar mechanical stimulus (ms). In the work of Vetter et al. [2011b], it was demonstrated that using volumetric strain as mechanical stimulus $ms = \Delta V/V$ leads to good agreement with the tissue patterns observed in experiments.

Especially during the early phase of bone healing an intricate interplay of cell migration into the callus, angiogenesis and cell communication via signaling molecules happens [Einhorn, 1998; Schmidt-Bleek et al., 2011]. These important biological influences of healing are phenomenologically summarized in a biological potential c, which takes values between 0 and 1. This potential is a simplified local scalar parameter describing how "biologically ready" the tissue element is to progress with healing (for details of the implementation see Section 3.2.2).

The change in elastic modulus ΔE for a volume element of location $\mathbf{r}$ in the callus at time point t, which occurs during a time step Δt, is described in our model as

$$\Delta E(\mathbf{r}, t) = \Delta E\,(ms, c, tt) = c(\mathbf{r}, t)\,k_{tt}\Delta t \tag{3.1}$$

where k_{tt} denotes the rate of stiffening of a specific tissue. The last equality holds only for an appropriate mechanical stimulation. The original model by Vetter et al. [2011b] had two mechanical thresholds MS_c and MS_b regulating not only whether maturation happens, but also deciding between endochondral ossification (i.e. bone formation via transient formation of cartilage) or intramembranous ossification (i.e. direct bone formation) occurs. Once a volume element of granulation/fibrous tissue, reaches its maximum value of elastic modulus E_{fib}^{max}, it is turned into cartilage, if $ms(t) > MS_b$, or into bone otherwise. Cartilage will turn into bone, once the elastic modulus exceeds E_{cart}^{max} (Figure 3.1).

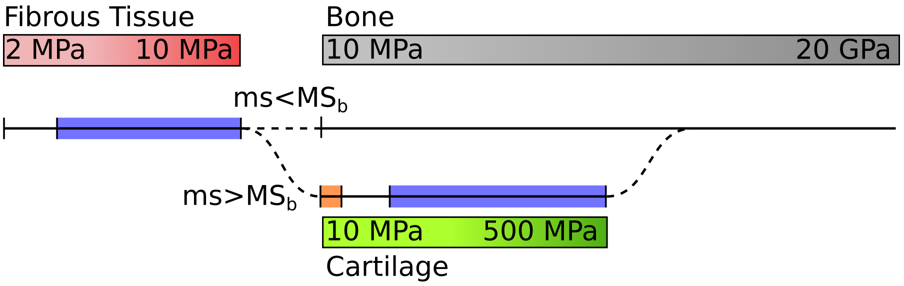

Figure 3.1: Tissue development for a small volume element within the callus. All tissue elements of the callus start as granulation/fibrous (denoted in red) tissue with $E_{fib}^{min} = 2\,\text{MPa}$ and stiffen if the mechanical stimulus ms is below MS_c. When the elastic modulus reaches $E_{fib}^{max} = 10\,\text{MPa}$, the volume element can either turn directly into bone (gray) or into cartilage (green) dependent on the mechanical stimulus ms. Colors in later figures (Figure 3.6, 3.7, 3.10) follow the color code introduced here. Color levels represent different stages of tissue maturation and therefore different elastic moduli. In the study of "committed maturation", we decouple the maturation process from the mechanical stimulus in two different scenarios. On the one hand we study decoupling in the late soft tissue development (highlighted in blue). On the other hand a stimulus independent maturation during the early cartilage formation is assumed (highlighted in orange).

To describe the late phases of healing, where resorption of the bony callus is essential, in this work a third mechanical threshold MS_r was introduced, where resorption sets in once the mechanical stimulation is below this threshold. Resorption occurs not only for the tissues of the callus, but also for the cortex, and leads to a reduction of the elastic modulus by ΔE_r.

In summary, the following four rules for mechano-regulation decide whether the right side of Equation 3.1 to calculate ΔE is applicable:

- Maturation of granulation/fibrous tissue for $MS_r < ms(t) < MS_c$ with maturation rate k_{fib}
- Maturation of cartilage for $MS_r < ms(t) < MS_b$ with maturation rate k_{cart}
- Maturation of bone for $MS_r < ms(t) < MS_b$ with maturation rate $k_{bone} = k_{bone}(E)$
- Resorption (decrease in elastic modulus) of all types tissues for $ms(t) < MS_r$ with resorption rate k_r

3.2.2 Implementation of the Model

To allow the comparison of the model with the healing of the tibia in sheep after an osteotomy [Epari et al., 2006] the bone geometry was chosen to approximate the experiment. The midshaft of the tibia around the osteotomy is approximated by a hollow cylinder of cortex with inner radius $r_1 = 4.85\,\text{mm}$ and outer radius $r_2 = 9.0\,\text{mm}$. The two fracture ends are separated by a gap distance $d_{gap} = 3$ mm. Assuming an axial compressive force F_{load} on top of the radial symmetric geometry, allows a representation of the model in two dimensions. Further a planar symmetry in the middle of the fracture gap was assumed. The external fixator was not modeled explicitly, instead initially the cortex was displaced by $u_{IFM} = 0.25$ mm in axial direction according to the monitored interfragmentary movement allowed by the external fixator [Schell et al., 2008]. The stiffening of the callus results in an increase of the force necessary to produce the given interfragmentary movement. When the force exceeded the full loading force of $F_{max} = 500\,\text{N}$, the boundary condition was changed and until the end of the simulation F_{max} was applied onto the cortex.

Our model is lattice based, thus individual radially symmetric volume elements are represented in two dimensions as pixels of size $(143\,\mu\text{m})^2$ having at each time point a certain tissue type and elastic modulus. In the iterative algorithm (in Equation 3.1 $\Delta t \approx 1\,\text{day}$), first strains in each volume element are calculated using Dune [Bastian et al., 2007] as a finite element solver (see Figure 3.11(a)). Changes in the elastic modulus are calculated according to Equation 3.1 if the mechanical simulation is appropriate (see the corresponding rules above). The maturation rates k_{tt} for granulation/fibrous tissue and cartilage were estimated from the experimental histological sections [Vetter et al., 2010]. Vetter et al. [2011b] estimated k_{bone} by describing the newly formed bone as a cellular solid with an elastic modulus given by the relationship of Gibson and Ashby [1999]

$$E = E_{mat}\rho^{\alpha}. \tag{3.2}$$

In this relation the elastic modulus of the bone material $E_{mat}(t)$ was obtained by nanoindentation [Manjubala et al., 2009], the bone area fractions as a function of time $\rho(t)$ were determined from histological sections [Vetter et al., 2010] and the exponent $\alpha = 1.83$ was chosen according to Morgan et al. [2003].

The spreading of the biological potential c is modeled as a diffusion process satisfying the standard diffusion equation

$$\frac{\partial c(\mathbf{r},t)}{\partial t} = D\nabla^2 c(\mathbf{r},t).$$

Based on earlier results [Vetter et al., 2011b] sources of biological potential c were set as Dirichlet boundary conditions $c_P = 10$ at the periost, and $c_E = 0.1$ at the endosteal marrow space. As initial condition c is set equal to zero everywhere else. After calculating the diffusion the potential is truncated to values $c \leq 1$. Choosing boundary conditions values larger than 1 followed by truncation results in a steeper diffusion front compared to a diffusion process with $c_P = 1$.

Table 3.1 summarizes the used parameters, starting with the material parameters. All the tissues are assumed isotropic and linear elastic, therefore mechanically characterized by the elastic modulus E and Poisson ratio ν. Once the elastic modulus of a volume element exceeds the maximum value of E for a specific tissue, the tissue type is changed.

Material parameters:
$E_{fib}^{min} = 2$ MPa(a)
$E_{fib}^{max} = E_{cart}^{min} = 10$ MPa(b)
$E_{cart}^{max} = 500$ MPa(c)
$E_{cort} = 20$ GPa(d)
$\nu_{fib} = \nu_{cart} = 0.4$(d)
$\nu_{bone} = 0.3$(d)
Loading Parameters:
$F_{\max} = 500$ N(e)
$u_{IFM} = 0.25$ mm(f)
Maturation Parameters:
$k_{fib} = 1$ MPa/day(c)
$k_{cart} = 50$ MPa/day(c)
Biological Parameters:
$D = 0.25$ mm^2/day(c)
$c_P = 10$(c)
$c_E = 0.1$(c)
Geometrical parameters:
$d_{gap} = 3$ mm(g)
$r_1 = 4.85$ mm(h)
$r_2 = 9.0$ mm(h)

Table 3.1: Table of parameter values used in the simulations.
(a) [Hori and Lewis, 1982], (b)[Isaksson et al., 2006b], (c)[Vetter et al., 2011b], (d)[Claes and Heigele, 1999], (e)[Duda et al., 1997],(f)[Schell et al., 2008], (g)[Epari et al., 2006], (h)[Vetter et al., 2010].

3.2.3 Model Extension for Late Healing Stages

For the initial stages of healing the time development of the stiffness of bone can be interpolated based on the measured local stiffness E_{mat}, volume density ρ and using Equation 3.2. For later stages the experimental data is extrapolated assuming that both E_{mat} and bone density ρ attain their maximal values ($E_{mat}^{max} = 30\,\mathrm{GPa}$ and $\rho^{max} = 1$) in an exponential way (Figure 3.2).

$$E_{mat}(t) = E_{mat}^{max}\left(1 - \exp(-\kappa_1 t)\right) \tag{3.3}$$

$$\rho(t) = \rho^{max}\left(1 - \exp(-\kappa_2 t)\right), \tag{3.4}$$

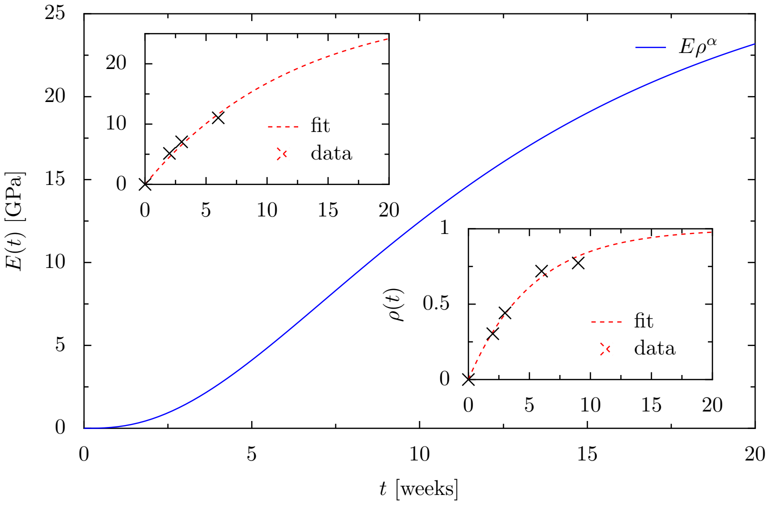

Figure 3.2: Master curve of the stiffening of bone with time calculated using Equation 3.2. Insets display experimental data and fitted dependencies using Equations 3.3, 3.4. The upper left inset shows the time evolution of bone material stiffness E_{mat} determined by nanoindentation [Liu et al., 2010], the lower right inset bone density ρ as determined by Vetter et al. [2010].

An important extension of the model is the **incorporation of resorption**. Again the mechano-regulation is described by a threshold value for the mechanical stimulus, MS_r. In contrast to the other two mechano-regulation parameters, this resorption threshold is not a free parameter but was determined based on the following considerations:

The simulation of the complete healing process should end in the restoration of the prefractured intact bone. To perpetuate the configuration of the intact bone, maturation and resorption have to be in balance. This situation is accomplished when the threshold for resorption is equal to the mechanical stimulus for the intact bone, $MS_r \approx ms_{intact}$. For the given geometry of a homogeneous hollow cylinder with cross section $A = \pi\left({r_2}^2 - {r_1}^2\right)$ and loading by an axial compressive force $F_{load} = 500\,\mathrm{N}$, the mechanical stimulus, i.e. the volumetric strain, $\Delta V/V$, is calculated as

$$\begin{aligned} ms_{intact} = \frac{\Delta V}{V} &= \left(1 + \frac{\Delta L}{L}\right)^{1-2\nu_{bone}} - 1 \\ &\approx (1 - 2\nu_{bone})\frac{\Delta L}{L} = (1 - 2\nu_{bone})\frac{F_{load}}{AE_{cort}} \\ &= 55\,\mu\epsilon, \end{aligned}$$

where $\frac{\Delta L}{L}$ denotes the strain in loading direction and 1 $\mu\epsilon$ corresponds to a deformation of $\Delta L/L = 10^{-6}$. This estimated threshold was verified by letting the simulations run into equilibrium and comparing the thickness of the final cortex as well as the stiffness of the bone within the cortex to the initial conditions. Best agreement was found for a resorption threshold of $MS_r = 60\ \mu\epsilon$ which was then used (see Section 3.3.2). To describe the kinetics of resorption and tissue transformation, in particular, reestablishing bone marrow in the medullary cavity, the decrease rate of the elastic modulus of fibrous tissue and cartilage was set equal to their negative maturation rate. For bone, several resorption kinetics (e.g. linear, exponential) were tested and compared to experimental data from cortex and callus bone density. Simulations presented here were obtained using a linear resorption rate $k_r = -128$ MPa/day (see Section 3.3.2.1).

3.2.4 Studies of the Cellular Mechano-Regulation

The questions raised in this study focus on the connection between the processing of the mechanical stimulus on the cellular level and the resulting pattern of tissues in the callus during healing. The processing of the stimulus is changed in the following ways:

Delayed stimulus: To account for the time delay between the mechanosensation of the stimulus by the cells and the formation and maturation of the tissue as response, not the actual stimulus was used in the simulations but the stimulus, which was present n iteration steps Δt in the past,

$$\widetilde{ms}(t) = ms(t - n\Delta t).$$

Alternatively, we tested the influence on healing when using an integrated stimulus over the same time period of n iteration steps Δt,

$$\widetilde{ms}(t) = \frac{1}{\sum_{i=0}^{n} c(t - i\Delta t)} \sum_{i=0}^{n} c(t - i\Delta t) ms(t - i\Delta t).$$

Variable mechanosensitivity: Most likely individual pluripotent cells respond differently to mechanical stimulation. Instead of assuming sharp mechanical thresholds for the mechano-regulation described by a step function, the thresholds were made fuzzy by convoluting the step function of the original sharp threshold with a bell shaped function of standard deviation σ representing the distribution of thresholds for the cells (Figure 3.3). The fuzziness of the three thresholds MS_x was tested in three scenarios for low to high fuzziness corresponding to a relative width $\sigma/MS_x = 16\,\%, 40\,\%, 60\,\%$, respectively.

Committed maturation: It is unclear whether the appropriate mechanical stimulation has to be maintained over all times to allow tissue maturation or an appropriate mechanical stimulus at a critical early moment is enough to trigger tissue maturation and the process continues without further stimulation. We study the decoupling from the mechanical stimulus of fibrous tissue and cartilage maturation once their elastic modulus reached 10 % of their final value (blue region in Figure 3.1). As a contrasting scenario we

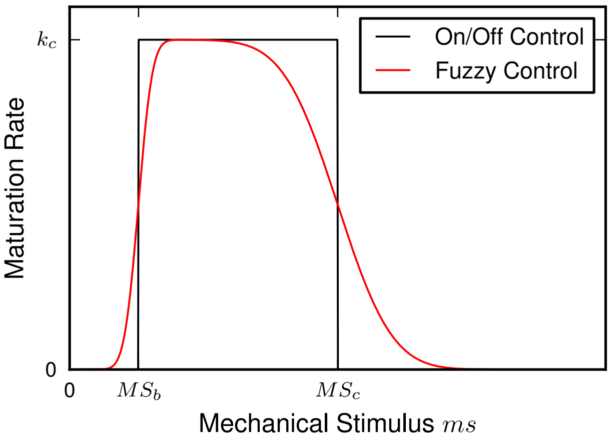

Figure 3.3: Maturation curve of cartilage comparing sharp thresholds (i.e. on/off control) to fuzzy thresholds obtained by convoluting the sharp threshold curve with a bell shaped function with a normalized standard deviation of $\frac{\sigma}{MS_x} = 16\,\%$.

investigate a stimulus independent maturation during the very early phase of cartilage formation, i.e. during the first 5% of the cartilage maturation (orange region in Figure 3.1). In this case, maturation of the cartilage also occurs according to (Equation 3.1) with a reduced k_c even if the local mechanical stimulus is above the mechanical threshold $ms > MS_b$.

3.2.5 Comparison with the Animal Experiment and Data Evaluation

The simulated tissue patterns are compared to the five experimental images corresponding to the healing stages II to VI described in Vetter et al. [2010]. A sixth image was added for comparison, which shows the fully restored cortex after completed healing (Figure 3.6). To assess the agreement between experiment and simulation, simulated images were compared to all experimental images on a pixel-to-pixel basis for each iteration of the simulation. We use two different rating values: One rating value for all tissue types and all stages (from II to final stage) which is defined as

$$m_{\text{tt,stage}}(t) = \frac{\#\text{ non-matching pixels}}{\#\text{ pixels within the callus}} \tag{3.5}$$

and a second one that specifically targets the development of cartilage

$$m_{\text{cart,stage}}(t) = \frac{\#\text{ non-matching pixels of cartilage}}{\#\text{ experimental cartilage pixels}} \tag{3.6}$$

(see definitions and details in the appendix of Vetter et al. [2011b]).

To understand how modifications of the mechano-regulation change the tissue patterns during healing, first a reference simulation was performed without considering a delayed stimulus, a variable mechanosensitivity or committed maturation. The values for the two decisive mechanical thresholds for the reference simulation, MS_b and MS_c are determined by minimizing the mismatch between the formed cartilage for the experimental image of Stage III and the simulation, $m_{\text{cart,III}}$ (Figure 3.4, left). Changing then the mechano-regulation, for example by considering a delayed stimulus, has the consequence that the "optimal" mechanical thresholds determined for the reference simulation are no longer optimal for the simulation with the changed mechano-regulation (Figure 3.4, right). Although the computational effort is increased drastically, the influence of changes in the mechano-regulation can be critically assessed only by first, finding new "optimal" mechanical thresholds, MS_b^* and MS_c^* for the scenario under investigation (Figure 3.4, right) and second, evaluating the simulation using these thresholds and compare the results with the reference simulation.

From the predicted tissue patterns within the callus for each day of healing, further quantities can be calculated, which characterize the progress of healing. Quantities presented in this study include the amount of cartilage present in the callus given as the cartilage area, the location of the cartilage within the callus quantified by its center of area in radial direction, the amount of bone within the callus as the area of bone and the mechanical performance of the healing bone osteotomy characterized by its total stiffness calculated as F_{load}/u, where u denotes the displacement between the upper and the lower end of the modeled cortex. These quantities are compared with data calculated in the same way from the experimental images from Stage II to VI as well as the restored cortex under consideration of the elastic modulus in the bony callus [Vetter et al., 2011a].

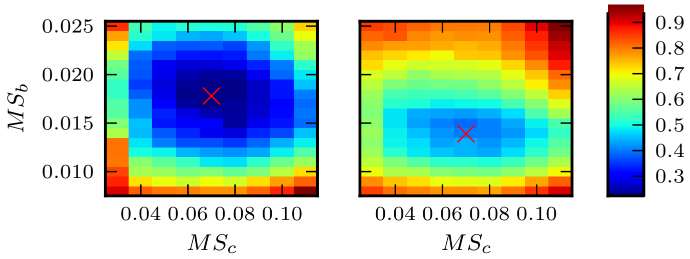

Figure 3.4: Each colored box in these phase diagrams corresponds to a simulation with a specific choice of the two thresholds for mechano-regulation, MS_b and MS_c. The color denotes the agreement between experiment and simulation, i.e. the minimum value of $m_{\mathrm{cart,III}}(t)$ for all t, where dark blue corresponds to best agreement. Left, reference simulations without considering a delayed stimulus, a variable mechanosensitivity or committed maturation (see text). Right, simulation assuming a mechanical stimulus, which is integrated over the last 5 days. Comparison of the two phase diagrams demonstrates that for both scenarios good agreement with experiments can be obtained, for different "optimal values" of MS_b and MS_c (red crosses).

3.3 Results

The incorporation of resorption into our model raises a set of new questions, which have to be answered before our investigations can focus on the mechano-regulation of healing. Firstly, is the introduction of a single mechanical threshold MS_r for resorption sufficient to describe the whole healing process ending in a restored cortex? Secondly, how does the value of MS_r influence the course of healing in particular the configuration at late times? How does the kinetics of resorption, i.e. the rate of how fast resorption occurs, influence the healing course? Finally, resorption is not limited to the callus tissue, but occurs also in the cortex [Vetter et al., 2010]. Does the decrease in cortex density agree between experiment and simulation?

3.3.1 Complete Course of Healing

Figure 3.6 shows the comparison between the experimental and computational images of the reference simulation for the healing Stages II–VI plus a final stage of a restored cortex. The main features of the early phases are similar: the growth of a periosteal bony callus and the formation of cartilage at the outside of the fracture gap, building the first bridge between the two fractured bone parts. At later phases of healing (Stage V to VI) the size of the bony callus decreases, while the density of the bone within the fracture gap increases. At very late times (more than a year) the simulation shows a fully restored cortex of virtually constant density, so that no traces of the fracture gap are visible any more. Small remnants of fibrous tissue in the marrow space are the only remainders of the osteotomy.

The good agreement to the experiment is more quantitatively shown in Figure 3.5. Comparing experimental and computational images pixel-to-pixel, the time development of the mismatch $m_{\mathrm{tt,stage}}$ (Equation 3.5) between the simulation and all the experimental stages including the final restored stage is plotted. In the case of a perfect agreement, each of the six curves would show a minimum of zero mismatch at a specific time. Our model comes close to this idealized situation: the minima of the mismatch are between 4 and 9%, only Stage V is slightly above 10%. The reason for this larger value for Stage V is that in the experiment during this stage the medullary cavity is sealed by woven bone. This is not the case in the simulation. Additionally, resorption within the bony callus results in the assignment of some tissue elements as fibrous tissue. Table 3.2 provides the values for the mismatch together with the iteration (day), when the minimum is obtained. These time points increase with the number of the stage demonstrating that the simulation runs through the stages in the correct order.

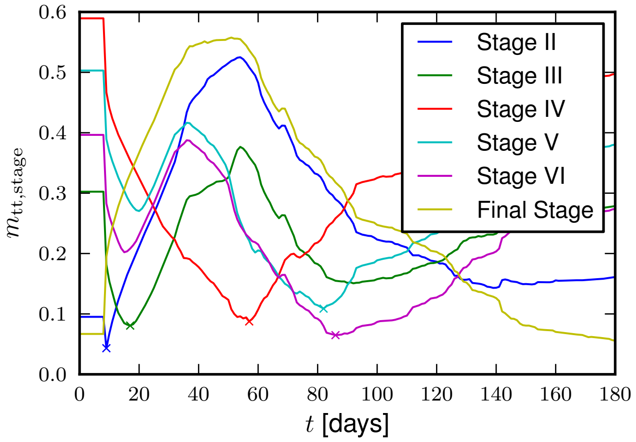

Figure 3.5: Time development of tissue mismatch between the reference simulation and each of the stages. For all stages the curves display a minimum with a mismatch around 0.1 or below. The minima (denoted by crosses) occur in the right order of stages (see also Table 3.2)

Stage	Time	$m_{\mathrm{tt,stage}}[\%]$
2	10	4.3
3	19	8.0
4	56	8.8
5	77	10.9
6	84	6.4
final	$\geqq$420	0.0

Table 3.2: Minima of the curves of $m_{\mathrm{tt,stage}}$ (Equation 3.5) for the reference simulation as shown in Figure 3.5.

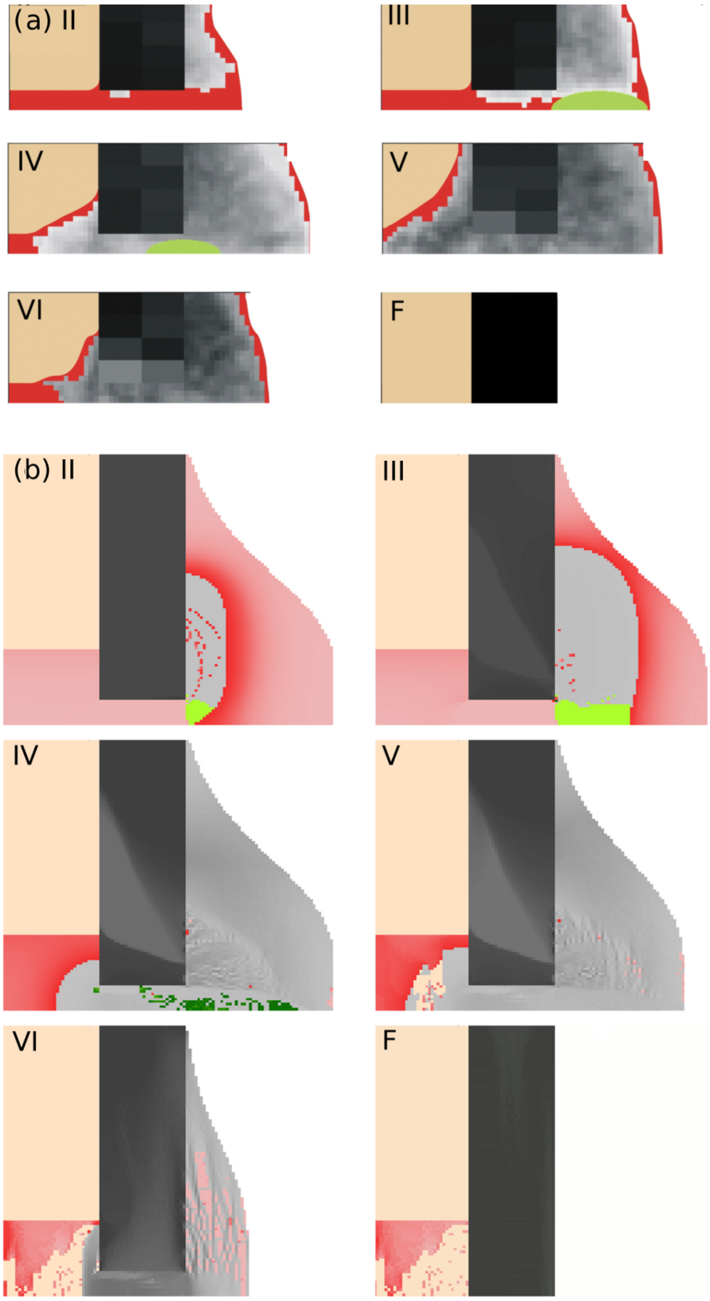

Figure 3.6: Complete course of healing: Due to symmetry all images are reduced to only a quarter of a cross section. Bone marrow is marked beige, all other colors are as in Figure 3.1. (a) Averaged experimental data (Stage II–VI [Vetter et al., 2010] plus the final stage of the restored cortex), (b) corresponding simulated data. After bone growth starts periosteal (Stage II), the gap is periosteally bridged via cartilage. Bony bridging occurs while the amount of cartilage diminishes and is shifted inwards (IV). Cartilage ossifies (V), and callus size reduces (VI) until the initial geometry of an intact cortex is restored (F).

3.3.2 Influence of the Resorption Threshold MS_r

When describing the introduction of the resorption threshold MS_r in Section 3.2.3, we argued that for a restoration of the cortex the value for MS_r should be close to the mechanical stimulus in an intact cortex, $ms_{intact} \approx 55\,\mu\epsilon$. Figure 3.7, which shows the late configurations using different values for MS_r, confirms our considerations. For a very high threshold (Figure 3.7(a)) not only the cortex thickness is clearly reduced, but also its bone density (denoted by the gray scale) and elastic modulus are lower (10.1 GPa). For a low value of MS_r (Figure 3.7) (b) the bony callus does not get completely resorbed, but periosteally a shell-like structure remains, while endosteally a bony bump marks the site of the osteotomy. For all the simulations presented in the following an intermediate resorption threshold of $MS_r = 60\,\mu\epsilon$ was chosen, which results in a full restoration of the cortex of the initial thickness and density (see last image of Figure 3.6). From these results the important conclusion can be drawn that in contrast to MS_c and MS_b, MS_r is not a free parameter of the mechano-regulation, but its value is more or less fixed under the condition that the pre-fractured state of the cortex should be restored.

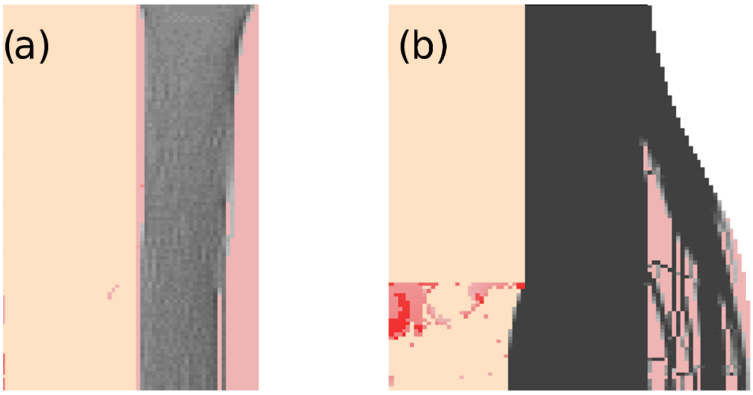

Figure 3.7: Final state of healing for two different resorption thresholds (a) $MS_r = 180\,\mu\epsilon$ and (b) $MS_r = 20\,\mu\epsilon$. The load of $F_{load} = 500$ N was applied to the same cortical cross section at the top of the image. The exact shape of the remaining bony callus depends on the boundary conditions and the shape of the callus, which is predefined and is not subject to mechanical control.

3.3.2.1 Resorption of the Callus

In contrast to tissue maturation, resorption results in a softening of the tissue ($\Delta E < 0$ in Equation 3.1). We found that a linear decrease in the elastic modulus compared to an exponential one can better describe both, the early decrease of elastic modulus in the cortex, as well as the removal of the bony callus. Figure 3.9 column (o) shows the time evolution of parameters describing cartilage, bone and total stiffness as a function of a linear resorption rate k_r. These results are contrasted to simulations without resorption ($MS_r = 0$) as well as with a vanishing resorption rate $k_r = 0$ but a non-vanishing MS_r causing that no changes in the elastic modulus occur in volume elements with a mechanical stimulus below the resorption threshold. For approximately the first 40 days, the obtained results are almost identical demonstrating that resorption does not play an important role in the early phases of healing. However, also in this early phase a few pixels in the periosteal callus receive a stimulation below MS_r with the consequence of resorption and a lower bone density. At later phases the amount of cartilage is slightly larger for intermediate resorption rates (Figure 3.9(a,o)). As expected, a higher resorption rate results in a lower amount of bone in the callus (Figure 3.9(c,o)). On a semilogarithmic plot the resulting differences in total elastic modulus of the fractured bone can hardly be distinguished (Figure 3.9(d,o)). Simulations with resorption attain already after about 80 days values for the total stiffness close to the value for the intact bone, for slow resorption this value is not approached from below, but a slight overshooting of 2.4% in stiffness compared to the value of the restored cortex can be observed. In the following simulations a resorption rate of 128 MPa/day was used.

3.3.2.2 Resorption of the Cortex

As experimentally observed [Vetter et al., 2010], during healing transiently also the density and therefore the elastic modulus of the cortex is declining. Figure 3.8 shows the averaged elastic modulus of the cortex at different distances from the symmetry plane in middle of the fracture gap.

Within the gap the elastic modulus increases with the progress of healing approaching the value of $E_{cort} = 20$ MPa. Cortex resorption results in a minimum of the cortex elastic modulus around day 90. For late times, homogenization of the elastic modulus is obtained, which is reflected by almost constant profiles in Figure 3.8. While the general trend is similar to experiments, the shape of the profile differs in the cortex region close to the gap. For early times the bone end receives enough mechanical stimulation to avoid resorption. In this part of the cortex resorption becomes active only in the time period between 60 and 90 days.

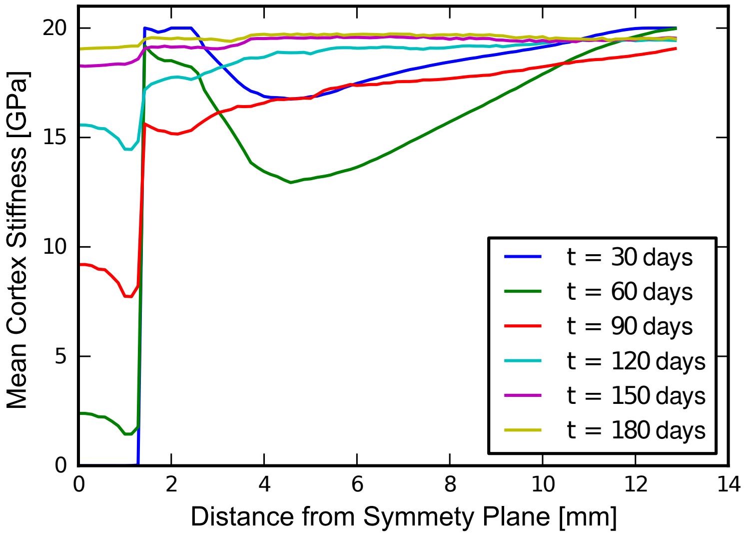

Figure 3.8: Mean elastic modulus of the cortex as a function of distance from the symmetry plane in the middle of the fracture gap. The used implementation of resorption does not discriminate between cortex and the rest of the callus; $MS_r = 60\,\mu\epsilon$, $k_r = -128$ MPa/day. Compared to the experiment (gray values of the cortex in Figure 3.6(a) the simulation shows an increase in elastic modulus at the bone ends (distance > 1.5 mm) at early stages.

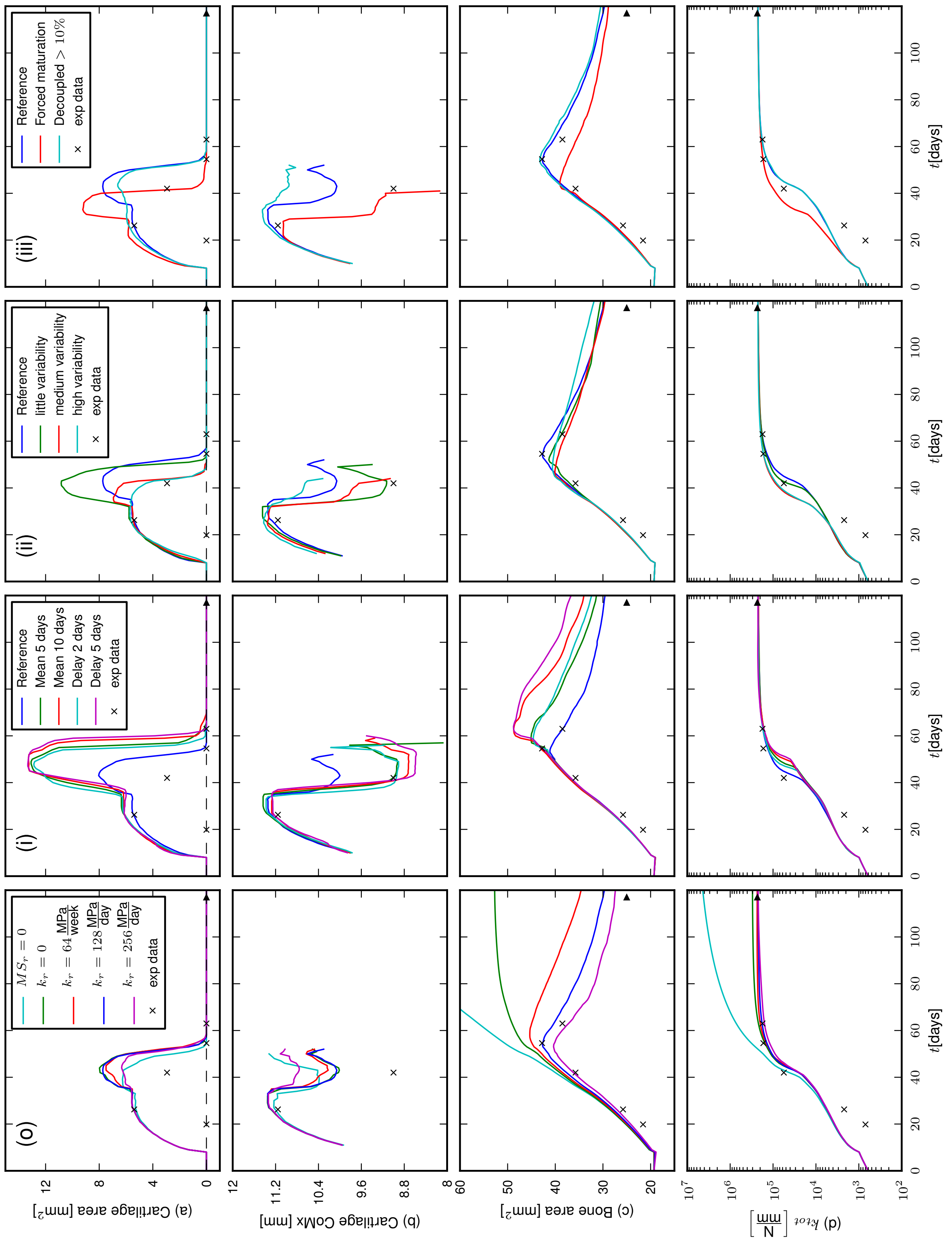

Figure 3.9: Time development of several evaluated parameters for the different healing scenarios. Vertically plotted are: (a) cartilage area, (b) position of cartilage, (c) bone area and (d) calculated total stiffness. Plotted horizontally are different healing scenarios: (o) different resorption rates (i) influence of delayed stimulus. (ii) variable mechanosensitivity. (iii) committed maturation; crosses correspond to experimental data of Stages II–VI. The triangles denote values of the restored cortex, which are attained only at times longer than the plotted 120 days.

3.3.3 Investigating Cellular Mechano-Regulation

3.3.3.1 Influence of a Delayed Stimulus

The plots of column (i) in Figure 3.9 show the time evolution of healing for four simulations, where either a mechanical stimulus 2 or 5 days in the past was used, or the stimulus was integrated over 5 or 10 days in the past. All the simulations are similar and comparable with the reference simulation until approximately day 35. Afterwards the largest differences to be observed are that considerably more cartilage is formed in the gap region (Figure 3.9(a,i)), resulting in a medial shift of the center of mass of cartilage (Figure 3.9(b,i)). The longer the delay of the stimulus, the later this increase and shift of cartilage starts and more bone is formed due to a later start of resorption (Figure 3.9(c,i)). The lower elastic modulus of the fractured bone (Figure 3.9(d,i)) corresponds to delayed healing. In all four plots it is obvious that the effect of delayed stimulus by 2 days results in similar tissue pattern during healing than an integrated stimulus over 5 days (similar for 5 days delay and 10 days integration).

3.3.3.2 Influence of Variable Mechanosensitivity

From the three studied influences, the introduction of fuzzy thresholds has the smallest effect on the course of healing. For the choice of a medium variability of the mechanosensitivity, the amount and position of the formed cartilage are in excellent agreement with the experiments (Figure 3.9(a and b,ii)). The amount of bone is generally decreased, never filling the whole available callus area (Figure 3.9(c,ii)). This is accompanied by a faster stiffening of the callus corresponding to an overall accelerated healing response.

3.3.3.3 Influence of Committed Maturation

The first scenario, where the maturation of the soft tissues (fibrous tissue, cartilage) is decoupled from a mechanical stimulation as early as after 10% to its way to full maturation (see Figure 3.1, blue bars), has hardly any effects on the course of healing. Small changes can be seen in the cartilage development (Figure 3.9(a and b,iii)), but the formation of bone and the overall stiffening of the fractured bone occurs analog to the reference simulation. However, the effect is much more significant in the second scenario, where only the very early phase of endochondral ossification was assumed independent of the mechanical stimulation (Figure 3.1, orange bar). Under these conditions, cartilage disappears earlier while shifting medially (Figure 3.9(a and b,iii)). The more stable conditions related to a cartilage-free callus, lead again to a smaller amount of bone to be formed and a faster stiffening of the fractured bone. From all the performed simulations, this condition resulted in the fastest healing.

3.3.4 Cartilage Development

In all the simulations the mechanical thresholds MS_c and MS_b were adjusted to make the early cartilage development comparable to the experiment (Figure 3.4). However, already the first two rows of Figure 3.9 demonstrate that the later cartilage development can proceed quite differently. For a closer investigation, Figure 3.10, shows simulated histological images of the gap region for different stimuli processing assumptions. For each assumption, the upper images of each scenario depict a time when the cartilage is formed and its maturation starts, the lower images at the later time point shortly before its disappearance. While the reference simulation produces a mixture of cartilage and bone within the fracture gap, assuming a delayed stimulus the gap gets completely filled with cartilage before maturation starts. For the scenarios of variable mechanosensitivity and committed maturation, fibrous tissue can be found in the gap when the maturation of cartilage starts. Besides these differences in the tissue composition in the gap region, it is worth noting that maturation of the cartilage starts at different locations. While in case of a variable mechanosensitiviy, the maturation starts laterally, for the case of committed maturation of cartilage formation, cartilage maturation proceeds in the region where cartilage was initially formed, i.e. medially close to the cortex.

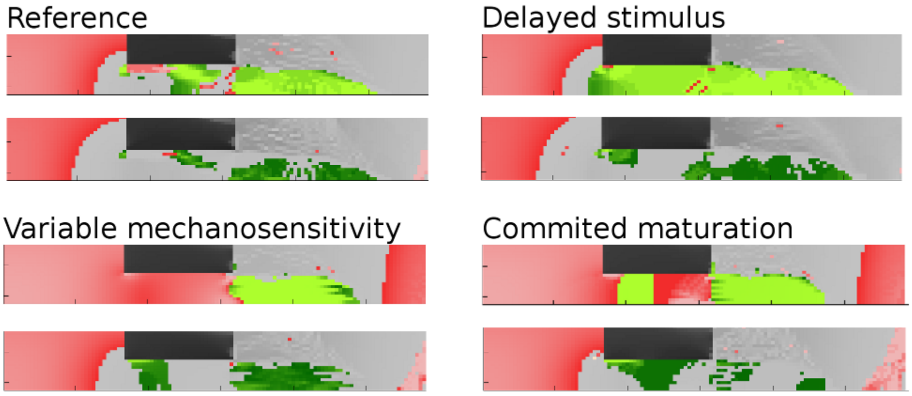

Figure 3.10: The development of cartilage for the reference simulation and all three changes in the mechano-regulation: delayed stimulus (2 days), variable mechanosensitvity and committed maturation (decoupled from mechanical stimulation during early cartilage phase). The upper images show the region around the fracture gap at the time when cartilage starts to mature (dark green), the lower images shortly before no more cartilage is visible.

3.4 Discussion

In this work we used a mechanobiological model, which describes the time evolution of tissue patterns during bone healing in sheep, to study the control of bone healing. The implementation of resorption allows to successfully model the complete healing process, where the agreement with the histological sections obtained from an animal experiment with 32 sheep is that each of the six experimental images is met with a mismatch between 4 and 11% in a pixel-by-pixel comparison. Keeping in mind that the experimental images are averaged images, but still carry an error due to the unavoidable biological variability between individual animals, this agreement between simulation and experiment has to be seen as satisfactory. Since our approach aims at a computer model which is mechanobiologically reasonable (e.g. by allowing ossification to happen endochondrally or intramembranously), but as simple as possible, this agreement is remarkable.

There is general agreement about the need to improve the corroborability of computational models of mechano-regulated tissue differentiation [Isaksson et al., 2006a; Khayyeri et al., 2013]. The rigorous quantitative comparison with experimental data as presented in this work is an important step in this direction. It is worth mentioning that this experimental data considers the variability of individuals. In the attempt to test mechanobiological theories of healing and (following the perspective of Karl Popper) try to falsify them [Khayyeri et al., 2013], one faces a dilemma in case of disagreement: it is unclear whether the mechanobiological theory is inadequate, or the problem arises from an incorrect choice of the model parameters, although the theory provides an accurate description of healing. Typically models in biology suffer from a very large number of free parameters. Most of biology is not yet quantitative enough for the needs of numerical simulation. This results in big uncertainties in the values of these parameters, which can even be hardly be estimated, so that an error by a factor of 10 cannot be excluded. In our opinion the only way out of this dilemma is, first, to reduce the number of free parameters, i.e. parameters with big uncertainties in their numerical value, and, second, to perform a thorough parameter study of the remaining free parameters. Simple mathematics shows that this is only possible if the number of free parameters is about five or below [Vetter et al., 2011b].

A look at the table of parameters used in our model (Table 3.1), shows that most of their values can be well defined. The geometry of the tibia and the osteotomy are the measured values from sheep. The loading parameters are given by the mechanical characterization of the fixator, by measurements of the ground reaction force and the interfragmentary movement [Duda et al., 1997]. A strong assumption in our model is to assume rotational symmetry and a purely compressive loading on the cortex. Material parameters of the tissues can be found in literature, where values of the Poisson's ratio are surely less reliable. Since the incorporation of mineral changes during healing changes the mechanical properties drastically, we included data obtained by nanoindentation [Manjubala et al., 2009] to describe the maturation of bone. Here a strong assumption is to assume isotropic, linear elastic material behavior even for soft tissues. The rates for tissue maturation are not so easily measurable, but can be reasonably estimated based on the histological sections at different time points of healing. Really unknown are only the mechanobiological control parameters. The multitude of biological factors and their insufficiently characterized interactions make a phenomenological description inevitable. To define a diffusive "biological potential" with specified sources is a very elementary reproduction of this complexity. The necessity of a strong source of the biological potential at the periost was shown [Vetter et al., 2011b] and is further discussed in the next section. A single mechanical stimulus, the volumetric strain, was employed in the model. It should be emphasized that we do not claim that pluripotent cells feel only a single stimulus. Rather all the manifold stimuli the cells are sensing (John Currey coined the term local proximate stimuli [Currey, 1995]) can be phenomenologically summarized under the local "ultimate stimulus", to describe cell behavior under mechanical stimulation.

The use of a single mechanical stimulus is in agreement with Occam's razor, which favors from competing hypotheses the one with the fewest assumptions [Khayyeri et al., 2013]. The development of the different tissues is then controlled by three thresholds of this mechanical stimulus, MS_b, MS_c and MS_r. This study showed that the resorption threshold MS_r cannot be seen as a "free parameter", since it is fixed by the condition that the cortex should be restored in its original geometry. A whole series of simulation can be performed in varying the two remaining thresholds, MS_c and MS_b, resulting in a phase diagram as shown in Figure 3.4. Such a phase diagram shows the agreement to the experiment as a function of the chosen values for MS_b and MS_c. For our investigation of the cellular mechano-regulation the possibility to characterize the model with such a phase diagram is essential. Changing the rules for the mechano-regulation also "detunes" the best values for MS_b and MS_c (see Figure 3.4). To isolate the effect of changed mechanobiological rules on the resulting tissue patterns it is therefore necessary to use "retuned" values for the mechanical thresholds. Without this "retuning" of the parameters we observed large effects of a changed mechano-regulation on the time course of healing.

Discrepancies between experiment and simulations are most prominent in a new quantity that we assessed for the first time for comparison with simulations, i.e. the bone density due to its porosity. The animal experiments show a reduction in bone density of the cortex close to the fracture gap [Vetter et al., 2010]. Simulations describe a similar reduction, but only at later phases of healing (Figure 3.8). The reason for this delay in resorption is that the uniaxial loading results in hoop strains at the cortex ends, which therefore protect this part of the cortex initially from resorption. The periosteally formed bony callus shows regions of bone development being influenced by the resorption threshold, leading to a lower bone density in the callus than observed. The callus in the simulation has micro-porosity which is not considered in the elastic modulus of the volume elements (i.e. ρ in Equation 3.2). While during the evaluation process this porosity could be accounted for by averaging the density of the callus, this would still result in a lower density than observed. This is the case since the master curve (Figure 3.2) was defined such that the development of the callus in the simulation fits the experimental data if no resorption is present. A possible way to compensate for this is to modify the master curve e.g. increase the initial densification rate of the bone until the development of the callus fits the experiment. How big such an increase needs to be and how this affects the rest of the healing progress needs to be found out.

Of major interest for this study was how a time delay between stimulation and tissue formation, a variable mechanosensitivity of the cells or a committed maturation independent of a mechanical stimulation influences the tissue patterns during healing. Most importantly we did not observe any qualitative differences in the time evolution of the tissue patterns. In all the scenarios a reasonable agreement with the early phase of cartilage formation (Stage III) could be obtained by adapting the values of MS_c and MS_b. Healing progressed very robustly towards full restoration of the cortex, with only major differences of how cartilage disappears form the callus. The extreme cases occurred with a large delayed stimulus, where a substantial amount of cartilage in the fracture gap was formed, resulting in a medial shift of the center of mass of the cartilage. Consequently more bone was formed due to a delay in bone resorption and the total stiffness of the broken bone showed that healing was slowed down. The other extreme occurred for medium and large variability in the mechanosensitvity, where the formation of cartilage was strongest suppressed. Also here a medial shift of the cartilage was observed since resorption occurred from lateral to medial. The amount of formed bone was minimal and healing progressed fast.

An observation worth mentioning is that a delayed stimulus changes the time development of the healing progression since this change in the mechano-regulation was implemented in other models of bone healing for reasons like numerical stability and others [Lacroix and Prendergast, 2002; Isaksson et al., 2008; Gómez-Benito et al., 2005]. While this can be partly compensated by adjusting parameters, this should be taken into account for the interpretation of the simulation results. That a variable mechanosensitvity changes the progress of healing is also not self-evident. The new fuzzy threshold is symmetric around the original sharp threshold so that one could conclude that the effects of increased/decreased stimulation would cancel out. However, healing progresses asymmetrically always towards stiffening (apart from processes including resorption), therefore even a slight increase in the elastic modulus and therefore a reduction in strain allows an earlier start of maturation. Our investigations concerning the "committed maturation" demonstrates that large parts of healing can be put independent of the mechanical stimulus without marked differences in the resulting tissue patterns. Where mechanical stimulation matters is more in the triggering of a new process. Our simulations show that supporting the very early phases of endochondral ossification leads to a clear speed-up of healing.

3.4.1 Outlook

The obtained results from a simulation always depend crucially on the assumptions made in the model. Therefore, the question is where to invest additional resources of man and computer time to improve the predictive quality of the results. Our lean model allowed to relate the observed development of the tissue to development of governing influences (i.e. mechanical stimulus and biological potential). In this section, based on the understanding gained from the work with the described model, recommendations are given how one should proceed, based on the experience obtained by using the presented model.

The assumption of a strictly axial loading allowed to represent the model in two dimensions with a cylindrical symmetry. In the sheep experiment the fixation device used on the sheep's tibia was placed on the leg's exterior allowing – to some extent – bending and shear. The feasibility of complete 3D models including the fixation device has been shown recently [Byrne et al., 2011]. An extension of the model to full 3D allows to test whether the spatial symmetry of the model has an influence on the choice of the mechanical stimulus. From the axial symmetric model we learned what are important features that have to be fulfilled in a model and volumetric strains proved to provide the best agreement with the tissue patterns observed in histological sections. This becomes clear as in Stage III, which was used to determine the values for MS_c and MS_b, the following arrangement of the different tissues types has been observed. New bone was formed on the periosteal side adjacent to the cortex, in the fracture gap the initial granulation/fibrous tissue is still present and in between some cartilage formed bridging the bone ends.

Assuming axial loading the volumetric stress produces a pattern that shows a maximum within the gap, and decays monotonous to both sides with small values periosteal to the cortex (Figure 3.11(a)). In contrast, the shear strains are very low except at the corners of the cortex (Figure 3.11(b)). In a 3D implementation of the geometry without axial symmetry it is now quite likely that shear strains take also maximal values within the fracture gap. Therefore, shear strain become a possible candidate as mechanical stimulus for tissue differentiation. The potential of different mechanical stimuli to control bone healing should be investigated using a full 3D model.

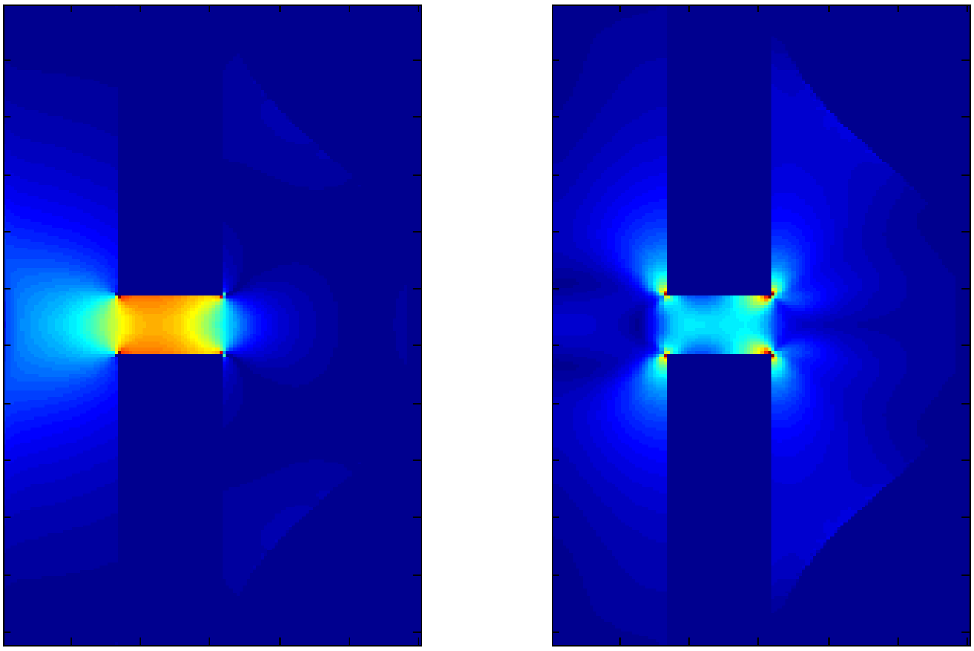

(a) Volumetric strain

(b) Shear strain

Figure 3.11: Strain descriptors as calculated for axial loading in the initial conditions with only fibrous tissue in the fracture callus, the dark blue rectangle (low values) corresponds to the position of the cortex. (a) The decaying volumetric strain from the gap (orange) around the outer edge allows to achieve a tissue patterns where the three different tissue types are contiguous and located as observed in the experiment, by using two mechanical thresholds. (b) The lobes of high shear strain at the edges of the fracture ends makes shear strain not a useful mechanical stimulus when only axial loading is assumed.

Values of the volumetric strain (when used as mechanical stimulus) decay from high values in the fracture gap to both sides, periosteally and endosteally. Using only mechanical thresholds this would lead to symmetric tissue development, i.e., cartilage formation, endosteally at the same time it is observed periosteally. The asymmetric development of both sides is the result of the biological potential with its main source at the periost. The diffusion of the biological potential explains the growth of the bony callus at the periosteal side of the cortex and also determines the speed of the growth. It is likely that this particular bone growth could also be achieved by a rule that bone is only allowed to form on already existing bone. Thus it could partly replace the function of the biological potential and would also result in a more controlled endochondral ossification.

Running many simulations with different scenarios of mechano-regulation as well as different mechanical thresholds, we observed that the course of healing was rather similar for all scenarios till attaining Stage III, but then the time evolutions showed a stronger divergence. A possible explanation of this observation is that initially the tissue pattern is not only controlled by the mechanical threshold but it is also influenced by the biological potential c. Initially the strain in the fracture gap is too high for the fibrous tissue to mature, only on the periosteal side where the volumetric strain (Figure 3.11(a)) is below MS_c and the c sufficiently high, the elastic modulus starts to increase. Assuming $c = 1$, 8 iteration steps later when its stiffness reaches E_{fib}^{max} those tissue elements will be either turned into bone or cartilage, depending on the magnitude of the stimulus relative to MS_b. Close to the fracture gap, where the strains are bigger than they are further away, this will result in the formation of cartilage (Figure 3.6(b), Stage II). Changing MS_c therefore shifts the interface between fibrous tissue and cartilage. While this interface depends on the strain in the initial set-up, the interface between cartilage on bone which can be controlled by MS_b is not defined at a single time point. The maturation of the soft tissue on the periosteal side leads to a load transfer, resulting in an initial increase of the strains in the region where the cartilage is found. The time when E_{fib}^{max} is reached depends on when the advancing of the biological potential started the tissue maturation. The interface where the decision between bone and cartilage is made therefore grows outwards (Figure 3.6(b), Stage III). This slow procession of the interface and a relatively continuous strain distribution result in a relatively stable advancing of the healing till Stage III. These considerations do not only explain the minimal mismatch in Stage III for a certain set of parameters, the changes in the phase diagrams due to an time delay (Figure 3.4), can also be explained.

The divergent development of different scenarios after Stage III, i.e. the strong variation of cartilage development within the fracture gap, has several reasons. As the biological potential is already maximal in this region when the mechanical stimulus drop below MS_c, thus starting the maturation, the developing tissue pattern is exclusively dependent on the mechanical stimulus with respect to the mechanical thresholds. The decision if tissue within the gap will directly turn into bone or if it will transiently turn into cartilage depends on how fast the stains decrease, as well as the difference between the thresholds MS_c-MS_b. Changing the mechanical thresholds to “re-tune” the model accounting for changes in the mechano-regulation can thus explain the differences in the amount of cartilage as observed in Figure 3.9(a). Where the cartilage is located, where it starts to mature, and where it remains longest (Figure 3.10) depends alone on the time development of mechanical stimulus. Once the cartilage is completely replaced by bone, the simulation converges against the steady state of an intact bone.

For a further progress of our mechanobiological understanding of bone healing, it seems necessary that standardized animal experiments are performed with well-defined loading conditions and a three-dimensional evaluation of the callus [Gerstenfeld et al., 2006]. Unfortunately detailed data is only available at one time point per animal, limiting the comparison to the average of the samples as presented. With our model describing healing in a large animal (sheep), an interesting question is how well the model predicts healing in small animals like mice and rats [Checa et al., 2011]. To test our model also for small animals would clearly improve the degree of independence of the model [Khayyeri et al., 2013]. Up to now no data set comparable to the sequence of images by [Vetter et al., 2010], which shows the mean healing progression as averaged over many animals, is available in the literature. For the execution of these animal experiments our simulations provide the recommendation to thoroughly document the intermediate phases of healing. In this phase, in which cartilage emerge in the callus and is replaced by bone, the biggest uncertainties are present.

The inclusion of resorption of not only the callus but also the cortical bone into the model allows to find conditions of mechanical stabilization that result with the fastest possible healing, which is a clear aim of such computer simulations. However, right now these model approaches are still far from a clinical application. For a further improvement of our model we suggest computational work along the following milestone:

- evaluation of histological sections and description of bone, fixator and forces in 3D
- finding the appropriate ultimate mechanical stimulus
- adjusting the densification/ossification rate of the bone tissue such that the initial development in the periosteal region fits the experiment
- considering alternative descriptions of the biological potential
- incorporating more biological understanding of how cartilage is replaced by bone

Chapter 4

Osteocyte Networks

4.1 Aim

More and more quantitative data is being published concerning the 3D properties of osteocyte lacunae [Schneider et al., 2007; Hannah et al., 2010; Hesse et al., 2014a], but hardly any information is available about the 3D structure of the canalicular network connecting the cell lacunae. However, for the function of the osteocyte lacuno-canalicular network (OLCN), the connections between cells seem particularly essential for communication and sensing purposes.

One step towards a functional understanding of the OLCN is to study its structure and topology. To interpret the structural observations in terms of functionality, one should keep in mind that structural features might also arise due to constraints during network formation. Therefore, this work tries to relate network properties to the structure of the bone tissue in which the network is located as well as to its formation process. The present study provides a 3D quantification of the OLCN in osteons. Osteons provide an ideal case study as they represent a spatially confined functional unit of cortical bone with a relatively well understood formation process (see Section 2.1.1 and Figure 2.3).

Our investigations on the OLCN structure can be summarized into three main questions:

1. How dense is the network in the osteon and how homogeneous is this density spatially distributed within osteons?
2. To what extent does the geometry of the osteon influence the structure of the network?
3. Many osteons show concentric lamellar structures around the central Haversian canal (Figure 4.1). Is the lamellar spatial periodicity of the tissue organization also reflected by the organization of the network?

In the following a few thoughts and more specific questions emphasize the topicality of the study. The network density as a function of the radius has already been addressed by Marotti et al. [1995a] based on 2D electron micrographs and light microscopic images. Based on the observation of a higher number of canaliculi on the side of the osteocytes

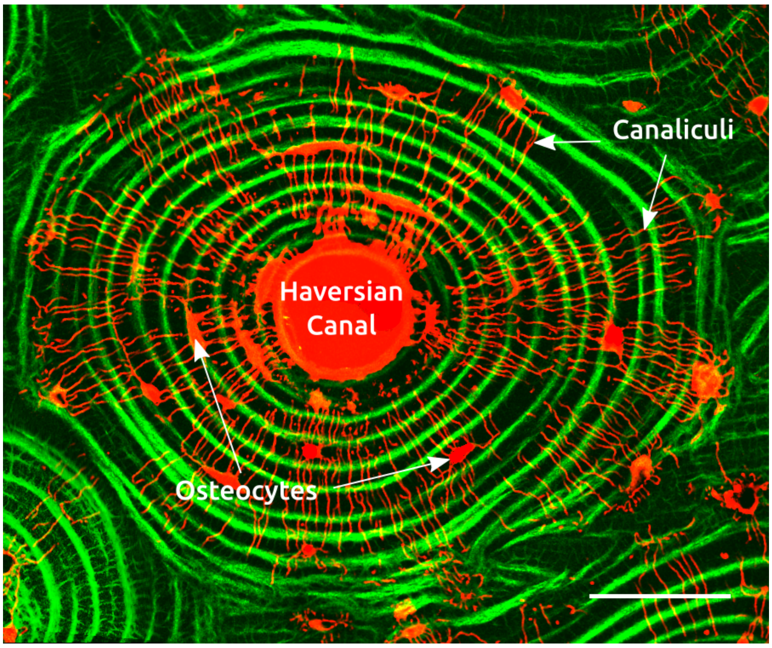

Figure 4.1: Projection of 3 μm of the osteocyte lacuno-canalicular network in an osteon. The red signal shows the imaged OLCN including osteocytes and canaliculi, the green signal is the intensity of second harmonic generated (SHG) light, showing the lamellar structures within the osteon. In the lower left corner the contrast of the SHG signal was enhanced to highlight "green canaliculi": canaliculi that used to be there but which are not accessible to the stain anymore. The scale bar equals 50 μm

facing the blood vessels than on the opposite side [Marotti et al., 1992], the authors expected an increasing network density when moving from the periphery of the osteon towards its center. A higher canalicular density close to the blood vessel is expected when assuming a constant nutrition/waste flux per canaliculus. A similar argument could explain a deceleration of bone since osteoblasts on the bone surface are exposed to increased amounts of inhibiting signaling secreted by osteocytes as the osteon gets filled (Section 2.1.1, [Marotti et al., 1992; Martin, 2000]). However Marotti et al. [1995a] could not show a significant decrease of the network density with increasing distance from the center of the osteon (Figure 4.1). It is reasonable that larger osteons as well as those having a higher density of cells need a higher network density for an efficient transport within the network. Therefore we study these relationships.

An obvious feature of the canaliculi network is its preferred orientation towards the center of the osteon. The origin of this preferred direction and its relation to the formation process of the osteon are unclear. From the perspective of the osteocytes two different types of cell processes* were described, those that radiate radially from the rather flat part of the oblate osteocytes (radial dendrites) and others that originate from the rim of the cell (equatorial dendrites) [Pazzaglia et al., 2012a]. The question arises whether the orientation of the canaliculi in the whole network also shows these two distinct directions, and whether different functions are attributed to differently oriented parts of the network.

Characteristic for lamellar bone is an organized arrangement of the collagen fibers (Section 2.1.2). Reports that osteocytes can be found only in loose lamellae [Marotti, 1993; Ardizzoni, 2001] and recent observations that canaliculi are confined to bone with unordered collagen [Reznikov et al., 2014b] indicate a relation between tissue organization and cells [Marotti, 1996]. However, these observations are not well established since they

---

*Which we can only observe in terms of canaliculi.

are not quantitatively described and often limited to small sample sizes. Studying the correlation between OLCN and the lamellae might not only provide a better understanding of the composite of cells and extracellular tissue, but allows to discuss the role of cells in the arrangement of collagen.

4.2 Material and Methods

4.2.1 Samples

All osteocyte networks studied in this work are imaged in samples of cross sections from the femural midshaft (i.e. central part of the femur, Figure 4.2(a)) of 4 female humans that died at an age between 48 and 56 years (Table 4.1) without any known metabolic disease. The samples were provided by the department of forensic medicine of the Medical University of Vienna and the study was performed in accordance with the ethic commission board of the institution (EK #: 1757/2013).

Sample	age in years
FM03	51
FM38	55
FM40	56
FM48	48

Table 4.1: Label of the sample and the age of the donor. The name of the samples does not have a specific meaning and is only used to simplify a comparison with future studies.

4.2.2 Sample Preparation and Imaging

The basic idea of the used imaging method is to immerse the bone sample in a liquid including a stain. The stain then enters into the accessible porosity of the bone sample, in particular the canalicular network where it attaches to the interface between pore and bone tissue. Then laser scanning confocal microscopy is used to visualize the location of the diffused stain. On arrival from our collaboration partners at the Ludwig Boltzmann-Institute of Osteology in Vienna (LBIO) the bone samples have already been cleaned from soft tissue. They were transversal cross section of cortical bone, roughly 0.5 mm thick and stored in 70% alcohol by volume.

In a first step, the dimensions of the cross section were reduced (to approximately $5 * 5\,\mathrm{mm}^2$) using a low-speed diamond saw (IsoMet; Buehler GmbH, Duesseldorf, Germany). Since the network can be well imaged only on samples with a smooth surface, one of the sample's surfaces was polished with grinding paper with a grit designation of P1200 (ISO 6344) under wet conditions to achieve a smooth surface that is parallel to the other. The sample was then stained by exposing it for 2 days under constant movement to phosphate buffered saline (PBS) solution in which rhodamine-6G powder was dissolved (0.02 % wt) (Figure 4.2(b)). The rhodamine diffuses into all accessible cavities and attaches to the surfaces of the accessible pores. Having a size of $(1*1*0.4)\,\mathrm{nm}^3$ [Lu and Penzkofer, 1986]

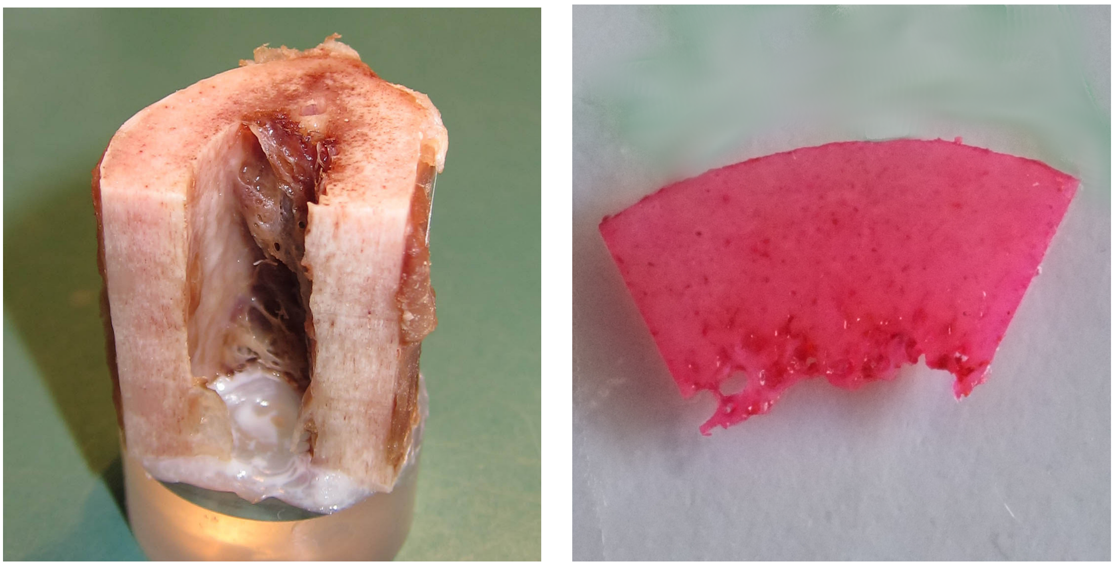

(a) Femoral bone (b) Stained sample

Figure 4.2: (a) Dissected sample of cortical bone obtained from the midshaft of a human femur, showing a longitudinal and a cross- section. (b) A thin transversal cross section was cut from this block, further reduced in size and stained with rhodamine for imaging of the osteocyte network.

rhodamine molecules can easily diffuse through the canalicular network. Imaging of the rhodamine fluorescence therefore allows to visualize the network by means of confocal microscopy [Kerschnitzki et al., 2011a].

All the image data obtained for this work has been generated using a Leica TCS SP5 laser scanning **confocal microscope**. Initial measurements were performed with a 63x water-immersion objective with a numerical aperture NA = 1.2. To improve the resolution in the direction of the optical axis, for the research presented in this work a 100x oil-immersion objective with a NA = 1.4 has been used.

The pinhole was set to the first minimum of the Airy disk to achieve a compromise between a high resolution along the imaging axis and a high light intensity. The theoretical lateral resolution of this setup was approximately 280 nm. Estimating the real resolution within the mineralized tissue, based on imaged canaliculi a lateral resolution of 500 nm was found to be more realistic. In the direction of the imaging axis, the resolution was close to 900 nm. While these dimensions are bigger than the real diameter of the canaliculi (published values range between 100 and 550 nm [Cardoso et al., 2013]), the limiting factor for an accurate measure of their topology is the distance of the canaliculi among each other which is typically higher. To image the sample in an inverted microscope setup without cover slip, the investigated sample was glued to a microscope slide. All measurements have been made with a voxel size of $(303 * 303 * 296)\,\mathrm{nm}^3$. Imaged volumes were typically $(155 * 155 * 40)\,\mu\mathrm{m}^3$ in size. The dimension along the optical axis was limited by the optical properties of bone, e.g. the light scattering by the mineral as well as the inhomogeneous arrangement of the optically anisotropic collagen matrix.

For imaging the canalicular network, rhodamine was exited with a combination of laser light with a wavelength of 488 and 514 nm. The fluorescence signal was detected in the range between 550–650 nm (red signal in Figure 4.1).

Information about the lamellar arrangement of the osteon was recorded by measuring the **second harmonic generated (SHG) signal of collagen** in backward direction (green signal in Figure 4.1). Interpretation of the SHG signal is not straightforward, but we assume that the signal originates from regions where collagen is oriented within the image plane. A more detailed discussion about the origin of the signal including test experiments is presented in Appendix C. A pulsed IR-laser with wavelength $\lambda = 820\,\mathrm{nm}$ was used to achieve the high energies needed for a sufficient SHG signal. Signals were detected between 405 and 415 nm and originate only from the focal spot of the laser as only there intensities are high enough for an efficient SHG signal. This allows to measure the SHG signal with an open pinhole to obtain a higher signal to noise ratio. As a consequence, image stacks were recorded acquiring the rhodamine fluorescence image with reduced pinhole size and the SHG image alternating for each z-layer. For both signals in each slice two images were acquired and averaged in order to reduce noise.

The **decay of intensity** of both signals with increasing imaging depth has been **compensated** by linearly interpolating the laser intensities and the voltages of the photo multiplier tubes (PMTs). This procedure provided best images at the top and the bottom of the imaged volume*.

Not all osteons in the samples were suited for answering our research question about the correlation of the lamellar structure of osteons and the canalicular network. Not selected for further investigations were dark osteons, i.e. osteons not showing the concentric lamellae (Section 2.1.2), and osteons with irregular shapes. In some osteons we observed lamellar geometries which were not favorable for the analysis: some lamellae did not form complete circles, they appeared to split into two lamellae or spiraled around the central Haversian canal (Figure 4.3). While recently Pazzaglia et al. [2012b] described such shapes of lamellae, it is surprising to see how often lamellae do not appear as closed circles when imaged with the method we used. To improve the statistics of our results, we selected osteons which showed at least 4 bright lamellae that had a regular shape. In order to find suitable osteons, first sample overviews were recorded using a lower magnification in an automated scan (Figure 4.4).

4.2.3 Image Processing and Data Analysis

A significant amount of the work of this project was the computational analysis of the images of the osteocyte network and its correlation to the lamellae in the osteon. In the following subsections the steps of this analysis are described providing some technical details, which are of particular importance for someone continuing this work. Most of the steps in the described analysis were done using the programing language Python [Guido van Rossum, 2001] and dedicated libraries (Numpy/Scipy [Oliphant, 2007], Matplotlib [Hunter, 2007]). The Python library Mayavi [Ramachandran and Varoquaux, 2011] was

---

*The intensity is expected to decay approximately exponential, but the software used to control the microscope only allows to control the laser intensity as well as PMT voltage in a linearly interpolated manner.

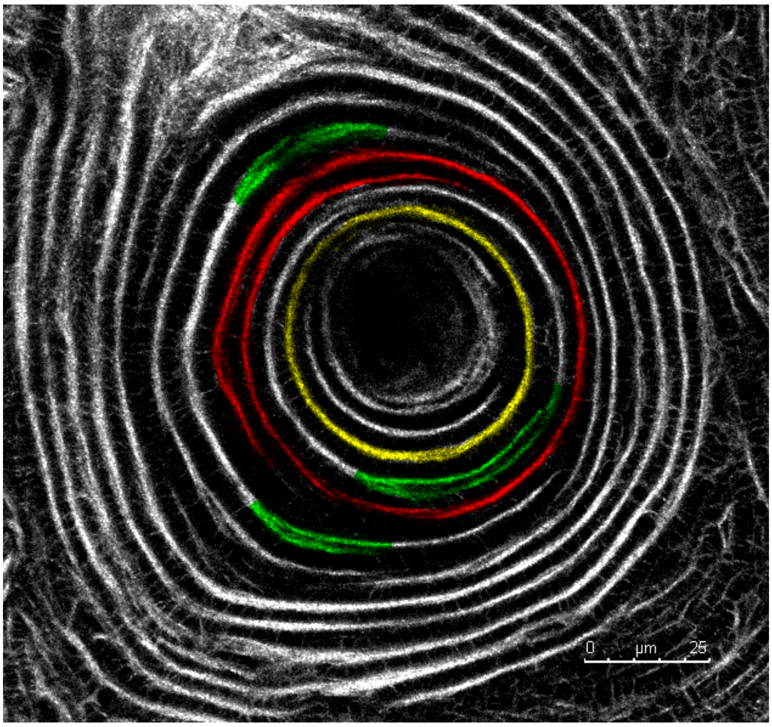

Figure 4.3: Lamellae within an osteon imaged using the SHG signal of collagen in backward direction. While most lamellae are closed circles (yellow), some lamellae form spirals (red) while others appear to split into two (green). This particular image was chosen as it contains all of these features. The lamellae in the osteons chosen for the analysis had a more regular circular appearance.

used to visualize 3D data and to test if the image analysis led to reasonable results.

4.2.3.1 Processing of Network Images to Graph Structures

A classical problem of image analysis is the thresholding of the data to distinguish, in our case, between voxels belonging to the OLCN and voxels that do not. Using a linearly interpolated laser intensity along the z-axis results in a depth dependent signal intensity. Additionally, in some samples there are also regions that are stained less intensely than other regions (Figure 4.5(a)). Using a high intensity value as global threshold to define the voxels belonging to the osteocyte network would result in a loss of network connectivity in less stained regions (Figure 4.5(c)). If, on the other hand, a low global threshold would be chosen, the lacuna size would be overestimated and canaliculi would merge in the more stained regions of the sample (Figure 4.5(b)). To avoid this problem a customized algorithm for **adaptive thresholding** was developed and employed.

Many methods have been developed for feature detection in images, e.g. difference of Gaussians (DOG) [Marr and Hildreth, 1980]. The idea of this method is to compare the image after smoothing with Gaussian functions of different kernel size (i.e. different standard deviation). The difference of two Gaussians with different kernels is, due to its shape, often referred to as Mexican hat function. Applying DOG on an image can be thought as application of a bandpass filter, highlighting local maxima in the length scale of the kernels.

The method we used for thresholding is along the lines of this method of difference of Gaussians. Instead of the difference, the ratio of two smoothed images is used for thresholding. With respect to the available image resolution, canaliculi are approxi-

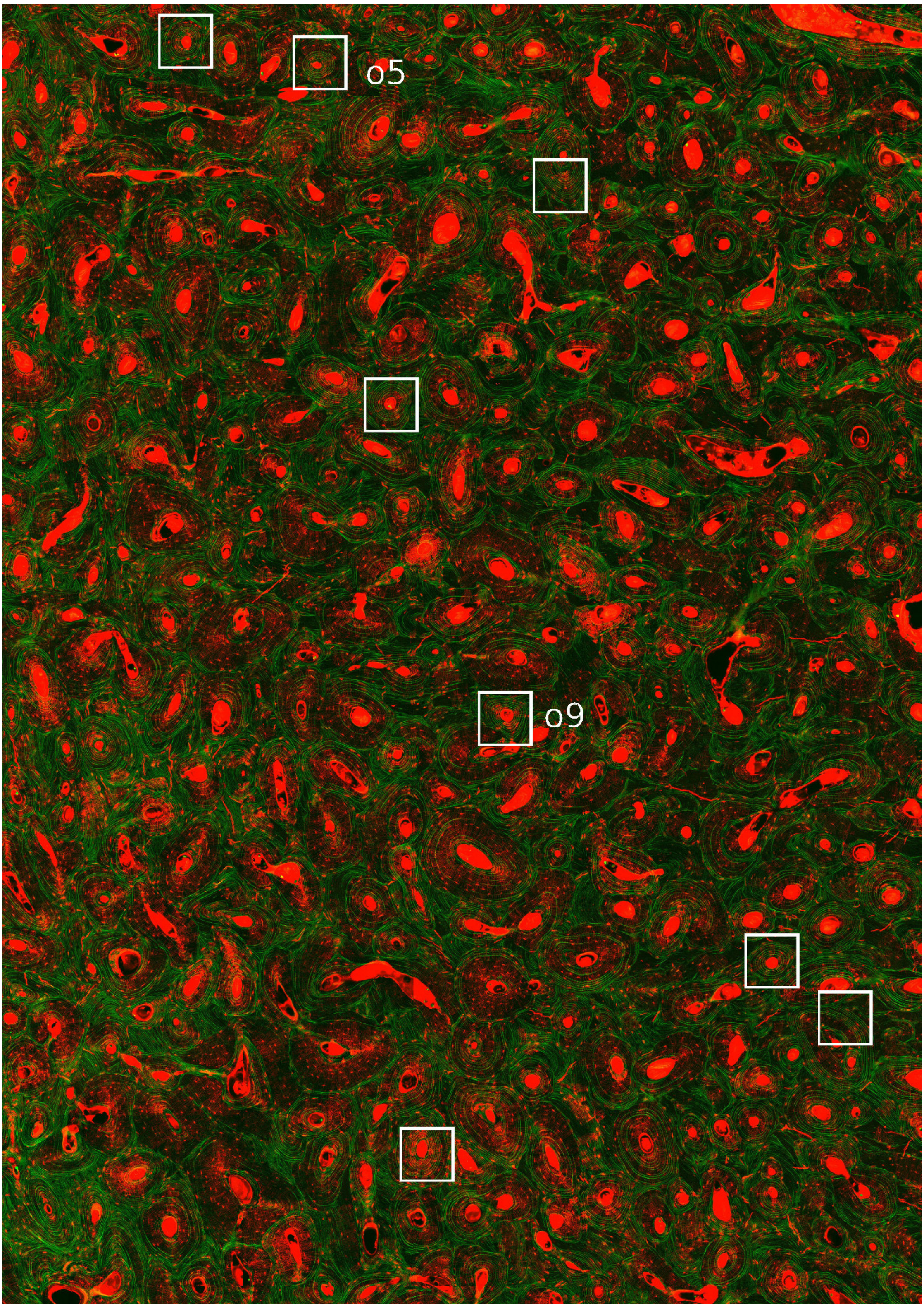

Figure 4.4: Part of the sample overview of sample FM38 showing many osteons (the big red structures are the Haversian canals) with colors as in Figure 4.1. The full resolution allows to easily identify individual lamellae as well as a fair impression of the quality of the staining. Each white square represents one dataset with a size of $155 * 155\,\mu\text{m}^2$. The complete image displays approximately $3 * 4\,\text{mm}^2$. The two osteons denoted by o5 and o9 are two osteons that will be used as "typical" examples in the course of this work.

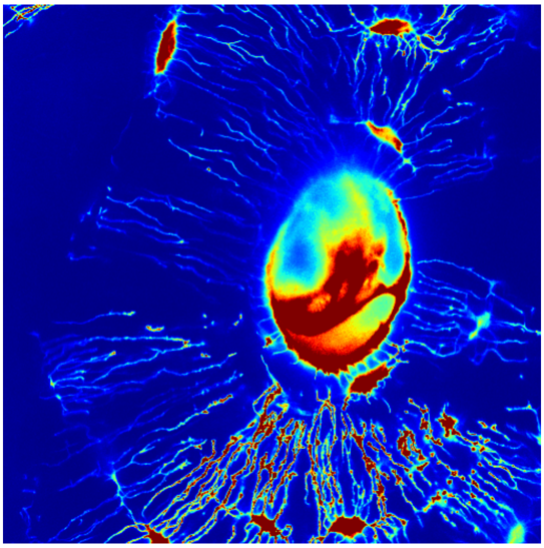

(a) Raw data

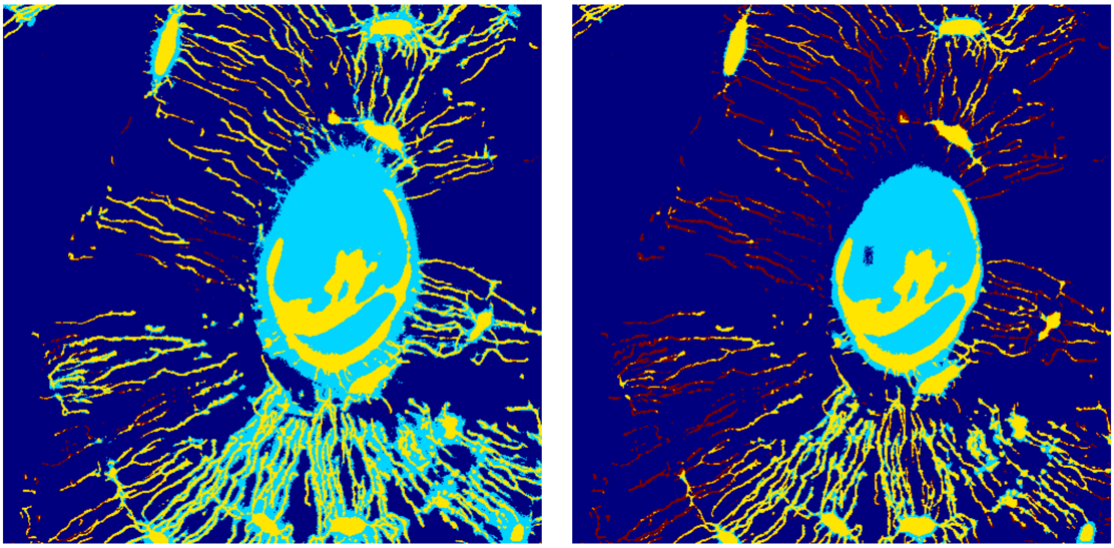

(b) Adaptive vs. low threshold

(c) Adaptive vs. high threshold

Figure 4.5: Example of a dataset with an inhomogeneous staining of the network. (a) The projected maximum of an image stack containing 10 image slices, corresponding to 3 μm thickness. Increasing intensities are color coded from blue to red. Big differences between the network on the left of the central vessel and the network at the bottom of the image are observed. In (b) adaptive thresholding is compared to global thresholding using a low global thresholds. In this image yellow voxels are the same for both methods, light blue voxels are not segmented by the adaptive method while being included in the global thresholding, red voxels label the opposite scenario. In the lower part the adaptive thresholding manages to separate canaliculi that would be indistinguishable with a low global threshold. (c) Adaptive thresholding compared to a global higher threshold with colors used as in (b). In this case, the chosen global threshold would hardly be able to detect any network on the left side of the vessel.

mately linear structures which appear in the images with a diameter of 2 to 3 voxels, where a voxel corresponds to 300 nm. Smoothing the 3D image with a Gaussian kernel of 1.27 voxels (FWHM 2 voxel) results in a noise reduced image with intensities I_1. A second image was calculated by filtering the original image with a larger Gaussian kernel of 1.8 voxels. The width of the second kernel was chosen in a way that for the FWHM of the first Gaussian the intensities are the same. The image calculated as the ratio between the two images, I_1/I_2, which was then binarized using a threshold value of 1.05 yields features in the image attributable to the canaliculi and to the borders of the osteocyte lacunae with a suitable signal to noise ratio. As lacunae are on a different length scale, few additional steps following the same line of considerations using different Gaussian kernel sizes were required to also properly threshold the lacunae.

As **lacunae and the haversian canals** are much bigger structures in the OLCN compared to the canaliculi, they have been **segmented** based on the distance of the voxels to the closest surface. The algorithm used in Kerschnitzki et al. [2013] was improved: voxels included in the thresholded data that were more than 4 voxels away from the surface and formed clusters bigger than 200 voxels served as seeds for possible lacunae. In an iterative process these seeds are then grown by adding layers of voxels (morphologically dilation). To avoid that the segmentation grows into the canaliculi the dilation was performed within the limits of the thresholded data which was eroded once, and further more, dilated voxel were only applied if the locally added volume counted more than 100 voxels.

The next step in the analysis is the conversion of the binarized images into a topological network structure, a process termed **skeletonization**. This has been done by using a customized MATLAB [2013] routine developed in our research group by Philip Kollmannsberger [Kerschnitzki et al., 2013]. This skeletonization algorithm iteratively removes surface voxels. If the removal of a surface voxel does not conserve the topology of the network, e.g. the voxel removal would result on a splitting of a canaliculus into two, the voxel remains in the image. Based on this image data, where the remaining voxels representing the mid axis of the canaliculi (also called skeleton) and the segmented lacunae, a graph (network) structure was created (Figure 4.6). Voxels of the skeleton with three or more voxel in their nearest neighborhood were defined as *nodes*, i.e. points in the network where canaliculi meet, while connections between these nodes are termed *edges*. As the result of this process all voxels of the skeletonized image were either assigned to be node, edge or lacuna. For further analysis, this data was converted to a graph structure in a format as provided by the NetworkX library [Hagberg et al., 2008] in the Python environment.

To allow a better quantification of the orientation of the canalicular network, the skeletonized network data, which still consists of discrete voxels, was fitted by third order smoothing splines [Dierckx, 1982] for each edge in the network. This fitting allows to calculate orientation (and curvature) for edge segments with a length that is comparable to the voxel size without having discrete angles (Figure 4.6). Position, **orientation and length** of these spline segments were calculated and saved for further analysis.

Quantities characterizing the network topology like the degree of nodes, i.e. the number of edges meeting at a node, and the clustering coefficient of a node, which describes the

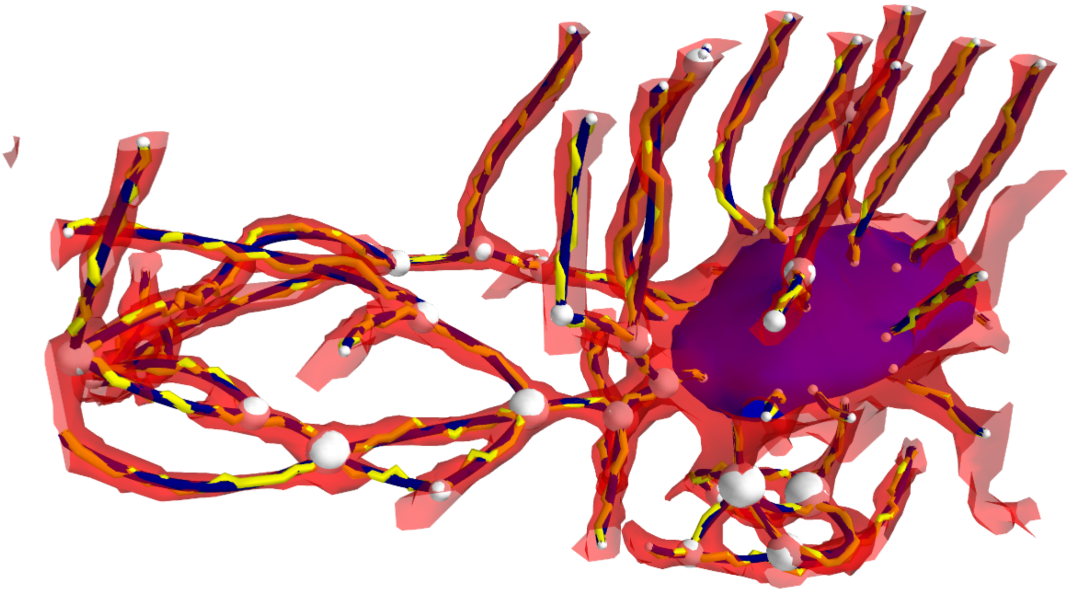

Figure 4.6: 3D visualization of the skeltonization of a $22 * 15 * 10\,\mu\text{m}^3$ subvolume of the canalicular network. The red surface corresponds to the thresholded data, the skeletonized canaliculi are drawn by connecting the center of the voxels with a yellow line. To provide a smooth and accurate representation of a canaliculus, this line was replaced by smoothing splines (blue). Nodes of the network are drawn as bright balls with the size being proportional to the degree of the node, i.e. the number of canaliculi meeting in this node. A segmented lacuna is visualized in purple.

local connectedness of the network [Bullmore and Sporns, 2009], were obtained using implemented functions of the NetworkX library [Hagberg et al., 2008]. However, a detailed topological analysis of these data is not part of the thesis.

4.2.3.2 Registration of Bright Lamella Using the SHG Images

To correlate the density of the canalicular network as well as its orientation to the lamellar tissue arrangement in the osteons, 2D surfaces have been registered in a semi-automatic way to the intensity maxima of the SHG images. The resulting surfaces represent the position of center of the bright lamellae. Only regions within the osteon in which lamellae appear as parallel and did neither split nor end (Figure 4.3) were chosen for the analysis.

While the lamellae in the end are represented in 3D, some processing steps are performed on the 2D images. The registration of the bright lamellae consists of several substeps:

1. Manual marking (initialization) of the lamellae of selected 2D images.
2. For a more objective description of the position of the lamellae, the maximum of the SHG signal is fitted as a function of the radius for several azimuthal angles and for all images in the image stack.
3. For each lamella all the fitted positions are combined to obtain a 3D representation using a bivariate smoothing spline in cylindrical coordinates.

The first substep has been performed using a customized developed tool based on the interactive visualization toolkit Chaco [2012]. Using 10 movable markers, each **lamella was initialized** (Figure 4.7(a)) on the top and bottom image of the image stack. To account for the circular structure of the lamella, the ten points were interpolated with a periodic cubic spline. The position of these initialized lamellae is linearly interpolated for all images in-between. The developed tool allows to adjust the position of markers in individual images in case of large deviations between marker position and SHG signal. Using the same marker tool the outer border of the osteon, i.e. its cement line, as well as the inner border, i.e. the surface of the Haversian canal, were defined.

Next, each SHG image was transformed into polar coordinates, where the lamellae were fitted as a function of the radius. For the transformation first the common center of curvature of the lamellae was calculated using the initialized lamellae. The center of each lamella was determined as the point that minimizes the standard deviation of the distance to the section of the initialized lamella*. The common center of curvature is than calculated as mean of the centers of the individual lamellae for each 2D image.

The transformation of the SHG images into polar coordinates was performed by binning the digital image information. A pixel i of the image $\mathbf{I}$ with Cartesian coordinates x_i, y_i is represented in polar coordinates $r_i = \sqrt{{x_i}^2 + {y_i}^2}$ and $\phi_i = \tan^{-1}(y_i/x_i)$. In polar coordinates the image was binned using a grid of $M+1$ equidistant edges $\hat{r}_0, \ldots, \hat{r}_M$ with

---

*As most osteons were too big to be imaged completely with the used objective, often only arches of the lamellae were imaged and, therefore, it was not possible to calculate the center straightforward as center of mass.

$M = 200$ for the radial coordinate and $N + 1$ azimuthal edges $\hat{\phi}_{,} \ldots, \hat{\phi}_N$ with $N = 60$ bins. $\hat{r}_0$ and $\hat{r}_M$ are chosen according to the minimal radius of the innermost lamella and the maximum of the outermost lamella, respectively. The angular section $[\hat{\phi}_0, \hat{\phi}_{N+1}]$ was chosen such that the corresponding sector of the osteon is fully included in the image. The area enclosed by edges $\hat{r}_m, \hat{r}_{m+1}$ and $\hat{\phi}_n, \hat{\phi}_{n+1}$ will be referred to as (m, n)th bin[*]. The intensity of the transformed image $I_{m,n}$ can be calculated as the average intensity of all pixels belonging to the (m, n)th bin.

For all transformed images in the image stack I_o, for all lamellae j and for all azimuthal angles ϕ_n a Gaussian peak was then fitted to obtain the radial distance r^j_{no}. As lacunae appear dark in the SHG image and therefore would affect the position of the fitting of the lamellae, lacunae and their immediate neighborhood were excluded from this fitting (Figure 4.7(b,c)).

Aligning the common center of curvature of the lamellae of each 2D image along the z-axis introduces a cylindrical coordinate system that we will later use. To **represent the lamellae in 3D**, in a final step a bivariate smoothing spline was fitted for each lamella j in this cylindrical coordinate system. For the definition of the spline each (successfully) fitted radial distance r^j_{no} of the last substep was weighted by $1/\sqrt{\Delta r}$ where Δr is the uncertainty of the peak position as found by the fit. The smoothing parameter for the bivariate spline was chosen so that the splines could still follow the ellipticity of the lamellae. The resulting positions of the registered lamellae were checked by visualizations of the sample (Figure 4.7).

4.2.3.3 Quantification of the Network Density and its Inhomogeneity

There are different possibilities to quantify the density of the canalicular network. A method that was used by Kerschnitzki et al. [2013] is to start from each voxel of the image which is filled with bone and determine the distance to the nearest canaliculus. The natural quantification of this method is then a frequency distribution, which describes how many "bone voxels" in the image are found with a given shortest distance to a canaliculi in the network. This distribution contains information about the **density of the network** as well as its homogeneity. In this work a more direct measure of the canalicular density is used. As the imaged network is reduced to a mathematical network, where each canaliculus is represented by a mathematical line (Figure 4.6), the canalicular density $\rho = L/V$ is calculated as the total length L of the canaliculi within a certain volume V and is therefore measured in $\mu\text{m}/\mu\text{m}^3$. In the evaluation only the bone volume V_{osteon} within the osteon was included, i.e. regions outside the cement line and the Haversian canal were excluded. In addition, lacunae were also excluded from the analysis of the network density reducing the evaluated network volume by $V_{lacunae}$. The network density of an osteon is, therefore, calculated by dividing the length L_{osteon} of the canaliculi within the osteon by the bone volume

$$\rho_{osteon} = L_{osteon}/(V_{osteon} - V_{lacunae}).$$

---

[*] Coordinates of an edge $\hat{X}$ will in the following always have a hat, to distinguish it from the coordinates of the bin $X_m = 1/2\left(\hat{X}_m + \hat{X}_{m+1}\right)$.

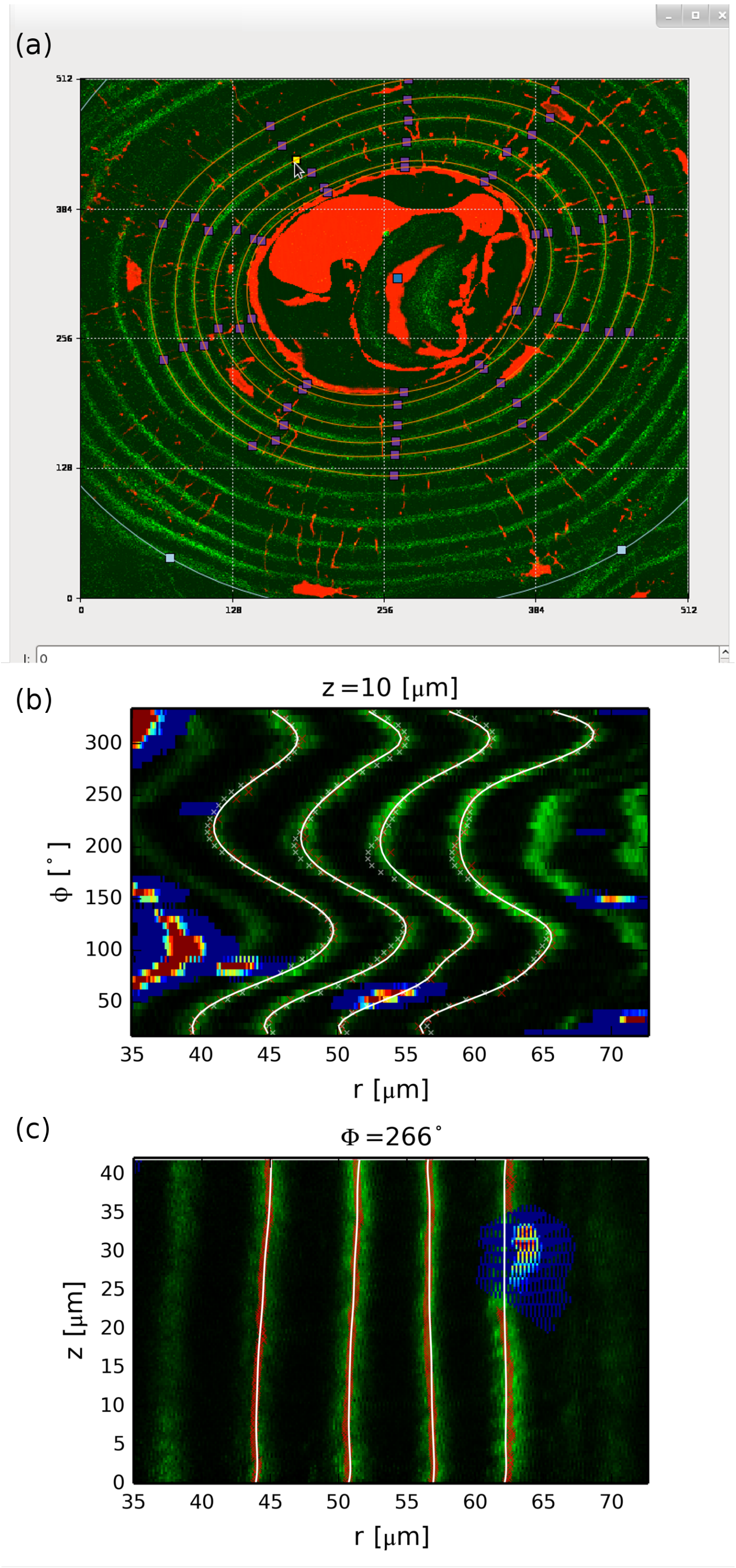

Figure 4.7: Determination of the positions of lamellae. (a) Screen shot of the graphical user interface designed to manually initialize lamellae of interest. The orange lines show the interpolation of the purple markers used for initialization. (b) A single SHG image transformed to polar coordinates. The white crosses show the position of the initialized lamella, red crosses the fitted centers of Gaussian peaks. The white lines show the values of the bivariate smoothing splines. Transformed lacunae (red) and their neighborhood (blue) are excluded. This way lamellae are not fitted around lacunae that are located in bright lamellae (in the middle of the image close to the bottom). (c) A (r, z)-section of the image transformed into polar coordinates with colors as in (b).

Using a very simple model for the arrangement of canaliculi a relation between a characteristic distance of the bone material to the network and the network density ρ can be obtained. In case of straight and parallel canaliculi the calculations can be reduced to a 2D problem. The smallest average distance for a given density is obtained when placing the canaliculi on a triangular lattice, where each canaliculus has a hexagonal unit cell. These hexagons can be approximated by a circle with 80% of the bone material being located within 64% of its radius. We define the characteristic distance

$$d_c = \frac{0.64}{\pi\sqrt{\rho}}. \tag{4.1}$$

In case of an inhomogeneous network the distance distribution becomes wider, which results in larger characteristic distances. The canalicular density in different osteons ρ_{osteon} can be compared to the size of the osteon, i.e. the radius of the cement line, as well as the volume fraction of the lacunae within the osteon $\rho^V_{lacunae} = V_{lacunae}/V_{osteon}$*.

The **inhomogeneity of the network** can be characterized by dividing each 3D network dataset into several subvolumes and analyzing the width of the distribution of the density within those subvolumes (see Figure 4.16 for examples of such frequency distributions). Binning was done with bins of volume $V_s = 400\,\mu m^3$. This value for the subvolume was chosen since it is small enough to analyze the heterogeneity in the osteon and large enough to include several canaliculi in most of the subvolumes. The chosen subvolume is also comparable to the volume of the osteocytes. To account for the geometry of the osteon the bins were defined in cylindrical coordinates, similar to binning in polar coordinates (Section 4.2.3.2).

The azimuthal angle ϕ and the depth coordinate z were subdivided equidistantly with $\Delta\hat{\phi} = \pi/72$ and $\Delta\hat{z} = 8\,\mu m$, respectively. The radial coordinate had to be subdivided in a non-equidistant manner to fulfill the constraint of equal volume of all bins (Figure 4.8). This constant volume is demanded as binning corresponds to a low pass filtering of the data.

As the volume of a bin at distance r_m is

$$V_s = \frac{\Delta\hat{z}\Delta\hat{\phi}}{2}\left(\hat{r}_{m+1}{}^2 - \hat{r}_m{}^2\right),$$

$\hat{r}_{m+1}$ is obtained as

$$\hat{r}_{m+1} = \sqrt{2\frac{V_s}{\Delta\hat{z}\Delta\hat{\phi}} + \hat{r}_m{}^2}.$$

At a radius of 80 μm which is approximately the mean radius of all subvolumes, this gives approximately cubic subvolumes.

---

* Usually the presence of osteocytes in an osteon is quantified by its number density, i.e. the mean number of osteocytes per volume with the osteon. Since the volume of the image data has a rather limited thickness due to the opaqueness of bone, many lacunae lie at the border of the image volume and are, therefore, only partly imaged. The volume fraction is less sensitive to such boundary effects. An estimation of the osteocyte number density $\rho^N_{lacunae} = \rho^V_{lacunae}/\bar{V}_l$ can be calculated using the average volume $\bar{V}_l$ of the lacunae that lay completely within the imaged volume.

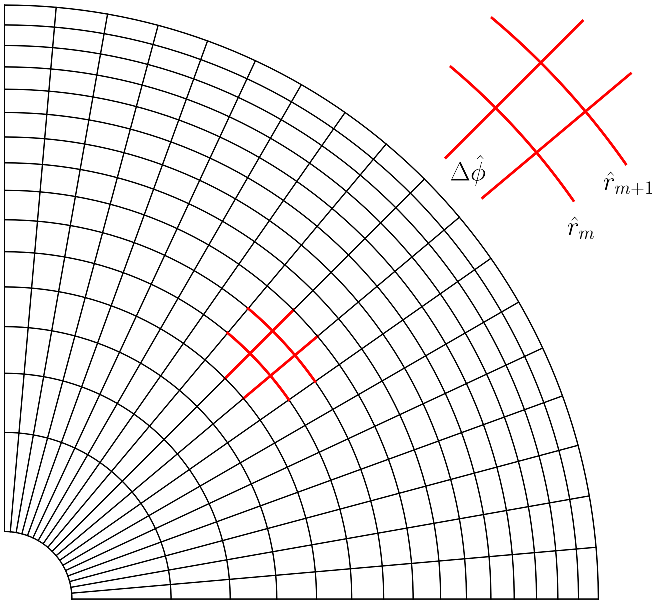

Figure 4.8: 2D cross section of subvolumes within a quarter of an osteon with the Haversian canal at the bottom left. The subvolumes were chosen to have the same size with equidistant subdivision in ϕ- and z-direction (z-axis not visualized) resulting in nonequal spacing in r-direction. The aspect ratio of this sketch are to scale for an osteon with a diameter of 260 μm and a 30 μm Haversian canal. The approximately square shaped red bin with an equivalent radius of 80 μm is highlighted and magnified to explain the nomenclature. At this average radius, the shape of the subvolume is approximately cubic.

In analogy to the calculation of the network density in an osteon, the network density within the subvolume mno, ρ_{mno}, is given by the length of the canaliculi within the subvolume $\mathbf{L}^{mno}$ divided by the volume of the bin $\mathbf{V}^{mno}$.

Having calculated the density of the subvolumes in a cylindrical coordinate system, it is straightforward to evaluate the **network density as a function of the radial distance** (Figure 4.9). To allow a better comparability between osteons of different sizes, a normalized radius r_n is introduced with $r_n = 0$ at the mean radius of the Haversian canal, and $r_n = 1$ at the mean radius of the cement line, which marks the outer border of the osteon. To investigate if there is a functional dependency between r_n and the normalized network density, ρ/ρ_{osteon}, a linear regression was performed for each osteon resulting in a value of the fitted slope m and the offset c,

$$\frac{\rho(r_n)}{\rho_{osteon}} = mr_n + c. \tag{4.2}$$

Additionally the network density can be plotted as a function of the azimuthal angle ϕ and the depth coordinate within the visualized volume z (Figure 4.17).

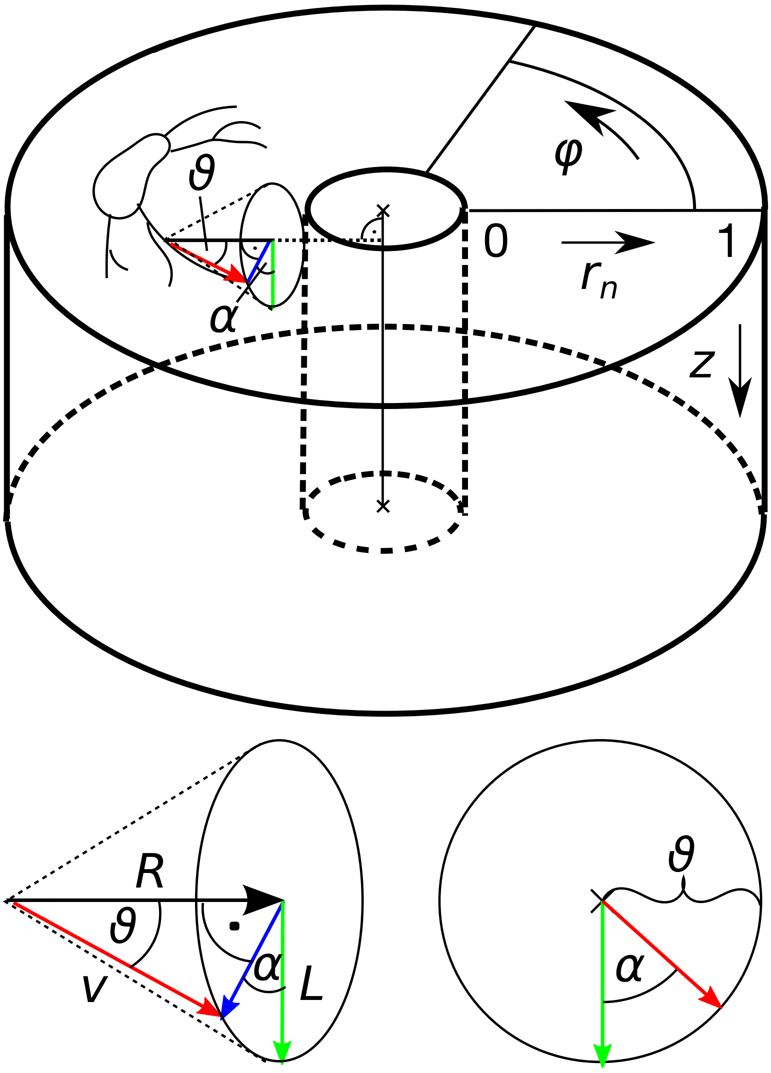

Figure 4.9: Definition of the polar coordinates and orientations in the osteon. The location of canaliculi and lacunae are described by r, ϕ, z. r_n is the normalized radius with $r_n = 0$ at the surface of the Haversian canal and $r_n = 1$ at the cement line. The orientation (Section 4.2.3.4) of lacunae and canaliculi (i.e. the red arrow $\mathbf{v}$) is described by two angles θ and α where θ is the angle between $\mathbf{v}$ and $\mathbf{R}$, i.e. the direction pointing to the center (black). α is the angle between the component $\mathbf{v}_{perp}$ that is normal to $\mathbf{R}$ (blue), and the direction of the blood vessel $\mathbf{L}$ (green). The lower left sketch shows a magnification of the definition of the orientations, the lower right sketch shows the very same cone as seen looking along the $\mathbf{R}$-direction, projecting the red vector on top of the blue vector.

For a more quantitative understanding of the spatial variations in the different directions, the autocorrelation function of the density ρ, $\gamma^d(\Delta d_m)$ was calculated as a function of the distance of m bins in one of three cylindrical directions $d \in \{r, \phi, z\}$. This relationship is calculated as average of the autocorrelation function $\gamma_j^d(\Delta d_m)$ which uses sets of subvolumes j, which are neighbors in direction d in a sense that the other two coordinates are kept constant:

$$\gamma_j^d(\Delta d_m) = \frac{\sum_i \tilde{\rho}_j(d_i)\tilde{\rho}_j(d_{i+m})}{\sum_i \tilde{\rho}_i^2}$$

with $\tilde{\rho}_i = \rho_i - \text{mean}(\rho)$ is the difference of the density of the subvolumes from the mean of all evaluated subvolumes in one osteon.

To average these autocorrelation functions γ_j^d of all sets of neighboring subvolumes, they are scaled in a way that distance is not measured in bins anymore but in μm.

4.2.3.4 Quantification of the Orientation of the Network

Looking at the images of the canalicular network (i.e. Figure 4.1) a predominant orientation roughly towards the center of the osteon can be observed.

The alignment of the canaliculi is evaluated along two slightly different radial directions, which are motivated by the following two hypotheses:

1. Ignoring the formation process one might assume the canaliculi head straight for the blood vessel. Consequently, the orientation of the canaliculi with respect to the vector $\mathbf{R}_1$ pointing along the closest connection to the central axis of the Haversian canal $\mathbf{L}_1$ is calculated.

2. Considering that the network is formed at the same time as the bone is formed, each lamella has been the surface of the new formed bone at a specific time. To account for this geometry, orientations of canaliculi with respect to the normal of the lamellae $\mathbf{R}_2$ are calculated.

To calculate the orientation of the canaliculi, first an orthonormal coordinate system has to be defined locally. In the first scenario $\mathbf{L}_1$ is considered as given and can be calculated using the center of the Haversian canal $\mathbf{cm}_1^H$ in the upper most image slice and the lowest image slice $\mathbf{cm}_2^H$.

$$\mathbf{L}_1 = \frac{\mathbf{cm}_2^H - \mathbf{cm}_1^H}{|\mathbf{cm}_2^H - \mathbf{cm}_1^H|}$$

The locally defined radial direction, $\mathbf{R}_1(\mathbf{r})$, is then calculated as the distance vector $\tilde{\mathbf{r}} = \mathbf{r} - \mathbf{cm}_1^H$ between the position $\mathbf{r}$ and a point on the mid-axis of the Haversian canal, i.e. $\mathbf{cm}_1^H$, projected perpendicular to $\mathbf{L}_1$

$$\mathbf{R}_1(\mathbf{r}) = \frac{\tilde{\mathbf{r}} - (\tilde{\mathbf{r}} \cdot \mathbf{L}_1)\mathbf{L}_1}{|\tilde{\mathbf{r}} - (\tilde{\mathbf{r}} \cdot \mathbf{L}_1)\mathbf{L}_1|}.$$

In the case of the second scenario the inward pointing lamella normal is used as locally defined radial direction, $\mathbf{R}_2(\mathbf{r})$. Then the orthogonal direction $\mathbf{L}_2$ is calculated as projection of $\mathbf{L}_1$ into the plane of the lamella

$$\mathbf{L}_2 = \frac{\mathbf{L}_1 - (\mathbf{L}_1 \cdot \mathbf{R}_2)\mathbf{R}_2}{|\mathbf{L}_1 - (\mathbf{L}_1 \cdot \mathbf{R}_2)\mathbf{R}_2|}.$$

Lamella normals are only defined at the position of the lamella therefore $\mathbf{R}_2(\mathbf{r})$ and $\mathbf{L}_2(\mathbf{r})$ are linearly interpolated.

In each of these two coordinate systems, the orientation of a short segment of a canaliculus $\mathbf{v}$ is defined by two angles θ and α (Figure 4.9). As the main orientation of the canaliculi towards the blood vessel seems obvious, a first angle $\theta = \angle(\mathbf{v}, \mathbf{R})$ is defined as angle between $\mathbf{v}$ (red arrow in Figure 4.9) and the vector $\mathbf{R}$ pointing towards the center of the osteon (black arrow). A second angle $\alpha = \angle(\mathbf{v}_{perp}, \mathbf{L})$ describes the orientation of the component $\mathbf{v}_{perp} = \mathbf{v} - (\mathbf{v} \cdot \mathbf{R})\mathbf{R}$ (blue arrow) that is perpendicular to $\mathbf{R}$ and the vector denoting the long axis of the osteon $\mathbf{L}$ (green arrow).

In this work, canaliculi with $\theta < 30°$ will be referred to as radial, while canaliculi with $\theta > 60°$ will be referred to as lateral. $\alpha = 0, 180°$ if $\mathbf{v}_{perp}$ is parallel to the blood vessel and $\alpha = \pm 90°$ in case $\mathbf{v}_{perp}$ points around the blood vessel.

To quantify the orientation in the two different scenarios, for each dataset density distributions of the orientation are calculated and visualized using a stereographic projection. This is done by binning the orientation of the network using equidistant edges $\hat{\theta}$ and $\hat{\phi}$ and calculating for all bins m, n the orientation density

$$\frac{\Delta L_{mn} / \Delta \Omega_{mn}}{\sum_{m,n} L_{mn}}$$

where ΔL^{mn} is the integrated length of all canaliculi with that specific orientation, normalized by the size of the solid angle of that bin

$$\Delta \Omega^{mn} = \int_{\hat{\theta}_m}^{\hat{\theta}_m + 1} \sin\theta \mathrm{d}\theta \int_{\hat{\alpha}_n}^{\hat{\alpha}_{n+1}} \mathrm{d}\alpha.$$

Similar to pole figures used in crystallography, this orientation density is than visualized (Figure 4.23) in a polar plot, where the distance to the center corresponds to θ and α is plotted as azimuthal angle. This corresponds to looking locally in the radial direction $\mathbf{R}$ towards the center of the osteon, determining where a canaliculus would hit a semi-sphere around this direction and then projecting the semi-sphere to obtain the 2-dimensional polar plot (lower right sketch in Figure 4.9).

4.2.3.5 Correlation of the Network with Lamellar Structures

To evaluate the network architecture and the position and alignment of lacunae in relation to the lamellae, a **new coordinate** q is introduced to replace the radial distance r in order to describe the local lamellar position. q is chosen such that it has integer values at the center of the bright lamellae, i.e. the surfaces fitted to the maxima of the SHG signal (Section 4.2.3.2). When the such defined coordinates are transformed into Cartesian coordinates, osteons appear as perfect cylinders with equidistant lamellae (Figure 4.10(b)).

Having integer values at the position of the bright lamella allows to average all lamellae by reducing the coordinates to $q' = q - \text{floor}(q) \in [0, 1)$. Therefore, $q' = 0$ corresponds to the center of the bright lamella, $q' = 0.5$ denotes the center of the dark lamella (Figure 4.10(c)). For a refined evaluation, this interval [0,1) of q' values is divided in 10 sublamellae to study the architecture of the network as a function of the position within the lamella. When comparing the architecture of the network located in dark lamelellae th the network within the bright lamellae, the 5 sublamellae with $q' \in [0, 0.2) \bigcup [0.7, 1)$ are combined to define the bright lamella and the other 5 sublamellae with with $q' \in [0.2, 0.7)$ define the dark lamella.

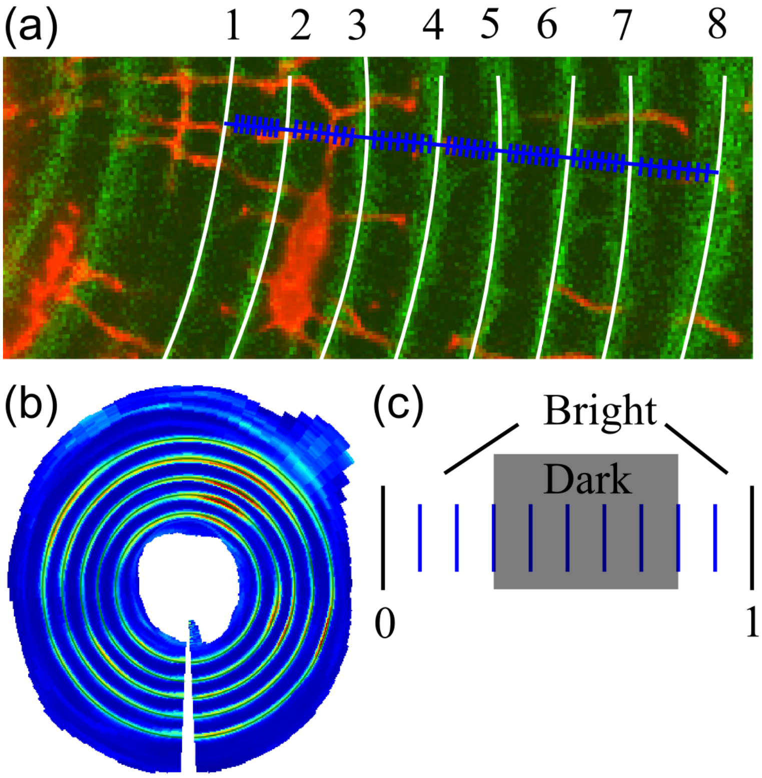

Figure 4.10: Using the maxima of the SHG signal allows to map lamellae onto a common coordinate system and to investigate network properties as a function of the position within the lamella. (a) A coordinate system is used where the position of the fitted maxima (Section 4.2.3.2) have integer values. (b) In Cartesian coordinates this corresponds to bringing the osteon into a cylindrical shape with equidistant lamellae. (c) To average data from several lamellae, each lamella is divided into 10 sublamellae and mapped onto a single lamella with a position coordinate q' taking values between 0 and 1. 5 sublamellae are grouped to define bright and dark lamellae, respectively.

4.2.3.6 Quantification of Shape and Orientation of Osteocyte Lacunae

As several studies reported correlation between osteocytes and lamellae, not only canaliculi density and orientations are correlated to the position within the lamella, but the same is performed with lacunar densities, $\rho_{lacunae}$, the degree of the cells as well as certain shape descriptors of the lacunae. To avoid artifacts from boundary effects, only lacunae which were completely within the imaged volume were considered in the evaluation. For several shape descriptors [Mader et al., 2013] as well as orientation of the lacunae with respect to the lamella, the gyration/covariance matrix $\mathbf{S}_{mn}$ is calculated for each lacuna, which is defined as

$$\mathbf{S}_{mn} = \frac{1}{N}\sum_{i=1}^{N} r_m^i r_n^i, \tag{4.3}$$

with r_m^i being the mth component of the position of voxel i of the lacunae, which includes N voxels. The origin of the reference coordinate system is defined such that

$$\sum_{i=1}^{N} \mathbf{r}_i = 0.$$

Diagonalization of $\mathbf{S}$ provides the eigenvalues ${\lambda_1}^2, {\lambda_2}^2, {\lambda_3}^2$ (where by definition $\lambda_3 > \lambda_2 > \lambda_1$) as well as the eigenvectors $\mathbf{e_1}, \mathbf{e_2}, \mathbf{e_3}$, of the lacunae (Figure 4.11). Approximating the lacuna by an ellipsoid, the total extend of the lacuna along the main axis i is $2\sqrt{5}$ times λ_i [McCreadie et al., 2004].

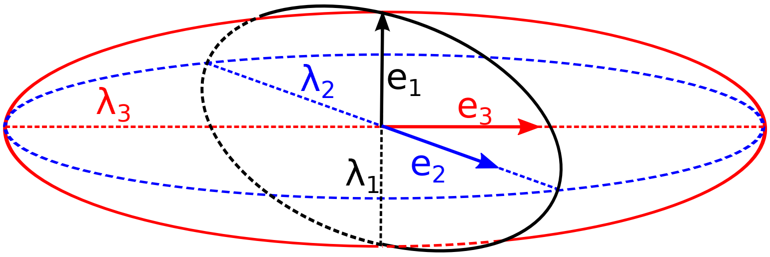

Figure 4.11: Covariance ellipsoid of a lacuna calculated using Equation 4.3. The principal axes of this ellipsoid are $\sqrt{5}$ times shorter than of the ellipsoid approximating the lacuna.

Besides lacuna volume and its degree (i.e., number of canaliculi that originate from the lacuna), for each lacuna the following quantities are calculated and compared for lacunae residing within either dark or bright lamellae:

Stretch:	$(\lambda_3 - \lambda_1)/\lambda_3$
Oblateness:	$2(\lambda_2 - \lambda_1)/(\lambda_3 - \lambda_1) - 1$
Angle between $\mathbf{e_1}$ and $\mathbf{R}$ (corresponds to θ):	$\cos^{-1}(\lvert\mathbf{e_1} \cdot \mathbf{R}\rvert)$
Angle between $\mathbf{e_3}$ and $\mathbf{L}$ (corresponds to α):	$\cos^{-1}(\lvert\mathbf{e_3} \cdot \mathbf{L}\rvert)$

4.3 Results

In this section results are presented in a conclusive manner: only example datasets as well as averaged data is presented. Appendix A includes tables that summarize quantities from all evaluated osteons. For all osteons several figures were generated and checked for obvious errors. One type of image that allows for a fair impression of the thresholded data, including segmentation of lacunae and the borders of the osteon, was obtained by generating projection images along the z-axis as shown in Figure 4.12 for two osteons, and which are included for all osteons in Appendix A.

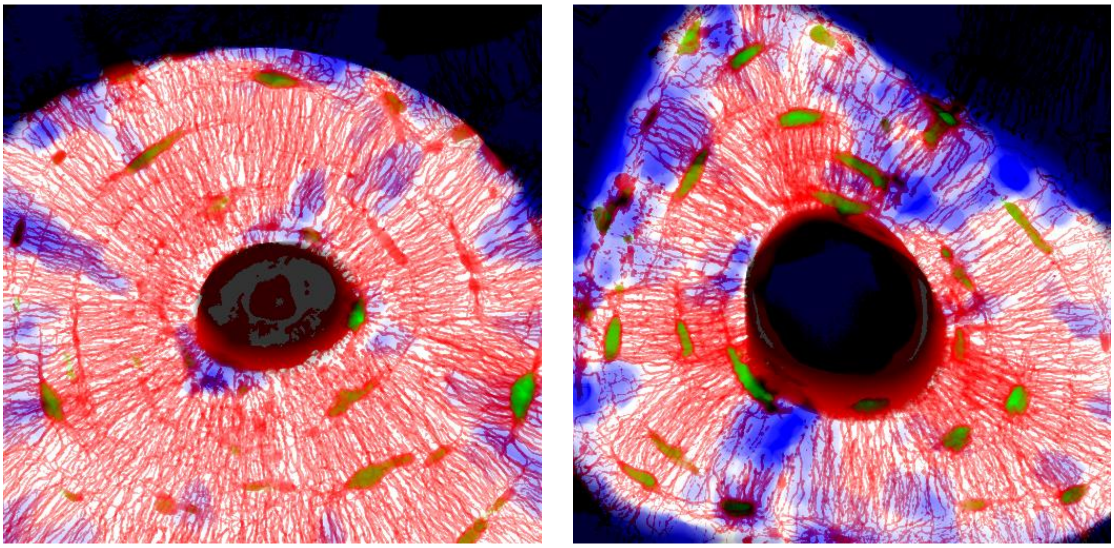

(a) Homogeneous osteon (o5) (b) Inhomogeneous osteon (o9)

Figure 4.12: Projections along the z-axis of typical datasets after thresholding (for the location of the two osteons see Figure 4.4). The thresholded image of the network stained by rhodamine is visualized in red, detected lacunae in green, regions outside of the osteon are darkened and regions that appear to have no network on a length scale bigger than 5 μm are highlighted in blue. The right subfigure shows an osteon that appears less homogeneous with more empty regions. Generally these empty regions often extend radially as spokes through the osteon, or form holes close to the outer border of the osteon.

4.3.1 Density of the Network and its Inhomogeneity

Averaging over all osteons, the mean density was found to be $\bar{\rho} = 0.0709 \pm 0.002\,\frac{\mu\text{m}}{\mu\text{m}^3}$ (standard deviation $\sigma(\rho) = 0.013\,\frac{\mu\text{m}}{\mu\text{m}^3}$)*. The network density within an osteon ρ does not show any significant correlation to the size of the osteon (Figure 4.13, Table 4.2), i.e. smaller osteons do not have a denser network. Neither does a significant correlation between the lacunar density and network density exist (Figure 4.14, Table 4.2), which means that osteons with higher lacunar density do not necessarily also have a higher network density.

Sample	cc_{size}	p-value	$cc_{lacunae}$	p-value
FM03	-0.06	0.87	0.49	0.17
FM40	0.48	0.13	-0.39	0.23
FM48	0.28	0.38	-0.39	0.20
FM38	-0.09	0.79	0.14	0.65

Table 4.2: Table of correlation coefficients of the network density with the size of the osteon cc_{size} and with the lacunar density $cc_{lacunae}$. Also shown are the corresponding p-values for all four samples.

To test if the mean densities of the osteons within the 4 samples differ, an ANOVA analysis (F-test) was performed. The separation of the densities of the osteons belonging to the different samples (Figure 4.13, Figure 4.14) was found to be significant with $p < 0.001$.

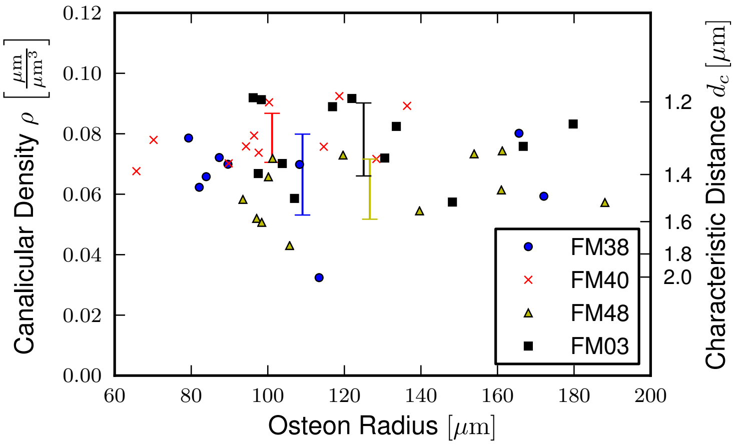

Figure 4.13: Canalicular density as a function of the radius of the osteon of all 4 samples. The error bars represent mean value and standard deviation of all osteons within one sample. The y-axis on the right side is calculated according to Equation 4.1.

The distribution of canaliculi within the datasets was studied by plotting the distribution of distances of bone material to the nearest canaliculus (Figure 4.15). While for most voxels the nearest canaliculi is within 3 μm, about 6 % of the bone volume have no network within 5 μm away from the network. The higher network density of samples Fm38 and Fm40 is reflected by a higher peak of the distance distribution at short distances. If the regions without network individually extend for more than 130 μm^3 they

---

*If not stated otherwise values after the ± denote standard error, values of the standard deviations are sometimes additionally provided to quantify the width of the distribution.

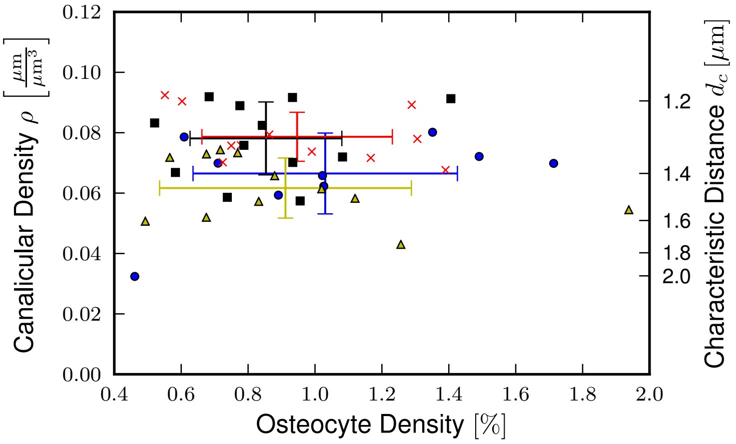

Figure 4.14: Canalicular density as a function of the lacunar density with colors/symbols as in Figure 4.13. Error bars represent mean and standard deviations of both quantities within each sample.

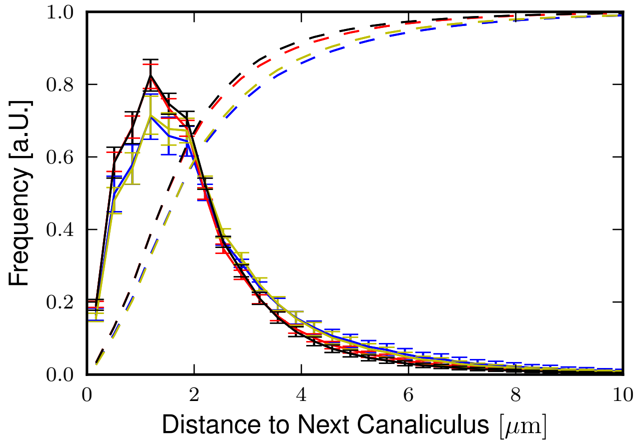

Figure 4.15: Distance transformation of bone material to the nearest canaliculus in osteons of all 4 investigated samples with colors as in Figure 4.13. Dashed lines show the corresponding cumulative distributions.

are highlighted blue in Figure 4.12. Several quantities were calculated excluding these regions without a network, the results are presented in Appendix B.

An alternative way to describe the spatial heterogeneity of the canalicular density is the distribution of densities within small subvolumes (Figure 4.16) of the 4 samples. The histograms, mean value and standard deviations are calculated using only subvolumes for which the calculated volume was $> 390\,\mu\mathrm{m}^3$ (i.e. excluding subvolumes that contained cells or were partly outside of the osteon boundaries), therefore the mean value differs slightly from the mean values in Figure 4.13 and 4.14. The widths of the obtained distributions are remarkably wide with a value of the standard deviation of 64–77 % of the mean value. 5–11% of subvolumes do not include any network.

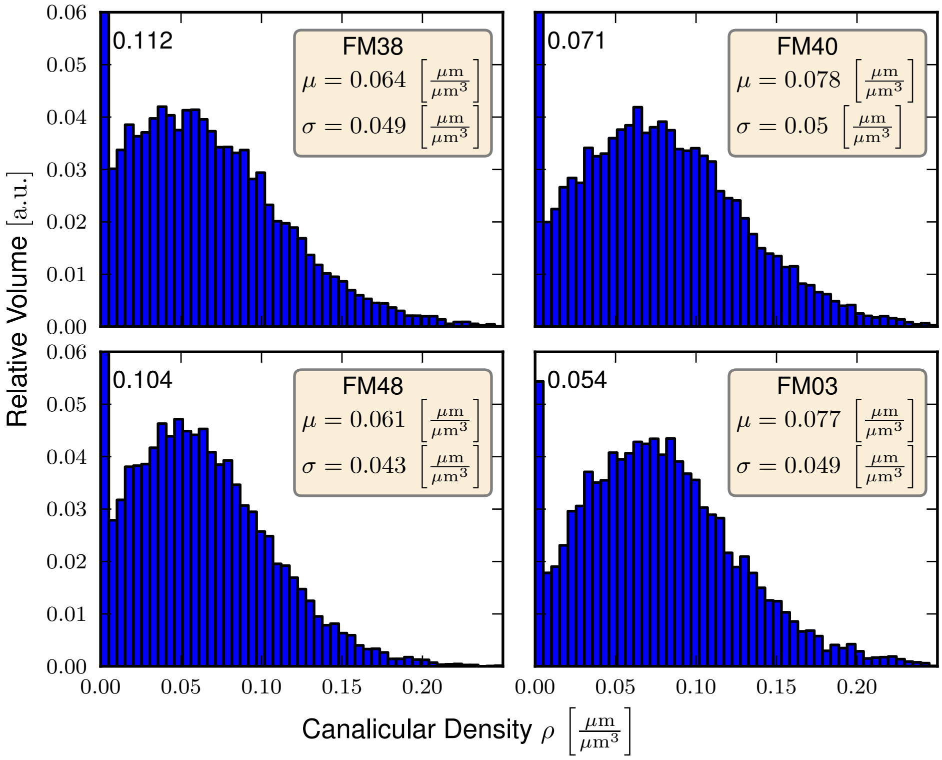

Figure 4.16: Frequency distribution of the canalicular density within subvolumes of $400\ \mu\mathrm{m}^3$ of all osteons within a sample. The number in the upper left corner refers to the height of the first bin.

The very same subvolumes were also used to analyze the spatial dependency of the network densities within cylindrical coordinates. Figure 4.17 compares the evaluations for the two datasets (i.e., the osteons o5 and o9) introduced in Figure 4.12. Both datasets show a decreasing canalicular density when increasing the radial distance from the inner to the outer boundary of the osteon, a trend that is more pronounced in the more homogeneous osteon. While the fluctuations of the densities in this plot should not be compared without caution*, the less homogeneous dataset (o9) shows higher fluctuations

---

*The volumes averaged to obtain each data point can be quite different. This influences the standard error of each point and therefore also the smoothness of the curves.

compared to the other osteon in the plot of the density as a function of the angle ϕ.

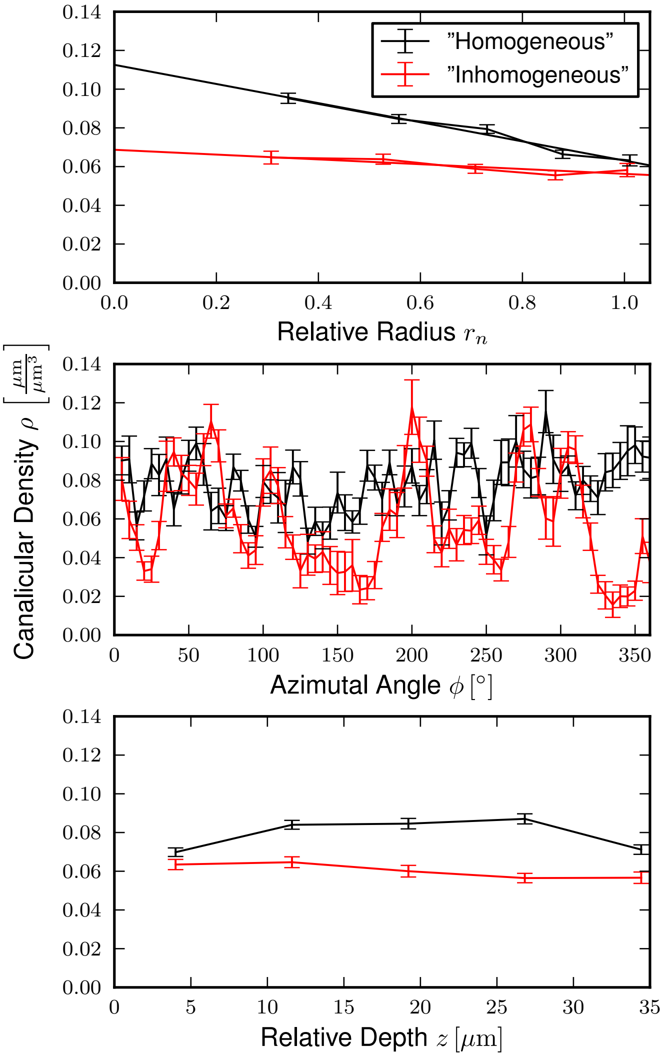

Figure 4.17: Spatial dependencies of the canalicular densities for the two osteons of figure 4.12. Black data corresponds to the more homogeneous osteon o5. Error bars in this image correspond to the standard error. In the subplot on top the straight lines are the results of a linear regression.

A plot of the slopes of the canalicular density as a function of the normalized radius (Equation 4.2) is shown in Figure 4.18. The mean slope for all osteons is $m = -0.46 \pm 0.5$ (standard deviation) which corresponds to a drop from 1.23 to 0.77 of the average density when moving from the inner to the outer border of the osteon. While the spread of the fitted slopes is bigger than the mean value, a t-test shows that the mean slope is smaller than 0 with a p-value of $p = 4 \cdot 10^{-5}$.

To determine spatial correlations in the canalicular density between neighboring subvolumes the autocorrelation function was calculated for each of the three directions in the cylindrical coordinate system. The autocorrelation function takes values close to zero for distances around 30 μm (Figure 4.19). Surprisingly the autocorrelation of the network density in the three directions is not equal. While in the azimuthal ϕ-direction the autocorrelation function has a value of 0.2 at 18 μm, in the z-direction the same value is already reached at approximately 12 μm.

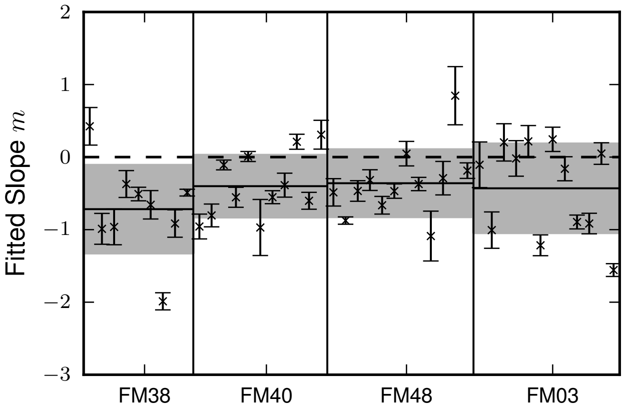

Figure 4.18: Fitted relative slopes of the network density as a function of the radius and the uncertainty as obtained from the linear regression. The black line indicates the mean value of all slopes for one sample, the gray band denotes the corresponding standard deviation. A relative slope of -1 implies a decrease from 1.5 to 0.5 of the values of the mean network density when moving from the inner to the outer border of the osteon.

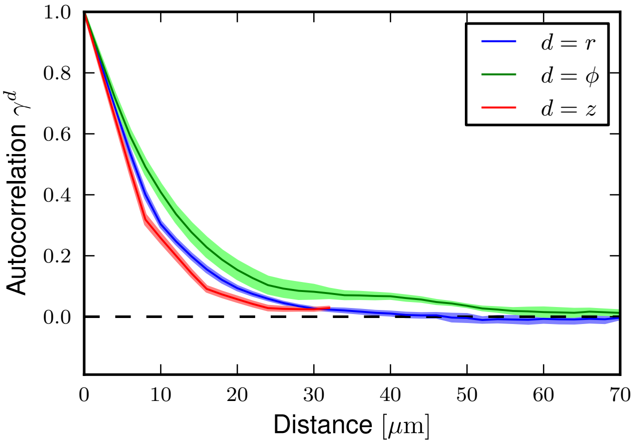

Figure 4.19: Autocorrelation function of the network density within subvolumes along three directions in a cylindrical coordinate system. The dark lines represent the mean value of the 4 samples, standard deviations within the samples are highlighted by lighter colors. In all samples, the autocorrelation function drops to 0.2 within 12–18 μm and appear to be larger in ϕ-direction.

4.3.2 Regions without Network

As seen in Figure 4.16, a considerable fraction of subvolumes had no network at all. These regions that appear empty were visualized in blue within the projection image (Figures 4.12, 4.20). Comparing projection images of all datasets (Appendix A) these empty regions can be classified depending on their appearance.

Many of the osteons show empty regions that appear wedge shaped extending from the cement line inwards but not always starting at the cement line (Figure 4.12(b)). Surprisingly, many osteons have an appearance like the one presented in Figure 4.20: a concentric empty region around the blood vessel. At the concentric ring canaliculi that originate from lacunae further outside are abruptly interrupted. The mineralized matrix and the network inside the concentric ring gives the appearance of a separated entity looking like a "mini osteon". Out of 43 analyzed osteons, in at least 22 osteons the majority of the connection of outer canaliculi to the blood vessel appear interrupted, in 11 of those, inside of this interruption a mini-osteon like structure is found. In case of two separated structures – a smaller osteon with an osteon – often osteocyte lacunae can be found that connect the inner and outer part of the network. This is similar to the connection of the network outside the osteons in the interstitial bone to the networks of osteons across the cement line.

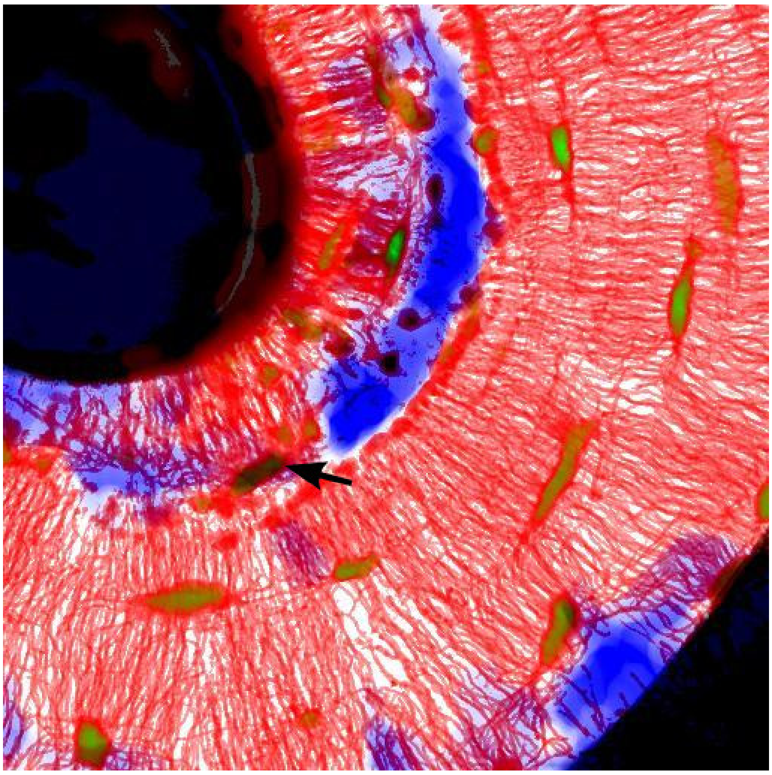

Figure 4.20: Projection image of an osteon showing a concentric region without network around the Haversian canal (colors as in Figure 4.12). The appearance of the network adjacent to this empty ring resembles that of the network at a cement line. The network outside this empty ring is connected to the inside via the lacuna at the bottom of the inner structure (arrow). Most part of the outer network is normally stained and seems, therefore, to be intact, despite the fact that its radial canaliculi end without a direct connection to the blood vessel.

Looking at such datasets, the question arises if the regions without network have already been present after the original formation of the osteon (Section 2.1.1). After the osteon with the network was formed, it can be assumed that no additional canaliculi are added to the network. On the contrary, canaliculi get lost since part of the network mineralize (e.g., by a process called micropetrosis, Section 2.2.1). Assuming that the original network is denser and more homogeneous and “deteriorates” with time, the variance of the network density σ^2 as a function of the mean canalicular density was plotted (Figure 4.21). The relation between variance and mean value is in agreement with a linear relationship that would be obtained for Poisson distributed data. An interesting trend is observed when plotting the mean network density versus the fitted linear decrease in density with the radial distance (Figure 4.22). This decrease is more pronounced for osteons with a high network density. Under the assumption that the network density can only decrease over time, the conclusion is reached that initially osteons exhibit a stronger radial decrease of network density, which throughout time is reduced.

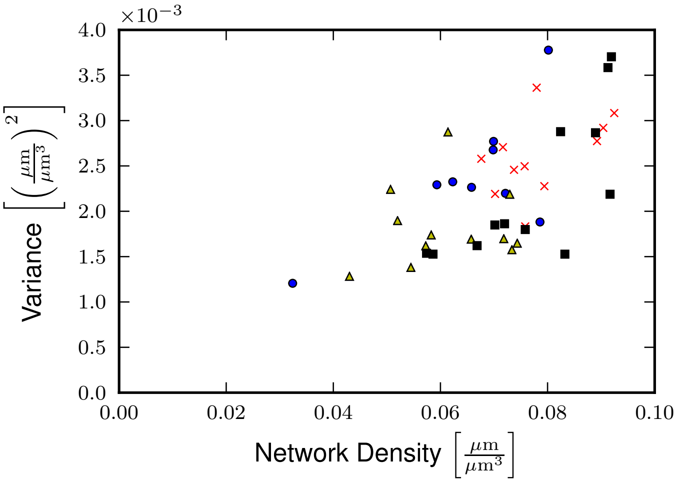

Figure 4.21: The inhomogeneity of the network density as quantified by its variance as a function of the network density plotted for all evaluated osteons.

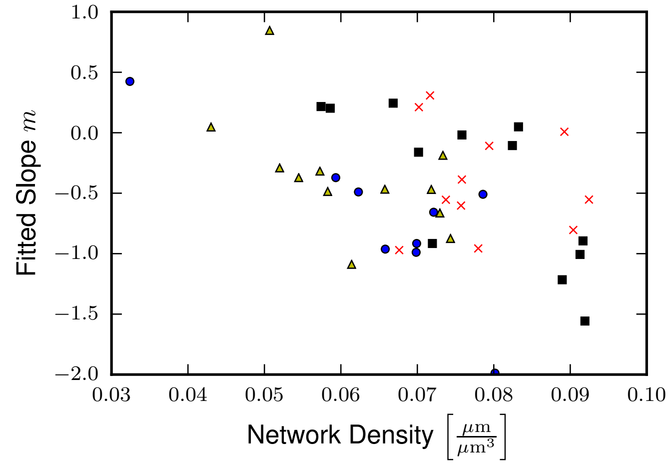

Figure 4.22: The normalized decay of the network density as a function of the radial distance is more pronounced for dense networks. Assuming that the network density decreases with time this indicated that originally osteons show a more pronounced gradient of the network density when moving from their inside to their outside border.

The results of a analysis excluding the regions that are highlighted in blue (Figures 4.12, 4.20) can be found in Appendix B.

4.3.3 Orientation of the Network

Distributions of the orientation of the canaliculi with respect to two reference orientations – either the center of the Haversian canal or the normal of the lamellae – both exhibit a high alignment of canaliculi with respect to the radial direction (Figure 4.23). In

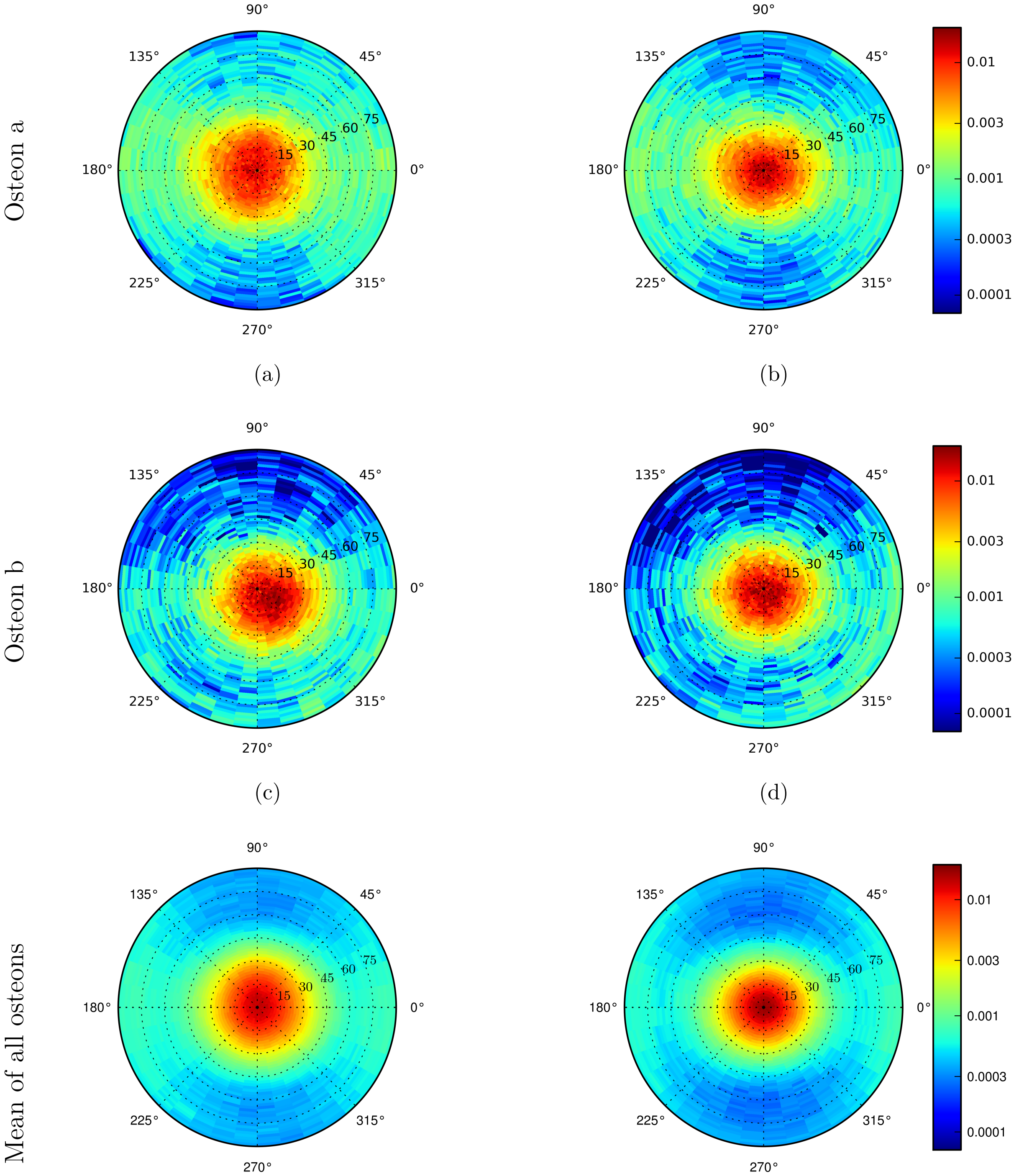

(a)

(b)

(c)

(d)

(e) Orientation with respect to the center of the Haversian canal

(f) Orientation with respect to the normal of the lamellae

Figure 4.23: Orientation of the canaliculi for two different osteons (first and second row), and the average over all osteons (last row). The two columns represent the orientation of canaliculi with respect to the center of the Haversian canal (1st column), and with respect to the normal of the lamellae (second column). The angle θ is plotted radially, α azimuthally (see Figure 4.9 for the definition of the angles). The relative density $dL/(Ld\Omega)(\theta,\alpha)$ is visualized using a logarithmic color code.

this Figure, the orientation of canaliculi is shown for two selected osteons and for the average over all osteons. While for the osteon on top the orientation map seems almost independent of the choice of the reference orientation (e.g. first row in Figure 4.23), the orientation distribution of the second osteon plotted below is less centered around the origin when using the center of the Haversian canal as reference. Also when averaging all datasets (third row), the orientation distribution shows a broader central peak when the Haversian canal is used as reference.

The reduced radial alignment for this reference orientation becomes clearer when the averaged data is integrated over the azimuthal angle (Figure 4.24): due to the reduced alignment of radial canaliculi the peak at small angles appears broader (see inset). A second broad peak of a lateral network ($\theta > 60°$) can be identified in a semi-logarithmic presentation of the same data (Figure 4.25). Again this peak is more pronounced in case the lamellae normals are used as reference orientation.

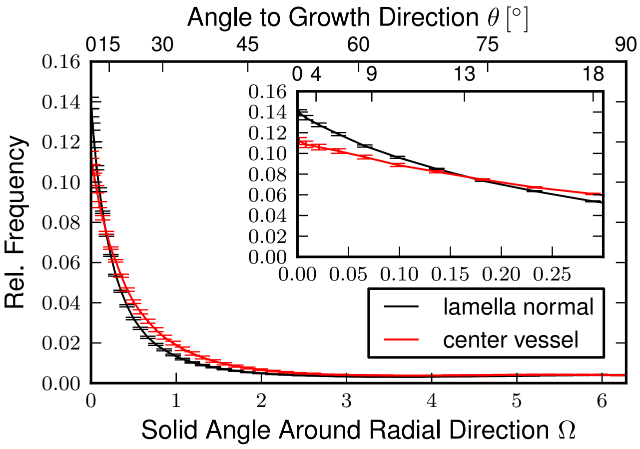

Figure 4.24: Integration of the orientation distribution (Figure 4.23) over the azimuthal angle α. Two different representations of the angle are used: for the x-axis on the bottom the solid angle around the reference direction R is plotted, while on the non-linear x-axis on top the corresponding two-dimensional angle θ is plotted. The inset shows the distribution of canaliculi orientation for small θ demonstrating that the peak of radial canaliculi is more pronounced when evaluated with respect to the lamellae normals (black) than when the center of the Haversian canal is used as reference (red).

Figure 4.26 shows the distribution of the length of the canaliculi as a function of θ as well as the corresponding cumulative distribution. $64 \pm 1\%$ of the length of the network is oriented with an angle of $\theta < 30°$ (and, therefore, by definition belonging to the radial network), while $16 \pm 1\%$ of the length is laterally oriented (i.e. $\theta > 60°$). The preferred radial orientation is reflected by the fact that $77 \pm 1\%$ of the network has a orientation angle θ less than 45°.

Already the plots at the bottom of Figure 4.23 show that there is an increased orientation of the lateral network ($\theta > 60°$) for azimuthal angles α around 0° and 180° (more greenish

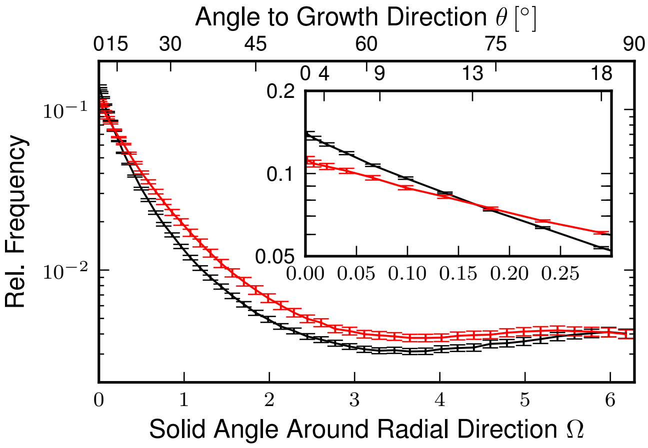

Figure 4.25: Semi-logarithmic plot of the data shown in Figure 4.24. In this representation a second, broad peak of lateral canaliculi around $\theta = 90°$ can be identified.

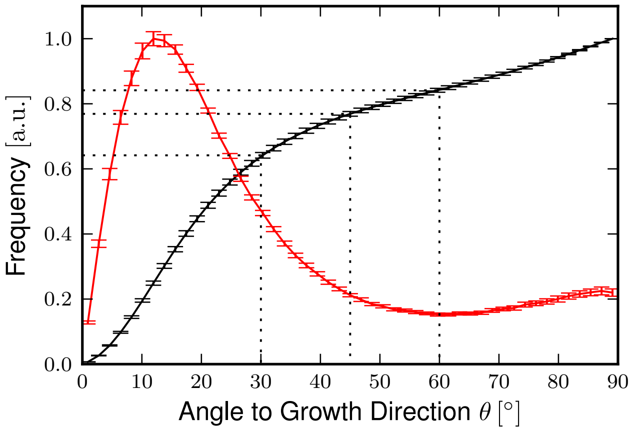

Figure 4.26: Relative network length as a function of the angle between canaliculus and lamella normal θ. The green curve shows the same data as presented in Figure 4.24 without consideration of the solid angle. The black curve shows the cumulative distribution. Dotted lines indicate the values of θ for the definition of the radial ($\theta = 30°$) and the lateral ($\theta = 60°$) network as well as for ($\theta = 45°$).

colors) compared to angles α around 90° and 270° (bluish colors). This observation is further endorsed when integrating the data radially over the angle θ (Figure 4.27). While for the radial network there is hardly any dependence on the angle α, the orientation of the lateral network shows a preferred orientation along the angles 0° and 180°, which corresponds to the direction parallel to the Haversian canal.

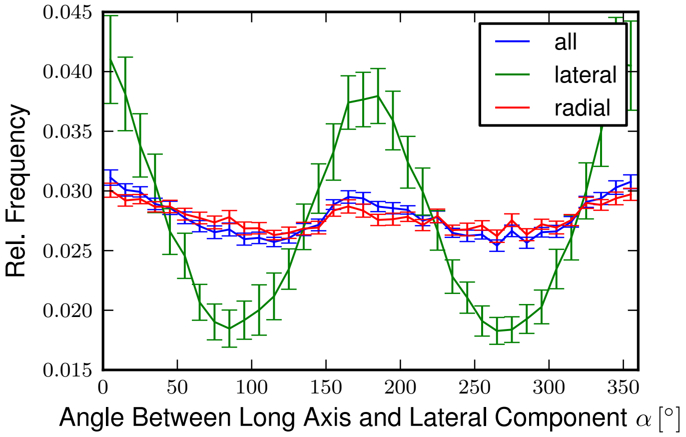

Figure 4.27: Azimuthal integration and normalization, of all canaliculi, only radial ($\theta < 30°$) and only lateral ($\theta > 60°$) canaliculi. A preferred alignment of the lateral canaliculi with the long axis ($0°, 180°$) of the osteon can be clearly observed.

4.3.4 Correlation of Network and Lamellae

The final evaluation step is now to look at the orientation of the canaliculi with respect to the lamellar pattern in the osteon. Calculating the canalicular orientation separately for dark and bright lamellae (for the definition based on the measured SHG signal see Figure 4.10), it becomes obvious that the orientation dependence of the lateral network is much more anisotropic in the dark lamellae compared to the bright ones (Figure 4.28). The main orientation of canaliculi parallel to the blood vessel is the same as the preferred collagen orientation within the dark lamellae (corresponding to a lower SHG intensity). This indicates an alignment of the canaliculi and the collagen matrix. The orientation within the bright lamellae does not show a clearly preferred orientation. For radial canaliculi a clear anisotropy cannot be identified neither in dark nor in bright lamellae (Figure 4.29).

A refined evaluation, where the distribution of the azimuthal angle of lateral canaliculi α is plotted not just for bright and dark lamellae as in Figure 4.28 , but for 10 sublamellae separately is shown in Figure 4.30. Not only does the amplitude of the curves increase from the center of the bright to the center of the dark lamellae corresponding to an stronger alignment of the lateral canaliculi in dark lamellae. When moving from the center of the bright lamella (denoted in dark blue at 0.0 or in dark red at 1.0) to the center of the dark lamella (denoted in green at 0.5) the main orientation of the lateral canaliculi shifts continuously from angles α close to 90° and 270° to angles around 0° and 180°. These angles mean that in the center of the bright lamellae the lateral canaliculi are oriented parallel to the image plane, while in the center of the dark lamellae they are oriented parallel to the Haversian canal.

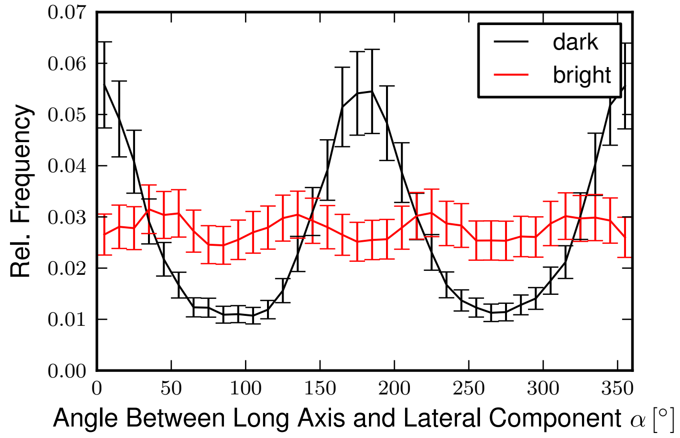

Figure 4.28: Azimuthal integration of the length of lateral canaliculi as shown in Figure 4.27, but now separated spatially into contributions from dark and bright lamellae. Within dark lamellae the lateral canaliculi tend to be aligned with a preferred direction parallel to the Haversian canal, while no preferred orientation can be identified for bright lamellae.

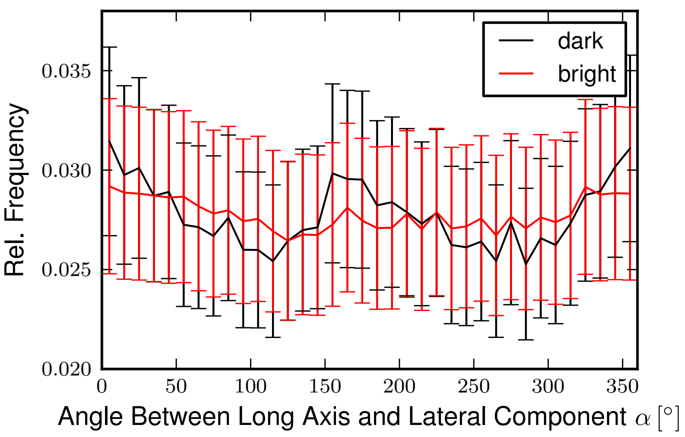

Figure 4.29: Azimuthal integration of the length of radial canaliculi analog to Figure 4.28. No clear angular dependence can be observed for neither bright nor dark lamellae.

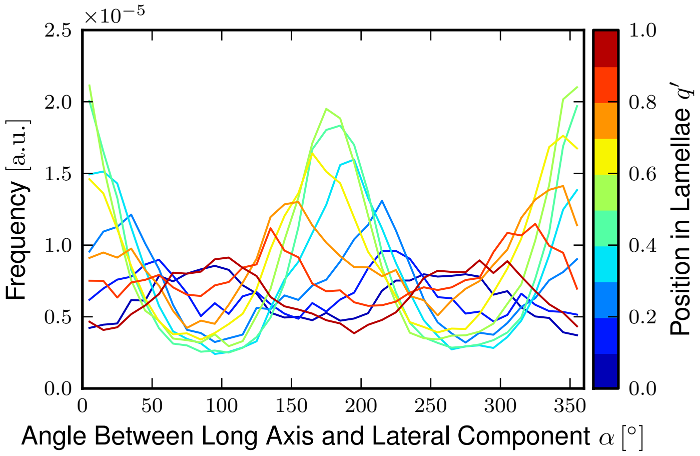

Figure 4.30: Azimuthal distribution of lateral canaliculi at different positions of the lamellae. The colors represent the positions within the lamellae: red and blue show canaliculi that are closest to the center of bright lamellae, green in the center of the dark lamellae. Not only can a shift of the peaks be observed, but the amplitude is also continuously decreasing from the center of the dark towards the center of the bright lamellae.

To evaluate this data further, for each sublamella the orientation distribution was fitted by two Gaussian peaks with an offset of 180° to take into consideration the periodicity of the angle α. The upper plot of Figure 4.31 shows for all sublamellae the position of the peaks (in black). The change in the preferred orientation of the lateral canaliculi does not change linearly, but is larger in the bright lamellae compared to the dark ones. In the same plot the relative amount of lateral network, i.e. the area underneath the curves of Figure 4.30, is shown in red. An increased density of the lateral network within the dark lamellae can be seen.

To study if the reduced amplitude of the orientation dependence of Figure 4.30 can be explained by these two quantities alone, an order parameter was calculated. This was done by measuring the fraction of the oriented network, i.e. the area under the peaks above the minimum divided by the total area under the curves. As the value depends on the lowest value of each curve, the order parameter was calculated both for the measured data as well as for the fitted peaks (lower plot of Figure 4.31).

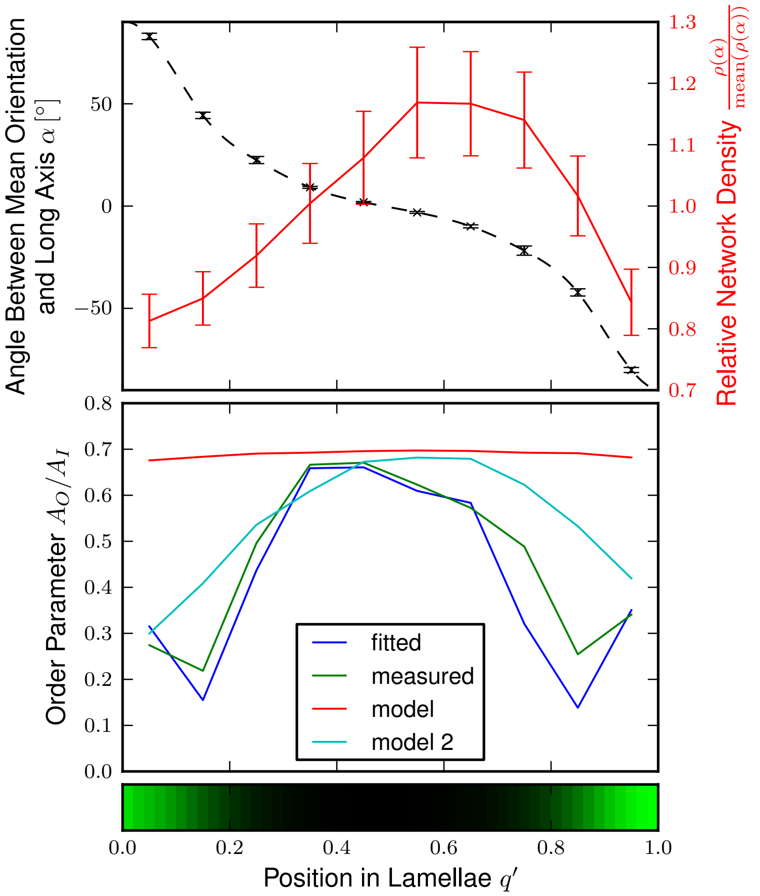

Figure 4.31: Quantification of Figure 4.30. The top graph shows in black the preferred orientation of the lateral canaliculi, i.e. the position of the fitted peaks shown in Figure 4.30 (error bars due to uncertainty of the fit are small). Plotted in red is the relative density distribution of the lateral network (error bars denote standard error within all 40 datasets) as the function of the sublamellae. A monotonous but non-linear change in the preferred orientation can be observed as well as a higher network density within dark lamellae. The bottom graph shows the calculated order parameter for fitted, measured as well as modeled orientations. The colored bar underneath visualizes the mean shg intensity of all lamellae for different positions within the lamellae.

For comparison the order parameter was also calculated for a simple model, which aims to estimate the reduction in order that arises due to the averaging of network orientation over a sublamella of finite width. As the orientation changes less rapidly in the center of the dark lamellae while the width of the averaged subvolumes does not change, this could explain why the network there appears more ordered.

To simulate this effect, the peak position of the fitted angle distribution (Figure 4.31) with the highest degree of order (i.e. the one from the center of the dark lamella) is shifted along the obtained mean orientation according to the position within the lamella (black dashed line in Figure 4.31). Then the average of the shifted orientations is calculated for each sublamellae and the order parameter of this model is calculated, imitating the effect of having constant order but different slope of orientation change. While the shape of this modeled order parameter has the same tendency as the measured values, the change in order that results from the different rate of change is much lower than the measured change. An artificial decrease in the order parameter comparable to the measured one can only be observed when instead of averaging one sublamella five sublamellae are averaged, denoted as model 2 in Figure 4.31. This shows that the observed differences in the order parameter are not due to inadequate spatial resolution of our method.

Evaluating the lacunae size, shape and orientation with respect to their position in the lamella gives the following results: similar to the density of the lateral network also the cell density is slightly increased within the dark lamellae (Figure 4.32). Studying the orientation of the short axis of the lacunae, it can be seen that it is well aligned with the normal of the lamellae (Figure 4.33). The long axis of the lacunae is more evenly distributed (Figure 4.34). Compared to the bright lamellae, some preferred orientation parallel to the Haversian canal can be seen in dark lamellae (Figure 4.35).

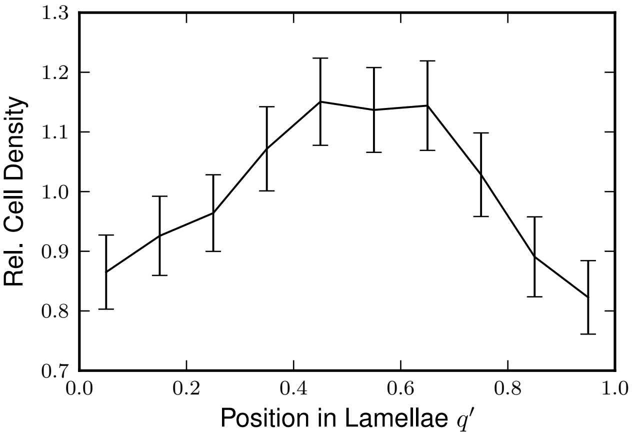

Figure 4.32: Lacunar density as a function of position with lamella. A slightly higher density was measured in the center of the lamellae.

Figure 4.36 shows some lacunar quantities (for their definition see Section 4.2.3.6) calculated for lacunae centered in the dark lamella and in the bright lamella, respectively. While the difference in shape is hardly significant (for stretch the p-value is 0.03), the difference in orientation is pronounced for bright and dark lamellae (p value for α: $7.4 \cdot 10^{-4}$).

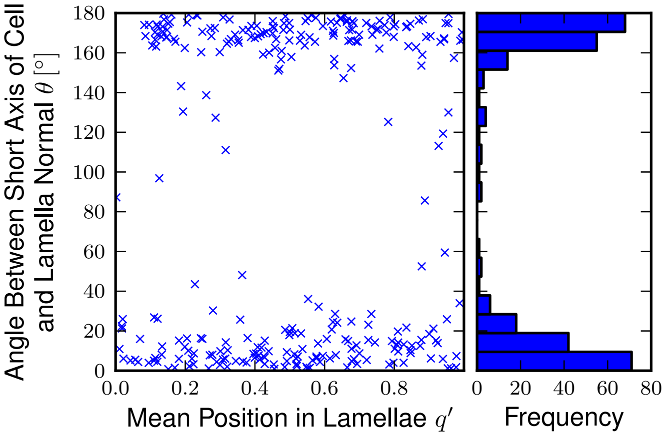

Figure 4.33: Orientation of the short axis of the lacunae with respect to the normal of the lamellae. The left plot shows the angle, which corresponds to α, between the two directions plotted for the mean position of all complete lacunae. α seems to be independent on the position of the lamellae. The histogram on the right side integrates over all lamellae.

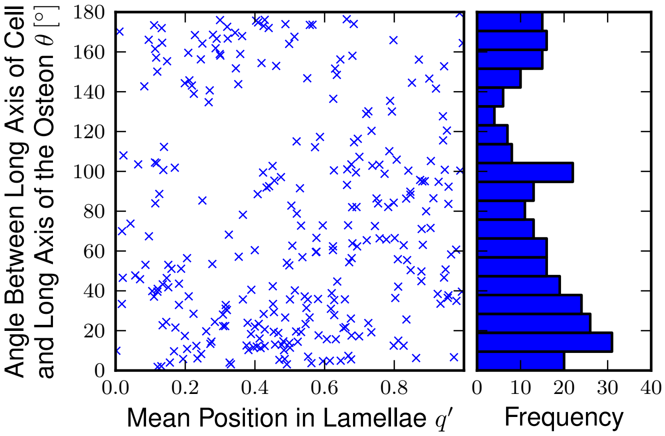

Figure 4.34: Orientation of the long axis of the lacunae with respect to long axis of the osteon. To test the impression if the lacunae in the center of the lamellae have an angle around $\theta = 0°, 180°$, Histograms as the one on the right hand side are calculated for dark and bright lamellae independently (Figure 4.35).

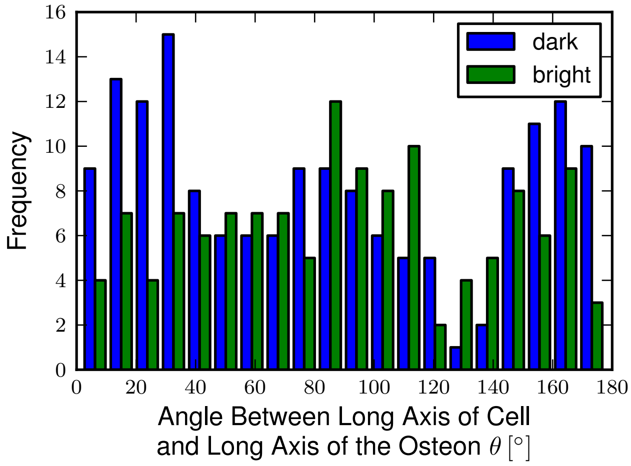

Figure 4.35: Histogram of the relative angle between the long axis of the lacunae and the blood vessel, separated for lacunae that are positioned in the center of the lamellae (dark/blue) and those that are within bright regions (green). Lacunae in the dark region of a lamellae are more likely to be parallel to the blood vessel than lacunae in the bright region of a lamella.

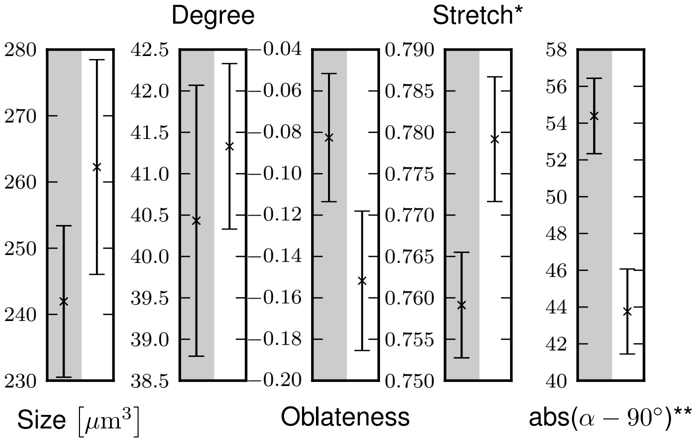

Figure 4.36: Comparison of lacunar properties for bright and dark lamellae. Left data corresponds to lacunae in dark lamellae, right to lacunae with their center of mass within the bright lamellae. Error bars denote standard errors. The $*$ sign denotes a p-value of the t-test below 0.05, $**$ denotes $p < 0.001$.

4.4 Discussion

In this chapter, the three-dimensional organization of the canalicular network in osteons was quantified and related to the structure of the osteon. Specifically, the variations in network density within an osteon, between osteons of the same sample and from different samples were analyzed, and the preferred orientation of the network relative to the center of the osteon as well as its relationship to collagen orientation was studied. The reason why density and orientation, out of the vast amount of possible quantities to look at, were analyzed is that these quantities are defined locally and are relatively robust against boundary effects due to a limited size in the imaged volume. Furthermore these quantities provide a intuitive relation to the functional aspects of the OLCN and can easily be related to the geometry of the osteon. In the following section, results will again be summarized and the possible implications as well as limitations will be discussed.

4.4.1 Density and Inhomogeneity

Most of the results presented in this work are based on **densities**, i.e. the length of the network (with a certain orientation) within a unit volume. The mean network density within all the osteons was $\bar{\rho} = 0.071 \pm 0.002\,\mu\text{m}/\mu\text{m}^3$ (standard deviation $\sigma(\rho) = 0.01\,\mu\text{m}/\mu\text{m}^3$). The only directly comparable value* [Sugawara et al., 2005] is a density of $0.26 \pm 0.02\,\mu\text{m}/\mu\text{m}^3$ measured in the calvaria (bone of the skull) of chicken embryos. This value is much higher than the density obtained from our human samples. As far as human bone samples are concerned, Marotti et al. [1995a] reported 5.5 ± 1.9 canaliculi per $100\,\mu\text{m}^2$ by looking at the canaliculi penetrating the surface of Haversian canals in a human tibia. This number fits very well to our finding of a density of radially oriented canaliculi with $\theta < 45°$ $\rho_{\theta<45} = (0.055 \pm 0.003)\,\frac{\mu\text{m}}{\mu\text{m}^3}$.

We found an average lacunar density $\rho^V_{lacunae} = (0.93 \pm 0.05)\,\%$, $(\sigma(\rho^V_{lacunae}) = 0.3\,\%)$, which corresponds roughly $\rho^N_{lacunae} = 37000 \pm 2000$ osteocytes per mm^3, assuming a

---

*As it comes from the analysis of skeletonized confocal microscopy data.

mean lacuna volume of $\bar{\rho}_l = (251 \pm 10)\,\mu\text{m}^3$ ($\sigma(\bar{\rho}_l) = 163\,\mu\text{m}^3$) for completely imaged lacunae. Published values for the osteocyte density vary considerably: Dong et al. [2014] measured a volume density between 0.68 and 0.83 % and number densities around 21000 per mm^3, Hannah et al. [2010] reported values around 70000 per mm^3, both numbers were obtained from samples of comparable locations (midshaft of the femur).

While network densities spread over a broad range within our samples, we could not find a correlation of the density with neither the size of the osteon nor with the lacunar density. Since the canaliculi network is thought to be functionally more important for mechano-sensing than the cell body within the lacuna (Section 2.2.1, [Thompson et al., 2012]) this shows that care has to be taken whenever lacunar densities are used to learn about mechano-sensitivity. However, in our data the variations of lacunar densities were bigger than of network densities. Possible reasons for these variations in the lacunar density are, firstly, our sample sizes are rather small and, therefore, contain only few lacunae per dataset. Secondly, thresholding and segmentation of lacunae still has some potential for optimization (Section 4.4.5).

In a previous work of our group, using the same experimental technique and comparable evaluation methods, Kerschnitzki et al. [2013] showed that in ovine fibrolamellar bone, 80% of the bone material can be found within 1.4 μm of the nearest canaliculus. In our human samples the density is lower resulting in a distance in which 80% of the bone material is contained within 2.5–3 μm. Assuming a homogeneous network with a mean density given from all four samples, the calculated value is reduced to 1.95–2.12 μm.

Calculating densities for smaller subvolumes allowed us to study variations of the density within one osteon. The variations of the network density as quantified by the width of the density distribution (Figure 4.16) were surprisingly high. The width of this distribution depends on the size of these subvolumes; we chose the subvolumes to be comparable to the volume of the lacunae, i.e. $400\,\mu\text{m}^3$ or approximately $8\,\mu$m in a linear dimension. The fact that the autocorrelation for the network density has values larger than zero for a distance around 20 μm, demonstrates that densities in neighboring subvolumes are not independent.

4.4.2 Functional Aspects of the Network and How it Changes During Time

It is not clear how the network inhomogeneity influences mechano-regulation. Part of the observed inhomogeneity results most likely from a dying network. It has been proposed that such a reduced network density triggers remodeling [Burr, 1993; Verborgt et al., 2000]. On the other hand, the adaption of cortical bone to the mechanical loading suggests that osteocytes do not only initiate resorption but also control the remodeling process*.

A part of the observed inhomogeneity of the network can be assigned to a **decrease of the network density with increasing radius**. All 4 samples showed a significant

---

*As described in Section 2.1.2 different osteon morphologies are located in regions with different loading conditions, and also the alignment of osteon with the main axis of the strain [van Oers et al., 2008] is most easily explained by a regulatory process.

($p < 0.05$) decrease of network density in the osteon for increasing distance from its center. If the main function of the OLCN is to distribute nutrition from the blood vessel to the cells and to transport waste products the other way, as well as the exchange of signaling molecules between the vascular system and the osteocytes, a decrease in the network density with increasing distance from the center is plausible. A higher density close to the Haversian canal would allow fluxes through the canaliculi to be independent of radial distance. The same considerations also hold for a flux of ions to support mineralization as well as during osteocytic osteolysis. These thoughts also fit to the alignment of the canaliculi with respect to the center of the osteon. However, the fact that some of the studied osteons showed a network density that increased as a function of the radius raises the question how important the radial dependence is for the function of the network. Another observation suggests that the distance-density relationship as well as the orientation towards the Haversian canal is not essential for the function of the network: not only do individual datasets show an inverted relationship, but many canaliculi aiming towards the blood vessel are actually not connected to it. While in many osteons canaliculi appear to stop shortly before the Haversian surface, which could arguably be an imaging artifact, in many cases radial canaliculi are interrupted by regions with no network that form an almost concentric ring around the vessel (Section 4.3.2). The morphology of the network adjacent to this empty ring resembles those of osteocytes close to the cement lines, indicating that this is not an imaging artifact. Several observations indicate that these structures indeed arise from a remodeling process that can be thought of as creation of a new osteon within an older one. In some of the imaged osteons the collagen arrangement changed at exactly this position as observed by an intersection of lamellae under a small angle. Measurement using electron backscatter microscopy performed by our collaboration partner at LBIO, Vienna [A. Roschger, personal communication, October 2014], showed in similar samples that these regions had an increased mineralization, suggesting the existence of a cement line. These observations also fits recent descriptions of low mineralized small concentric osteons as observed using computed tomography [Arhatari et al., 2011]. It is quite surprising that about one quarter of our analyzed osteons had such features. The observation that canaliculi which are interrupted by these remodeling processes seem to stay unmineralized[*] despite the fact that mineralization has to be actively suppressed, suggests a different function for these canaliculi than the transport between osteocytes and blood vessel. One possible reason to maintain these interrupted canaliculi could be to preserve a high surface area, beneficial for osteocytic osteolysis. Unmineralized canaliculi additionally provide porosity for fluid flow in case of loading, which would facilitate mechano-sensing.

In order to learn about the function of the OLCN by describing its structure, one has to keep in mind that the structures might **change during time**, and that the network might fulfill different functions at different times. While we cannot observe the time development of the OLCN directly, besides the concentric remodeling described earlier, there is evidence for the assumption that regions without any network are due to a dying of the network. We observed structures in SHG images (“green canaliculi” e.g. in the lower left corner in Figure 4.1) which seems to originate from collagen that runs parallel to (radial) canaliculi that are not accessible and, therefore, not stained by rhodamine. To

---

[*] At least for long enough that several osteons with this feature can be observed.

study in how far the presented results stay the same if such empty regions are excluded from analysis, the quantification was repeated with this respect (Appendix B). This analysis by definition results in a higher network density and reduced inhomogeneity. The distribution of the density of the subvolumes appear more like a Poisson distribution with a relative standart deviation of $\sigma/\mu = 0.5$. Remarkably this value is equal to the expected value if the network is approximated by randomly distributed one-dimensional canaliculi. This finding supports that the network density is determined by a stochastic process with a clustering on a larger length scale.

Thus we assume that osteons with a lower network density corresponds to networks which are more altered (most likely present on older osteons). Figure 4.22 shows that in osteons with a higher network density, the relative decrease in density as a function of the radius is more pronounced. This indicates that when the network was formed, the increasing network density from the cement line to the blood vessel was clearly present and the dying of the network reduced this trend. To test this hypothesis, the age of the osteons could be estimated based on the degree of mineralization which is correlated to the tissue age and can be measured by quantitative backscattered electron imaging (qBEI) [Roschger et al., 2008]. Marotti et al. [1995a] listed several reasons why they expected the decreasing relationship of the network density, discussing how a higher density closer to the Haversian canal could explain the exponentially decaying bone formation rate by inhibiting bone formation signals from osteocytes which are in contact to the bone forming osteoblasts via canaliculi. After the secretion of osteoid, huge amounts of mineral need to be transported into the newly formed tissue. Transport via the OLCN is more effective than the diffusion through the partly mineralized extracellular matrix. In a mature, highly mineralized osteon, this function is not as important anymore. Trying to compensate for a dying of the network and excluding regions that show no canaliculi at all, reduces the trend of the decay but the decreasing density is still significant if all osteons are combined (Appendix B).

Studying the **orientation of the canalicular network**, we observed not only a strong alignment of radial canaliculi, but also a second peak in the density as a function of the angle θ between canaliculi and the center of the osteon (Figure 4.24) at $\theta = 90°$, i.e. within the plane of the lamellae. This indicates that there might be an important function of those canaliculi which we refer to as lateral network. As mentioned before, radial canaliculi often do not reach the Haversian canal, which seems to be a result of changes over time. However, the osteocytes remain connected to the Haversian canal as apparent by the staining. An important function of the lateral network could, therefore, be that it increases the robustness of the network against local interruptions maintaining the connectivity of the network.

Besides these functional considerations, it is also possible to ask how the **orientation of the network correlates to the formation process**. We interpret the lamellae as bone surface that was once present when osteoblasts deposited the unmineralized matrix of the osteon. We saw that the network is more aligned with respect to the normal of the lamella than it is to the center of the Haversian canal. This fits to the proposed formation process of the network in which the radial canaliculi try to stay in contact with the osteoblasts on the surface and therefore appear orthogonal to the lamellae (Section 2.2.2.1). Lateral canaliculi represent dendrites that followed the surface of the bone during the closure of the osteon. Bonewald [2005] suggested that osteocytes can also form canaliculi within the mineralized bone tissue. While this could explain the observations of intermediate angles, most likely this process can only provide a minor contribution to the observed network, and the majority of the canaliculi were built at the same time as the bone was deposited.

Differences of the directional distributions of lateral network components in bright and dark lamella demonstrate a close relation between the orientation of canaliculi and the orientation of the material in which the network is located (Section 4.4.3). The orientation of the cells parallel to the collagen have not only been described for osteocytes but also for osteoblasts (Section 2.2.2). It is not clear if the osteoblasts were actively responsible for the alignment of the collagen, or if the extension of the cell including the cell processes follows the orientation of previously self assembled collagen. In case of the former, it might be that the lateral network is a remnant of cell processes already present during the active phase of the osteoblast and was used to arrange the collagen [Yamamoto et al., 2012]. This also fits to descriptions of Pazzaglia et al. [2010] and the dendrites shown in Figure 2.10. While these two possibilities can not be differentiated with our method, it is apparent that how the bone was formed is reflected in the structure of the network. Our quantification supports descriptions of Kusuzaki et al. [2000]; Ferretti et al. [2006]; Kerschnitzki et al. [2011a] that the structure of the OLCN can be used to draw conclusions about the collagen structure and the formation process.

4.4.3 Network Properties and Lamellar Features

As we measured the orientation of the **lateral network** as a function of the position within the lamellae, an interesting question is how this **orientation correlates to the orientation of the collagen matrix**. Even though the orientation of collagen was not directly measured, and an interpretation of the SHG signal in terms of collagen orientation is not straightforward (Appendix C), the changes in orientation of the lateral canaliculi as a function of the position within the lamella can be compared to models of the collagen arrangement in lamellae. As described in Section 2.1.2 there are two main explanations for the optical contrast that is then interpreted as lamellae. One explanation describes dark and bright lamellae as rather two distinct materials with different composition/structure, while the more accepted explanation uses differences of collagen orientation to differentiate lamellae.

Our observation of a continuous shift of the main orientation of the lateral network when passing through a lamella (Figures 4.30 and 4.31) fits very well to this second explanation that is known as the twisted plywood model, also referred to as fanning lamellae. In this model the orientation of collagen in the osteon wall can be seen as continuously turning with all bright and all dark lamellae having a similar orientation. The spatial periodicity of the orientation angle is given by the angle between the main orientation of the collagen matrix and the imaged plane (which is often the surface of the sample). In the other explanation of lamellae, the bone matrix has distinct compositions for the two types of lamellae. Several of our measured quantities promote such compositional/structural differences between bright and dark lamellae: We did indeed find increased densities of lacunae as well as of the lateral network within dark lamellae. Also the amount of order of the network showed differences between dark and bright lamellae.

How can we integrate our observations into these apparently contradictory models? Using reflective SHG imaging to identify lamellae allows us to also study prismatic samples. Looking at circumferential lamellae in bovine bone from orthogonal perspectives inverts the contrast of the lamellae* (Appendix C) which made us believe that the SHG signal is mostly orientation dependent, supporting the twisted plywood model.

To answer if **the differences in order** as observed by the reduced amplitudes of the curves in Figure 4.30 between bright and dark lamellae can also be explained by a continuous but nonlinear rotation of the collagen orientation, a model was used to average orientation within individual sublamellae. The drop in order in this model is much lower if orientations are averaged only in individual sublamellae. However, a comparable magnitude was obtained when two neighboring sublamellae in both directions (i.e. half of the complete lamella) are included in the averaging (light blue line in lower plot of Figure 4.31).

A possible explanation for an averaging over several sublamellae is the difference between the real position of the bright lamellae and its position in the imaged plane due to an inclination of the osteon. A possible error is introduced as the SHG signal depends on the relative angle between collagen and incident light. As some osteons are tilted with respect to the image plane, this can shift the position of the maximum signal. The local tilt of the lamellae with respect to the imaging axis can be measured using the orientation of $\mathbf{L}_2$, i.e. the orientation of the blood vessel projected in to the lamellar plane. To test whether this tilt changes our conclusions, the analysis of the orientation was repeated excluding canaliculi where the tilt of the closest lamellae exceeded 15° ($\angle(\mathbf{L}, \mathbf{Z}) > 15°$)†. Besides a slightly more pronounced non-linearity of the fanning, the results remained comparable (Figure 4.37) to the earlier result (Figure 4.31), demonstrating that the tilt of the lamellae does not strongly influence our results. Alternatively errors in the position of the lamellae can arise during initialization and the sequential fitting of lamellae. As described in Section 4.2.3.2 all registered lamellae were checked for obvious errors, to minimize such an influence. In addition, a stochastic error in the position of the lamellae would signify that differences in lacunar and lateral network density would be even higher than the differences reported, which would promote the hypothesis of structural differences between the two types of lamellae.

As we had to **average** several hundred **lamellae** to obtain the orientation of the lateral network as a function of the position, we cannot rule out that this averaging affects our conclusions. Possibly the collagen orientation does not behave the same in all the averaged lamellae besides the fact that we limited our analysis to regular (e.g. lamellae that do not split or end within the analyzed volume) alternating lamellae. Lamellae are also known to change direction of twisting/fanning, and in addition unidirectional lamellae with sudden jumps of the orientation have been reported [Reznikov et al., 2014b].

---

[*] Unfortunately so far we did not successfully image alternating lamellae in a prismatic sample of a human osteon cut in a way that it would allow us to see if the contrast of alternating lamellae is again inverted at the edge.

[†] The angle of 15° was chosen for a low signal to noise ratio.

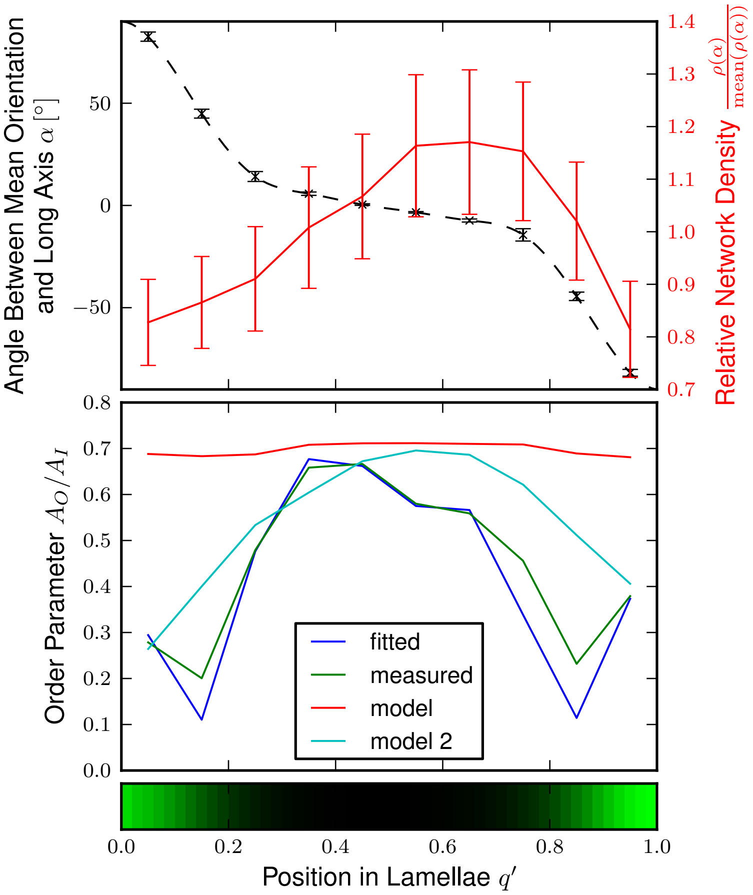

Figure 4.37: Quantification of the orientation of the lateral canalicular network comparable to Figure 4.31, but this time the network is only analyzed if the tilt of the osteon/lamella was less than 15°. The position of fitted peaks (black dashed line) shows the same trend as in Figure 4.31 but with an even more pronounced non-linearity in the rotation of the main orientation of the lateral network. The measured order parameter (green line) did not increase in the region where the orientation rotates the fastest, showing that the tilt of the lamellae with respect to the imaging axis hardly influences the observed order. The modeled order parameter, based on this reduced data did not show significant differences.

Besides possible implications of this averaging, published data on collagen orientation in circumferential lamellae [Reznikov et al., 2014b] supports that changes in the amount of order appear in the collagen arrangement of fanning lamellae. While in this publication it has not been explicitly stated, the presented data (Figure 4.38) indicates that the changes in order have the same periodicity as the rotation in the analyzed lamellae. Therefore, we assume that if we would extend the imaged volume of individual lamellae (thereby improving the signal to noise ratio), we would also observed a change in the order of the lateral network.

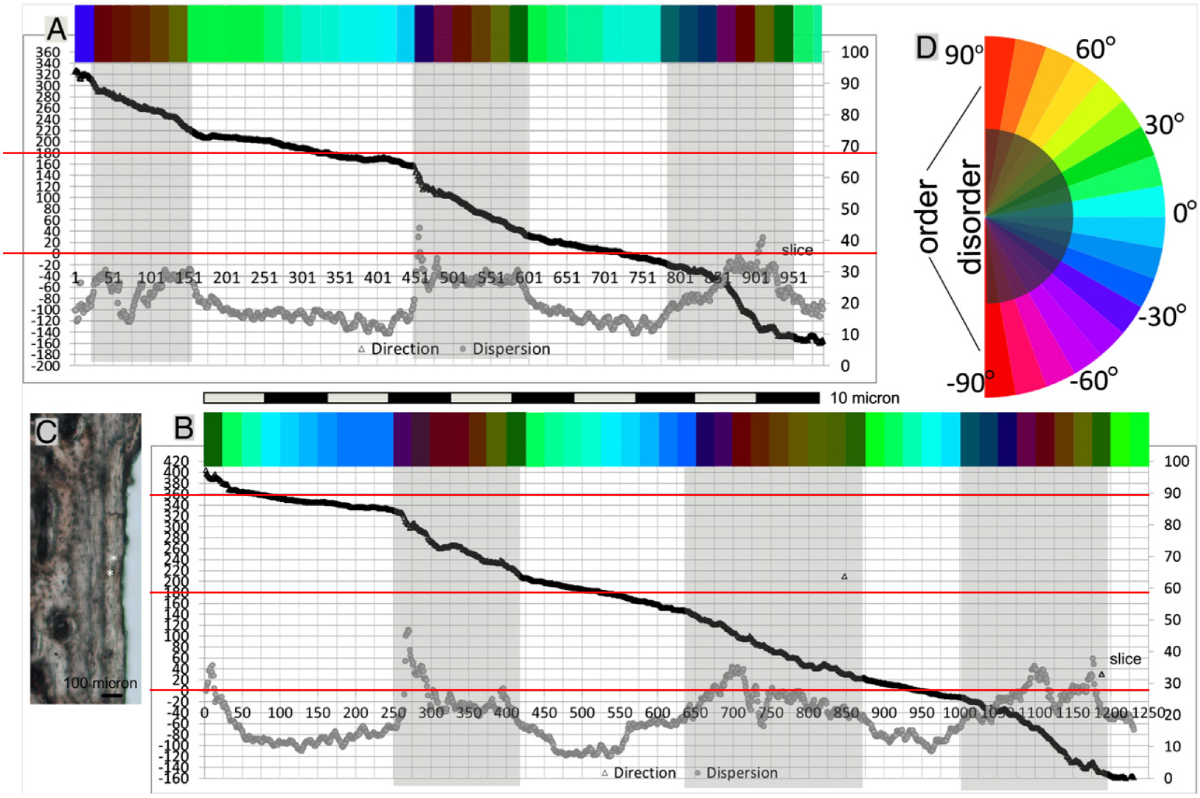

Figure 4.38: Collagen orientation and order in circumferential lamellae in human femural bone. The black data show the mean orientation of collagen (y-axis) within an image slice (x-axis) obtained by FIB/SEM, the gray values shows a parameter measuring order. Regions that appeared relatively unordered are highlighted in gray. The red lines were added to show that the centers of the regions that are more ordered (bright in this plot) are centered around angles 0°, 180°, 360° supporting our observation that the amount of order has the same periodicity as the rotation of the orientation. Reprinted from Reznikov et al. [2014b] with permission from Elsevier.

Therefore our data suggest that:

1. Lateral canaliculi and collagen have comparable properties (orientation, order) within a sublamella
2. In addition to the rotation of its predominant orientation, there are also structural differences (density, order parameter) in the studied lamellae that exhibit the same periodicity as the change of orientation.

4.4.4 Conclusion

Our results show that the density of the OLCN in human osteonal bone exhibit a high inhomogeneity, with many regions free of network. These empty regions at least partly reflect a change of the network with time. We showed that the network density decreases with the distance to the Haversian canal, and this is even more pronounced for osteons with a high network density. This made us believe that this functional dependence is more important during formation of the osteon than later on, where the network might have a different role than during the formation of the osteon. The organization of the network hints at a strong correlation to the formation process. Using the three-dimensional images of osteocyte networks we could not only learn about functional aspects of the osteocytes: by showing that the canaliculi orientation correlates to the collagen orientation, the applied method can additionally provide information on the tissue organization. We found support that dark and bright lamellae are structurally different materials.

4.4.5 Problems and Outlook

During the evaluation of the data, variations int intensities due to **staining** were among the most challenging technical **problems**. An adaptive thresholding algorithm has been developed that improves the image quality considerably compared to the use of a global threshold. A remaining problem are lacunae that have been observed in some samples that were inadequately stained (see for example Figure 4.12), sometimes to an extent that the segmentation of the lacunae did not succeed in identifying them. Besides an underestimation of the lacunar density, this increases uncertainties in the shape descriptors of the lacunae and their calculated degree, i.e. the number of canaliculi originating from them. While these quantities were not the focus of this work, an improperly detected lacunae can also affect the position of the registered lamellae. When lacunae are located in the bright lamellae, this produces a local minimum in the SHG signal. To avoid artifacts during the registration, we excluded the surrounding volumes of segmented lacunae during the registration of the lamellae. If a lacuna located in the center of a bright lamella was not detected, there is a local minimum in the SHG signal at this position and, as a consequence, the lamella will be registered in the maximum on one side of the lacuna instead of its center. All in all we think that this artifact is negligible even if a high fraction of the lacunae would not be detected properly: with the osteocyte density of about 1 %, and the fact that less than half of the lacunae are located within bright lamellae, the possible influenced volume is negligible.

In this work we tried to deal with the staining problem on the data processing side, this problem might also be reduced on the experimental side by a better control of staining times. To avoid a demineralization of the canaliculi and thus alteration of the observed network, the bone was only stained for 2 days. Performing a dedicated study of the long term influence of staining would provide information about an optimal exposure time to the stain. Also, rhodamine dissolved in alcohol can be used, as it is done by our collaboration partners at the Ludwig Boltzmann Institute of Osteology (LBIO), Vienna, so that the stained samples can still be used to measure the degree of mineralization.

A big challenge is to image the **canalicular network deep within the bone**. In the human bone samples used in this study, the limit for an appropriate image quality was about 40 μm. Even limiting the imaging to 40 μm a reduced autocorrelation in the z-direction compared to the ϕ-direction was observed, indicating higher fluctuations in this direction which could be a result of a depth dependent contrast. A depth of 40 μm is sufficient for the determination of many quantities as described in this thesis, but a larger imaging depth would be desirable, especially to study the connectivity of the lateral network as well as to obtain better statistics for the study of the orientation within individual lamellae. Some test experiments to overcome this limit have been made that are not described in this work. In a first approach, bone was demineralized after it was stained and embedded. Trying to remove the organic matrix, in a way that the network casted in PMMA [Abe et al., 1992] including the fluorochrome remains intact, turned out to be more complicated than expected. More promising was the second approach in which a depth of 40 μm was imaged, followed by grinding down 20 μm of the sample and a subsequent image acquisition. The obtained imaged volumes could then be registered using the NIPY [2013] library and then stitched together. Due to the limited field of view of the objective used, and difficulties to image exactly the same volume, first a tile scan was performed scanning 2x3 tiles in one layer before grinding. Figure 4.1 shows a cropped cross section of the successfully stitched image tiles obtained in this approach. The serial imaging and grinding was done 4 times resulting in an imaged depth of roughly 100 μm. Figure 4.39 shows a longitudinal cut through the successfully stitched image volume of the same dataset, demonstrating that using this approach, in principle, volumes of almost arbitrary dimensions can be imaged.

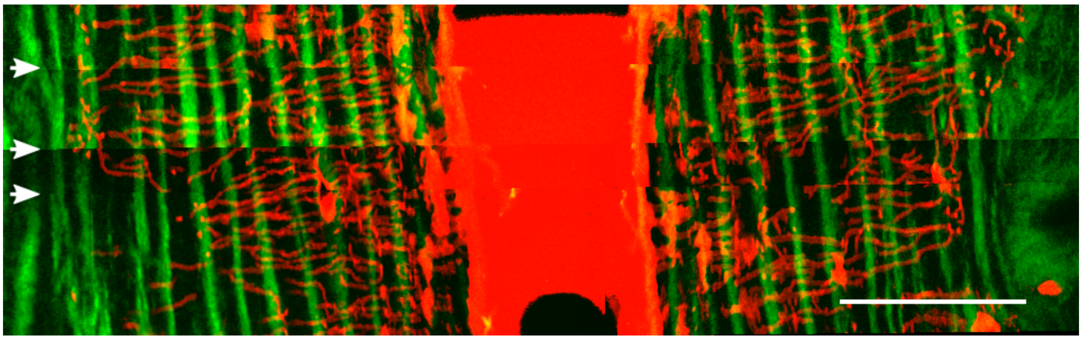

Figure 4.39: Projection of 3 μm of the osteocyte lacuno-canalicular network in an osteon, longitudinal section of the same dataset as in Figure 4.1. The vertical direction of the image from top to bottom corresponds to the increasing imaging depth. The opacity of bone necessitates multiple imaging with a grinding of the surface in-between. Sudden changes of the intensity of the SHG signal (green) indicate where the imaged volumes were stitched together (white arrows). Registration of the rhodamine images (red) was overall satisfactory with displacements of canaliculi being typically below 1–2 voxels. The scale bar equals 50 μm.

To further support the observation of structural differences between dark and bright lamellae, circumferential lamellae could also be measured. This would not only allow to extend the analyzed volume of the lamella; Using prismatic samples (see Appendix C) would in addition allow to compare quantities from the very same lamella, measured from two orthogonal directions corresponding to two surfaces of the sample. Based on the presented results, we expect both, higher order, and a higher network density within the bright lamellae in a longitudinal cross- section.

Most calculated quantities in this work and the preceding work [Kerschnitzki et al., 2013] focused on the description of the canalicular network, with only little attention on the relation of the network to the lacunae. Once the staining problems are solved and a bigger image depth is achieved, it would be interesting to study the connectedness of the lacunae, in particular the influence of the lateral network on the network topology.

By analyzing 3D images of the OLCN, many different descriptors were calculated, some showing high variability. Which quantities are useful and provide the most meaningful information in terms of the function of the network will be better understood once this method is extended to **samples with controlled differences**. The samples studied in this work were chosen to be relatively similar (all human, healthy, similar skeletal site, age, osteonal bone with lamellar appearance) to establish a kind of reference for further investigations. Extending this work to different species would allow us to see if functional relationships to network properties can be observed. As continuation of our collaboration with the LBIO it is planned to measure the OLCN in human samples of different age, where the age of the tissue is determine via its degrees of mineralization. This will allow us to study if and how network properties indeed change with time.

To learn about responses to mechanical loading, a collaboration with the Julius Wolff Institute (Charité) was formed. The aim of this study is to analyze the OLCN located in bone that was formed during a time when loading conditions were controlled: either physiological loading or additional loading applied by a special device, while the animal was alive. Additionally animal models for bone diseases will be studied to see changes in network properties in collaboration with the LBIO. This method can also be applied to human bone biopsies taken for diagnostic reasons. When comparing the network within the biopsy to healthy reference data, network and osteocyte quantities might contribute to a more comprehensive description of the bone pathology. Staining and analyzing such samples can be done without expected problems.

The developed tools can furthermore be used to quantify 3D images of other network-like structures. Dentin is a mineralized tissue present in teeth, where cell processes are housed in tubules, quite comparable to canaliculi. Using the same staining and similar analysis, the orientation of these tubules in elephant tusks was analyzed. Even though Haversian canals have different dimensions, the orientation of Haversian canals can be analyzed using the same method. Using micro-CT scans of bones from different species, in Atkins et al. [2014] the orientation of blood vessels was used to support the hypothesis that also bone remodeling takes place in bone that has no osteocytes. Another field of application is a quantitative analysis of the network-like architecture of trabecular bone. First attempts to skeletonize microCT scans of trabecular bone to quantify angles between trabeculae turned out to be very promising.

Bibliography

Aarden, E. M., P. J. Nijweide, and E. H. Burger. Function of osteocytes in bone. *Journal of Cellular Biochemistry*, 55(3):287–299, July 1994. doi: 10.1002/jcb.240550304.

Abe, K., H. Hashizume, and T. Ushiki. An EDTA-KOH method to expose bone cells for scanning electron microscopy. *J Electron Microsc (Tokyo)*, 41(2):113–115, April 1992.

Adachi, T., Y. Aonuma, M. Tanaka, M. Hojo, T. Takano-Yamamoto, and H. Kamioka. Calcium response in single osteocytes to locally applied mechanical stimulus: Differences in cell process and cell body. *Journal of Biomechanics*, 42(12):1989–1995, August 2009. doi: 10.1016/j.jbiomech.2009.04.034.

Anderson, E. J., S. M. Kreuzer, O. Small, and M. L. K. Tate. Pairing computational and scaled physical models to determine permeability as a measure of cellular communication in micro- and nano-scale pericellular spaces. *Microfluid Nanofluid*, 4(3):193–204, March 2008. doi: 10.1007/s10404-007-0156-5.

Anderson, H. Normal and abnormal mineralization in mammals. *ASAIO Journal*, 27(1):702–708, 1981.

Ardizzoni, A. Osteocyte lacunar size–lamellar thickness relationships in human secondary osteons. *Bone*, 28(2):215–219, February 2001. doi: 10.1016/S8756-3282(00)00417-8.

Arhatari, B. D., D. M. L. Cooper, C. D. L. Thomas, J. G. Clement, and A. G. Peele. Imaging the 3d structure of secondary osteons in human cortical bone using phase-retrieval tomography. *Physics in Medicine and Biology*, 56(16):5265–5274, August 2011. doi: 10.1088/0031-9155/56/16/012.

Arnold, J. S., H. M. Frost, and R. O. Buss. The osteocyte as a bone pump : Clinical orthopaedics and related research, 1971.

Ascenzi, A. and A. Benvenuti. Orientation of collagen fibers at the boundary between two successive osteonic lamellae and its mechanical interpretation. *Journal of Biomechanics*, 19(6):455–463, 1986. doi: 10.1016/0021-9290(86)90022-9.

Ascenzi, A. and E. Bonucci. Relationship between ultrastructure and ”pin test” in osteons. *Clin. Orthop. Relat. Res.*, 121:275–294, December 1976.

Ascenzi, A., E. Bonucci, and D. Steve Bocciarelli. An electron microscope study of osteon calcification. *Journal of Ultrastructure Research*, 12(3):287–303, April 1965. doi: 10.1016/S0022-5320(65)80100-9.

Ascenzi, A. and E. Bonucci. The compressive properties of single osteons. *The Anatomical Record*, 161 (3):377–391, 1968. doi: 10.1002/ar.1091610309.

Ascenzi, M.-G. and A. Lomovtsev. Collagen orientation patterns in human secondary osteons, quantified in the radial direction by confocal microscopy. *Journal of Structural Biology*, 153(1): 14–30, January 2006. doi: 10.1016/j.jsb.2005.08.007.

Ascenzi, M.-G., J. Gill, and A. Lomovtsev. Orientation of collagen at the osteocyte lacunae in human secondary osteons. *Journal of Biomechanics*, 41(16):3426–3435, 2008. doi: 10.1016/j.jbiomech.2008.09.010.

Ascenzi, M., J. M. Kabo, and M. Andreuzzi. Mathematical modeling of human secondary osteons. *Scanning*, 26(1):25–35, January 2004. doi: 10.1002/sca.4950260105.

Atkins, A., M. N. Dean, M. L. Habegger, P. J. Motta, L. Ofer, F. Repp, A. Shipov, S. Weiner, J. D. Currey, and R. Shahar. Remodeling in bone without osteocytes: Billfish challenge bone structure–function paradigms. *PNAS*, page 201412372, October 2014. doi:

10.1073/pnas.1412372111.

Atkins, G. J. and D. M. Findlay. Osteocyte regulation of bone mineral: a little give and take. *Osteoporos Int*, 23(8):2067–2079, August 2012. doi: 10.1007/s00198-012-1915-z.

Bao, C. L. M., E. Y. Teo, M. Chong, Y. Liu, M. Choolani, and J. Chan. Advances in bone tissue engineering. *Regenerative medicine and tissue engineering. Rijeka: Intech*, pages 599–614, 2013.

Bastian, P., M. Blatt, A. Dedner, C. Engwer, R. Klöfkorn, M. Ohlberger, and O. Sander. A generic grid interface for parallel and adaptive scientific computing. part i: Abstract framework. September 2007.

Baud, C. A. Morphology and inframicroscopic structure of osteocytes. *ACTA ANAT (BASEL)*, 51(3): 209–&, 1962.

Bélanger, D. L. F. Osteocytic osteolysis. *Calc. Tis Res.*, 4(1):1–12, December 1969. doi: 10.1007/BF02279101.

Bezooijen, R. L. v., P. t. Dijke, S. E. Papapoulos, and C. W. G.M. Löwik. SOST/sclerostin, an osteocyte-derived negative regulator of bone formation. *Cytokine & Growth Factor Reviews*, 16(3): 319–327, June 2005. doi: 10.1016/j.cytogfr.2005.02.005.

Bonewald, L. Osteocytes as multifunctional cells. *J Musculoskelet Neuronal Interact*, 6(4):331–333, 2006.

Bonewald, L. F. Generation and function of osteocyte dendritic processes. *Journal Of Muscoskeletal and Neuronal Interactions*, 5(4):321, 2005.

Bonewald, L. Osteocytes as dynamic multifunctional cells. *Annals of the New York Academy of Sciences*, 1116(1):281–290, November 2007. doi: 10.1196/annals.1402.018.

Bonewald, L. F. The amazing osteocyte, the amazing osteocyte. *Journal of Bone and Mineral Research, Journal of Bone and Mineral Research*, 26, 26(2, 2):229, 229–238, 238, February 2011. doi: 10.1002/jbmr.320,10.1002/jbmr.320.

Bonewald, L. F. and M. L. Johnson. Osteocytes, mechanosensing and wnt signaling. *Bone*, 42(4): 606–615, April 2008. doi: 10.1016/j.bone.2007.12.224.

Boyde, A. and M. H. Hobdell. Scanning electron microscopy of lamellar bone. *Cell and Tissue Research*, 93(2):213–231, June 1968. doi: 10.1007/BF00336690.

Boyde, A. and C. Riggs. The quantitative study of the orientation of collagen in compact bone slices. *Bone*, 11(1):35–39, 1990. doi: 10.1016/8756-3282(90)90069-B.

Boyle, W. J., W. S. Simonet, and D. L. Lacey. Osteoclast differentiation and activation. *Nature*, 423 (6937):337–342, May 2003. doi: 10.1038/nature01658.

Britz, H. M., C. D. L. Thomas, J. G. Clement, and D. M. L. Cooper. The relation of femoral osteon geometry to age, sex, height and weight. *Bone*, 45(1):77–83, July 2009. doi: 10.1016/j.bone.2009.03.654.

Bruder, S. P., D. J. Fink, and A. I. Caplan. Mesenchymal stem cells in bone development, bone repair, and skeletal regenaration therapy. *J. Cell. Biochem.*, 56(3):283–294, November 1994. doi: 10.1002/jcb.240560303.

Bruns, V. v. *Lehrbuch der allgemeinen Anatomie des Menschen: Nach eigenen Untersuchungen zum gebrauche bei Vorlesungen.* F. Vieweg und sohn, 1841.

Buenzli, P. R., P. Pivonka, and D. W. Smith. Bone refilling in cortical basic multicellular units: insights into tetracycline double labelling from a computational model. *Biomech Model Mechanobiol*, pages 1–19, 2013. doi: 10.1007/s10237-013-0495-y.

Bullmore, E. and O. Sporns. Complex brain networks: graph theoretical analysis of structural and functional systems. *Nature Reviews Neuroscience*, 10(3):186–198, February 2009. doi: 10.1038/nrn2575.

Burger, E. H., J. Klein-Nulend, et al. Mechanotransduction in bone-role of the lacunocanalicular network. *Faseb Journal*, 13:101–112, 1999.

Burke, D. P. and D. J. Kelly. Substrate stiffness and oxygen as regulators of stem cell differentiation during skeletal tissue regeneration: A mechanobiological model. *PLoS ONE*, 7(7):e40737, July 2012. doi: 10.1371/journal.pone.0040737.

Burr, D. B. Remodeling and the repair of fatigue damage. *Calcif Tissue Int*, 53(1):S75–S81, February 1993. doi: 10.1007/BF01673407.

Byrne, D., D. Lacroix, and P. Prendergast. Simulation of fracture healing in the tibia: Mechanoregulation of cell activity using a lattice modeling approach. *Journal of Orthopaedic*

Research, 29(10):1496–1503, 2011.

Cardoso, L., S. P. Fritton, G. Gailani, M. Benalla, and S. C. Cowin. Advances in assessment of bone porosity, permeability and interstitial fluid flow. *Journal of Biomechanics*, 46(2):253–265, January 2013. doi: 10.1016/j.jbiomech.2012.10.025.

Carter, D. R., P. R. Blenman, and G. S. Beaupre. Correlations between mechanical stress history and tissue differentiation in initial fracture healing. *Journal of Orthopaedic Research*, 6(5):736–748, 1988.

Case, N., B. Sen, J. A. Thomas, M. Styner, Z. Xie, C. R. Jacobs, and J. Rubin. Steady and oscillatory fluid flows produce a similar osteogenic phenotype. *Calcif Tissue Int*, 88(3):189–197, March 2011. doi: 10.1007/s00223-010-9448-y.

Chaco. *version 4.2*. Enthought, Austin, Texas, 2012. URL `http://code.enthought.com/projects/chaco/`.

Checa, S., P. J. Prendergast, and G. N. Duda. Inter-species investigation of the mechano-regulation of bone healing: Comparison of secondary bone healing in sheep and rat. *Journal of Biomechanics*, 44 (7):1237–1245, 2011.

Checa, S. and P. J. Prendergast. A mechanobiological model for tissue differentiation that includes angiogenesis: A lattice-based modeling approach. *Ann Biomed Eng*, 37(1):129–145, January 2009. doi: 10.1007/s10439-008-9594-9.

Ciani, C., S. B. Doty, and S. P. Fritton. An effective histological staining process to visualize bone interstitial fluid space using confocal microscopy. *Bone*, 44(5):1015–1017, May 2009. doi: 10.1016/j.bone.2009.01.376.

Claes, L. and C. Heigele. Magnitudes of local stress and strain along bony surfaces predict the course and type of fracture healing. *Journal of Biomechanics*, 32(3):255–266, March 1999. doi: 10.1016/S0021-9290(98)00153-5.

Cowin, S. C., G. Gailani, and M. Benalla. Hierarchical poroelasticity: movement of interstitial fluid between porosity levels in bones. *Philosophical Transactions of the Royal Society of London A: Mathematical, Physical and Engineering Sciences*, 367(1902):3401–3444, September 2009. doi: 10.1098/rsta.2009.0099.

Creative Commons Attribution 3.0. Creative Commons, 2007.

Currey, J. D. The validation of algorithms used to explain adaptive bone remodeling in bone. In A, O. and W. H, editors, *Bone Structure and Remodeling*, pages 9–13. World Scientific, 1995.

Dallas, S. L., M. Prideaux, and L. F. Bonewald. The osteocyte: an endocrine cell ... and more. *Endocr. Rev.*, 34(5):658–690, October 2013. doi: 10.1210/er.2012-1026.

de Jong, W. F. La substance minérale dans les os. *Recl. Trav. Chim. Pays-Bas*, 45(6):445–448, January 1926. doi: 10.1002/recl.19260450613.

Dempster, D. W., J. E. Compston, M. K. Drezner, F. H. Glorieux, J. A. Kanis, H. Malluche, P. J. Meunier, S. M. Ott, R. R. Recker, and A. M. Parfitt. Standardized nomenclature, symbols, and units for bone histomorphometry: A 2012 update of the report of the ASBMR histomorphometry nomenclature committee. *J Bone Miner Res*, 28(1):2–17, January 2013. doi: 10.1002/jbmr.1805.

Deutsch, K. *De penitiori ossium structura observationes: Diss. inaug. anat.-physiol. : cum tab. lith.* Vratislavia, 1834.

Dierckx, P. Algorithms for smoothing data with periodic and parametric splines. *Computer Graphics and Image Processing*, 20(2):171–184, October 1982. doi: 10.1016/0146-664X(82)90043-0.

Discher, D. E., D. J. Mooney, and P. W. Zandstra. Growth factors, matrices, and forces combine and control stem cells. *Science*, 324(5935):1673–1677, June 2009. doi: 10.1126/science.1171643.

Dong, P., S. Haupert, B. Hesse, M. Langer, P.-J. Gouttenoire, V. Bousson, and F. Peyrin. 3d osteocyte lacunar morphometric properties and distributions in human femoral cortical bone using synchrotron radiation micro-CT images. *Bone*, 60:172–185, March 2014. doi: 10.1016/j.bone.2013.12.008.

Doty, S. Morphological evidence of gap junctions between bone cells. *Calcified Tissue International*, 33(1):509–512, 1981. doi: 10.1007/BF02409482.

Duda, G. N., K. Eckert-Hübner, R. Sokiranski, A. Kreutner, R. Miller, and L. Claes. Analysis of inter-fragmentary movement as a function of musculoskeletal loading conditions in sheep. *Journal of Biomechanics*, 31(3):201–210, December 1997.

Ebner, V. v. Sind die Fibrillen des Knochengewebes verkalkt oder nicht? *Archiv f. mikrosk. Anatatomie*, 29(1):213–236, December 1887. doi: 10.1007/BF02955499.

Ebner, V. v. *Über den feineren Bau der Knochensubstanz.* Nabu Press, 1875.

Einhorn, T. A. The cell and molecular biology of fracture healing. *Clin. Orthop. Rel. Res.*, (355): S7–S21, October 1998.

Epari, D. R., H. Schell, H. J. Bail, and G. N. Duda. Instability prolongs the chondral phase during bone healing in sheep. *Bone*, 38(6):864–870, June 2006. doi: 10.1016/j.bone.2005.10.023.

Feldkamp, L. A., S. A. Goldstein, M. A. Parfitt, G. Jesion, and M. Kleerekoper. The direct examination of three-dimensional bone architecture in vitro by computed tomography. *J Bone Miner Res*, 4(1):3–11, February 1989. doi: 10.1002/jbmr.5650040103.

Ferretti, M., M. A. Muglia, F. Remaggi, V. Canè, and C. Palumbo. Histomorphometric study on the osteocyte lacuno-canalicular network in animals of different species. II. parallel-fibered and lamellar bones. *Ital J Anat Embryol*, 104(3):121–131, September 1999.

Ferretti, M., C. Palumbo, M. Contri, and G. Marotti. Static and dynamic osteogenesis: two different types of bone formation. *Anatomy and Embryology*, 206(1):21–29, December 2002. doi: 10.1007/s00429-002-0265-6.

Ferretti, M., C. Palumbo, L. Bertoni, F. Cavani, and G. Marotti. Does static precede dynamic osteogenesis in endochondral ossification as occurs in intramembranous ossification? *The Anatomical Record Part A: Discoveries in Molecular, Cellular, and Evolutionary Biology*, 288A(11): 1158–1162, 2006. doi: 10.1002/ar.a.20386.

Franken, P. A., A. E. Hill, C. W. Peters, and G. Weinreich. Generation of optical harmonics. *Phys. Rev. Lett.*, 7(4):118–119, August 1961. doi: 10.1103/PhysRevLett.7.118.

Franz-Odendaal, T. A., B. K. Hall, and P. E. Witten. Buried alive: How osteoblasts become osteocytes. *Developmental Dynamics*, 235(1):176–190, January 2006. doi: 10.1002/dvdy.20603.

Fratzl, P. and R. Weinkamer. Nature's hierarchical materials. *Progress in Materials Science*, 52(8): 1263–1334, November 2007. doi: 10.1016/j.pmatsci.2007.06.001.

Freund, I., M. Deutsch, and A. Sprecher. Connective tissue polarity. optical second-harmonic microscopy, crossed-beam summation, and small-angle scattering in rat-tail tendon. *Biophys J*, 50 (4):693–712, October 1986.

Frost, H. M. Vital biomechanics: Proposed general concepts for skeletal adaptations to mechanical usage. *Calcif Tissue Int*, 42(3):145–156, May 1988. doi: 10.1007/BF02556327.

Frost, H. M. Micropetrosis. *J Bone Joint Surg Am*, 42(1):144–150, January 1960.

Frost, H. M. *Bone remodelling dynamics.* Thomas, 1963.

Frost, H. M. Tetracycline-based histological analysis of bone remodeling. *Calc. Tis Res.*, 3(1):211–237, December 1969. doi: 10.1007/BF02058664.

Fukada, E. and I. Yasuda. On the piezoelectric effect of bone. *Journal of the Physical Society of Japan*, 12(10):1158–1162, 1957.

Galvis, L., J. W. C. Dunlop, G. Duda, P. Fratzl, and A. Masic. Polarized raman anisotropic response of collagen in tendon: Towards 3d orientation mapping of collagen in tissues. *PLoS ONE*, 8(5): e63518, May 2013. doi: 10.1371/journal.pone.0063518.

Garcia, P., T. Histing, J. H. Holstein, M. Klein, M. W. Laschke, R. Matthys, A. Ignatius, B. Wildemann, J. Lienau, A. Peters, B. Willie, G. Duda, L. Claes, T. Pohlemann, and M. D. Menger. Rodent animal models of delayed bone healing and non-union formation: a comprehensive review. *Eur Cell Mater*, 26:1–14, 2013.

Gebhardt, W. über funktionell wichtige Anordnungsweisen der feineren und gröberen Bauelemente des Wirbeltierknochens. *Archiv für Entwicklungsmechanik der Organismen*, 20(2):187–322, November 1905. doi: 10.1007/BF02162810.

Gegenbaur, C. Ueber die Bildung des K nochengewebes. *Jena. Z. Med. Naturw*, 1:343–369, 1864.

Geris, L., J. Vander Sloten, and H. Van Oosterwyck. In silico biology of bone modelling and remodelling: regeneration. *Philosophical Transactions of the Royal Society A: Mathematical, Physical and Engineering Sciences*, 367(1895):2031–2053, May 2009. doi: 10.1098/rsta.2008.0293.

Geris, L., A. Gerisch, J. V. Sloten, R. Weiner, and H. V. Oosterwyck. Angiogenesis in bone fracture healing: A bioregulatory model. *Journal of Theoretical Biology*, 251(1):137–158, March 2008. doi: 10.1016/j.jtbi.2007.11.008.

Gerstenfeld, L. C., D. M. Cullinane, G. L. Barnes, D. T. Graves, and T. A. Einhorn. Fracture healing as a post-natal developmental process: Molecular, spatial, and temporal aspects of its regulation. *J. Cell. Biochem.*, 88(5):873–884, April 2003. doi: 10.1002/jcb.10435.

Gerstenfeld, L. C., Y. M. Alkhiary, E. A. Krall, F. H. Nicholls, S. N. Stapleton, J. L. Fitch, M. Bauer, R. Kayal, D. T. Graves, K. J. Jepsen, and T. A. Einhorn. Three-dimensional reconstruction of fracture callus morphogenesis. *J Histochem Cytochem*, 54(11):1215–1228, November 2006. doi: 10.1369/jhc.6A6959.2006.

Gibson, L. J. and M. F. Ashby. *Cellular Solids: Structure and Properties.* Cambridge University Press, July 1999.

Giraud-Guille, M. M. Twisted plywood architecture of collagen fibrils in human compact bone osteons. *Calcif Tissue Int*, 42(3):167–180, May 1988. doi: 10.1007/BF02556330.

Giraud Guille, M. M., G. Mosser, C. Helary, and D. Eglin. Bone matrix like assemblies of collagen: From liquid crystals to gels and biomimetic materials. *Micron*, 36(7–8):602–608, October 2005. doi: 10.1016/j.micron.2005.07.005.

Giraud-Guille, M.-M., L. Besseau, and R. Martin. Liquid crystalline assemblies of collagen in bone and in vitro systems. *Journal of Biomechanics*, 36(10):1571–1579, October 2003. doi: 10.1016/S0021-9290(03)00134-9.

Gómez-Benito, M. J., L. A. González-Torres, E. Reina-Romo, J. Grasa, B. Seral, and J. M. García-Aznar. Influence of high-frequency cyclical stimulation on the bone fracture-healing process: mathematical and experimental models. *Philosophical Transactions of the Royal Society A: Mathematical, Physical and Engineering Sciences*, 369(1954):4278–4294, 2011.

Gómez-Benito, M., J. García-Aznar, J. Kuiper, and M. Doblaré. Influence of fracture gap size on the pattern of long bone healing: a computational study. *Journal of Theoretical Biology*, 235(1): 105–119, July 2005. doi: 10.1016/j.jtbi.2004.12.023.

Guido van Rossum. *Python Reference Manual.* PythonLabs, Virginia, USA, 2001.

Haapasalo, H., H. Sievanen, P. Kannus, A. Heinonen, P. Oja, and I. Vuori. Dimensions and estimated mechanical characteristics of the humerus after long-term tennis loading. *Journal of Bone and Mineral Research*, 11(6):864–872, 1996. doi: 10.1002/jbmr.5650110619.

Hagberg, A. A., D. A. Schult, and P. J. Swart. Exploring network structure, dynamics, and function using NetworkX. In Varoquaux, G., T. Vaught, and J. Millman, editors, *Proceedings of the 7th Python in Science Conference*, pages 11 – 15, Pasadena, CA USA, 2008.

Hannah, K. M., C. D. L. Thomas, J. G. Clement, F. De Carlo, and A. G. Peele. Bimodal distribution of osteocyte lacunar size in the human femoral cortex as revealed by micro-CT. *Bone*, 47(5): 866–871, November 2010. doi: 10.1016/j.bone.2010.07.025.

Havers, C. *Osteologia nova, or some new Observations of the Bones, and the Parts belonging to them, with the manner of their Accretion and Nutrition.* 1691.

Heinonen, A., H. Sievänen, H. Kyröläinen, J. Perttunen, and P. Kannus. Mineral mass, size, and estimated mechanical strength of triple jumpers' lower limb. *Bone*, 29(3):279–285, September 2001. doi: 10.1016/S8756-3282(01)00574-9.

Hesse, B., M. Langer, P. Varga, A. Pacureanu, P. Dong, S. Schrof, N. Männicke, H. Suhonen, C. Olivier, P. Maurer, G. J. Kazakia, K. Raum, and F. Peyrin. Alterations of mass density and 3d osteocyte lacunar properties in bisphosphonate-related osteonecrotic human jaw bone, a synchrotron μCT study. *PLoS ONE*, 9(2):e88481, February 2014a. doi: 10.1371/journal.pone.0088481.

Hesse, B., P. Varga, M. Langer, A. Pacureanu, S. Schrof, N. Männicke, H. Suhonen, P. Maurer, P. Cloetens, F. Peyrin, and K. Raum. Canalicular network morphology is the major determinant of the spatial distribution of mass density in human bone tissue - evidence by means of synchrotron radiation phase-contrast nano-CT. *J Bone Miner Res*, pages n/a–n/a, August 2014b. doi: 10.1002/jbmr.2324.

Heřt, J., P. Fiala, and M. Petrtýl. Osteon orientation of the diaphysis of the long bones in man. *Bone*, 15(3):269–277, May 1994. doi: 10.1016/8756-3282(94)90288-7.

Hori, R. Y. and J. L. Lewis. Mechanical properties of the fibrous tissue found at the bone-cement interface following total joint replacement. *J. Biomed. Mater. Res.*, 16(6):911–927, November 1982. doi: 10.1002/jbm.820160615.

Hunter, J. D. Matplotlib: A 2d graphics environment. *Computing in Science & Engineering*, 9(3): 90–95, May 2007. doi: 10.1109/MCSE.2007.55.

Isaksson, H. Recent advances in mechanobiological modeling of bone regeneration. *Mechanics Research Communications*, 42(0):22–31, June 2012. doi: 10.1016/j.mechrescom.2011.11.006.

Isaksson, H., C. C. van Donkelaar, R. Huiskes, and K. Ito. Corroboration of mechanoregulatory algorithms for tissue differentiation during fracture healing: comparison with in vivo results. *Journal of Orthopaedic Research*, 24(5):898–907, May 2006a. doi: 10.1002/jor.20118.

Isaksson, H., W. Wilson, C. C. van Donkelaar, R. Huiskes, and K. Ito. Comparison of biophysical stimuli for mechano-regulation of tissue differentiation during fracture healing. *Journal of Biomechanics*, 39(8):1507–1516, 2006b. doi: 10.1016/j.jbiomech.2005.01.037.

Isaksson, H., C. C. van Donkelaar, R. Huiskes, and K. Ito. A mechano-regulatory bone-healing model incorporating cell-phenotype specific activity. *Journal of Theoretical Biology*, 252(2):230–246, May 2008. doi: 10.1016/j.jtbi.2008.01.030.

Jäger, I. and P. Fratzl. Mineralized collagen fibrils: a mechanical model with a staggered arrangement of mineral particles. *Biophys J*, 79(4):1737–1746, October 2000.

Jaschouz, D., O. Paris, P. Roschger, H.-S. Hwang, and P. Fratzl. Pole figure analysis of mineral nanoparticle orientation in individual trabecula of human vertebral bone. *Journal of Applied Crystallography*, 36(3):494–498, April 2003. doi: 10.1107/S0021889803000566.

Jaworski, D. Z. F. G. Lamellar bone turnover system and its effector organ. *Calcif Tissue Int*, 36(1): S46–S55, March 1984. doi: 10.1007/BF02406133.

Jilka, R. L., R. S. Weinstein, T. Bellido, A. M. Parfitt, and S. C. Manolagas. Osteoblast programmed cell death (apoptosis): Modulation by growth factors and cytokines. *J Bone Miner Res*, 13(5): 793–802, May 1998. doi: 10.1359/jbmr.1998.13.5.793.

Jones, S. J., A. Boyde, and J. B. Pawley. Osteoblasts and collagen orientation. *Cell and Tissue Research*, 159(1):73–80, 1975. doi: 10.1007/BF00231996.

Kalajzic, I., B. G. Matthews, E. Torreggiani, M. A. Harris, P. Divieti Pajevic, and S. E. Harris. In vitro and in vivo approaches to study osteocyte biology. *Bone*, 54(2):296–306, June 2013. doi: 10.1016/j.bone.2012.09.040.

Kamioka, H., T. Honjo, and T. Takano-Yamamoto. A three-dimensional distribution of osteocyte processes revealed by the combination of confocal laser scanning microscopy and differential interference contrast microscopy. *Bone*, 28(2):145–149, February 2001. doi: 10.1016/S8756-3282(00)00421-X.

Kamioka, H., S. A. Murshid, Y. Ishihara, N. Kajimura, T. Hasegawa, R. Ando, Y. Sugawara, T. Yamashiro, A. Takaoka, and T. Takano-Yamamoto. A method for observing silver-stained osteocytes in situ in 3-μm sections using ultra-high voltage electron microscopy tomography. *Microscopy and Microanalysis*, 15(05):377–383, 2009. doi: 10.1017/S1431927609990420.

Kamioka, H., Y. Kameo, Y. Imai, A. D. Bakker, R. G. Bacabac, N. Yamada, A. Takaoka, T. Yamashiro, T. Adachi, and J. Klein-Nulend. Microscale fluid flow analysis in a human osteocyte canaliculus using a realistic high-resolution image-based three-dimensional model. *Integr. Biol.*, 4 (10):1198–1206, September 2012. doi: 10.1039/C2IB20092A.

Kasper, G., J. D. Glaeser, S. Geissler, A. Ode, J. Tuischer, G. Matziolis, C. Perka, and G. N. Duda. Matrix metalloprotease activity is an essential link between mechanical stimulus and mesenchymal stem cell behavior. *STEM CELLS*, 25(8):1985–1994, 2007. doi: 10.1634/stemcells.2006-0676.

Kelly, D. and C. Jacobs. The role of mechanical signals in regulating chondrogenesis and osteogenesis of mesenchymal stem cells. *Birth Defects Research Part C - Embryo Today: Reviews*, 90(1):75–85, 2010.

Kennedy, O. D., B. C. Herman, D. M. Laudier, R. J. Majeska, H. B. Sun, and M. B. Schaffler. Activation of resorption in fatigue-loaded bone involves both apoptosis and active pro-osteoclastogenic signaling by distinct osteocyte populations. *Bone*, 50(5):1115–1122, May 2012. doi: 10.1016/j.bone.2012.01.025.

Kerschnitzki, M. Bone material characteristics influenced by osteocytes. 2013.

Kerschnitzki, M., W. Wagermaier, Y. Liu, P. Roschger, G. N. Duda, and P. Fratzl. Poorly ordered bone as an endogenous scaffold for the deposition of highly oriented lamellar tissue in rapidly growing ovine bone. *Cells Tissues Organs*, 194(2-4):119–123, 2011a. doi: 10.1159/000324467.

Kerschnitzki, M., W. Wagermaier, P. Roschger, J. Seto, R. Shahar, G. N. Duda, S. Mundlos, and P. Fratzl. The organization of the osteocyte network mirrors the extracellular matrix orientation in bone. *Journal of Structural Biology*, 173(2):303–311, February 2011b. doi: 10.1016/j.jsb.2010.11.014.

Kerschnitzki, M., P. Kollmannsberger, M. Burghammer, G. N. Duda, R. Weinkamer, W. Wagermaier, and P. Fratzl. Architecture of the osteocyte network correlates with bone material quality. *Journal of Bone and Mineral Research*, 28(8):1837–1845, 2013. doi: 10.1002/jbmr.1927.

Khayyeri, H., S. Checa, M. Tägil, P. Aspenberg, and P. J. Prendergast. Variability observed in mechano-regulated in vivo tissue differentiation can be explained by variation in cell mechano-sensitivity. *Journal of Biomechanics*, 44(6):1051–1058, April 2011. doi: 10.1016/j.jbiomech.2011.02.003.

Khayyeri, H., H. Isaksson, and P. J. Prendergast. Corroboration of computational models for mechanoregulated stem cell differentiation. *Computer Methods in Biomechanics and Biomedical Engineering*, 0(0):1–9, 2013. doi: 10.1080/10255842.2013.774381.

Kilian, K. A., B. Bugarija, B. T. Lahn, and M. Mrksich. Geometric cues for directing the differentiation of mesenchymal stem cells. *PNAS*, 107(11):4872–4877, March 2010. doi: 10.1073/pnas.0903269107.

Klein-Nulend, J., A. D. Bakker, R. G. Bacabac, A. Vatsa, and S. Weinbaum. Mechanosensation and transduction in osteocytes. *Bone*, 54(2):182–190, June 2013. doi: 10.1016/j.bone.2012.10.013.

Knese, K.-H., D. Voges, and I. Ritschl. Untersuchungen über die Osteon- und Lamellenformen im Extremitätenskelet des Erwachsenen. *Z.Zellforsch*, 40(4):323–360, July 1954. doi: 10.1007/BF00394137.

Knese, K.-H. and M. v. Harnack. über die Faserstruktur des Knochengewebes. *Zeitschrift für Zellforschung*, 57(4):520–558, July 1962. doi: 10.1007/BF00339881.

Knothe Tate, M. L. "Whither flows the fluid in bone?" an osteocyte's perspective. *Journal of Biomechanics*, 36(10):1409–1424, October 2003. doi: 10.1016/S0021-9290(03)00123-4.

Knothe Tate, M. L., J. R. Adamson, A. E. Tami, and T. W. Bauer. The osteocyte. *The International Journal of Biochemistry & Cell Biology*, 36(1):1–8, January 2004. doi: 10.1016/S1357-2725(03)00241-3.

Kölliker, A. *Handbuch der Gewebelehre des Menschen.* Wilhelm Engelmann, 1859.

Kölliker, A. and V. v. Ebner. *Handbuch der Gewebelehre des Menschen.* Leipzig : W. Engelmann, 1889.

Kollmannsberger, P., C. Bidan, J. Dunlop, and P. Fratzl. The physics of tissue patterning and extracellular matrix organisation: How cells join forces. *Soft Matter*, 7(20):9549–9560, 2011.

Krempien, B., C. Manegold, E. Ritz, and J. Bommer. The influence of immobilization on osteocyte morphology. *Virchows Arch. A Path. Anat. and Histol.*, 370(1):55–68, March 1976. doi: 10.1007/BF00427310.

Kusuzaki, K., N. Kageyama, H. Shinjo, H. Takeshita, H. Murata, S. Hashiguchi, T. Ashihara, and Y. Hirasawa. Development of bone canaliculi during bone repair. *Bone*, 27(5):655–659, November 2000. doi: 10.1016/S8756-3282(00)00383-5.

Kwiecinski, G. G., L. Krook, and W. A. Wimsatt. Annual skeletal changes in the little brown bat, myotis lucifugus lucifugus, with particular reference to pregnancy and lactation. *Am. J. Anat.*, 178 (4):410–420, April 1987. doi: 10.1002/aja.1001780410.

LaComb, R., O. Nadiarnykh, S. S. Townsend, and P. J. Campagnola. Phase matching considerations in second harmonic generation from tissues: Effects on emission directionality, conversion efficiency and observed morphology. *Opt Commun*, 281(7):1823–1832, April 2008. doi: 10.1016/j.optcom.2007.10.040.

Lacroix, D. and P. Prendergast. A mechano-regulation model for tissue differentiation during fracture healing: analysis of gap size and loading. *Journal of Biomechanics*, 35(9):1163–1171, September 2002. doi: 10.1016/S0021-9290(02)00086-6.

Lacroix, D., P. J. Prendergast, G. Li, and D. Marsh. Biomechanical model to simulate tissue differentiation and bone regeneration: Application to fracture healing. *Medical & Biological Engineering & Computing*, 40(1):14–21, January 2002. doi: 10.1007/BF02347690.

Landis, W. J., K. J. Hodgens, J. Arena, M. J. Song, and B. F. McEwen. Structural relations between collagen and mineral in bone as determined by high voltage electron microscopic tomography. *Microscopy Research and Technique*, 33(2):192–202, 1996a.

Landis, W. J., K. J. Hodgens, M. J. Song, J. Arena, S. Kiyonaga, M. Marko, C. Owen, and B. F. McEwen. Mineralization of collagen may occur on fibril surfaces: Evidence from conventional and high-voltage electron microscopy and three-dimensional imaging. *Journal of Structural Biology*, 117 (1):24–35, July 1996b. doi: 10.1006/jsbi.1996.0066.

Liu, Y., I. Manjubala, H. Schell, D. R. Epari, P. Roschger, G. N. Duda, and P. Fratzl. Size and habit of mineral particles in bone and mineralized callus during bone healing in sheep. *Journal of Bone* *and Mineral Research*, 25(9):2029–2038, 2010. doi: 10.1002/jbmr.84.

Lu, Y. and A. Penzkofer. Absorption behaviour of methanolic rhodamine 6g solutions at high concentration. *Chemical physics*, 107(2):175–184, 1986.

Lutz, V., M. Sattler, S. Gallinat, H. Wenck, R. Poertner, and F. Fischer. Impact of collagen crosslinking on the second harmonic generation signal and the fluorescence lifetime of collagen autofluorescence. *Skin Research and Technology*, 18(2):168–179, 2012. doi: 10.1111/j.1600-0846.2011.00549.x.

Mader, K. S., P. Schneider, R. Müller, and M. Stampanoni. A quantitative framework for the 3d characterization of the osteocyte lacunar system. *Bone*, 57(1):142–154, November 2013. doi: 10.1016/j.bone.2013.06.026.

Mahamid, J., A. Sharir, D. Gur, E. Zelzer, L. Addadi, and S. Weiner. Bone mineralization proceeds through intracellular calcium phosphate loaded vesicles: A cryo-electron microscopy study. *Journal of Structural Biology*, 174(3):527 – 535, 2011. doi: http://dx.doi.org/10.1016/j.jsb.2011.03.014.

Malladi, P., Y. Xu, M. Chiou, A. J. Giaccia, and M. T. Longaker. Effect of reduced oxygen tension on chondrogenesis and osteogenesis in adipose-derived mesenchymal cells. *American Journal of Physiology - Cell Physiology*, 290(4):C1139–C1146, April 2006. doi: 10.1152/ajpcell.00415.2005.

Manjubala, I., Y. Liu, D. Epari, P. Roschger, H. Schell, P. Fratzl, and G. Duda. Spatial and temporal variations of mechanical properties and mineral content of the external callus during bone healing. *Bone*, 45(2):185–192, 2009.

Marotti, G. The structure of bone tissues and the cellular control of their deposition. *Ital J Anat Embryol*, 101(4):25–79, December 1996.

Marotti, G. The osteocyte as a wiring transmission system. *J Musculoskelet Neuronal Interact*, 1(2): 133–136, December 2000.

Marotti, G. and M. Muglia. A scanning electron microscope study of human bony lamellae proposal for a new model of collagen lamellar organization. *Archivio Italiano di Anatomia e di Embriologia*, 93(3):163–176, 1988.

Marotti, G., M. Ferretti, M. Muglia, C. Palumbo, and S. Palazzini. A quantitative evaluation of osteoblast-osteocyte relationships on growing endosteal surface of rabbit tibiae. *Bone*, 13(5): 363–368, July 1992. doi: 10.1016/8756-3282(92)90452-3.

Marotti, G., M. Ferretti, F. Remaggi, and C. Palumbo. Quantitative evaluation on osteocyte canalicular density in human secondary osteons. *Bone*, 16(1):125–128, January 1995a. doi: 10.1016/8756-3282(95)80022-I.

Marotti, G., M. A. Muglia, and C. Palumbo. Collagen texture and osteocyte distribution in lamellar bone. *Ital J Anat Embryol*, 100 Suppl 1:95–102, 1995b.

Marotti, G. Osteocyte orientation in human lamellar bone and its relevance to the morphometry of periosteocytic lacunae. *Metabolic Bone Disease and Related Research*, 1(4):325–333, 1979. doi: 10.1016/0221-8747(79)90027-4.

Marotti, G. A new theory of bone lamellation. *Calcified Tissue International*, 53(0):S47–S56, February 1993. doi: 10.1007/BF01673402.

Marotti, G., M. Ferretti, and C. Palumbo. The problem of bone lamellation: An attempt to explain different proposed models. *Journal of Morphology*, 274(5):543–550, 2013. doi: 10.1002/jmor.20114.

Marotti, P. G. The original contributions of the scanning electron microscope to the knowledge of bone structure. In M.D, E. B. and P. M. M. M.D, editors, *Ultrastructure of Skeletal Tissues*, number 7 in Electron Microscopy in Biology and Medicine, pages 19–39. Springer US, January 1990.

Marr, D. and E. Hildreth. Theory of edge detection. *Proceedings of the Royal Society of London. Series B, Biological Sciences*, 207(1167):187–217, February 1980.

Martin, R. B., D. B. Burr, and N. A. Sharkey. *Skeletal Tissue Mechanics*. Springer, October 1998.

Martin, R. Does osteocyte formation cause the nonlinear refilling of osteons? *Bone*, 26(1):71–78, January 2000. doi: 10.1016/S8756-3282(99)00242-2.

Martin, R. and D. Burr. A hypothetical mechanism for the stimulation of osteonal remodelling by fatigue damage. *Journal of Biomechanics*, 15(3):137–139, 1982.

Martin, R., V. Gibson, S. Stover, J. Gibeling, and L. Griffins. Osteonal structure in the equine third metacarpus. *Bone*, 19(2):165–171, August 1996a. doi: 10.1016/8756-3282(96)00167-6.

Martin, R., S. Lau, P. Mathews, V. Gibson, and S. Stover. Collagen fiber organization is related to mechanical properties and remodeling in equine bone. a comparsion of two methods. *Journal of*

Biomechanics, 29(12):1515–1521, December 1996b. doi: 10.1016/S0021-9290(96)80002-9.

MATLAB, . *version 8.1.0 (R2013a).* The MathWorks Inc., Natick, Massachusetts, 2013.

Mayya, A., A. Banerjee, and R. Rajesh. Mammalian cortical bone in tension is non-haversian. *Sci. Rep.*, 3, August 2013. doi: 10.1038/srep02533.

McCreadie, B. R., S. J. Hollister, M. B. Schaffler, and S. A. Goldstein. Osteocyte lacuna size and shape in women with and without osteoporotic fracture. *Journal of Biomechanics*, 37(4):563–572, April 2004. doi: 10.1016/S0021-9290(03)00287-2.

McCulloch, C. a. G. and J. N. M. Heersche. Lifetime of the osteoblast in mouse periodontium. *Anat. Rec.*, 222(2):128–135, October 1988. doi: 10.1002/ar.1092220204.

McNally, E. A., H. P. Schwarcz, G. A. Botton, and A. L. Arsenault. A model for the ultrastructure of bone based on electron microscopy of ion-milled sections. *PLoS ONE*, 7(1):e29258, January 2012. doi: 10.1371/journal.pone.0029258.

Menton, D. N., D. J. Simmons, S. L. Chang, and B. Y. Orr. From bone lining cell to osteocyte—an SEM study. *The Anatomical Record*, 209(1):29–39, 1984. doi: 10.1002/ar.1092090105.

Meyer, E. G., C. T. Buckley, S. D. Thorpe, and D. J. Kelly. Low oxygen tension is a more potent promoter of chondrogenic differentiation than dynamic compression. *Journal of Biomechanics*, 43 (13):2516–2523, September 2010. doi: 10.1016/j.jbiomech.2010.05.020.

Miescher, F. and J. X. Müller. *De inflam matione ossium, eorumque anatome generali. Cum tabulis quatuor aeneis. -Berolini, Eichler 1836.* Eichler, 1836.

Mikuni-Takagaki, Y., Y. Kakai, M. Satoyoshi, E. Kawano, Y. Suzuki, T. Kawase, and S. Saito. Matrix mineralization and the differentiation of osteocyte-like cells in culture. *J. Bone Miner. Res.*, 10(2): 231–242, February 1995. doi: 10.1002/jbmr.5650100209.

Miller, D. S. C. and W. S. S. Jee. The bone lining cell: A distinct phenotype? *Calcif Tissue Int*, 41(1): 1–5, January 1987. doi: 10.1007/BF02555122.

Morgan, E. F., H. H. Bayraktar, and T. M. Keaveny. Trabecular bone modulus–density relationships depend on anatomic site. *Journal of Biomechanics*, 36(7):897–904, July 2003. doi: 10.1016/S0021-9290(03)00071-X.

Müller, J. *Archiv für Anatomie, Physiologie und wissenschaftliche Medicin.* Veit & Comp., 1836.

Nefussi, J. R., J. M. Sautier, V. Nicolas, and N. Forest. How osteoblasts become osteocytes: a decreasing matrix forming process. *J Biol Buccale*, 19(1):75–82, March 1991.

Neve, A., A. Corrado, and F. Cantatore. Osteoblast physiology in normal and pathological conditions. *Cell and Tissue Research*, 343(2):289–302, 2011. doi: 10.1007/s00441-010-1086-1.

NIPY, 2013. URL `http://nipy.org/`.

Oliphant, T. E. Python for scientific computing. *Computing in Science & Engineering*, 9(3):10–20, May 2007. doi: 10.1109/MCSE.2007.58.

Omelon, S., M. Ariganello, E. Bonucci, M. Grynpas, and A. Nanci. A review of phosphate mineral nucleation in biology and geobiology. *Calcif Tissue Int*, 93(4):382–396, October 2013. doi: 10.1007/s00223-013-9784-9.

Pacureanu, A., M. Langer, E. Boller, P. Tafforeau, and F. Peyrin. Nanoscale imaging of the bone cell network with synchrotron x-ray tomography: optimization of acquisition setup. *Medical Physics*, 39 (4):2229–2238, 2012. doi: 10.1118/1.3697525.

Palumbo, C., S. Palazzini, and G. Marotti. Morphological study of intercellular junctions during osteocyte differentiation. *Bone*, 11(6):401–406, 1990a. doi: 10.1016/8756-3282(90)90134-K.

Palumbo, C. A three-dimensional ultrastructural study of osteoid-osteocytes in the tibia of chick embryos. *Cell and Tissue Research*, 246(1):125–131, October 1986. doi: 10.1007/BF00219008.

Palumbo, C., S. Palazzini, D. Zaffe, and G. Marotti. Osteocyte differentiation in the tibia of newborn rabbit: An ultrastructural study of the formation of cytoplasmic processes. *Cells Tissues Organs*, 137(4):350–358, 1990b. doi: 10.1159/000146907.

Palumbo, C., M. Ferretti, and G. Marotti. Osteocyte dendrogenesis in static and dynamic bone formation: An ultrastructural study. *The Anatomical Record Part A: Discoveries in Molecular, Cellular, and Evolutionary Biology*, 278A(1):474–480, May 2004. doi: 10.1002/ar.a.20032.

Pannarale, L., P. Braidotti, L. d'Alba, and E. Gaudio. Scanning electron microscopy of collagen fiber orientation in the bone lamellar system in non-decalcified human samples. *Acta Anat (Basel)*, 151 (1):36–42, 1994.

Parfitt, A. M. The cellular basis of bone turnover and bone loss: a rebuttal of the osteocytic resorption–bone flow theory. *Clin. Orthop. Relat. Res.*, 127:236–247, 1977.

Parfitt, A. M. The cellular basis of bone remodeling: The quantum concept reexamined in light of recent advances in the cell biology of bone. *Calcif Tissue Int*, 36(1):S37–S45, March 1984. doi: 10.1007/BF02406132.

Parfitt, A. M. Osteonal and hemi-osteonal remodeling: The spatial and temporal framework for signal traffic in adult human bone. *Journal of Cellular Biochemistry*, 55(3):273–286, 1994. doi: 10.1002/jcb.240550303.

Parfitt, A. M., M. K. Drezner, F. H. Glorieux, J. A. Kanis, H. Malluche, P. J. Meunier, S. M. Ott, and R. R. Recker. Bone histomorphometry: Standardization of nomenclature, symbols, and units: Report of the asbmr histomorphometry nomenclature committee. *J Bone Miner Res*, 2(6):595–610, December 1987. doi: 10.1002/jbmr.5650020617.

Parfitt, A. The physiologic and clinical significance of bone histomorphometric data. *Bone histomorphometry: techniques and interpretation*, pages 143–223, 1983.

Pauwels, F. Eine neue Theorie über den Einfluß mechanischer Reize auf die Differenzierung der Stützgewebe. *Anatomy and Embryology*, 121(6):478–515, 1960. doi: 10.1007/BF00523401.

Pavone, F. S. and P. J. Campagnola. *Second Harmonic Generation Imaging*. CRC Press, June 2013.

Pazzaglia, U. E., T. Congiu, M. Marchese, G. Zarattini, and C. Dell'Orbo. The canalicular system and the osteoblast domain in human secondary osteons. *Anatomia, Histologia, Embryologia*, 2012a. doi: 10.1111/j.1439-0264.2012.01150.x.

Pazzaglia, U., T. Congiu, M. Marchese, and C. Dell'Orbo. The shape modulation of osteoblast–osteocyte transformation and its correlation with the fibrillar organization in secondary osteons. *Cell and Tissue Research*, 340(3):533–540, June 2010. doi: 10.1007/s00441-010-0970-z.

Pazzaglia, U., T. Congiu, G. Zarattini, M. Marchese, and D. Quacci. The fibrillar organisation of the osteon and cellular aspects of its development. *Anatomical Science International*, 86(3):128–134, 2011. doi: 10.1007/s12565-010-0099-x.

Pazzaglia, U. E. and T. Congiu. The cast imaging of the osteon lacunar-canalicular system and the implications with functional models of intracanalicular flow. *J. Anat.*, 222(2):193–202, February 2013. doi: 10.1111/joa.12004.

Pazzaglia, U. E., T. Congiu, M. Marchese, F. Spagnuolo, and D. Quacci. Morphometry and patterns of lamellar bone in human haversian systems. *The Anatomical Record: Advances in Integrative Anatomy and Evolutionary Biology*, 295(9):1421–1429, 2012b. doi: 10.1002/ar.22535.

Perren, S. and J. Cordey. The concept of interfragmentary strain. In Uhthoff, H., editor, *Current concepts of internal fixation of fractures*, pages 67–77O. Springer, 1980.

Polig, E. and W. S. S. Jee. A model of osteon closure in cortical bone. *Calcif Tissue Int*, 47(5): 261–269, November 1990. doi: 10.1007/BF02555907.

Qin, Y.-X., C. T. Rubin, and K. J. McLeod. Nonlinear dependence of loading intensity and cycle number in the maintenance of bone mass and morphology. *J. Orthop. Res.*, 16(4):482–489, July 1998. doi: 10.1002/jor.1100160414.

Qing, H. and L. F. Bonewald. Osteocyte remodeling of the perilacunar and pericanalicular matrix. *Int J Oral Sci*, 1(2):59–65, June 2009. doi: 10.4248/ijos.09019.

Ramachandran, P. and G. Varoquaux. Mayavi: 3d visualization of scientific data. *Computing in Science & Engineering*, 13(2):40–51, March 2011. doi: 10.1109/MCSE.2011.35.

Ranvier, L. A. *Traité technique d'histologie 1889*. F. Savy, 1889.

Reichert, J. C., S. Saifzadeh, M. E. Wullschleger, D. R. Epari, M. A. Schütz, G. N. Duda, H. Schell, M. van Griensven, H. Redl, and D. W. Hutmacher. The challenge of establishing preclinical models for segmental bone defect research. *Biomaterials*, 30(12):2149–2163, April 2009. doi: 10.1016/j.biomaterials.2008.12.050.

Reid, S. A. A study of lamellar organisation in juvenile and adult human bone. *Anatomy and Embryology*, 174(3):329–338, January 1986. doi: 10.1007/BF00698783.

Reina-Romo, E., M. Gómez-Benito, J. Domínguez, F. Niemeyer, T. Wehner, U. Simon, and L. Claes. Effect of the fixator stiffness on the young regenerate bone after bone transport: Computational approach. *Journal of Biomechanics*, 44(5):917–923, March 2011. doi: 10.1016/j.jbiomech.2010.11.033.

Rensberger, J. M. and M. Watabe. Fine structure of bone in dinosaurs, birds and mammals. *Nature*, 406(6796):619–622, August 2000. doi: 10.1038/35020550.

Reznikov, N., R. Almany-Magal, R. Shahar, and S. Weiner. Three-dimensional imaging of collagen fibril organization in rat circumferential lamellar bone using a dual beam electron microscope reveals ordered and disordered sub-lamellar structures. *Bone*, 52(2):676–683, February 2013. doi: 10.1016/j.bone.2012.10.034.

Reznikov, N., R. Shahar, and S. Weiner. Bone hierarchical structure in three dimensions. *Acta Biomater*, 10(9):3815–3826, September 2014a. doi: 10.1016/j.actbio.2014.05.024.

Reznikov, N., R. Shahar, and S. Weiner. Three-dimensional structure of human lamellar bone: The presence of two different materials and new insights into the hierarchical organization. *Bone*, 59: 93–104, February 2014b. doi: 10.1016/j.bone.2013.10.023.

Rho, J.-Y., L. Kuhn-Spearing, and P. Zioupos. Mechanical properties and the hierarchical structure of bone. *Medical Engineering & Physics*, 20(2):92–102, March 1998. doi: 10.1016/S1350-4533(98)00007-1.

Riggs, C. M., L. E. Lanyon, and A. Boyde. Functional associations between collagen fibre orientation and locomotor strain direction in cortical bone of the equine radius. *Anat Embryol*, 187(3):231–238, March 1993. doi: 10.1007/BF00195760.

Robinson, R. A. and M. L. Watson. Collagen-crystal relationships in bone as seen in the electron microscope. *Anat. Rec.*, 114(3):383–409, November 1952. doi: 10.1002/ar.1091140302.

Rodionova, N. V., V. S. Oganov, and N. V. Zolotova. Ultrastructural changes in osteocytes in microgravity conditions. *Advances in Space Research*, 30(4):765–770, 2002. doi: 10.1016/S0273-1177(02)00393-9.

Roschger, P., E. P. Paschalis, P. Fratzl, and K. Klaushofer. Bone mineralization density distribution in health and disease. *Bone*, 42(3):456–466, March 2008. doi: 10.1016/j.bone.2007.10.021.

Rouiller, C., L. Huber, E. Kellenberger, and E. Rutishauser. LA STRUCTURE LAMELLAIRE DE l&rsquo;OST&eacute;ONE. *Cells Tissues Organs*, 14(1-2):9–22, 1952. doi: 10.1159/000140589.

Roux, W. Beitrage zur Morphologie der funktionnellen Anspassung. *Arch Anat Physiol Anat Abt*, 9: 120–158, 1885.

Rubin, C. T. and K. J. McLeod. Promotion of bony ingrowth by frequency-specific, low-amplitude mechanical strain. *Clinical orthopaedics and related research*, 298:165–174, 1994.

Ruth, E. B. Bone studies. i. fibrillar structure of adult human bone. *American Journal of Anatomy*, 80 (1):35–53, 1947. doi: 10.1002/aja.1000800104.

Saparin, P., H. Scherf, J.-J. Hublin, P. Fratzl, and R. Weinkamer. Structural adaptation of trabecular bone revealed by position resolved analysis of proximal femora of different primates. *The Anatomical Record: Advances in Integrative Anatomy and Evolutionary Biology*, 294(1):55–67, 2011. doi: 10.1002/ar.21285.

Schaffler, M. B., W.-Y. Cheung, R. Majeska, and O. Kennedy. Osteocytes: Master orchestrators of bone. *Calcif Tissue Int*, 94(1):5–24, January 2014. doi: 10.1007/s00223-013-9790-y.

Schell, H., M. S. Thompson, H. J. Bail, J.-E. Hoffmann, A. Schill, G. N. Duda, and J. Lienau. Mechanical induction of critically delayed bone healing in sheep: Radiological and biomechanical results. *Journal of Biomechanics*, 41(14):3066–3072, October 2008. doi: 10.1016/j.jbiomech.2008.06.038.

Schmidt-Bleek, K., H. Schell, N. Schulz, P. Hoff, C. Perka, F. Buttgereit, H.-D. Volk, J. Lienau, and G. N. Duda. Inflammatory phase of bone healing initiates the regenerative healing cascade. *Cell and Tissue Research*, 347(3):567–573, July 2011. doi: 10.1007/s00441-011-1205-7.

Schneider, P., M. Stauber, R. Voide, M. Stampanoni, L. R. Donahue, and R. Müller. Ultrastructural properties in cortical bone vary greatly in two inbred strains of mice as assessed by synchrotron light based micro- and nano-CT. *Journal of Bone and Mineral Research*, 22(10):1557–1570, 2007. doi: 10.1359/jbmr.070703.

Schneider, P., M. Meier, R. Wepf, and R. Müller. Towards quantitative 3d imaging of the osteocyte lacuno-canalicular network. *Bone*, 47(5):848–858, November 2010. doi: 10.1016/j.bone.2010.07.026.

Schneider, P., M. Meier, R. Wepf, and R. Müller. Serial FIB/SEM imaging for quantitative 3d assessment of the osteocyte lacuno-canalicular network. *Bone*, 49(2):304–311, August 2011. doi: 10.1016/j.bone.2011.04.005.

Schrof, S., P. Varga, L. Galvis, K. Raum, and A. Masic. 3d raman mapping of the collagen fibril orientation in human osteonal lamellae. *Journal of Structural Biology*, 187(3):266–275, September

2014. doi: 10.1016/j.jsb.2014.07.001.

Seeman, E. and P. D. Delmas. Bone quality — the material and structural basis of bone strength and fragility. *New England Journal of Medicine*, 354(21):2250–2261, May 2006. doi: 10.1056/NEJMra053077.

Shahar, R., C. Lukas, S. Papo, J. W. C. Dunlop, and R. Weinkamer. Characterization of the spatial arrangement of secondary osteons in the diaphysis of equine and canine long bones. *The Anatomical Record: Advances in Integrative Anatomy and Evolutionary Biology*, 294(7):1093–1102, July 2011. doi: 10.1002/ar.21405.

Shapiro, F. Bone development and its relation to fracture repair. the role of mesenchymal osteoblasts and surface osteoblasts. *Eur Cell Mater*, 15:53–76, December 2007.

Sharma, D., C. Ciani, P. A. Ramirez Marin, J. D. Levy, S. B. Doty, and S. P. Fritton. Alterations in the osteocyte lacunar-canalicular microenvironment due to estrogen deficiency. *Bone*, 51(3): 488–497, September 2012. doi: 10.1016/j.bone.2012.05.014.

Skedros, J., M. Mason, M. Nelson, and R. Bloebaum. Evidence of structural and material adaptation to specific strain features in cortical bone. *The Anatomical Record*, 246(1):47–63, 1996.

Skedros, J. G., J. L. Holmes, E. G. Vajda, and R. D. Bloebaum. Cement lines of secondary osteons in human bone are not mineral-deficient: New data in a historical perspective. *Anat. Rec.*, 286A(1): 781–803, September 2005. doi: 10.1002/ar.a.20214.

Skedros, J. G., S. D. Mendenhall, C. J. Kiser, and H. Winet. Interpreting cortical bone adaptation and load history by quantifying osteon morphotypes in circularly polarized light images. *Bone*, 44(3): 392–403, March 2009. doi: 10.1016/j.bone.2008.10.053.

Skedros, J. G., C. J. Kiser, K. E. Keenan, and S. C. Thomas. Analysis of osteon morphotype scoring schemes for interpreting load history: evaluation in the chimpanzee femur. *Journal of Anatomy*, 218 (5):480–499, 2011. doi: 10.1111/j.1469-7580.2011.01348.x.

Smith, J. W. The arrangement of collagen fibres in human secondary osteones. *JBJS*, 42 B:588–605, 1960.

Steiner, M., L. Claes, A. Ignatius, F. Niemeyer, U. Simon, and T. Wehner. Prediction of fracture healing under axial loading, shear loading and bending is possible using distortional and dilatational strains as determining mechanical stimuli. *J R Soc Interface*, 10(86), September 2013. doi: 10.1098/rsif.2013.0389.

Sugawara, Y., H. Kamioka, T. Honjo, K.-i. Tezuka, and T. Takano-Yamamoto. Three-dimensional reconstruction of chick calvarial osteocytes and their cell processes using confocal microscopy. *Bone*, 36(5):877–883, May 2005. doi: 10.1016/j.bone.2004.10.008.

Sutherland, R. L. *Handbook of Nonlinear Optics*. CRC Press, April 2003.

Tami, A. E., M. B. Schaffler, and M. L. Knothe Tate. Probing the tissue to subcellular level structure underlying bone's molecular sieving function. *Biorheology*, 40(6):577–590, 2003.

Taylor, A. F., M. M. Saunders, D. L. Shingle, J. M. Cimbala, Z. Zhou, and H. J. Donahue. Mechanically stimulated osteocytes regulate osteoblastic activity via gap junctions. *Am J Physiol Cell Physiol*, 292(1):C545–C552, January 2007. doi: 10.1152/ajpcell.00611.2005.

Teitelbaum, S. L. Bone resorption by osteoclasts. *Science*, 289(5484):1504–1508, September 2000. doi: 10.1126/science.289.5484.1504.

Teti, A. and A. Zallone. Do osteocytes contribute to bone mineral homeostasis? osteocytic osteolysis revisited. *Bone*, 44(1):11–16, January 2009. doi: 10.1016/j.bone.2008.09.017.

Thompson, W. R., S. Modla, B. J. Grindel, K. J. Czymmek, C. B. Kirn-Safran, L. Wang, R. L. Duncan, and M. C. Farach-Carson. Perlecan/hspg2 deficiency alters the pericellular space of the lacunocanalicular system surrounding osteocytic processes in cortical bone. *J. Bone Miner. Res.*, 26 (3):618–629, March 2011. doi: 10.1002/jbmr.236.

Thompson, W. R., C. T. Rubin, and J. Rubin. Mechanical regulation of signaling pathways in bone. *Gene*, 503(2):179–193, July 2012. doi: 10.1016/j.gene.2012.04.076.

Turner, C., A. Robling, R. Duncan, and D. Burr. Do bone cells behave like a neuronal network? *Calcified Tissue International*, 70(6):435–442, 2002. doi: 10.1007/s00223-001-1024-z.

Vaes, G. Cellular biology and biochemical mechanism of bone resorption: a review of recent developments on the formation, activation, and mode of action of osteoclasts. *Clinical orthopaedics and related research*, 231:239–271, 1988.

Van, P. T., A. Vignery, and R. Baron. Cellular kinetics of the bone remodeling sequence in the rat.

The Anatomical Record, 202(4):445–451, 1982. doi: 10.1002/ar.1092020403.

van Hove, R. P., P. A. Nolte, A. Vatsa, C. M. Semeins, P. L. Salmon, T. H. Smit, and J. Klein-Nulend. Osteocyte morphology in human tibiae of different bone pathologies with different bone mineral density - is there a role for mechanosensing? *Bone*, 45(2):321–329, August 2009. doi: 10.1016/j.bone.2009.04.238.

van Oers, R. F., R. Ruimerman, E. Tanck, P. A. Hilbers, and R. Huiskes. A unified theory for osteonal and hemi-osteonal remodeling. *Bone*, 42(2):250–259, February 2008. doi: 10.1016/j.bone.2007.10.009.

Varga, P., A. Pacureanu, M. Langer, H. Suhonen, B. Hesse, Q. Grimal, P. Cloetens, K. Raum, and F. Peyrin. Investigation of the three-dimensional orientation of mineralized collagen fibrils in human lamellar bone using synchrotron x-ray phase nano-tomography. *Acta Biomaterialia*, 2013. doi: 10.1016/j.actbio.2013.05.015.

Verborgt, O., G. J. Gibson, and M. B. Schaffler. Loss of osteocyte integrity in association with microdamage and bone remodeling after fatigue in vivo. *Journal of Bone and Mineral Research*, 15 (1):60–67, 2000. doi: 10.1359/jbmr.2000.15.1.60.

Vetter, A., Y. Liu, F. Witt, I. Manjubala, O. Sander, D. Epari, P. Fratzl, G. Duda, and R. Weinkamer. The mechanical heterogeneity of the hard callus influences local tissue strains during bone healing: A finite element study based on sheep experiments. *Journal of Biomechanics*, 44(3):517–523, February 2011a. doi: 10.1016/j.jbiomech.2010.09.009.

Vetter, A., F. Witt, O. Sander, G. N. Duda, and R. Weinkamer. The spatio-temporal arrangement of different tissues during bone healing as a result of simple mechanobiological rules. *Biomechanics and Modeling in Mechanobiology*, 11(1-2):147–160, March 2011b. doi: 10.1007/s10237-011-0299-x.

Vetter, A., D. R. Epari, R. Seidel, H. Schell, P. Fratzl, G. N. Duda, and R. Weinkamer. Temporal tissue patterns in bone healing of sheep. *Journal of Orthopaedic Research*, 28(11):1440–1447, November 2010. doi: 10.1002/jor.21175.

Vetter, A. C. *Mechanobiology of healing and regeneration of bone*. PhD thesis, Humboldt-Universität zu Berlin, Mathematisch-Naturwissenschaftliche Fakultät I, June 2010.

Wagermaier, W., H. S. Gupta, A. Gourrier, M. Burghammer, P. Roschger, and P. Fratzl. Spiral twisting of fiber orientation inside bone lamellae. *Biointerphases*, 1(1):1–5, March 2006. doi: 10.1116/1.2178386.

Waldeyer, H. über den Ossificationsprozess. *Arch. f. mikrosk. Anat. Bd. I*, 1865.

Wang, Y., L. M. McNamara, M. B. Schaffler, and S. Weinbaum. A model for the role of integrins in flow induced mechanotransduction in osteocytes. *Proc Natl Acad Sci U S A*, 104(40):15941–15946, October 2007. doi: 10.1073/pnas.0707246104.

Weidenreich, F. Knochenstudien. *Z. Anat. Entwickl. Gesch.*, 69(4-6):382–466, July 1923. doi: 10.1007/BF02593627.

Weiner, S. and H. D. Wagner. The material bone: Structure-mechanical function relations. *Annual Review of Materials Science*, 28(1):271–298, 1998. doi: 10.1146/annurev.matsci.28.1.271.

Weiner, S., T. Arad, I. Sabanay, and W. Traub. Rotated plywood structure of primary lamellar bone in the rat: Orientations of the collagen fibril arrays. *Bone*, 20(6):509–514, June 1997. doi: 10.1016/S8756-3282(97)00053-7.

Weiner, S. and W. Traub. Organization of hydroxyapatite crystals within collagen fibrils. *FEBS Letters*, 206(2):262–266, October 1986. doi: 10.1016/0014-5793(86)80993-0.

Weinkamer, R. and P. Fratzl. Mechanical adaptation of biological materials — the examples of bone and wood. *Materials Science and Engineering: C*, 31(6):1164–1173, August 2011. doi: 10.1016/j.msec.2010.12.002.

Wolff, J. Das Gesetz der Transformation der Knochen. *DMW - Deutsche Medizinische Wochenschrift*, 19(47):1222–1224, 1893. doi: 10.1055/s-0028-1144106.

Worster, A. A., B. D. Brower-Toland, L. A. Fortier, S. J. Bent, J. Williams, and A. J. Nixon. Chondrocytic differentiation of mesenchymal stem cells sequentially exposed to transforming growth factor-β1 in monolayer and insulin-like growth factor-i in a three-dimensional matrix. *J. Orthop. Res.*, 19(4):738–749, July 2001. doi: 10.1016/S0736-0266(00)00054-1.

Wysolmerski, J. J. Osteocytic osteolysis: time for a second look? *BoneKEy Rep*, 1:229, December 2012. doi: 10.1038/bonekey.2012.229.

Yamamoto, T., T. Domon, S. Takahashi, N. Islam, and R. Suzuki. Twisted plywood structure of an alternating lamellar pattern in cellular cementum of human teeth. *Anat Embryol*, 202(1):25–30, June 2000. doi: 10.1007/PL00008241.

Yamamoto, T., T. Hasegawa, M. Sasaki, H. Hongo, C. Tabata, Z. Liu, M. Li, and N. Amizuka. Structure and formation of the twisted plywood pattern of collagen fibrils in rat lamellar bone. *J Electron Microsc (Tokyo)*, February 2012. doi: 10.1093/jmicro/dfs033.

You, J., C. E. Yellowley, H. J. Donahue, Y. Zhang, Q. Chen, and C. R. Jacobs. Substrate deformation levels associated with routine physical activity are less stimulatory to bone cells relative to loading-induced oscillatory fluid flow. *J Biomech Eng*, 122(4):387–393, August 2000.

You, L., S. Weinbaum, S. C. Cowin, and M. B. Schaffler. Ultrastructure of the osteocyte process and its pericellular matrix. *The Anatomical Record Part A: Discoveries in Molecular, Cellular, and Evolutionary Biology*, 278A(2):505–513, June 2004. doi: 10.1002/ar.a.20050.

Young, R. W. Cell proliferation and specialization during endochondral osteogenesis in young rats. *The Journal of cell biology*, 14(3):357–370, 1962.

Zhang, J., G. Harbottle, C. Wang, and Z. Kong. Oldest playable musical instruments found at jiahu early neolithic site in china. *Nature*, 401(6751):366–368, 1999.

Ziegler, D. Studien über die feinere Strukur des Röhrenknochens und dessen Polarisation. *Deutsche Zeitschrift f. Chirurgie*, 85(1):248–266, December 1906. doi: 10.1007/BF02894991.

Zoumi, A., A. Yeh, and B. J. Tromberg. Imaging cells and extracellular matrix in vivo by using second-harmonic generation and two-photon excited fluorescence. *PNAS*, 99(17):11014–11019, August 2002. doi: 10.1073/pnas.172368799.

Appendix A

Osteon Properties and Results

This appendix aims to summarize properties from all evaluated osteons and report results of which only average values have been described in the main text. Listed in Tables A.1 and A.2, several calculated quantities are presented using the standardized nomenclature common in the bone community [Parfitt et al., 1987; Dempster et al., 2013].

The *osteon radius* $On.R$ and the *radius of the Haversian canal* $HCa.R$ were determined based on a manual selection (Section 4.2.3.2). The *volume of the evaluated bone* $eB.V$ was calculated by counting voxels of the dataset that lie between Haversian canal and cement line. The *canalicular density* $Ca.Dn = aCa.L/eB.V$ is calculated as the ratio of the integrated length of all canaliculli divided by the evaluated bone volume.

The *inhomogeneity of the network density* $\sigma(Ca.Dn)$ was determined using subvolumes of $400\,\mu\text{m}^3$ (Section 4.2.3.3). Using the orientation of the network with respect to the normal of the lamellae (Section 4.2.3.4), the *fraction of lateral network* $lCaL/aCa.L$ was calculated. Furthermore the *number of registered lamellae* $Lm.N$* with an *average thickness of the lamellae of* $Lm.\Delta Rd$ is listed. The *volume used for the evaluation of lamellar properties* e.g. the volume between inner and outermost registered lamella $elB.V$ is limited by the *angular section* $\Delta\phi$ that lies completely within the image.

Using the *lacunar volume density* $Lc.V/eB.V$ and the volume of an average lacuna $Lc.V = 251\,\mu\text{m}^3$ a *lacuna number density* $Lc.N/eB.V$ was estimated. In the dataset, $cLc.N$ *complete lacunae* did not extend beyond the border of the image, nor did they “touch” the cement line or the Haversian canal, allowing to calculate properties of the lacunae (Section 4.2.3.6). The *mean degree* of these complete lacunae is $Lc.\text{deg}$.

The symbol $iCmLn.Rd$ denotes the *radius* of a feature that we refer to as inner cement line, i.e. a region concentric around the Haversian canal without any canaliculi and a small network inside which resembles the morphology of a network close to a cement line (Section 4.3.2). In some datasets canaliculi do not reach the blood vessel without an apparent clear inner network structure. Such datasets are marked with an X, while a dash denotes osteons where the network is well connected to the Haversian canal. Last, *the angle between* the long axis of the *Haversian canal and the imaging axis* is reported as $HCa.\beta$. Additionally, projection images of all datasets in the style of Figure 4.12 are shown in Figures A.1–A.4.

---

* As the evaluated lamellae lie between two registered bright lamella, only $Lm.N - 1$ complete lamellae are evaluated.

FM03	o20	o21	o23	o24	o25	o26	o37	o39	o40	o41	o42	o43
$On.R\,[\mu\mathrm{m}]$	134	98.3	107	167	148	117	97.5	104	122	131	180	96.2
$HCa.R\,[\mu\mathrm{m}]$	30.6	26	41.7	111	55.4	27.3	42.2	40.3	34.2	26.4	74.4	25.7
$eB.V\,[10^6\,\mu\mathrm{m}^3]$	0.75	0.68	0.6	0.37	0.68	0.57	0.63	0.59	0.78	0.68	0.63	0.73
$Ca.Dn\,[\frac{\mu\mathrm{m}}{\mu\mathrm{m}^3}]$	0.082	0.088	0.061	0.076	0.058	0.084	0.069	0.07	0.091	0.068	0.083	0.09
$\sigma(Ca.Dn)\,[\frac{\mu\mathrm{m}}{\mu\mathrm{m}^3}]$	0.053	0.058	0.04	0.043	0.039	0.051	0.042	0.043	0.047	0.041	0.039	0.06
$lCa.L/aCa.L\,[\%]$	13.8	18.5	14.6	22.1	14.3	18.2	13.6	14.6	17.4	13.1	13.3	18.8
$Lm.N$	5	6	5	6	6	8	4	6	7	6	7	5
$Lm.\Delta Rd\,[\mu\mathrm{m}]$	6.99	8.27	8.37	7.28	8.03	7.26	8.78	7.82	6.67	8.79	8.59	8.21
$elB.V\,[10^6\,\mu\mathrm{m}^3]$	0.2	0.28	0.24	0.2	0.26	0.21	0.24	0.29	0.28	0.21	0.3	0.29
$\Delta\phi\,[°]$	135	165	142	56.2	103	123	188	143	183	134	82	306
$Lc.V/eB.V\,[\%]$	0.84	1.41	0.74	0.79	0.96	0.78	0.58	0.93	0.93	1.08	0.52	0.68
$Lc.N/eB.V\,[10^3\,\mu\mathrm{m}^{-3}]$	33.6	56	29.4	31.4	38.1	30.9	23.2	37.2	37.2	43.1	20.7	27.2
$cLc.N$	16	30	14	9	23	18	11	16	23	19	15	22
$Lc.\mathrm{deg}$	46.2	50	28.7	33.6	29.9	35.9	33.9	28.1	41.3	46.4	30.9	37.1
$iCmLn.Rd\,[\mu\mathrm{m}]$	60.9	X	X	-	67.8	-	X	X	-	-	83.9	-
$HCa.\beta\,[°]$	10.6	17.1	17.5	5.41	28.3	14.8	20.2	8.77	9.33	7.5	16.5	4.94

FM38	o1	o2	o3	o4	o5	o6	o7	o8	o9
$On.R\,[\mu\mathrm{m}]$	113	108	83.9	172	79.3	87.3	166	89.6	82.1
$HCa.R\,[\mu\mathrm{m}]$	38.3	21.2	23.6	52.4	19.1	21.4	53.6	26.2	27.6
$eB.V\,[10^6\,\mu\mathrm{m}^3]$	0.65	0.84	0.57	0.81	0.74	0.75	0.7	0.77	0.68
$Ca.Dn\,[\frac{\mu\mathrm{m}}{\mu\mathrm{m}^3}]$	0.032	0.064	0.065	0.057	0.079	0.071	0.076	0.067	0.06
$\sigma(Ca.Dn)\,[\frac{\mu\mathrm{m}}{\mu\mathrm{m}^3}]$	0.034	0.047	0.047	0.046	0.043	0.046	0.059	0.05	0.047
$lCa.L/aCa.L\,[\%]$	23.9	19.4	15.4	15.9	14.9	16.1	14.3	13.3	16.8
$Lm.N$	4	6	4	7	5	5	4	6	4
$Lm.\Delta Rd\,[\mu\mathrm{m}]$	5.37	6.33	7.06	7.61	7.26	6.96	8.16	7.24	7.42
$elB.V\,[10^6\,\mu\mathrm{m}^3]$	0.14	0.22	0.12	0.25	0.3	0.34	0.15	0.3	0.23
$\Delta\phi\,[°]$	126	149	184	61.1	354	355	77.8	210	351
$Lc.V/eB.V\,[\%]$	0.46	1.71	1.02	0.89	0.61	1.49	1.35	0.71	1.03
$Lc.N/eB.V\,[10^3\,\mu\mathrm{m}^{-3}]$	18.4	68.3	40.7	35.5	24.3	59.4	53.8	28.3	40.9
$cLc.N$	12	31	19	22	11	27	25	18	18
$Lc.\mathrm{deg}$	33.8	56.4	40.1	44.8	49.5	47.8	50.3	40.3	44.5
$iCmLn.Rd\,[\mu\mathrm{m}]$	56.1	42.5	X	102	-	35.3	-	X	X
$HCa.\beta\,[°]$	21.7	32.6	27.5	10.3	9.47	5.26	11.9	6.81	14.2

Table A.1: Table with summarized properties and results of all evaluated osteons of sample FM03 and FM38.

FM40	o1	o4	o5	o10	o11	o12	o13	o14	o7	o8	o9
$On.R\,[\mu\mathrm{m}]$	70.2	100	96.4	97.6	136	65.7	119	94.3	89.8	115	128
$HCa.R\,[\mu\mathrm{m}]$	19.9	43.2	26.8	31.7	31.9	12.2	37.9	15.9	26.9	38.1	26
$eB.V\,[10^6\,\mu\mathrm{m}^3]$	0.58	0.6	0.77	0.78	0.71	0.46	0.78	0.91	0.76	0.57	0.78
$Ca.Dn\,[\frac{\mu\mathrm{m}}{\mu\mathrm{m}^3}]$	0.074	0.092	0.079	0.073	0.087	0.064	0.091	0.074	0.07	0.073	0.071
$\sigma(Ca.Dn)\,[\frac{\mu\mathrm{m}}{\mu\mathrm{m}^3}]$	0.055	0.055	0.047	0.049	0.051	0.048	0.055	0.042	0.047	0.048	0.051
$lCa.L/aCa.L\,[\%]$	16.1	32.1	10.1	13.3	11.7	21.2	13.6	17.6	16.6	12	12.6
$Lm.N$	4	5	4	4	5	3	7	3	4	4	6
$Lm.\Delta Rd\,[\mu\mathrm{m}]$	8.54	8.78	9.38	8.73	8.43	8.12	7.23	9.56	8.73	8.44	7.21
$elB.V\,[10^6\,\mu\mathrm{m}^3]$	0.25	0.25	0.18	0.24	0.21	0.19	0.24	0.24	0.25	0.18	0.23
$\Delta\phi\,[°]$	355	158	183	246	119	354	102	302	308	143	111
$Lc.V/eB.V\,[\%]$	1.31	0.6	0.86	0.99	1.29	1.39	0.55	0.78	0.72	0.75	1.17
$Lc.N/eB.V\,[10^3\,\mu\mathrm{m}^{-3}]$	52	24	34.4	39.5	51.4	55.4	22	31	28.9	29.9	46.5
$cLc.N$	12	10	20	25	24	11	15	25	18	13	20
$Lc.\mathrm{deg}$	49.4	36.3	49.4	37.6	51.2	53.2	44	39.2	38.9	50.2	55.4
$iCmLn.Rd\,[\mu\mathrm{m}]$	-	-	38.8	-	55.2	-	-	41	-	-	66.1
$HCa.\beta\,[°]$	11.9	26.9	15.3	16.3	13.8	16.8	8.79	11.6	17	8.75	26.3

FM48	o10	o11	o12	o13	o14	o15	o3	o4	o5	o6	o7	o9
$On.R\,[\mu\mathrm{m}]$	93.5	161	100	188	120	101	106	140	161	97.1	98.4	154
$HCa.R\,[\mu\mathrm{m}]$	24.2	61.2	35.9	94	31.8	33.8	38.1	60.1	23.8	29.2	35.9	44.9
$eB.V\,[10^6\,\mu\mathrm{m}^3]$	0.84	0.69	0.77	0.68	0.77	0.68	0.52	0.82	0.89	0.86	0.71	0.79
$Ca.Dn\,[\frac{\mu\mathrm{m}}{\mu\mathrm{m}^3}]$	0.056	0.073	0.065	0.057	0.072	0.072	0.04	0.053	0.059	0.051	0.051	0.073
$\sigma(Ca.Dn)\,[\frac{\mu\mathrm{m}}{\mu\mathrm{m}^3}]$	0.04	0.04	0.041	0.04	0.046	0.041	0.033	0.036	0.051	0.043	0.047	0.039
$lCa.L/aCa.L\,[\%]$	17.5	23.2	14.9	14.2	14.2	13.5	15.1	13.3	13.6	13.2	14.4	11.3
$Lm.N$	5	8	4	7	6	7	7	11	8	6	5	12
$Lm.\Delta Rd\,[\mu\mathrm{m}]$	5.9	5.91	5.8	6.92	6.75	5.39	6.19	6.43	6.36	6.86	6.31	7.14
$elB.V\,[10^6\,\mu\mathrm{m}^3]$	0.24	0.3	0.21	0.25	0.21	0.25	0.24	0.31	0.33	0.29	0.31	0.36
$\Delta\phi\,[°]$	355	97.4	317	69.5	186	161	138	75.9	95.1	234	308	73.3
$Lc.V/eB.V\,[\%]$	1.12	0.72	0.88	0.83	0.68	0.57	1.26	1.94	1.02	0.68	0.49	0.77
$Lc.N/eB.V\,[10^3\,\mu\mathrm{m}^{-3}]$	44.6	28.6	35	33.1	26.9	22.5	50.1	77.2	40.6	26.9	19.6	30.6
$cLc.N$	21	20	23	21	27	20	14	35	30	15	14	20
$Lc.\mathrm{deg}$	40.6	42.3	38.5	41.9	34.4	26.9	52.9	53.7	45.5	48.9	44.1	36.9
$iCmLn.Rd\,[\mu\mathrm{m}]$	-	-	X	-	-	X	-	X	79.7	-	X	-
$HCa.\beta\,[°]$	8.26	10.1	7.71	10	19.5	1.58	5.75	9.46	16.9	7.21	10.2	14.1

Table A.2: Table with summarized properties and results of all evaluated osteons of sample FM40 and FM48.

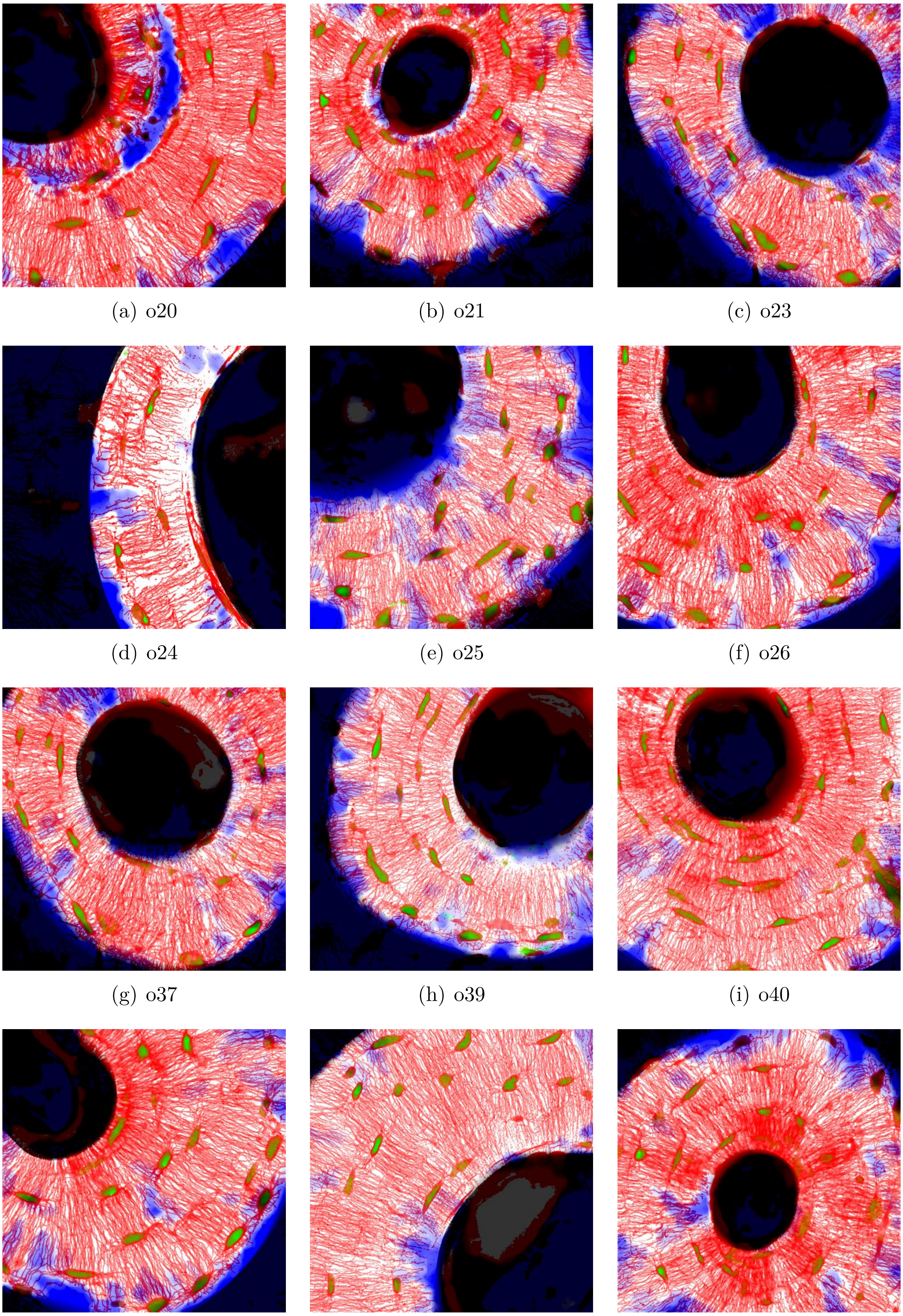

(a) o20 (b) o21 (c) o23

(d) o24 (e) o25 (f) o26

(g) o37 (h) o39 (i) o40

(j) o41 (k) o42 (l) o43

Figure A.1: Projection images of all datasets of sample FM03, with colors equivalent to Figure 4.12.

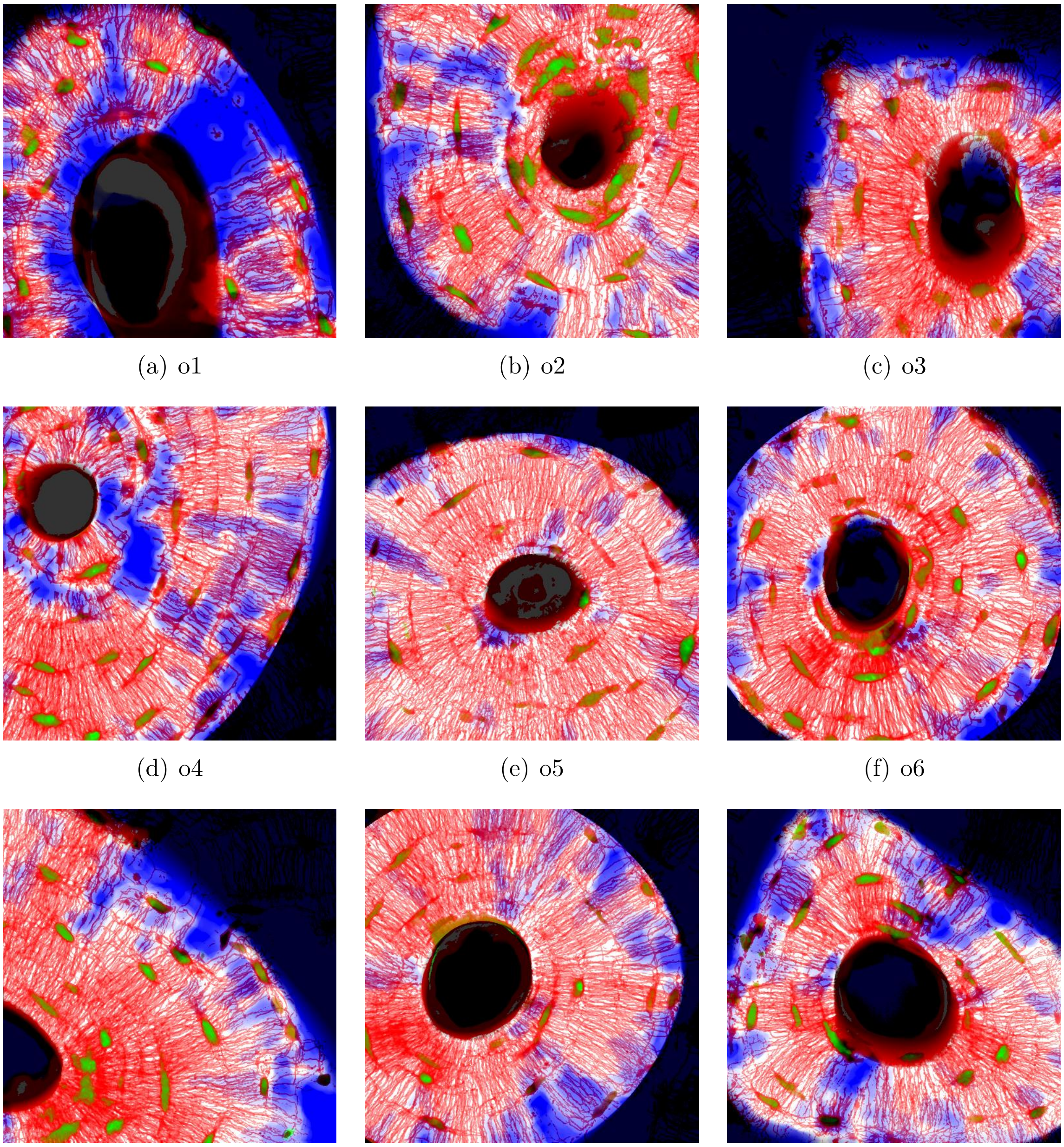

(a) o1 (b) o2 (c) o3

(d) o4 (e) o5 (f) o6

(g) o7 (h) o8 (i) o9

Figure A.2: Projection images of all datasets of sample FM38, with colors equivalent to Figure 4.12.

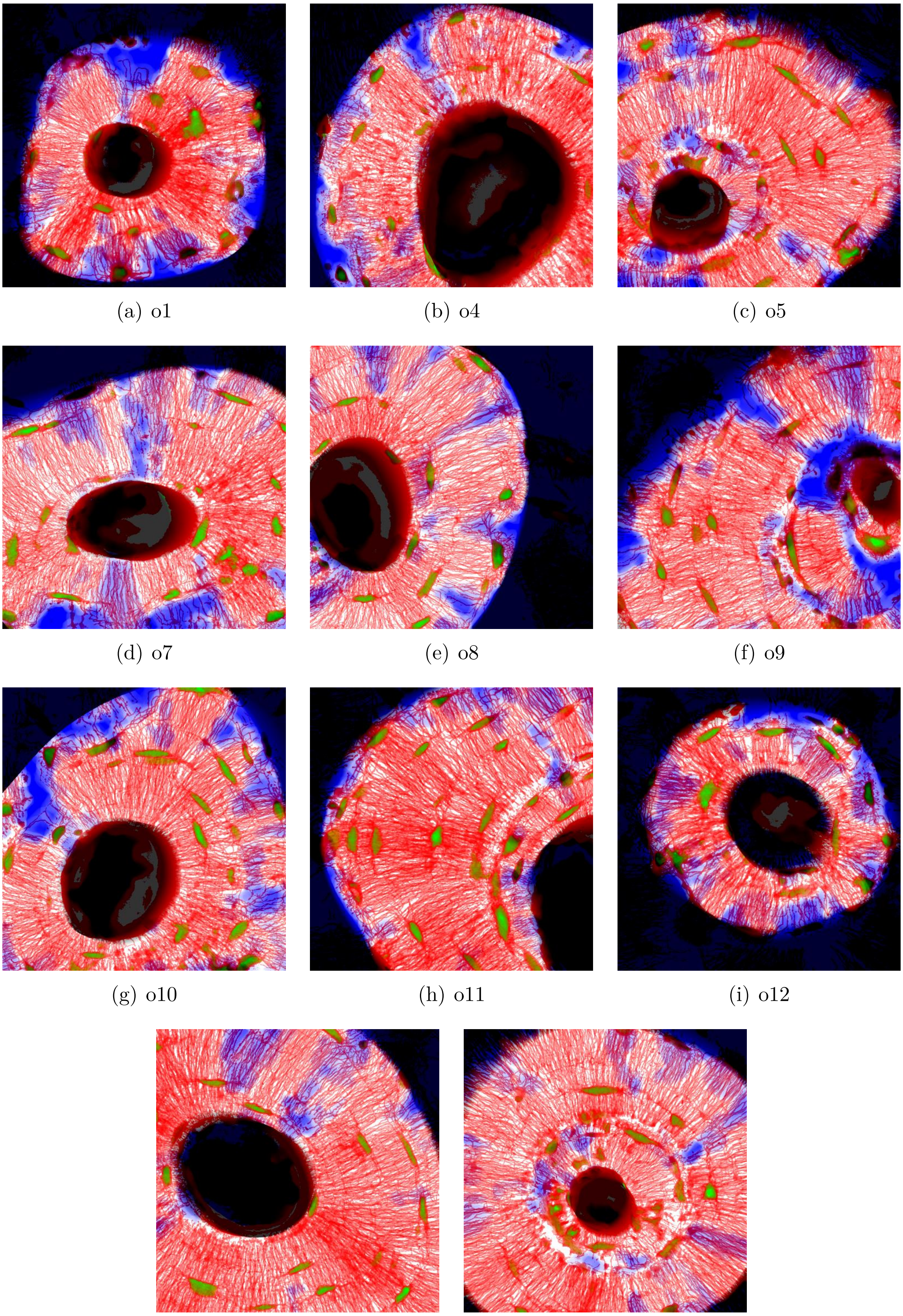

(a) o1

(b) o4

(c) o5

(d) o7

(e) o8

(f) o9

(g) o10

(h) o11

(i) o12

(j) o13

(k) o14

Figure A.3: Projection images of all datasets of sample FM40, with colors equivalent to Figure 4.12.

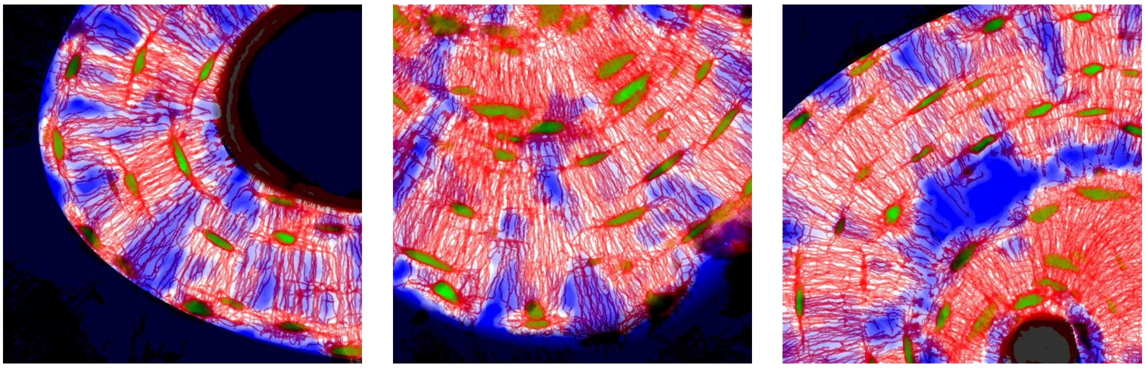

(a) o3 (b) o4 (c) o5

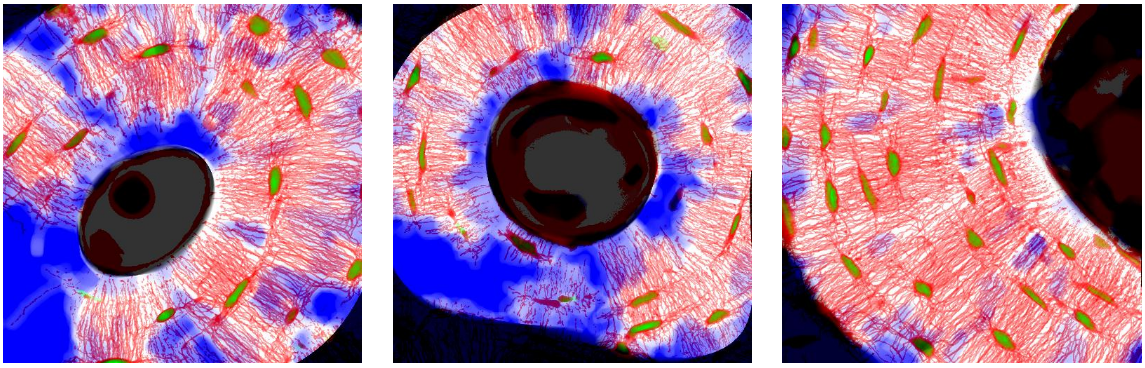

(d) o6 (e) o7 (f) o9

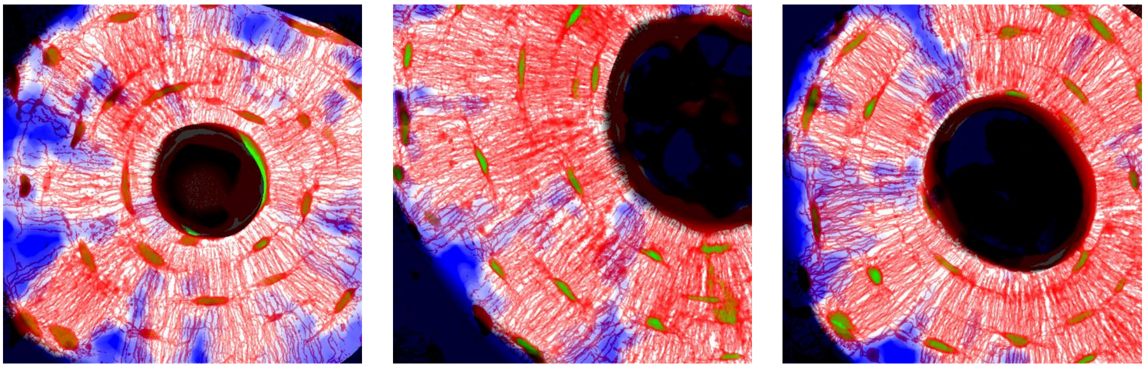

(g) o10 (h) o11 (i) o12

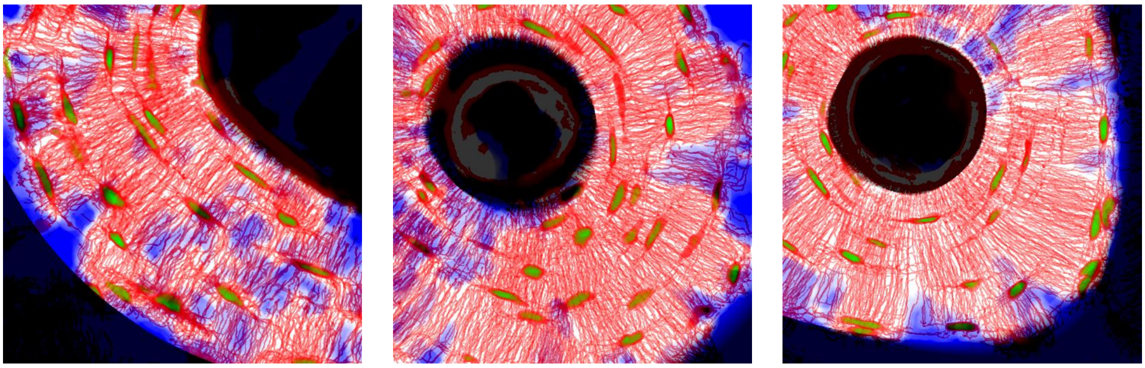

(j) o13 (k) o14 (l) o15

Figure A.4: Projection images of all datasets of sample FM48, with colors equivalent to Figure 4.12.

APPENDIX B

REGIONS WITHOUT NETWORK

In this appendix results of network densities and the inhomogeneity found within the datasets are presented when regions are excluded where no network is within a range of 5 μm and and the region extends over more than 130 μm^3. These regions will be referred to as "empty regions". All the calculation are performed as described in Section 4.2.3.3. Figures B.1 and B.2 show that the network densities of the different osteons become more similar than of the raw data (Figures 4.13 and 4.14)

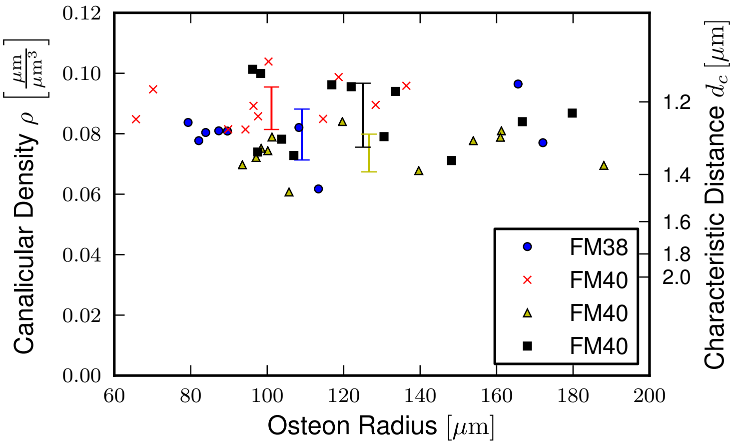

Figure B.1: Canalicular density vs. radius of the osteon of all osteons of the 4 samples, excluding bigger empty regions (see Figure 4.13 for the corresponding plot including the whole osteon). Within each sample, network density of the individual osteons become much more similiar. Still no correlation can be observed between the two plotted quantities.

In the frequency distributions of the density (Figure B.3) not only the first bin of the network density almost vanishes, but also the first few bins become lower, making the distributions look more like Poisson distributions than the original data.

The inhomogeneity gets reduced to $\sigma(\rho)/\mu(\rho) \approx 0.5$ (as seen in Figure B.3, compared to the value of $\sigma(\rho)/\mu(\rho) \approx 0.7$ in case the complete dataset is analyzed (Figure 4.16)). These values can be compared to the density distribution of a randomly arranged network. Assuming a random network of parallel canaliculi, e.g. unidirectional canaliculi the subvolume can be reduced to an area. 400 μm^3 of bone with a density of $\rho = 0.08\,\mu m^{-2}$ corresponds to $\mu_N = 4.3$ canaliculi per 54 μm^2. If the positions of the canaliculi are assumed to be random, the number of canaliculi per subvolume follows Poisson statistics, with a relative standard deviation of $\sigma(\rho)/\rho = 1/\sqrt{(\mu_N)} = 0.48$. This fits very well for

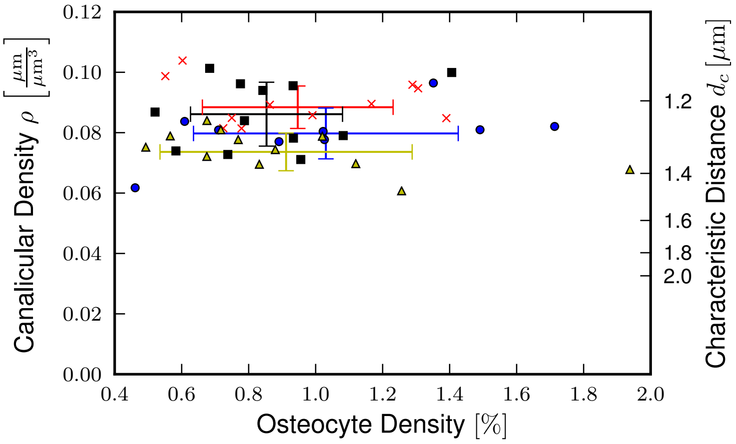

Figure B.2: Canalicular density vs. lacunar density all osteons, excluding bigger empty regions (see Figure 4.14 for the corresponding plot including the whole osteon). Within each sample, network density of the individual osteons become much more similiar. Still no correlation can be observed between the two plotted quantities.

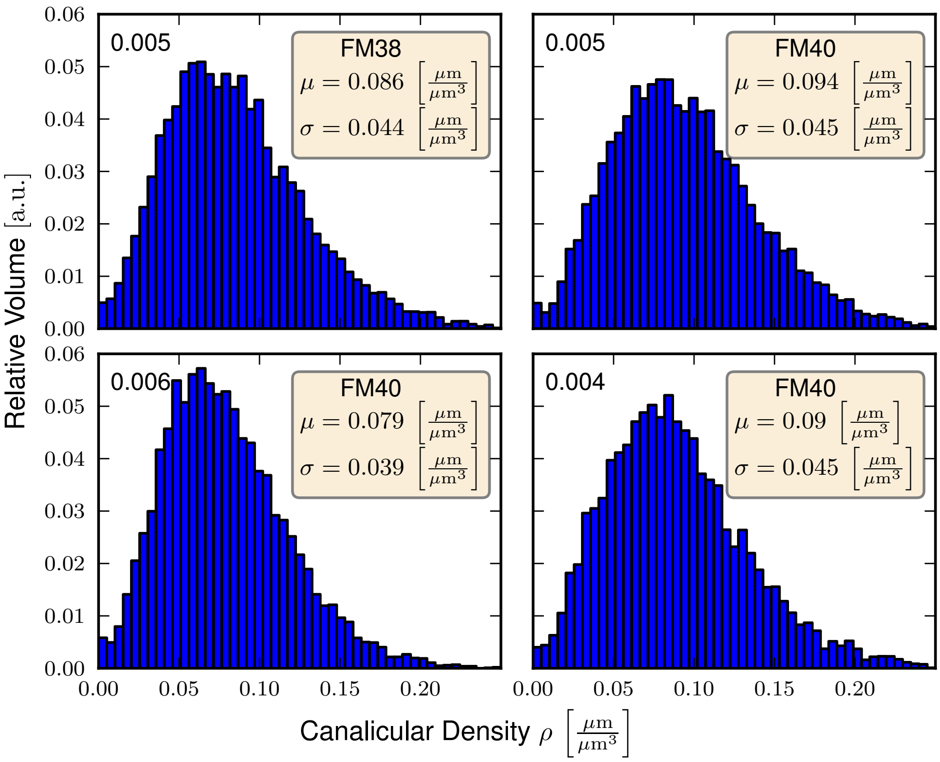

Figure B.3: Frequency distribution of the density within subvolumes of 400 μm^3 within the 4 samples. The number in the upper left corner refers to the hight of the first bin. The histograms, mean value and standard deviations are calculated using only subvolumes for which the calculated volume was $> 390\,\mu m^3$ after excluding bigger empty regions. Compared to the whole osteons, the mean density is higher, and the distribution appear more symmetric around the maximum.

the data which excluded the empty regions. Figure B.3 shows that the distributions of the density also look more like Poisson distributions. This suggests that the network is initially randomly distributed, and a clustering on a length scale of the cells further increases the inhomogeneity. This clustering could already be present in the initial network, due do an inhomogeneous distribution of cells, or arises later due to a local dying of the network (Section 4.4.2).

Figure B.4 shows the autocorrelation functions along the three axis. They appear to be a bit more equal than without the exclusion of empty regions (Figure 4.19).

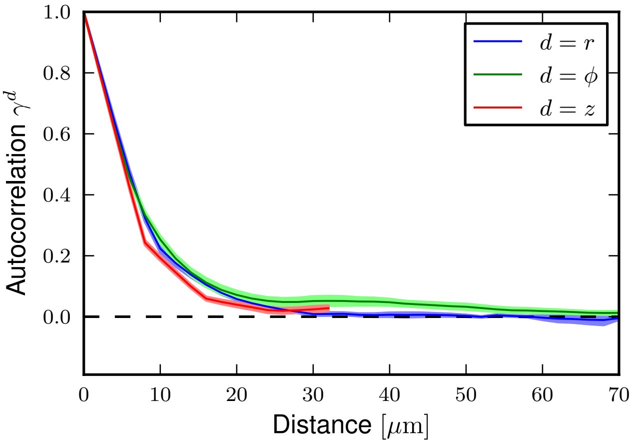

Figure B.4: Autocorrelation of the network density within subvolumes along three orthogonal directions excluding bigger empty regions (see Figure 4.19 for the corresponding plot including the whole osteon). The lines represent the mean value of the 4 samples, standard deviations within the samples are highlighted. Compared to the unmasked data, autocorrelations of r- and z-direction appear more similar when empty regions are excluded.

The spatial dependencies of the two osteons appear more similar after removing empty regions (Figure B.6). While both examples datasets now show densities that decrease as a function of the radius, the overall slope of the radial dependence is reduced to $m_{masked} = -0.23 \pm 0.4$ (standard deviation) compared to the original value of $m = -0.46$ but is still significant with $p = 3 \cdot 10^{-4}$. This means that half of the slope can be accounted to fluctuations in the network density on a length scale bigger than 5 μm.

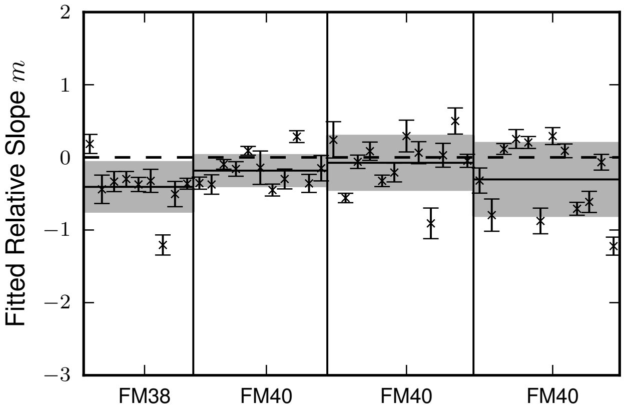

Figure B.5: Fitted slope of all osteons, excluding bigger empty regions (see Figure 4.18 for the corresponding plot including the whole osteon). The black lines spanning each sample indicate the mean value of all data points, gray denotes the standard deviation of slopes within one sample. The mean slope is below 0 for most osteons.

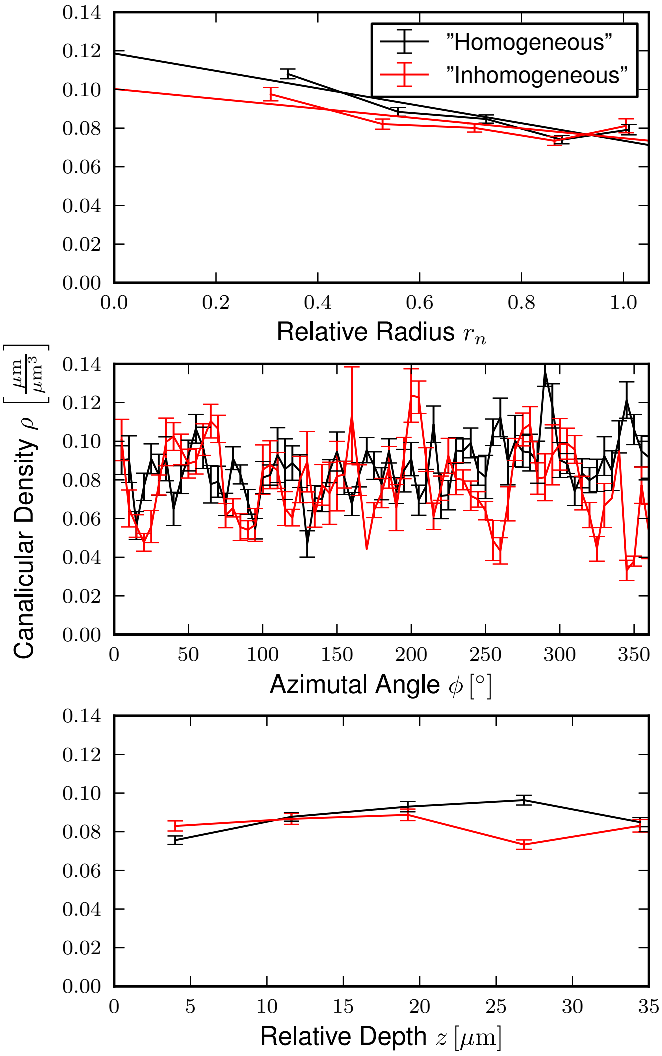

Figure B.6: Spatial dependencies of network densities for the two osteons of Figure 4.12. The two osteons which appeared to be quite different appear more similar after excluding bigger empty regions. (compare to Figure 4.17)

Appendix C

Second Harmonic Generation

Second harmonic generation (SHG) is a nonlinear, optical process which produces light of twice the frequency of the incident light. To correlate the osteocyte network to the lamellar structure of bone, we used the (SHG) signal generated by collagen to register the position of the lamellae. Not only is the exact structure of the lamellae unknown (Section 2.1.2), there are several possible origins of the contrast in the images we used: the signal intensity depends on collagen concentration, amount of order, orientation of the collagen [Freund et al., 1986], the diameter of the fibrils [LaComb et al., 2008] and the amount of cross linking of the collagen [Lutz et al., 2012]. Besides a brief introduction of the theory of SHG the terminology and the experimental setup, this Appendix summarizes some of experimental efforts which we made in order to understand the origin of the contrast observed in lamellar bone.

SHG is a process well described in literature [Franken et al., 1961; Sutherland, 2003] and frequently used for imaging biological materials [Pavone and Campagnola, 2013; Zoumi et al., 2002]. The dielectric polarization density **P** that is induced when light interacts with matter, can be developed as a Taylor series.

$$\mathbf{P}(t) = \varepsilon_0(\chi^{(1)}\mathbf{E}(t) + \chi^{(2)}\mathbf{E}^2(t) + \chi^{(3)}\mathbf{E}^3(t) + \ldots)$$

where $\chi^{(n)}$ is the n-th order susceptibility, ε_0 is the electric permittivity of vacuum and **E** is the electric field. The first nonlinear component

$$P_i^{(2)} = \varepsilon_0 \chi_{ijk}^{(2)} E_j E_k \tag{C.1}$$

oscillates with twice the frequency of the incident light, as can easily be seen when the time dependence of the two electrical field component $E_{j,k} \propto e^{i\omega t}$ are multiplied.

While for many materials $\chi^{(2)} \approx 0$, for collagen it has non vanishing entries: based upon macroscopic samples, collagen in dried rat tendon is known to exhibit piezo- and pyroelectric effects [Fukada and Yasuda, 1957][*]. This macroscopic polarity is related to the ability of SHG of light [Freund et al., 1986].

---

[*] This can by explained by the helical structure of collagen molecules and therefore an absence of center of inversion. Such piezo- and pyroelectric effects can only be observed if furthermore order on a macroscopic length scale is present, as otherwise the effects cancel out.

To achieve significant intensities a high energy density is needed. This is why we used a pulsed infrared laser for the imaging. Using a confocal microscope, high intensities are only achieved within the focus of the laser, therefore no pinhole is needed for optical slicing. However the confocal setup we used detects light in reflective (backward) direction while the second harmonic is typically generated in the forward direction.

The intensity of second harmonic light that is locally generated is not only dependent on the concentration and order of collagen, but also on the **orientation between collagen and polarization** of the ground wave (Equation C.1 is a vectorial equation). If collagen is parallel to the incident light no second harmonic is generated. While this alone is sufficient to explain the intensity distribution we observe (Figures 4.1, C.1), related to the detection in the backward direction, we also have to take other explanations into account.

In the quantum description of light, SHG can be understood as the creation of a new photon with twice the energy of the two incident photons. Energy conservation demands that the generated photon has twice the frequency of the incident photons. Opposed to fluorescence where photons typically origin from spontaneous emission, SHG is a coherent process. For an efficient generation of an SHG signal it is important that the generated light is in phase with the light that is generated at different positions within the sample. This phase-matching can be interpreted as conservation of the momentum as the wave vectors have to add up

$$k_{SHG} = k_1 + k_2.$$

Note that this obviously only applies for media which are nondispersive ($n(\omega_1) = n(\omega_2)$). From technical applications of SHG different approaches are known to fulfill this condition. If phase matching is achieved the majority of the light is expected propagate in the forward direction, whereas if a confocal microscope is used, the signal is detected in backward direction (reflection). LaComb et al. [2008] argues that depending on the fibril diameter and packing a **quasi-phase matching** can be achieved and the ratio of forward to backward generated light may be dependent on these properties.

Besides the option that light is generated in backward direction, it is also possible that **light that is emitted in forward direction is reflected**. Indeed, reflective confocal imaging provides results which are similar to our observations using SHG (Figure C.2), but has a reduced image quality .

A **comparison with other methods** is more helpful for interpreting SHG images. Two dimensional methods like electron microscopy of mineralized (and in some cases fractured) as well as unmineralized samples have been used in the past to describe collagen arrangement in bone without providing an universally accepted theory (Section 2.1.2). Raman imaging of the same regions could be used to measure collagen orientation [Galvis et al., 2013; Schrof et al., 2014]. FIB/SEM can also be used to obtain 3D images with a resolution high enough to resolve individual fibers but has the disadvantage of being a time consuming, destructive method [Reznikov et al., 2013, 2014b].

A comparison with SEM and polarized light images demonstrates that the SHG technique shows indeed what is usually defined as lamellae (Figure C.3). Since the used method in use is reflective, it allows to measure thick samples and, therefore, to image two perpendicular bone surfaces in bovine with circumferential lamellae running orthogonal

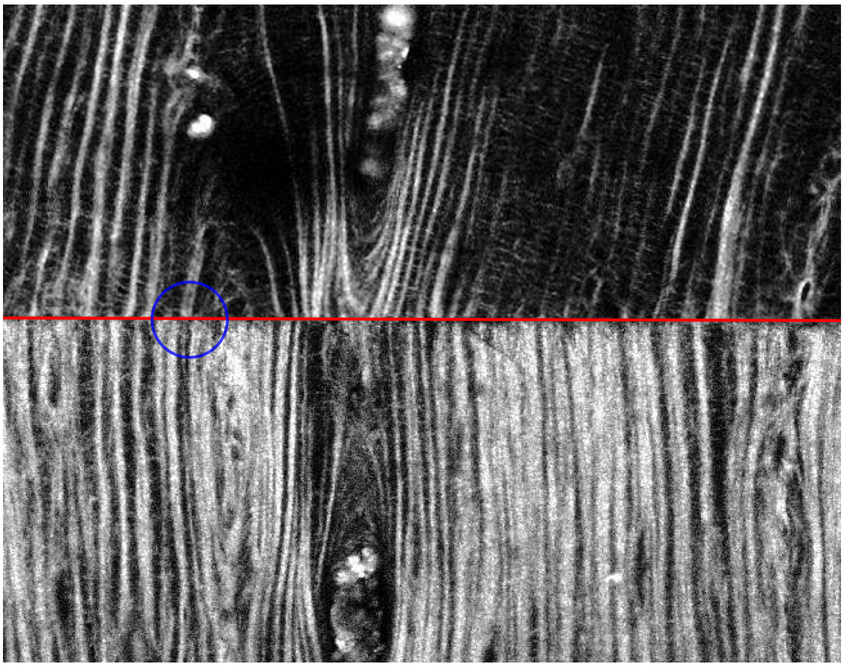

(a) Bovine bone

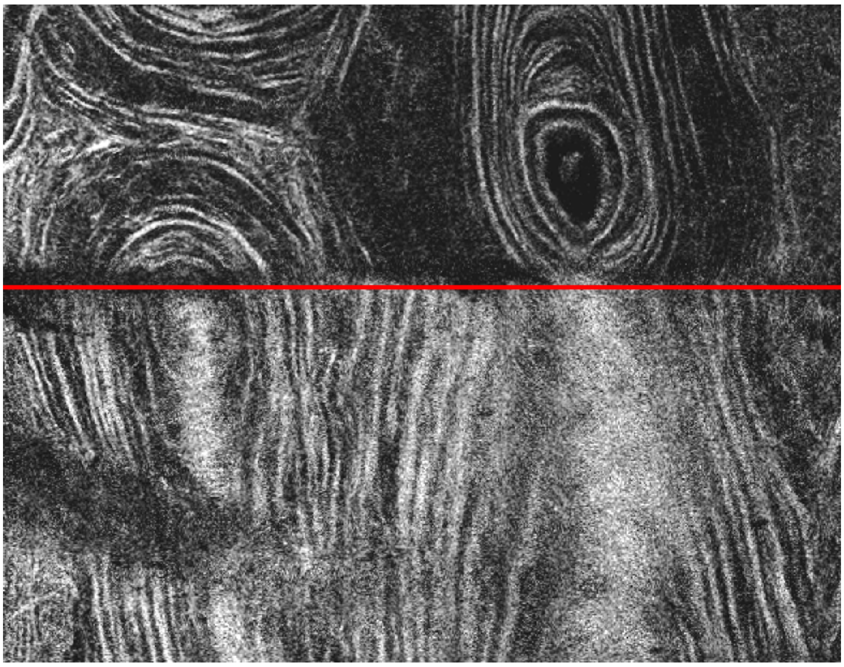

(b) Human bone

Figure C.1: Stitched images of SHG images of prismatic bone samples, e.g. thick samples with a 90° edge imaged from orthogonal directions. The red line indicates the 90° edge. (a) Bovine lamellar circumferential bone: the features of one surface seem inverted on the perpendicular surface, ranging from a big (dark region in the center of the lower side) to small length scales (thin lamella in blue circle). This shows that the observed signal has a strong dependence on the angle of collagen with respect to the imaging plane. In (b) human osteonal bone is shown. The same effect is less clear compared to (a) since in the sample an alternate lamellar pattern is not cut perpendicularly. However, the right osteon in (b) shows a weak lamellar pattern in the lower part, while it is dark in the upper part. This fits to the description of dark osteons with a collagen orientation oscillating around the long axis of the osteon.

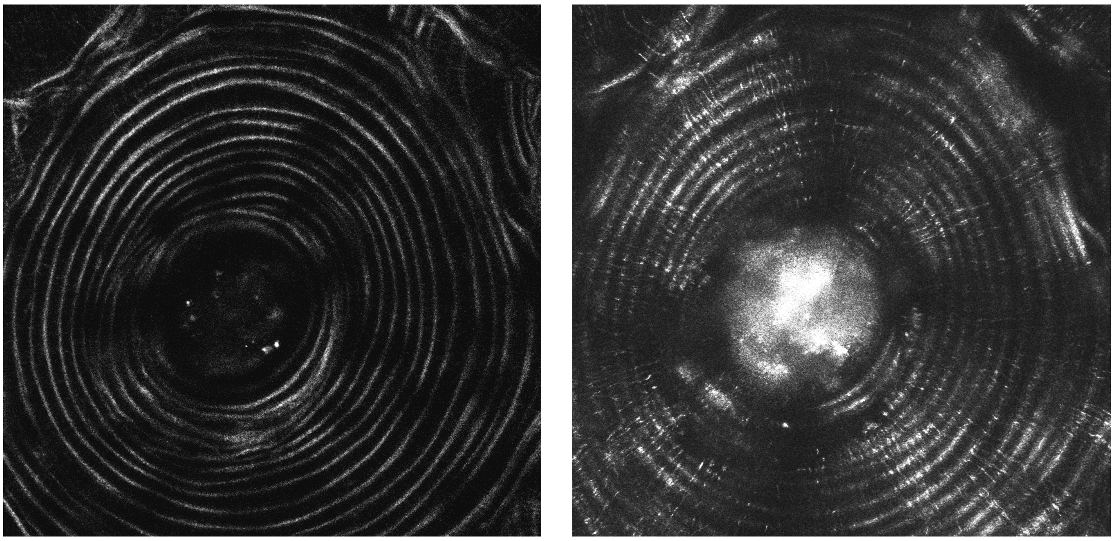

(a) SHG (b) Confocal reflection

Figure C.2: Comparison between the results of (a) SHG imaging and (b) classical confocal reflective imaging: Classical confocal reflective imaging shows the same general features as SHG imaging. The dark SHG signal at the Haversian canal and the location of lacunae and an overall better image quality of the SHG images make this method better suitable for our analysis.

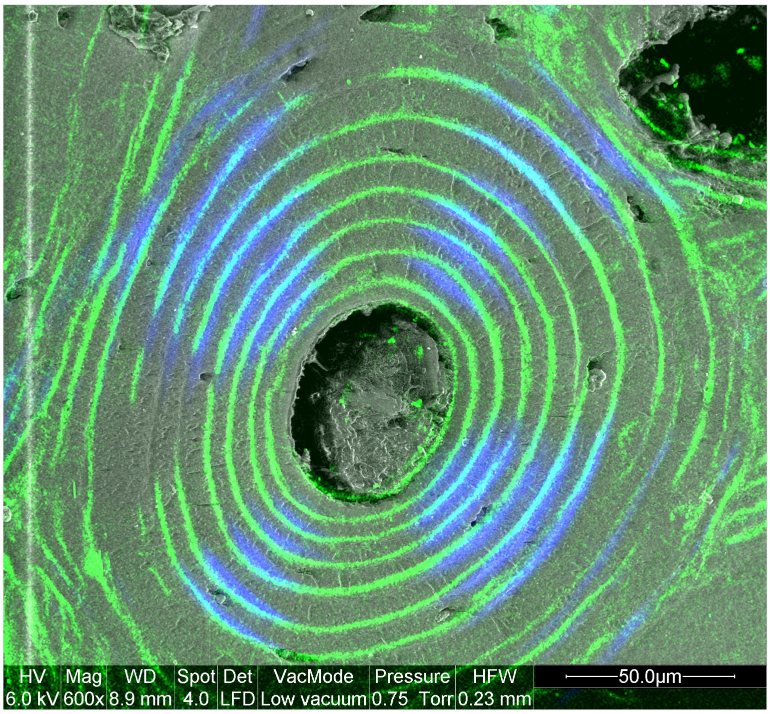

Figure C.3: Comparison between different imaging methods: The SHG image (green) fits so well with the SEM image that it completely hides the lamellae everywhere but on the left side of the image where due to an image artifact no SHG signal is detected (compare also Figure 2.4(a)). The signal from polarized light microscopy (blue) also superimposes well, but is only limited to a cross. As the light propagates through the sample with finite thickness, lamellae might appear wider then they are.

to both of the planes*. The contrast of the SHG image is changing from dark to bright when a lamella is imaged from an orthogonal plane (Figure C.1). This is strong evidence for the orientation dependence of the signal. However, it does not rule out that order can also influence the signal and might be the dominant source of contrast in different samples. A similar image of human osteonal bone is more difficult to get, as the center of an osteon with a clear lamellar structure needs to be located at the edge of the sample to obtain orthogonal lamellae at the two surfaces of the sample.

All in all, it seems reasonable that bright regions indicate collagen which is approximately orthogonal to the Poynting vector of the laser, and more parallel in dark regions. This fits necessary conditions of SHG, but is also in agreement with an reflected SHG signal as more surfaces are orthogonal to the incident light.

---

*Marotti [1993] referred to such samples as prismatic samples when studying them by SEM.

ACKNOWLEDGMENT

The are many people whom I want to thank, as during the time I have been working on this thesis I met many helpful people who helped me in different ways. There were those whose scientific input provided valuable ideas, others motivated me to finish this work.

First of all I have to thank Peter, as he was not only my official supervisor, but without him, neither the infrastructure, the colleagues nor my own funding would have existed. His spirit is also responsible for the incredible atmosphere within our department, facilitating fruitful collaborations and friendly relations to everyone. During the discussions on the osteocyte networks with Richard and Wolfgang he provided great insight. Richard I have to thank equally, as he was my direct supervisor he had to show a lot of patience to cope with my dealing of the stressful situation of working on a phd thesis. His support allowed me to follow my own interests while giving me great hinds and helped me to formulate my visions clearly. I would like to show gratitude to the committee, especially Prof. Dr. Igor Sokolov and Prof. Dr. Philip Thurner for reviewing this thesis.

I want to thank Wolfgang as he was not only tightly connected to the osteocyte network, with great emerging collaborations with Marta and Marie, he also made the collaboration with the INTEMA in Mar del Plata, Argentina possible. Further I have to thank Philip, Andreas V. and Micha whose initial work in the different projects I relied on, and who supported me in many different ways. Many thanks go to Sidney, who spend a lot of time assisting me in structuring writing the introduction and the background chapter. Also thanks to Ben, Clemens, Corina, Emely, Ingo, Jens, Kubok, Hannah, Lorenzo, Marc, Rebecca, Ronald, especially for proofreading parts of the thesis. I enjoyed in particular the scientific discussions with and introduction to instrument from, Andreas R., Anne, Birgit, Carmen, Clara, Luca, John, Mason, Marie, Marta, Matthieu, Paul R. Paul Z. and Ron. I should not forget all the other people in our department at our institute which made the breaks more enjoyable. For the great time in Argentina I have to thank José, Sheila, Ianina and Lucas.

Not to forget friends outside the MPI who had to handle my complains in difficult times, especially as they also discussed aspects of my thesis with me: Sven, Friedemann, Dana, Christoph, Dom, Denise, Luke, Willy, Vladimir, Kristina and my house mates. The warmest thanks go to my family which supported me all along the way.

EIDESSTATTLICHE ERKLÄRUNG

Hiermit versichere ich, dass ich meine Dissertation mit dem Titel "Computational Analysis of Dynamic Bone Structure and Processes –Osteocyte Networks & Healing –" selbstständig erarbeitet und verfasst habe, und keine anderen, als die von mir angegebenen Hilfsmittel und Quellen verwendet habe. Ich versichere, dass ich bisher an keiner Universität, weder im In- noch im Ausland, einen Promotionsversuch unternommen habe.

Ich erkläre hiermit außerdem, dass ich die Promotionsordnung der Mathematisch- Naturwissenschaftlichen Fakultät der Humboldt-Universität zu Berlin in der Fassung vom 06. Juli 2009 anerkenne.

Felix Repp

Berlin, Dezember 2014